Functional Analysis of Human Genetic Variants Using Zebrafish

Dissertation

Zur Erlangung des Doktorgrades der Mathematisch Naturwissenschaftlichen Fakultät der

Christian-Albrechts-Universität zu Kiel

vorgelegt von

Asalbanoo Farahvashi

October 7, 2024

Asalbanoo Farahvashi
Functional Analysis of Human Genetic Variants Using Zebrafish
Dissertation zur Erlangung des Doktorgrades der Mathematisch-Naturwissenschaftlichen Fakultät der Christian-Albrechts-Universität zu Kiel

Erstgutachter:	Prof. Dr. Hinrich Schulenburg
Zweitgutachter:	Prof. Dr. med. Marc Phillip Hitz, PhD

Tag der mändlichen Prüfung: 15. November 2024
Zum Druck genehmigt: 20. September 2024

Contents

Summary

Utilizing zebrafish as a model organism, this study investigates the genetic factors contributing to congenital heart defects (CHD) and cardiomyopathy (CM). Zebrafish offer unique advantages in cardiovascular research, such as optical transparency and rapid development, making them well-suited for studying developmental processes and disease pathogenesis. Molecular cytogenetic techniques identified novel variants in the *PRDM16* gene associated with ARVC. Additionally, ES (Exome sequencing) identified variants in the *CAPZβ* gene linked to patients with CHD. Functional analysis in zebrafish embryos revealed phenotypic similarities to human disease, implicating *CAPZβ* as a candidate gene for CHD and *PRDM16* in ARVC. Specifically molecular cytogenetic techniques identified four novel variants in the *PRDM16* gene in patients with ARVC and ES led to the identification of four novel variants in the *CAPZβ* gene among patients with CHD. Functional analysis in zebrafish embryos revealed that the CAPZβ-Ser192Asn variant led to impaired cardiac contractility and morphological defects resembling aspects of human CHD phenotypes. These findings suggest that *CAPZβ* may serve as a novel candidate gene for CHD and shed light on its role in early cardiac development. Similarly, transgenic zebrafish lines expressing *PRDM16* variants showed reductions in ventricle size and cardiac output, along with morphological defects during embryogenesis. In adult hearts, specific variants PRDM16-D628N and PRDM16-S1059L displayed increased presence of lipid droplets. Additionally, regeneration analysis revealed an impairment in the regenerative potential of zebrafish expressing a truncated variant of *PRDM16*. Taken together, these findings underscore the role of *PRDM16* in cardiac regeneration and its potential as a candidate gene for ARVC, highlighting its significance in disease pathogenesis. Overall, this study offers valuable insights into the genetic mechanisms associated with CHD and

CM, underscoring the significance of zebrafish models in unraveling disease pathogenesis and identifying potential therapeutic targets. Notably, the present research highlights the dual utility of zebrafish, serving as a developmental model for understanding heart formation and as an adult model for certain pathologies, enhancing its relevance in cardiovascular research. Further investigations are warranted to comprehensively elucidate the molecular pathways involving *PRDM16* and *CAPZβ* and to explore therapeutic strategies targeting these genes for the treatment of cardiovascular diseases and promotion of cardiac regeneration.

Zusammenfassung

Unter Verwendung des Zebrabärblings als Modellorganismus untersucht diese Studie die genetischen Faktoren, die zur Entstehung angeborener Herzfehler (AHF) und Kardiomyopathien (KM) beitragen. Zebrabärblinge bieten einzigartige Vorteile in der kardiovaskulären Forschung, wie optische Transparenz und schnelle Entwicklung, was sie besonders geeignet macht, Entwicklungsprozesse und die Pathogenese von Krankheiten zu untersuchen. Molekulare zytogenetische Techniken identifizierten neue Varianten im *PRDM16*, die mit der ARVC assoziiert sind. Darüber hinaus identifizierte die ES (Exom Sequenzierung) Varianten im *CAPZβ*, die mit AHF in Patientenkohorten in Verbindung stehen. Funktionelle Analysen in Zebrabärblingsembryonen zeigten phänotypische Ähnlichkeiten mit menschlichen Erkrankungen und legten nahe, dass *CAPZβ* als Kandidatengen für AHF und *PRDM16* für ARVC fungieren könnten. So konnte die Studie vier neue Varianten im *PRDM16* bei Patienten mit ARVC und vier neue Varianten im *CAPZβ* bei Patienten mit AHF identifizieren. Funktionelle Analysen in Zebrabärblingsembryonen zeigten, dass die CAPZβ-Ser192Asn-Variante zu einer beeinträchtigten Herzkontraktilität und morphologischen Defekten führte, die Aspekte menschlicher CHD-Phänotypen ähneln. Diese Ergebnisse legen nahe, dass *CAPZβ* als neues Kandidatengen für AHF dienen könnte und werfen Licht auf seine Rolle in der frühen kardialen Entwicklung. Ebenso zeigten transgene Zebrabärblingslinien, die PRDM16-Varianten exprimierten, eine Verringerung der Ventrikelgröße und des Herzzeitvolumens sowie morphologische Defekte während der Embryogenese. In adulten Herzen wiesen spezifische Varianten PRDM16-D628N und PRDM16-S1059L eine erhöhte Anwesenheit von Lipiddroplets auf. Darüber hinaus zeigte die Regenerationsanalyse eine Beeinträchtigung des regenerativen Potenzials von Zebrabärblingen, die eine trunkierende Variante von *PRDM16* exprimierten. Zusammenfassend

unterstreichen diese Ergebnisse die Rolle von *PRDM16* in der kardialen Regeneration und sein Potenzial als Kandidatengen für ARVC, was seine Bedeutung in der Krankheitspathogenese hervorhebt. Insgesamt bietet diese Studie wertvolle Einblicke in die genetischen Mechanismen, die mit AHF und KM verbunden sind, und betont die Bedeutung von Zebrabärblingsmodellen bei der Aufklärung der Krankheitspathogenese und der Identifizierung potenzieller therapeutischer Ziele. Bemerkenswert ist, dass die Forschung die doppelte Verwendung des Zebrabärblings hervorhebt, der sowohl als Entwicklungsmodell zum Verständnis der Herzformation als auch als Erwachsenenmodell für bestimmte Pathologien dient und somit seine Relevanz in der kardiovaskulären Forschung hervorgehoben wird. Weitere Untersuchungen sind erforderlich, um die molekularen Signalwege, die *PRDM16* und *CAPZβ* betreffen, umfassend zu verstehen und therapeutische Strategien zur Behandlung von Herz-Kreislauf-Erkrankungen und zur Förderung der kardialen Regeneration zu erforschen.

Abbreviations

% (v/v)	Volume concentration (volume/volume)
% (w/v)	Mass concentration (weight/volume)
°C	Degree Celsius
A	Adenine, Ampere or Alanine
Aa	Amino acids
AB	Allelic balance
ACC	American College of Cardiology
ACM	Arrhythmogenic cardiomyopathy
Actc	Actin alpha cardiac muscle 1
AHA	American Heart Association
AHF	angeborener Herzfehler
ALPM	anterior lateral plate mesoderm
Amp	Ampicillin
AOV	aortic valve
AP	Alkaline Phosphatase
ARVC	Arrhythmogenic right ventricular cardiomyopathy
AS	Aortic valve stenosis
ASDs	Atrial septal defects
ATP	Adenosine triphosphate
AV	Atrioventricular
AVS	Atrioventricular septum
AVSDs	Atrioventricular septal defects
BAV	Bicuspid aortic valve
BMP	Bone morphogenic protein
bp	Base pairs
bpm	Beat per minute

BSA	Bovine Serum Albumin
C	Cysteine
CADD	Combind Annotation Dependent Depletation
CAP	Actin capping protein
Capzα	Actin capping protein subunit Alpha
Capzβ	Actin capping protein subunit Beta
Capzγ	Actin capping protein subunit Gamma
cDNA	Complementary DNA
CHD	Congenital heart defects
CLSM	Confocal Laser Scanning Microscopy
CM	Cardiomyopathy
cm	Centimeter or compact myocardium
CMR	Cardiac magnetic resonance
CNCCs	Cardiac neural crest cells
Cx43	Connexin 43
CoA	coarctation of the aorta
CO	cardiac output
D	Aspartic acid
DAPI	4',6-Diamidino-2-phenylindo
DCM	Dilated Cardiomyopathy
DeTCT	Differential expression transcript counting technique
DGK	German Society of Cardiology
DGPK	German Society for Pediatric Cardiology
DNA	Deoxyribonucleic acid
DNAase	Deoxyribonuclease
dNTP	Deoxynucleotide triphosphat
DNVs	*de novo* variants
dpa	days post amputation
DPC	Day post coitum
ECAR	Extracellular acidification rate
ECM	Extracellular matrix
EDTA	Ethylenediaminetetraacetic Acid
EM	Electron microscope
EMT	Epithelial-to-Mesenchymal Transition
EPDC	Epicardium drived cells
ES	Exome sequencing, Exom Sequenzierung

ESC	European Society of Cardiology
E3	Embryo water
F	Forward
FACS	fluorescence-activated cell sorting
FPLD	familial partial lipodystrophy
FBS	Fetal bovine serum
FC	Fold Change
FGF	Fibroblast growth factor
FHF	First heart field
Fig.	Figure
g	Gravity
G	Glycine
GFP	Green fluorescent protein
GO	Gene Ontology
GS	Genome sequencing
h	Hour (s)
H2O	Millipore water
HCM	Hypertrophic cardiomyopathy
H&E	Hematoxylin and eosin
HEPES	4-(2-hydroxyethyl)-1-piperazineethanesulfonic acid
HLHS	Hypoplastic left heart syndrome
hpf	hours post fertilization
HCL	Hydrochloric Acid
IA	Injured Area
IAS	Interatrial septum
IVS	Interventricular septum
Kan	Kanamycin
Kb	Kilo base pairs
kDa	Kilo dalton
KOH	Potassium hydroxide
KM	Kardiomyopathien
L	Liter or Leucine
LA	left atrium
LB	Lauria Bertani (bacterial growth broth)
LoF	loss-of-function
LV	Left ventricle

LVNC	Left ventricular non-compaction
LVOT	Left ventricular outflow tract
M	molar
m	Milli
MA	Mitral atresia
mA	milliampere
Mb	millions of base pairs
Me2c	Myocyte-specific enhancer factor 2C
mg	Milligram
mM	milli molar
min	Minute(s)
mRNA	Messenger-RNA
MV	mitral valve
μ	Micro
μg	Microgram
μl	Microliter
μM	Micromolar
N	Asparagine or Number of replicates
n	sample size
NaOH	Sodium Hydroxide
NCBI	National Center for Biotechnology Information
Ng	Nanogram
NGS	Next-generation sequencing
nL	Nanoliter
n.s	Nonsignificant
OCR	Oxygen consumption rate
ORF	Open reading frame
P	peptide or Leucine
PA	Pulmonary artery
PBS	Phosphate Buffered Saline
PBT	PBS with Tween20
PCA	Principal Component Analysis
PCGC	Pediatric Cardiac Genomics Consortium
PCR	Polymerase Chain Reaction
PCNA	Proliferating cell nuclear antigen
PDA	Patent ductus arteriosus

PE	Pericardium
pmol	picomoles
PPS	pulmonary stenosis
PRDM16	Positive regulatory domain zinc finger region protein 16
PV	Pulmonary Valve
PVS	pulmonary valve stenosis
QC	Quality control
R	Reverse
RA	Right Atrium
RCM	Restrictive cardiomyopathy
RFP	Red fluorescent protein
RNA	Ribonucleic Acid
rpm	Rounds per minute
RO	Reverse Osmosis
ROS	reactive oxygen species
RT	Room Temperature or Reverse Transcription
RV	Right Ventricle
S	Serine
SCD	sudden cardiac death
SD	Standard deviation
SDS	Food or Sodiumdodecylsulfate
sec	Seconds
SHF	Secondary heart field
SEM	Standard Error of the Mean or Scanning electron microscope
SL	semilunar valve
T	Thymine
TAE	Tris-Acetate-EDTA-buffer
Taq	Thermophilus aquaticus
TEM	Transmission electron microscopy
TGA	Transposition of the great arteries
TOF	Tetralogy of fallot
Tm	Melting temperature
tm	trabecular myocardium
Tmod	Tropomodulin
Tris	Tris-(Hydroxymethyl) -Aminomethane
TV	tricuspid valve

U	Units
U	Units
UTR	Untranslated region
UV	Ultraviolet Light
V	Volt or valine
VSD	Ventricular septal defect
ES	Exome sequencing
WT	Wild Type
YFP	Yellow fluorescent protein

Chapter 1

Introduction

1.1 Heart Anatomy

The human heart, a conical and hollow muscular organ, is situated within the mediastinum (the central compartment of the thoracic cavity), closely surrounded by the thoracic skeleton and the lungs [1]. Predominantly located on the left side of the chest, the heart comprises integral components, including the fibrous skeleton, cardiac muscle, and a conduction system facilitating electrical impulse transmission and converting it to mechanical and rhythmical contraction. Encasing the heart is the pericardium, a double-membrane sac filled with fluid, providing a protective barrier for both the heart and associated blood vessels (Figure 1.1) [2]. Functioning as an anchor, the pericardium ensures stability by connecting the heart to the mediastinum [2]. At the exit of the large vessels, the innermost layer of the pericardium transforms into the epicardium, the outer connective tissue of the heart, which securely fuses with the heart [3]. The epicardium serves a dual function. Firstly, it acts as a protective layer for the inner heart tissues. Secondly, it actively contributes to the generation of pericardial fluid. This fluid occupies the pericardial cavity, which minimises friction between the pericardial membranes. Situated beneath the epicardium are essential components such as lymphatic vessels, nerves, veins, and coronary arteries. The epicardium constitutes the outermost layer of the heart wall [4]. The coronary vessels, extending into the underlying muscle layer called the myocardium, traverse a layer of fatty tissue beneath the epicardium. This arrangement is crucial for ensures the

blood supply to the heart muscle. The myocardium forms the middle layer of the heart wall and comprises specialized cells known as cardiomyocytes. These cardiomyocytes possess a distinctive structure and are the driving force behind the heart's contractions [5]. The endocardium forms the innermost layer of the heart wall and is characterized by its thinness. It envelops the heart valves and establishes a connection with the endothelium of major blood vessels. In the heart's atria and ventricle, the endocardium comprises both the endothelium and the subendothelial layer of connective tissue [6]. The human heart is comprises of four distinct chambers (refer to Figure 1.1), each with clear morphological and functional characteristics: the upper left and right atria, and the lower left and right ventricles. The atria are divided by an interatrial septum (IAS), while the ventricles are separated by an interventricular septum (IVS). Positioned between the IAS and IVS is the atrioventricular septum (AVS), which is relatively small. In humans, the AVS is called the membranous septum due to its thin fibrous structure [7]. Valves play a crucial role in coordinating blood flow by preventing it from flowing backward [8]. A healthy human heart possesses four valves. Among them, two are known as Atrioventricular (AV) valves, situated between the atria and ventricles. The right atrium and ventricle are interconnected by the tricuspid valve, characterized by its three separate leaflets. Conversely, the left atrium and ventricle are separated by the mitral valve, which features two distinct leaflets. The aortic and pulmonary semilunar (SL) valves separate the ventricles from the major arteries [9]. The leaflets of both the aortic and pulmonary valves are crescent moon-shaped, earning them the name "semilunar valves" [9]. The aortic valve is positioned between the left ventricle and the aorta. Its function is to prevent oxygen-rich blood from flowing back into the left ventricle [10]. On the other hand, the pulmonary valve acts as a link between the right ventricle and the pulmonary trunk. Furthermore, the leaflets of the AV valves are tethered to the papillary muscles via chordae tendineae [9]. These chordae tendineae serve as conduits, transmitting the contractions of the papillary muscles to the valve leaflets [9]. The primary role of the pulmonary valve is to facilitate the flow of deoxygenated blood towards the lungs. All four valves are situated in close proximity to essential components of the heart's electrical conduction system, including the sinoatrial node (SAN), atrioventricular node, bundle of His, and Purkinje fibers. These elements collectively contribute to the coordinated and rhythmic beating of the heart [11]. A typical double-beating of the heart occurs due to the opening and closing of the heart valves.

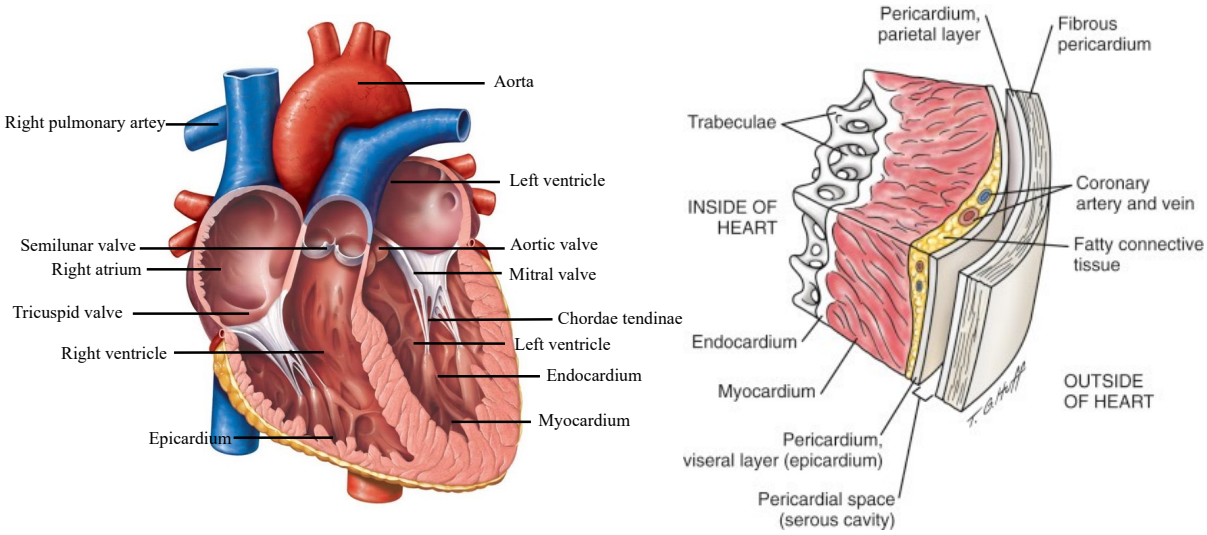

Figure 1.1: *The left panel indicates a schematic depiction of the human heart, deoxygenated blood from the body enters the right atrium through the superior and inferior vena cava. It then flows through the tricuspid valve (TV) into the right ventricle. From the right ventricle, the deoxygenated blood progresses through the pulmonary valve (PV) and then proceeds via the left and right pulmonary arteries, collectively referred to as the pulmonary trunk. The blood then flows to the lungs, where it undergoes oxygenation. Following its oxygenation in the lungs, the blood re-enters the heart through four pulmonary veins, entering the left atrium. Subsequently, it traverses through the mitral valve (MV) into the left ventricle. From there, the blood moves through the aortic valve (AOV) and embarks on its journey to the rest of the body through the aorta. Figure modified from (Marieb, 2012). The right panel shows structure of Heart wall [12].*

1.2 Cardiogenesis

During the initial three weeks of human embryonic development, the heart begins to take shape (around 15 days post coitum). Cardiogenesis, the process of cardiac development, can be categorized into four primary phases as despite in Figure 1.2:

1. Formation of cardiac crescent

2. Development of linear heart tube

3. Looping of the heart tube

4. Formation of septa, vessels, and heart valves

These phases delineate the intricate progression of heart formation during embryonic development [13]. The establishment of the heart, organized in the cardiac crescent, is orchestrated by cardiac gene program, which activation is governed by spatial and temporal cues mediated by signaling pathways including Wnt, fibroblast growth factor, and bone morphogenetic protein [14–16]. Core cardiac transcription factor genes, including *GATA4*, *NKX2-5* and *TBX5*, play a pivotal role in facilitating the expression of cardiac-specific genes [17]. The cardiogenesis encompass various cell types, including cardiomyocytes, endothelial cells, fibroblasts, and smooth muscle cells. The interplay between two distinct progenitor populations, namely the first heart field (FHF) and the second heart field (SHF), is pivotal in driving the process of cardiogenesis [18, 19]. The cardiac crescent, primarily composed of FHF progenitors, undergoes reorganization to develop into a linear heart tube. At 21 days post coitum (DPC), the heart tube begins to beat, marking the initiation of cardiac activity [13, 18]. Meanwhile, SHF progenitors play a role in elongating the heart during looping, and in the processes of cardiac chamber ballooning and septation [14, 20]. The migration of SHF progenitors plays a pivotal role in expanding the heart tube. This enlarged heart tube facilitates the establishment of a one-way flow of blood through peristaltic-like contractions [21]. Following the looping and ballooning phases, the individual ventricles of the heart tube experience lateral expansion, widening their structure [15, 22]. Moreover, the myocardial cells originating from the SHF migrate towards both ends of the tubular heart, contributing to the development of the inflow and outflow tract [22].

The interaction between cells from both the FHF and SHF is imperative for the proper formation of the right ventricle and atria [23–25]. The atrioventricular canal and outflow tract take shape during the right-directed looping process. This process involves a specific subset of mesenchymal cells that later play a crucial role in the developing of septa and heart valves [26]. The process of septation commences after 26 to 30 DPC. It is initiated through the participation of cardiac neural crest cells (CNCCs) and the formation of endocardial cushions. This intricate process leads to the separation of the atria, ventricles, and cardiac outflow tract [13]. The migration of cardiac neural crest cells as mesenchymal progenitor cells into the cardiac outflow tract contributes to the development of the aortic trunk and pulmonary trunk. This process is instrumental in promoting vascular development [27]. Concurrently, the development of semilunar valves—specifically the aortic valve and pulmonary valve—initiates around 42 to 44 DPC, while the completion of these valves and the formation of AV (mitral and tricuspid) occur at around 44 to

48 DPC. By the 60th DPC, marking the conclusion of the developmental phase, a fully formed four-chambered heart has emerged (Figure 1.2 [15,16]). The development of a fully functional and healthy heart results from precise coordination and interaction between genetic and epigenetic factors. This intricate process is tightly regulated by flow-dynamic stimuli and complex intra- and intercellular signaling mechanisms [28–30]. Disruptions and disturbances in heart development, including harmful gene variants and mutations, can lead to improper heart formation. This can result in the emergence of congenital cardiac malformations.

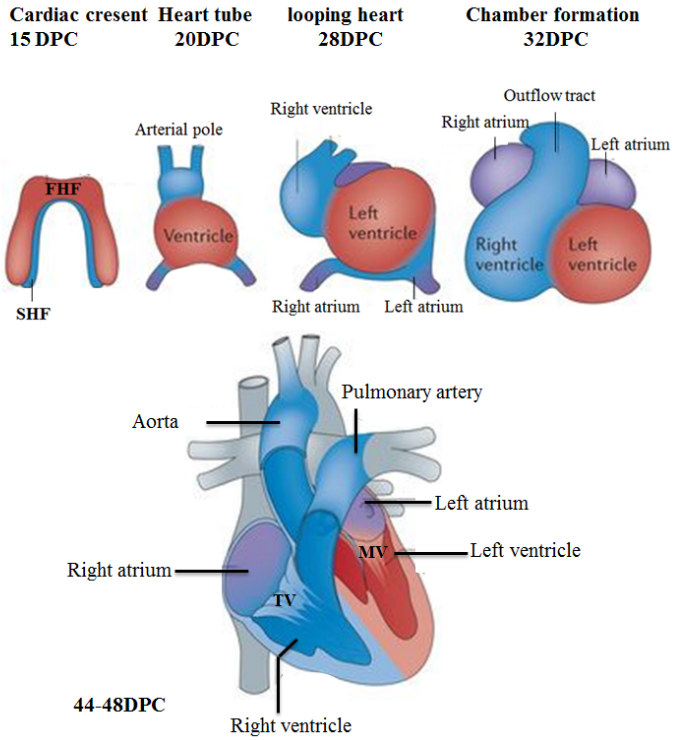

Figure 1.2: *A schematic depiction of cardiac morphogenesis reveals a sequence of events. Cardiogenic precursors converge to form a cardiac crescent, which then undergoes specification to shape distinct segments of the linear heart tube. This tube is subsequently patterned along the anterior-posterior axis, giving rise to the diverse regions and chambers of the mature, looped heart. Every cardiac chamber extends outward from the outer curvature of the looped heart tube in a segmented manner, creating distinct ballooning regions. Neural crest cells populate both sides of the bilaterally symmetrical aortic arch arteries and the aortic sac. This collective contribution aids in the formation of particular segments of the fully developed aortic arch, with each segment color-coded for distinction. Mesenchymal cells play a role in the creation of cardiac valves originating from the conotruncal and atrioventricular valve segments. The corresponding days of human embryonic development are indicated to signify the timeline of these crucial events. Figure modified from [31].*

1.3 Congenital Heart Disease

Congenital Heart Disease (CHD) is a prevalent birth defect, affecting approximately 6 to 13 per 1,000 newborns babies [32–35]. CHD refers to structural abnormalities in the heart's architecture that can impede normal blood flow, disrupt septation, and compromise the proper functioning of the valves [36]. Approximately 25% of cases of CHD necessitate immediate surgical and palliative interventions within the first year of life [37]. Due to the surgical and medical interventions, the mortality rate of CHD during infancy has been notably diminished [38]. Presently, around 90% of patients diagnosed with CHD survive into adulthood [38]. Nonetheless, cardiac malformations can vary from single defects (e.g. ventricular septal defect) to the presence of multiple and complex malformations [15]. Roughly 20%-30% of newborn babies with CHD are affected by neurodevelopmental delay [39]. When non-cardiovascular anomalies accompany CHD, it falls under the classification of syndromic CHD [40]. Beside syndromic and non-syndromic defects, CHDs can also be categorized based on their anatomical subtype and the oxygen saturation of blood. This classification divides CHDs into two main groups: cyanotic cardiac malformations and non-cyanotic cardiac malformations as illustrated in figure 1.3 [32]. Cyanotic CHDs, including Transposition of the Great Arteries (TGA), Tetralogy of Fallot (ToF), tricuspid atresia, and hypoplastic left heart syndrome (HLHS), cause cyanosis, where infants appear blue due to the mixing of oxygenated and deoxygenated blood [41]. Non-cyanotic CHDs are divided into shunt defects and valvular defects. Shunt defects, classified as pre-tricuspid or post-tricuspid, include: Pre-tricuspid: Atrial septal defects (ASDs), anomalous pulmonary venous connections, partial atrioventricular septal defects (pAVSDs). Post-tricuspid: Ventricular septal defects (VSDs), complete atrioventricular septal defects (cAVSDs), patent ductus arteriosus (PDA), aortopulmonary windows [32,41]. Valvular anomalies encompass a range of disorders affecting the heart valves and associated structures. These include stenosis or insufficiency of the tricuspid valve, such as in Ebstein anomaly, as well as anomalies of the pulmonary valve and arteries. Additionally, conditions affecting the mitral and aortic valves, including bicuspid aortic valve (BAV), and aortic coarctation are also noted [41], as depicted in figure 1.3.

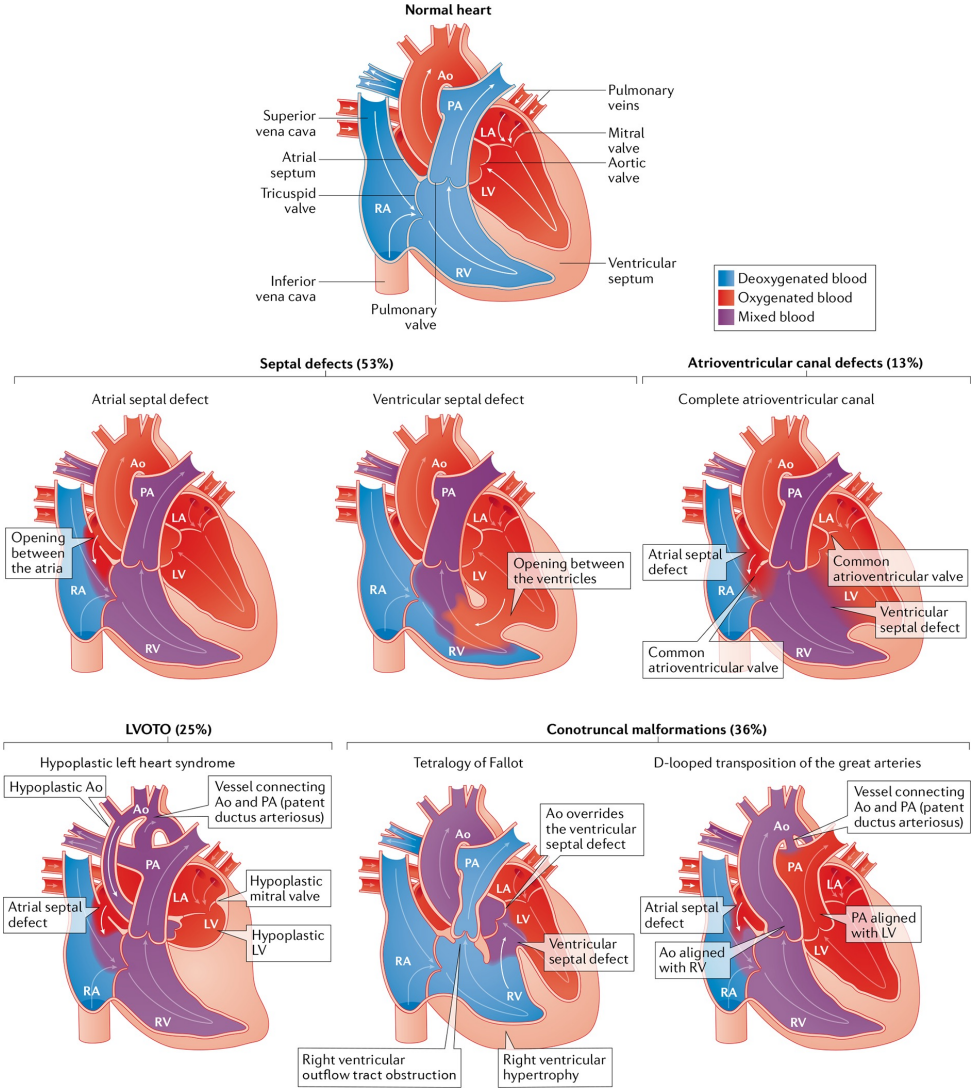

Figure 1.3: *Common types of congenital heart disease: A schematic representation of congenital heart defects can be organized based on anatomical subtypes. Irregular connections between the heart chambers, such as atrial or ventricular septal defects or atrioventricular canal defects, generally result in acyanotic conditions due to the left-to-right shunting of oxygenated blood into the pulmonary circulation. Left ventricular outflow tract obstructions (LVOTOs) encompass a spectrum of anomalies from isolated aortic stenosis to combinations of anomalies like hypoplastic left heart syndrome with mitral and aortic stenosis. These conditions can be associated with cyanosis due to shunting of deoxygenated blood into the systemic circulation. Examples of conotruncal malformations LVOTOs include tetralogy of Fallot and transposition of the great arteries. Ao, aorta; LA, left atrium; LV, left ventricle; PA, pulmonary artery; RA, right atrium; RV, right ventricle. Figure taken from [32].*

1.4 Genetic factors of Congenial Heart Disease

The etiology of CHD is multifactorial, with both genetic and environmental factors implicated. Specific genetic causes are detectable in approximately 40% of CHD cases [42–44]. Genetic factors play a significant role in the development of CHD, and understanding these factors is crucial for diagnosis, management, and potential prevention [45]. Although many genes have been identified in the pathogenesis of syndromic CHD, determining the genetic contributors of non-syndromic CHD is more challenging due to genetic heterogeneity, incomplete segregation, and potentially oligogenic or polygenic origins. Due to technical advancements, such as massively parallel or next-generation sequencing (NGS), rare variants in new candidate genes likely contributing to non-syndromic CHD have been discovered [42, 46–48]. Genetic causes of CHD include chromosomal anomalies or aneuploidies (approximately 13%, with a range of 9% to 18%) [43, 46], copy number variants (CNVs) (about 10–15%, with 3% to 25% in syndromic CHD and 3% to 10% in non-syndromic CHD) [46, 49–51], and single-gene disorders (12%) [42, 44, 46, 52].

1.4.1 Chromosomal anomalies and CHDs

Chromosomal aneuploidies, involving morphological or numerical alterations in one or more autosomes or sex chromosomes [53], are among the earliest recognized genetic factors contributing to CHDs [54]. Numerous chromosomal syndromes are linked to CHDs. Notably, around 45-50% of individuals with trisomy 21 have CHDs [55], with about 76% of these patients exhibiting atrioventricular septal defects (AVSD) [56]. Additionally, 60-80% of those with trisomy 13 and trisomy 18 [57] and 23-50% of individuals with Turner syndrome (10-15% of whom have aortic coarctation) exhibit structural heart defects [58]. These chromosomal abnormalities demonstrate a connection to various CHDs with differing frequencies. As a result, it is challenging to attribute a specific CHD phenotype to a particular chromosomal aberration [59]. Overall, approximately 30% of congenital heart disease cases are linked to other syndromes [60]. Out of these syndromic cardiac defects, around 25%-30% can be attributed to unbalanced chromosome disorders, encompassing aneuploidies and structural chromosomal alterations, including submicroscopic chromosomal abnormalities CNV [61].
The most prevalent CNV associated with CHD is a 3 Mb deletion on chromosome 22q11.2, linked to Velocardiofacial syndrome (also known as microdeletion syndrome 22q11.2),

with approximately 75% of individuals exhibiting CHD [62]. This CNV is observed in approximately 15% of all cases of ToF, occurring in around one out of 4000-6000 live birth [63].
Although the 22q11.2 deletion impacts more than 30 genes, sequence analysis and animal models have indicated a diminished gene dosage of the transcription factor *TBX1* as a significant factor. The *TBX1* gene is supposed to play a role in regulating cell proliferation within the second heart field, making it a potential causative factor in the development of cardiac malformations [64]. Additional well-defined CNVs associated with CHD include chromosome 1p36 deletion syndrome (1p36DS), which is characterized by a deletion of genetic material on the short arm of chromosome 1 at position 36 [65]. The deletion size in chromosome 1p36 deletion syndrome (1p36DS) is variable, up to 16.5 Mb, and not always associated with phenotype severity [66]. Congenital heart defects are present in 43–71% of cases, mostly ventricular septal defects (VSD) at 14%, and cardiomyopathy occurs in 22–27% of cases [65]. Analyses have revealed CNVs that are causally associated with isolated CHDs. For instance, large *de novo* CNVs have been identified in isolated cases of left-sided CHDs (LS-CHDs) like HLHS, [67, 68] and other sporadic instances of CHD [69–71]. Additional chromosome disorders associated with CHD include Cri-du-Chat syndrome (resulting from a deletion in 5p15.2, with CHD present in 15-30% of cases) [72], Cat Eye Syndrome (caused by an inversion and duplication in 22q11, with CHD present in 30-60% of cases) [73], Jacobsen syndrome (arising from a deletion in 11q23, with CHD present in 56% of cases) [74], and Williams-Beuren syndrome (typically associated with supravalvar aortic stenosis and involving a deletion in 7q11.23, with CHD present in 75-80% of cases) [54, 75].

Monosomy 1p36 deletion

Deletions affecting a specific region in the short arm (p) of chromosome 1, known as 1p36 deletions, occur in approximately 1 in 5,000 newborns, making them the most frequently observed terminal deletions in humans [65]. Numerous individuals documented in these reports exhibited unbalanced translocations, wherein their 1p36 deletions were coupled with an acquisition of genetic material from a non-homologous chromosome [76]. The 1p36 deletion syndrome is characterized by prominent features including craniofacial dysmorphism, structural brain abnormalities, seizure disorder, hearing loss, intellectual disability, and growth delay [65, 76, 77]. A notable percentage (ranging from 22% to 27%)

of individuals with 1p36 deletion syndrome exhibit cardiomyopathy, which can manifest with or without structural heart abnormalities [65, 66, 77, 78]. Due to the widespread clinical use of array-based copy number detection assays, there is a growing identification of small interstitial deletions spanning the 30 Mb DNA region of chromosome 1p36. In numerous instances, the phenotypes observed in these individuals are different from those with terminal deletions, as they result from haploinsufficiency of a specific set of genes [79, 80]. The majority of genes responsible for the various phenotypes associated with 1p36 deletions remain undiscovered. Additionally, many of the observed 1p36-related phenotypes could arise from the haploinsufficiency of multiple genes within a specific genomic region. Recent studies have confirmed that haploinsufficiency of *MMP23B*, *GABRD*, *SKI*, *PRDM16*, *KCNAB2*, and *LUZP1* are implicated in the manifestation of various phenotypes associated with 1p36 deletions [65, 81].

1.4.2 Monogenic disorders associated with CHD

In addition to chromosomal abnormalities, a *de novo* or inherited genetic variant can be identified as pathogenic in approximately one-third of CHD cases. This can be classified as monogenic if it is determined to be the underlying cause of a heart defect. Structural heart defects are prevalent in several monogenic syndromes. For example, around 90% of individuals with Alagille syndrome, which is attributed to loss-of-function mutations in the *JAG1* gene, present with congenital cardiac anomalies such as PPS, TOF, PA [46, 82–84]. Other syndromes frequently associated with CHD include Noonan syndrome, which arises from pathogenic and likely pathogenic variants in the RAS signaling pathway, leading to CHD in 80-90% of patients, predominantly manifesting as dysplastic pulmonary valve stenosis (PVS) [46, 85, 86]. Additionally, 75-85% of individuals with CHARGE syndrome, caused by mutations in the *CHD7* gene, exhibit TOF [46, 87]. Approximately 60% of those with Ellis-van Creveld syndrome, due to causal variants in the *EVC* and *EVC2* genes, present with common atrium [46, 88]. Furthermore, 50% of individuals with Kabuki syndrome, associated with pathogenic and likely pathogenic variants in the *KMT2D* and *KDM6A* genes, also exhibit a variety of congenital heart defects, including CoA, BAV, VSD, TOF, TGA, and HLHS [46, 89]. With the advancement of modern sequencing technologies like ES, numerous previously unidentified syndromes have come to light in recent years. A comprehensive study by the Pediatric Cardiac Genomics Consortium (PCGC), involving 2,871 CHD probands, identified deleterious rare transmitted variants and *de novo* variants

(DNVs) in 8% of patients with sporadic CHD. Notably, the study found that DNVs were more prevalent in syndromic cases (28%) compared to non-syndromic cases (3%) [90, 91]. This aligns with the observation that syndromic CHD often arises from *de novo* mutations, while isolated CHD is more often based on more complex inheritance pattern such as variants inherited from healthy parent [42]. The identified DNVs were predominantly located in genes involved in chromatin modification, transcriptional regulation, and RNA processing. Additionally, a gene-burden analysis of 2,391 CHD trios revealed that cilia-related genes are enriched for rare, damaging recessive variants but less so for damaging DNVs [92].

1.5 Cardiomyopathies

Cardiomyopathies can be defined as a diverse collection of pathologies characterized by structural and functional alterations in the heart [93]. Throughout the years, numerous efforts have been made to classify cardiomyopathies. The American Heart Association (AHA) employs a distinct approach compared to the European Society of Cardiology (ESC). The AHA classifies primary cardiomyopathies, which primarily affect the heart, into genetic, acquired, or mixed categories based on their underlying causes [94]. In contrast, the ESC's 2023 classification system is based on phenotypic and genetic characteristics, dividing cardiomyopathies into familial and non-familial (secondary) forms. Nonetheless, due to overlapping phenotypic manifestations and varying penetrance, cardiomyopathies frequently cannot be precisely categorized [95]. For this section, the ESC classification system was utilized. Cardiomyopathy can be primarily classified into distinct categories: 1. Dilated cardiomyopathy (DCM): characterized by ventricular dilatation, impaired function of one or both ventricles, and contractile dysfunction [96, 97], 2. Non-dilated left ventricular cardiomyopathy (NDLVC): can be further delineated based on the presence or absence of systolic dysfunction, which may be either regional or global [95], 3. Hypertrophic cardiomyopathy (HCM): this is the most prevalent inherited cardiomyopathy, primarily caused by causal variants in various genes [95], 4. Restrictive cardiomyopathy (RCM): this form of heart-muscle disorder is distinguished by the stiffness of the ventricular walls [95], 5. Arrhythmogenic cardiomyopathy (ARVC): this type is marked by the replacement of myocardium with fibrofatty tissue, leading to the emergence of arrhythmias, diminished systolic function, and a heightened risk of sudden cardiac death, particularly in young patients [95, 98]. In the 2023 ESC Guidelines, Left Ventricular Non-Compaction

(LVNC) is no longer classified as a distinct cardiomyopathy but is instead considered a morphological trait that may be associated with various cardiomyopathies or present as an isolated finding without accompanying cardiomyopathy. Similarly, Takotsubo syndrome is not strictly categorized as a separate cardiomyopathy under these guidelines [95]. However, both the American Heart Association (AHA) and the German Society of Cardiology continue to classify both LVNC and Takotsubo syndrome as forms of cardiomyopathy [99]. LVNC is a condition characterized by excessive trabeculation of the left ventricular myocardium, resulting in the presence of both compacted and non-compacted layers [100], Takotsubo syndrome is defined by the sudden onset of left ventricular dysfunction [101]. Furthermore, cardiomyopathies can be classified as either primary or secondary. Primary cardiomyopathies are disorders that predominantly affect the heart muscle. These disorders can arise due to genetic factors and include for example the arrhythmogenic right ventricular dysplasia, hypertrophic cardiomyopathy, ion channel disorders, left ventricular non-compaction, and mitochondrial myopathies. Additionally, primary cardiomyopathies can be non-genetic or acquired in nature, as seen in cases of myocarditis, peripartum cardiomyopathy, and tachycardia-induced cardiomyopathy [96]. Secondary cardiomyopathies involve myocardial damage as a consequence of systemic or multi-organ diseases. They can emerge either as primary myocardial disorders or as secondary effects of various conditions, including myocardial ischemia, inflammation, infection, elevated myocardial pressure or volume load, and exposure to toxins [96].

1.5.1 Arrhythmogenic right ventricular cardiomyopathy

Arrhythmogenic cardiomyopathy (ACM) is cardiac disorder characterized by the progressive loss of cardiomyocytes, which is accompanied by the replacement of these cells with fat and connective tissue. This replacement predisposes individuals to malignant ventricular arrhythmias and SCD [102, 103]. Originally, the disease was termed arrhythmogenic right ventricular dysplasia, as it was believed to be a congenital defect of the RV myocardium [104]. Further discoveries revealed that the disease is often caused by genetic defects in cardiac desmosomes, leading to its reclassification as a cardiomyopathy ARVC [104]. Findings from autopsies, genotype–phenotype studies, and contrast-enhanced cardiac magnetic resonance (CMR) have shown that the disease often involves the LV [104]. The presence of adipose and fibro-fatty tissue significantly disrupts electrical conduction, increasing the risk of electrical instability in cardiomyocytes and potentially affecting

both ventricles [104] (Figure 1.4). This can result in ventricular tachycardia, the loss of myocytes, and the atrophy of the ventricular myocardium. The right ventricle is particularly susceptible to cardiomyocyte loss in cases of ARVC. Scarring and fibrolipomatous changes in the ventricular walls and septum lead to arrhythmias, syncope, heart failure and, as an extreme form, SCD even in childhood [105]. ARVC is classified as a rare disease, with a prevalence estimated to be within the range of 1 in 2,000 to 1 in 5,000 individuals [106, 107]. The inheritance pattern of ARVC is traditionally classified as autosomal dominant, featuring variable penetrance that can change with age [108].

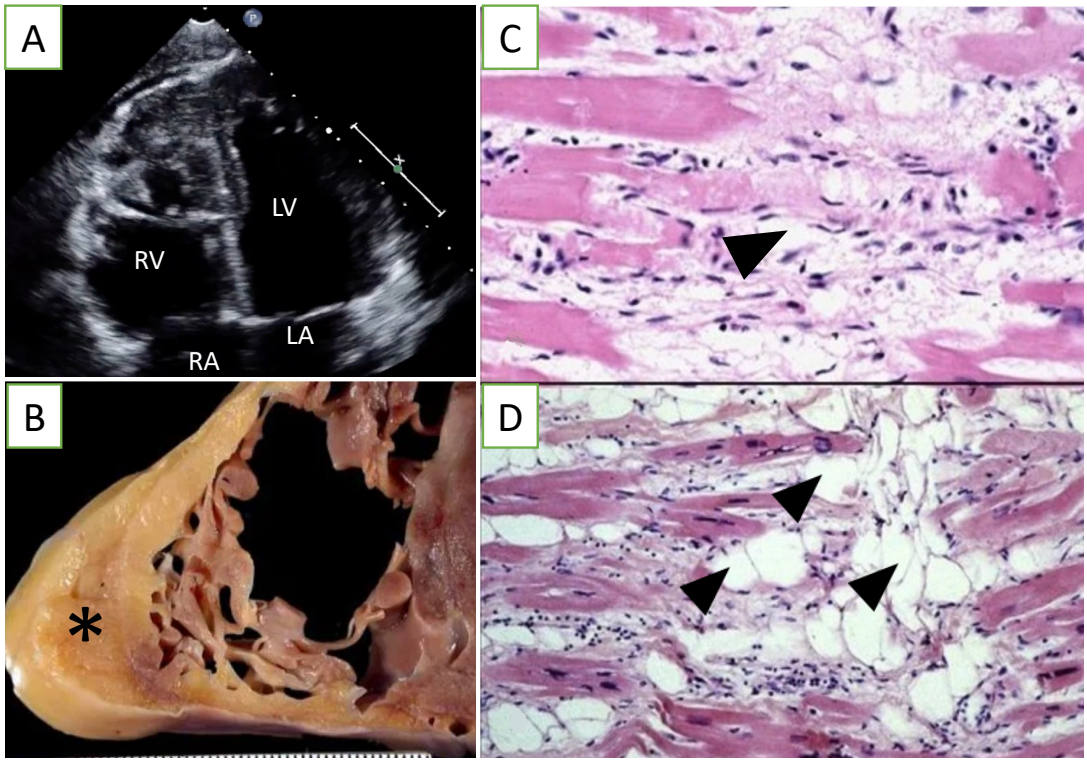

Figure 1.4: *A: An echocardiographic image showing ARVC. RV: right ventricle, LV: left ventricle, RV: right atrium, LA: left atrium. B: A biventricular autopsy image of the heart demonstrating increased fat in the outer walls of the right ventricle and left ventricular posterolateral walls (*) [106]. The anterior wall is nearly completely replaced with fat, and there is fibrofatty irregular involvement of the posterior wall. C, D: Typical histologic features of ARVC, including ongoing myocyte death (C) with early fibrosis (arrowhead) and infiltration of adipocytes (D) Figure modified from [109].*

The primary cause of ARVC is primarily attributed to causal variants in genes encoding desmosomal proteins [102], such as plakophilin-2 (*PKP2*) , which accounts for 34-74% of cases [110, 111], desmoplakin (*DSP*) [112, 113], and plakoglobin (*PG*) [111, 114], which accounts for 2-39% of cases. The overexpression of PG has been correlated with an increased

differentiation of cardiac progenitor cells into adipocytes. Desmosomes, specialized membrane protein complexes, play a critical role in cell-to-cell adhesion and the maintenance of structural integrity in the ventricular myocardium. Structural defects in desmosomes can lead to cardiac myocyte detachment and death, remodeling of gap junctions, and disruption of the Wnt–beta-catenin pathway [115]. These structural abnormalities may contribute to the replacement of normal myocardial tissue with fibrofatty tissue, resulting in electrical instability within the heart [102] (Figure 1.4).

1.5.2 Left ventricular non-compaction cardiomyopathy

As mentioned previously, the 2023 ESC Guidelines no longer classify LVNC as a distinct cardiomyopathy but instead consider it a morphological variant. However, according to the German Society of Cardiology (DGK) and the German Society for Pediatric Cardiology (DGPK), LVNC is classified as a cardiomyopathy. This classification is crucial for accurate diagnosis, treatment, and genetic counseling. It underscores the importance of exploring the genetic mechanisms underlying various cardiomyopathies, including LVNC, to better understand these disorders within the broader spectrum of cardiomyopathies. This type of cardiomyopathy has a prevalence of about 1 in 5,000 in the general population of adults [116,117]. LVNC is believed to result from a disruption in normal fetal cardiogenesis. This condition is characterized by a thin compacted epicardial layer and a thick non-compacted endocardial layer within the left ventricle (Figure 1.5). This results in the formation of distinctive ventricular trabeculations and deep intertrabecular recesses, which can contribute to the clinical manifestations of the disease [96, 116, 118]. Noncompacted myocardium, including LVNC, has been found to be associated with various other cardiac abnormalities, including cyanotic congenital heart disease and Ebstein's anomaly [119]. Moreover, LVNC has been observed to be associated with various neuromuscular disorders, including dystrophinopathies and mitochondrial diseases. [117, 120]. Furthermore, LVNC can also be associated with genetic syndromes like the 1p36 deletion syndrome, which is characterized by the loss of genetic material on the short arm of chromosome 1. This syndrome can lead to a range of developmental and health issues, including cardiac abnormalities such as LVNC [121, 122]. The irregular modulation of growth signals, including TGF-β and NOTCH pathways, results in disruptions of the regulation of the cell cycle and abnormal proliferation of cardiomyocytes. These deviations have already been uncovered in animal models, shedding light on their significance [123, 124]. Additionally,

PRDM16, *TBX20* and *NKX2-5* as cardiac transcription factors, play a role in regulating cardiomyocyte proliferation through interactions with the TGFβ signaling pathway [125]. Sarcomere genes associated with LVNC, including *ACTC1*, *MYH7*, *TNNT2*, and *TTN*, contribute to the pathogenesis of LVNC [117].

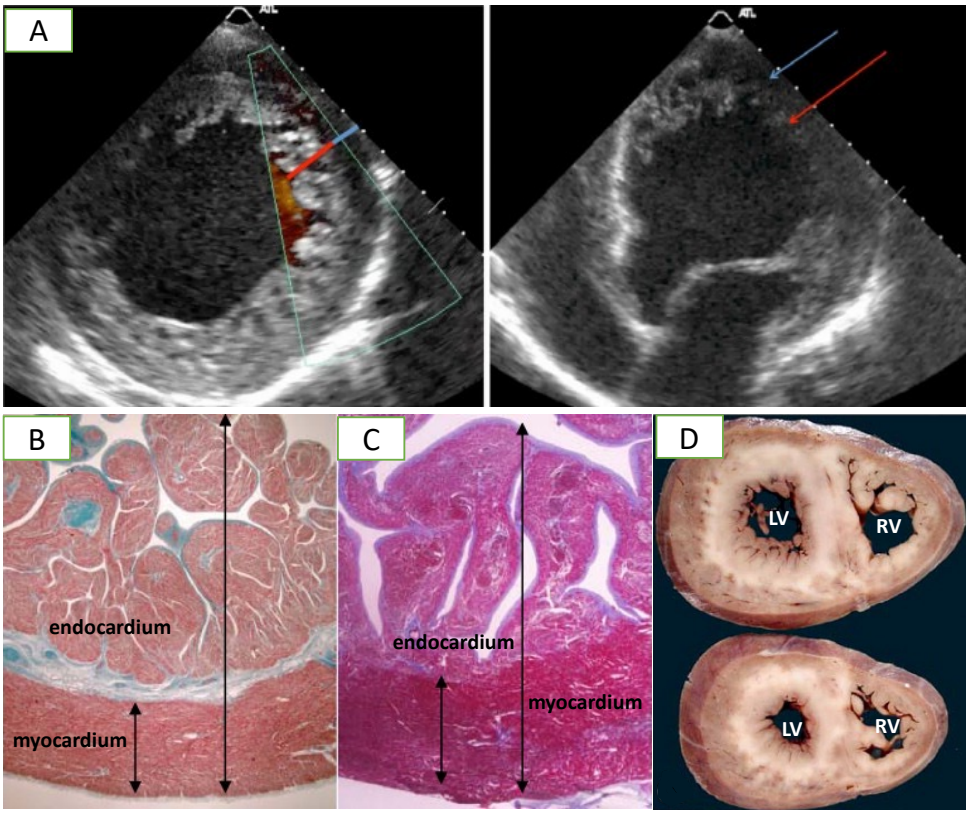

Figure 1.5: *Hallmarks of LVNC. A: Echocardiographic images of LVNC. Image on the left panel: A systolic short-axis image illustrating the transition from the compacted layer (indicated by the blue line) to the non-compacted layer (highlighted by the red line). Image on the right panel: A diastolic four-chamber image showcasing LVNC, with the non-compacted layer marked by the red arrow and the compacted layer by the blue arrow [126]. B,C: LVNC histological features. B: Irrespective of the overall pattern, LVNC exhibits distinctive microscopic features. These include a relatively smooth endocardial surface on the left, where anastomosing broad trabeculae create irregular and large staghorn-like spaces lined by the endocardium. C: The endocardial surface displays a polypoid pattern of trabeculae, characterized by invaginated branching recesses. At the inner tips of these recesses, staghorn-like structures are once again formed. Additionally, a prominent fibrous band demarcates the spongy region from the compact portion of the myocardium. D: LVNC: gross appearance. Figure modified from [127].*

1.5.3 Dilated cardiomyopathy

The current estimated prevalence of dilated cardiomyopathy is approximately 1 case per 2,500–3,000 population [128]. DCM refers to the enlargement of the heart, often affecting all four chambers, particularly in the later stages of the disease. Most commonly, DCM is associated with reduced left ventricular (LV) function or systolic function (Figure 1.6). However, in the early stages of the disease, the left ventricle may be dilated with only minimal reduction in function [129]. Nonetheless, this syndrome can cover a broad spectrum of genetic and acquired conditions that can exert varying degrees of influence on the patient's health and quality of life over the course of their lifespan [97].

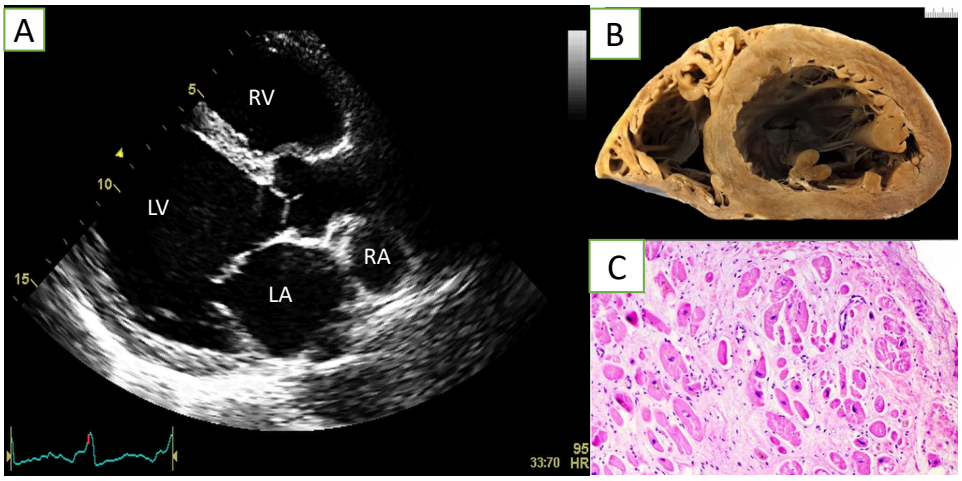

Figure 1.6: *Hallmark of DCM. A: The echocardiographic image displays a dilated left atrium and left ventricle in diastole [130]. B: The macroscopic short-axis cut reveals a dilated left ventricle chamber with thinning of the left ventricular free wall. C: The histological section displays interstitium and replacement collagen mixed with hypertrophied and degenerate myocytes, which is consistent with Dilated Cardiomyopathy (DCM). This was visualized using a hematoxylin and eosin stain. Figure modified from [131].*

Familial DCM refers to the cases where DCM follows a Mendelian inheritance pattern, inherited as a single gene disorder. This condition typically exhibits autosomal dominant inheritance, often characterized by reduced penetrance and variable expressivity [132]. Additionally, mitochondrial mutations can also contribute to DCM, showing an inheritance pattern consistent with maternal lineage [129]. Less commonly, autosomal-recessive inheritance can also lead to familial DCM. Additionally, X-linked recessive inheritance has been associated with several genes implicated in DCM, including dystrophin, tafazzin, and emerin. Several genes associated with proteins have been implicated in dilated

cardiomyopathy (DCM), including TTN (15-20% of cases), LMNA (6%), MYH7 (4%), as well as various ion channel genes [97, 129, 132].
Apart from genetic factors, myocardial ischemia continues to be a prevalent cause of DCM, constituting around half of all DCM cases. Toxic, metabolic, and immunologic factors have also been linked to DCM, alongside conditions like hypertension and valvular heart disease [129].

1.6 Molecular techniques to identify genetic causes of CHD and and cardiomyopathy

The identification of genetic causes for CHD and CM has advanced significantly through various molecular techniques, which enable the discovery of genetic variants contributing to these conditions' pathogenesis. Historically, cytogeneticists identified chromosomal anomalies by examining karyotypes and analyzing distinctive banding patterns. Since its development in the 1970s, cytogenetic banding analysis has been a primary method for evaluating patients with congenital anomalies. This technique can detect chromosomal deviations as small as approximately 5 megabases (Mb), classifying these alterations as "microscopic" rearrangements [133]. In recent times, researchers have progressively embraced modern cytogenetic techniques. Among these, fluorescence in situ hybridization (FISH) has gained prominence. FISH employs fluorescently labeled probes to pinpoint the locations of particular DNA sequences on chromosomes. Another widely adopted method is comparative genomic hybridization (CGH), offering an alternative approach for comprehensive screening of genome-wide copy number variations [134].
The extensive use of next-generation sequencing (NGS) technologies over the past decade has greatly enhanced our understanding of the genetic mechanisms underlying complex diseases like CHD and CM. Advancements in ES and GS have made the identification of genomic variants, such as DNVs and somatic alterations, more precise and sensitive compared to traditional methods like array-based comparative genomic hybridization (aCGH) [47, 135]. NGS is revolutionizing genetic diagnosis due to its cost-effectiveness and exceptional throughput. It is advancing cardiovascular research by identifying variants linked to diseases and as a resulted forstering the identification of new drug targets, and personalized therapies, thus surpassing the capabilities of earlier cytogenetic techniques.

1.6.1 *PRDM16*: A Metabolic Transcription Factor Involved in Cardiac Biology Identified by Comparative Genomic Hybridization

In contrast to conventional methods used for identifying copy number changes, which rely on examining a specific target and prior information about the region being studied, comparative genomic hybridization (CGH) provides the ability to comprehensively assess an entire genome for imbalances. Furthermore, CGH does not require cells that are actively undergoing division [136].
However, similar to previous cytogenetic techniques, the resolution of CGH has been limited to detecting alterations of around 5-10 megabases (Mb) in most clinical scenarios. Array comparative genomic hybridization (aCGH) offers a higher detection rate, increased accuracy, and reduced sample failure compared to conventional cytogenetic analysis [137]. Recent studies have already shown that patients with CHD have a higher likelihood of having microdeletions and microduplications [138]. However, aCGH may not yield significant diagnostic results in cases of isolated CHD. Further research using larger datasets would be beneficial in identifying candidate genes associated with CHD [138]. aCGH was utilized to investigate cardiomyopathy associated with monosomy 1p36, LVNC and DCM [139].

PRDM16 (Positive regulatory domain zinc finger region protein 16) belongs to the PRDM family, which comprises 17 members with a shared N-terminal PR domain and varying zinc finger counts [140]. PRDM16 directly engages DNA via its two zinc finger domains. Additionally, *PRDM16* features a proline-rich domain, a repressor domain, and a C-terminal acidic domain, though the exact roles of these domains remain partially to be elucidated [141]. The human *PRDM16* gene is located on the chromosome 1 at p36 arm and produces four protein isoforms. The extensively studied ones are the full-length 170 kDa and a shorter 150 kDa variant without the N-terminal PR domain. The roles of the other two isoforms are less understood [140]. *PRDM16* assumes a central role in diverse biological processes, notably in cell differentiation and development. Additionally, *PRDM16* exerts critical influences across various cell types and tissues, including skeletal muscle development and function [142], hematopoiesis [143], palatogenesis, cardiac development [144], and immune response regulation. The PRDM16 protein family, functioning as transcription factors, is crucial for regulating gene expression [145]. PRDM16's significance was first recognized in positive leukemia cell development [146]. Notably, one of its

significant functions lies in its contribution to determining cell fate and specifying tissue development [147]. Moreover, *PRDM16* is a key regulator in the formation of brown fat cells, vital for energy metabolism and thermogenesis. Its interaction with EHMT1, which represses skeletal muscle and white fat genes through epigenetic modifications, leads to gene suppression and activation of thermogenesis [148]. For the initiation of brown fat development, *PRDM16* collaborates with C/EBPβ to form a transcriptional complex, which subsequently boosts the expression of additional transcription factors and co-activators like PPARγ and PGC1α [140]. Additionally, *PRDM16* forms a complex with CTBP1 and CTBP2 to directly repress certain white fat genes through promoter binding. TLE3 acts as an antagonist, competing with *PRDM16* for PPARγ complex formation, inducing white fat-specific gene expression [140]. In the context of neuronal development, *PRDM16* has been recognized as a potential regulator of mitochondrial reactive oxygen species. It is specifically expressed by progenitor cells in the ventricular zone of the neuronal cortex [149]. Subsequent to that, there have been limited number of publications focused on PRDM16 in cardiac research. In a recent study, genome-edited iPSC-CMs with a *PRDM16* mutation showed reduced proliferation and increased TGFβ signaling response [125]. Patient-specific iPSC-CMs with an LVNC-related *TBX20* mutation exhibited disrupted TGFβ signaling and decreased *PRDM16* expression. This suggests a potential TBX20-PRDM16-TGFβ axis contributing to LVNC [125]. Recent evidence has strengthened the link between *PRDM16* and cardiac conditions [150]. In a cardiac conditional knockout mouse model, a null variant of *PRDM16* was introduced, leading to notable changes. Electrocardiographic analysis revealed increased QRS duration and QTc interval. The affected mice displayed fibrosis, hypertrophic cardiomyocytes, and disrupted expression of cardiac ion channels, ultimately resulting in impaired cardiac conduction [151]. These discoveries primarily highlight the involvement of *PRDM16* in heart development and related cardiac issues. However, the exact molecular mechanisms remain unclear, underscoring the need for further research to comprehend the impact of genetic changes in *PRDM16* for potential therapeutic avenues.

1.6.2 Capping Actin Protein of Muscle Z-Line Subunit Beta: A Novel CHD Candidate Identified Through Exome Sequencing

The emergence of ES has opened new avenues for analyzing the causes, underlying mechanisms, potential treatments, and prognoses of diseases. In a recent studies, exome sequencing has been successfully applied to analyze sporadic cases of CHD. These studies have identified a significant increase in *de novo* coding gene variants that are expressed during cardiac development [52]. The presumed mode of inheritance in families with Mendelian inheritance is well-suited for incorporating exome sequencing into the filtering strategy. ES has successfully identified pathogenic variants in the majority of these families. However, it can be challenging to definitively determine if the identified variant was solely responsible for the CHD [152]. ES can be divided into two main processes: target enrichment and sequencing. Target enrichment involves the selection and capture of the exome from DNA samples. This is achieved through methods like array-based exome enrichment or in-solution capturing [153]. Sequencing aims to determine the sequence of all the deoxyribonucleotides in the exome. This process can help us understand potential pathophysiological alterations. By sequencing around 20,000 genes and analyzing the data, it becomes possible to identify genes that are mutated more frequently than would be expected by chance [154]. Additionally, exome sequencing has facilitated the discovery of novel disease genes across a spectrum of conditions, spanning from autism to congenital malformations [155] to cancer [153]. As a result, exome sequencing was employed to detect rare mutations in a newly proposed candidate gene, *CAPZβ* , among four patients diagnosed with CHD (unpublished).

The intricate control of actin filament formation, dynamics, maintenance, and their stability is evident through the involvement of numerous actin-binding proteins that govern processes like capping, severing, and crosslinking of actin filaments [156]. Among these, actin capping protein (CAP) and tropomodulin (Tmod) play crucial roles as capping proteins, interacting with the barbed ends of actin filaments to regulate their assembly. These proteins are pivotal for managing actin dynamics and ensuring consistent filament length [157]. CapZ, a heterodimer consisting of α and β subunits, binds to the barbed ends of actin filaments and is found in various eukaryotic cells [158] (Figure 1.7). The isoforms of these subunits are well-conserved among vertebrates. Vertebrates possess three isoforms of the α subunit, encoded by two distinct genes, while the β subunits are generated through alternative

splicing of a single transcript. Muscle cells contain two isoforms of the beta subunit: beta1, which is located at the Z-line, and beta2, which is found at the intercalated disc and cell periphery [157] (Figure 1.7).

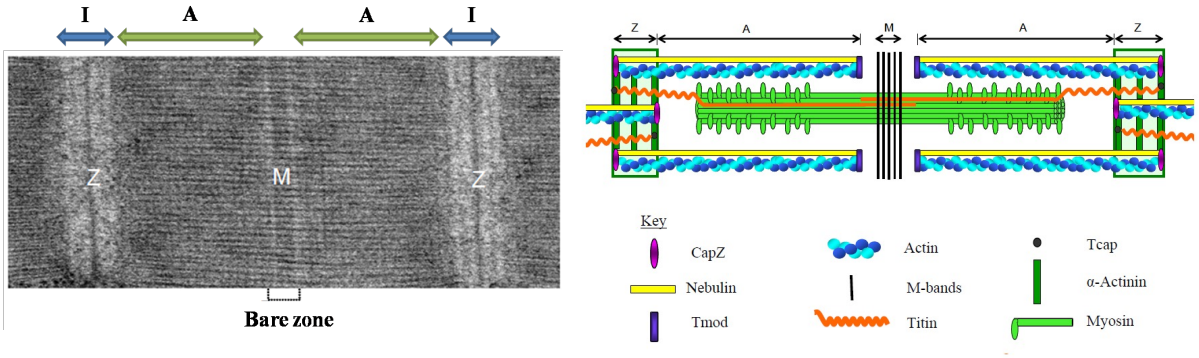

Figure 1.7: *CAPZβ is an essential component of the sarcomere. Left panel provides a transmission electron microscope image of a zebrafish sarcomere, which is a structural unit within muscle fibers. This sarcomere image highlights essential components: Z-lines (Z): These serve as boundary markers for each sarcomere. M-band (M): Located centrally within the bare zone of the sarcomere. I-band (I): Positioned between sarcomeres, it spans the region of thin filaments attached to the Z-line. A-bands (A): These constitute the majority of the sarcomere and consist of interdigitated thin and thick filaments. The diagram on the right illustrates the sarcomere, emphasizing its key components: Thin filament is composed of filamentous actin (blue), capped at each end by capZ (purple) and Tmod (violet). Nebulin (yellow) spans the length of the thin filament. The thick filament consists of bundles of myosin (light green), cross-linked at the M-band (black). Titin (orange), a giant protein, plays a central role in sarcomere organization by positioning myosin at the sarcomere's midpoint. Additionally, it is tethered to the Z-line through its interaction with telethonin (Tcap). a-Actinin (dark green) connecting thin filaments between adjacent sarcomeres, and playing a significant role in the formation and maintenance of the Z-line [159].*

Chicken, mouse, and human, each harbor two isoforms of CapZα (CapZα1 and CapZα2) and two isoforms of the β (CapZβ1 and CapZβ2), with minimal variations between species, arising from alternative splicing of the last exon [160]. In mammals, an additional isoform of the α and β subunits (capZα3 and capZβ3) has been identified, expressed specifically in sperm [161]. Zebrafish possess a single *capzβ* isoform. Comparative analysis suggests that zebrafish *capzβ* corresponds to the β2 isoform found in other species [159]. In humans, the *CAPZβ* gene is situated on the short arm of chromosome 1. *CAPZβ* exhibits high expression in pharyngeal arch 1, an embryonic structure conserved across species, which develops into the palate and lower jaw structures during human development's fourth and fifth week [162]. In terms of function, *Capzβ* loss-of-function (LOF) in mice *($Capz\beta^{-/-}$)*

results in embryonic lethality. Conversely, transgenic mice overexpressing *Capzβ* display myofibrillar disarray, cardiac hypertrophy, and premature mortality [157]. *(capzβ$^{-/-}$)* zebrafish mutants manifest craniofacial and muscle defects. The absence of *capzβ* influences cell morphology, differentiation, and neural crest migration [162]. *capzβ* is crucial for the differentiation of both myogenic stem cells and neural crest cells [162]. The role of *CAPZβ* in embryonic heart development and the pathogenesis of CHDs remains poorly understood. Therefore, it is imperative to gain a deeper understanding of *CAPZβ*'s function in the development and differentiation of early cardiomyocytes and to elucidate the underlying molecular signaling pathways.

1.7 Zebrafish as a model for cardiac disease

In recent times, the zebrafish has emerged as a favored *in vivo* model organism for exploring diverse developmental processes, particularly in the realm of cardiovascular research. This includes investigations into congenital heart defects, arrhythmias, cardiomyopathy, and regeneration [163]. Despite teleost fish diverging more than 400 million years ago, they are more closely related to humans than invertebrates. Major pathways, cellular processes, and biological functions presented in humans are conserved in zebrafish, allowing researchers to study embryonic development, physiology, and related diseases. Zebrafish (*Danio rerio*) are aquatic animals from to the cyprinid family of teleost fish, originating from the Ganges River in India [164]. In 1972, George Streisinger introduced the freshwater tropical zebrafish as a genetic model for studying vertebrate development [165]. Zebrafish model system offers major advantages [166]. Additionally, there are various benefits to maintaining them at the laboratory level. The small size of zebrafish (3-5 cm) facilitates their care in large numbers. Their breeding is influenced by photoperiodicity, and they are typically maintained under a day-night cycle regulated by an automatic timer [166]. Zebrafish embryos develop *ex utero* and are transparent, enabling easy observation of internal structures like the heart. Genetic manipulation of zebrafish is relatively straightforward [166].

The developmental process of zebrafish embryos is rapid, progressing from a single cell to a recognizable embryo within just 24 hpf [166]. Around four to eight hpf, several distinctive processes take place, such as epiboly, involution, and convergent extension. The processes commence with the migration of approximately 1200 cells over the yolk, leading to extensive rearrangements. Within the subsequent three hours, these movements give rise

to the three primary embryonic germ layers, a phenomenon known as gastrulation. Upon the completion of gastrulation, typically around eleven hpf, the fundamental vertebrate body plan is established, and the formation of the initial individual somites commences. The somitogenesis begins at the anterior (near the head) and proceeds sequentially towards the embryo's tail (posterior). By 18 hpf, a total of 18 pairs of somites have formed, and the final count of somite pairs can range from 30 to 34. At 24 hpf, the embryo's heartbeat becomes discernible, accompanied by the initiation of blood circulation. By the time 48 hpf has elapsed, most of the distinctive body characteristics shared by vertebrates have already developed. Subsequently, the larvae will undergo hatching and gain the ability to swim and forage for sustenance within a span of 5 days (Figure 1.8).

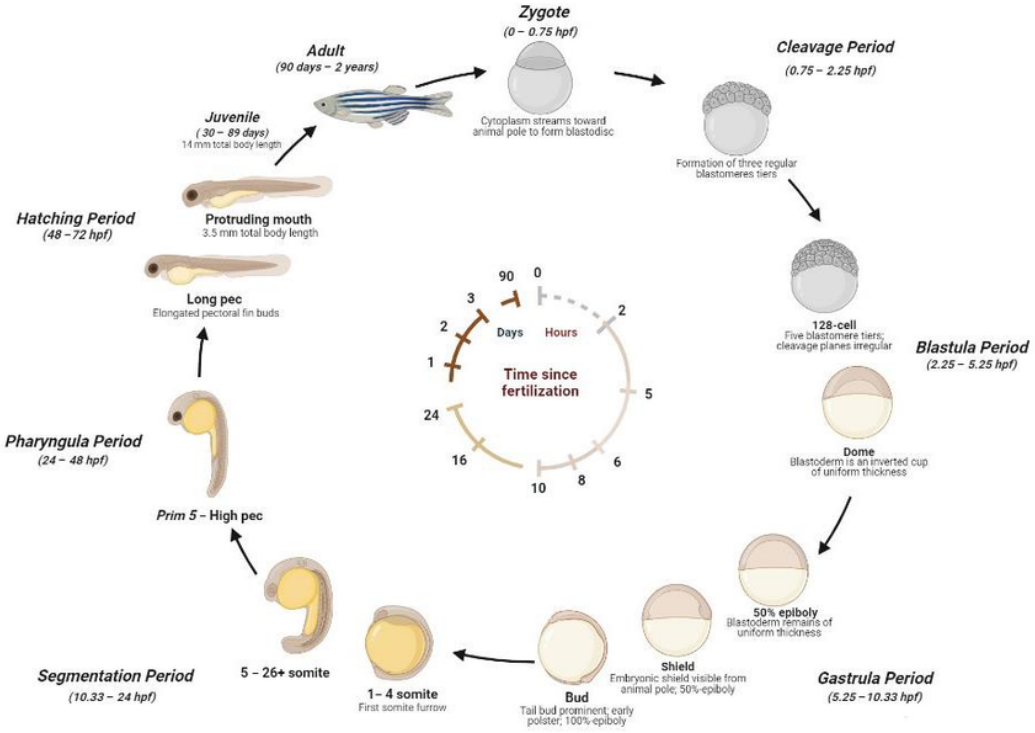

Figure 1.8: *A schematic representation of the developmental stages of zebrafish. The cycle starts at the top with a fertilized single stage. The embryos develop quickly to a 14-somite stage within 16 hours. After 24 hours, the complete body plan of the embryo is established. Two days after fertilisation, the embryos hatch and swim freely. Zebrafish are adult at 3 months of age and fertile. Figure was taken from [167]*

The zebrafish's generation time is relatively short, taking about 2 to 3 months to reach maturity (Figure 1.8). These advantages provide a unique opportunity for a comprehensive exploration of cardiac biology. The zebrafish model not only offers valuable insights into

intricate developmental processes but also holds the potential to reveal novel therapeutic avenues for addressing CHD in humans [168].

1.7.1 Zebrafish heart development

During vertebrate embryogenesis, the heart is one of the earliest organs to form and to become functional [169]. Zebrafish heart development can be divided into three initial stages, which involve the specification, migration, and differentiation of cardiomyocyte progenitor cells as they integrate into the forming heart tube [170, 171].
The process of zebrafish heart development begins with the establishment of myocardial and endocardial progenitor cells (Figure 1.9). Prior to the onset of gastrulation, myocardial progenitor cells (atrial and ventricular) are positioned in the lateral marginal zone on both sides of the embryo, whereas endocardial progenitors are dispersed throughout the marginal zone without any distinct organization [172]. Atrial progenitor cells are situated in a more ventral position compared to the ventricular progenitor cells [169]. Following gastrulation, the cardiomyocyte progenitor cells within the lateral mesoderm undergo a transformation and migrate to the anterior lateral plate mesoderm (ALPM). At the 12-somite stage, the process of cardiogenic differentiation is triggered in the future ventricular myocardial cells through the activation of cardiac myosin expression [173]. During the mid- and late-somite stages, the ongoing cardiogenic differentiation of future atrial myocytes results in the enlargement of myocardial tissue into lateral areas of the anterior lateral plate mesoderm (ALPM). In parallel, endocardial cells have already migrated from the ALPM towards the midline, and myocardial cells exhibit a similar behavior slightly afterward [169]. Subsequently, these cells migrate and merge, culminating in the creation of the cardiac crescent where atrial cardiomyocytes envelop ventricular cardiomyocytes [169]. The cardiac disc then undergoes elongation, giving rise to the linear heart tube, which commences its rhythmic contractions at around 24 hpf [174]. The cells that differentiate earlier and contribute to the formation of the initial heart tube are known as the first heart field (FHF) [175, 176].

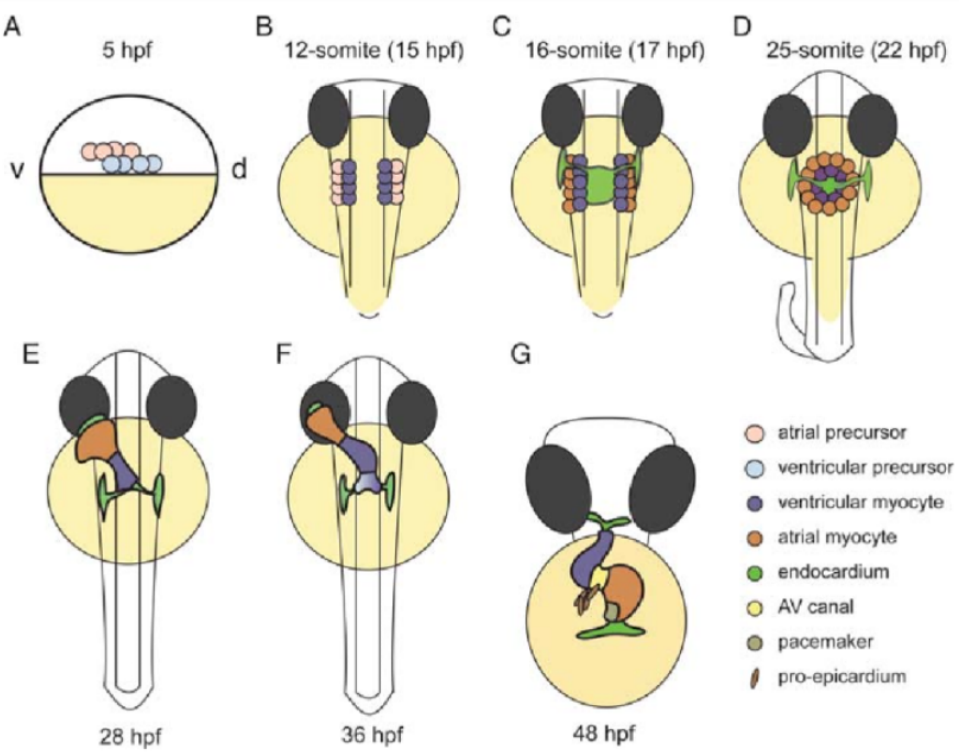

Figure 1.9: *A schematic representation of the cardiac development in zebrafish. At 5 hpf, cardiac progenitor cells are situated bilaterally in the lateral marginal zone while the blastula envelops about 50% of the yolk sac. Atrial progenitor cells (pink) are positioned ventrally, while ventricle progenitor cells (light blue) are located slightly dorsally. As gastrulation progresses, these cardiac progenitor cells migrate dorsally toward the mid-line and eventually settle in the anterior lateral plate mesoderm (ALPM). By the 12-somite stage, the initiation of cardiogenic differentiation in the future cardiac chambers is marked by the expression of cardiac myosins (purple). During mid- and late-somite stages, the myocardial tissue continues to expand as a result of continuous cardiogenic differentiation. This leads to the extension of myocardial tissue into the more lateral regions of the ALPM, primarily through the differentiation of future atrial myocytes (orange) — a process associated with venous differentiation. Notably, myocardial cells lag behind endocardial cells (light green) in migration from the ALPM towards the midline. The bilateral midline cardiac fields merge to form a cardiac disc structure. Within this structure, the endocardial cells occupy the central hole, the ventricular myocytes line the periphery, and the atrial myocytes encircle the ventricular myocytes. Subsequently, cardiac morphogenesis transforms the cardiac disc into a linear heart tube, with the venous pole situated anteriorly on the left and the arterial pole fixed at the mid-line by 28 hpf. (F) At the arterial pole, the process of cardiogenic differentiation persists, leading to the augmentation of cardiomyocyte numbers in this region (purple gradient). By 36 hpf, cardiac looping initiates, characterized by the ventricle's displacement towards the mid-line and the emergence of a constriction at the location of the atrioventricular (AV) canal. This looping process proceeds, forming an S-shaped configuration by 48 hpf (G). Finally, the pacemaker, represented by a region with inherent rhythmic activity, is positioned in the inner curvature of the atrium near the venous pole (dark green). Figures were taken from [169].*

Distinct cell population that differentiate later is referred to as the second heart field (SHF). These cells contribute to both the venous and arterial poles as the heart tube elongates and grows [174, 177]. The endocardium constitutes the inner lining of the myocardial tube. By 28 hpf, the linear heart tube jogs leftward, with the venous pole positioned at the anterior left and the arterial pole at the midline. Cardiac looping is initiated, causing the ventricle to shift towards the mid-line around 36 hpf. Subsequently, the heart tube undergoes continuous looping, forming an S-shaped configuration. By 48 hpf, the looping process concludes, resulting in the formation of the two chambers [171]. By 72 hpf, well-developed trabeculation in the ventricle as well as valve leaflets are visible, and distinct mechanisms govern the maturation of the atria and ventricle [178]. Deoxygenated blood enters the sinus venosus and then passes through a single atrium before reaching the ventricle. The ventricle propels venous blood through the bulbus arteriosus, which leads to the ventral aorta for distribution to the gills where oxygenation occurs [168]. The adult zebrafish heart comprises a single atrium and a single ventricle. Although smaller and less complex than the mammalian heart, its histological and structural composition closely resembles that of other vertebrates [179].

1.7.2 Zebrafish heart regeneration

Zebrafish is a widely popular animal model in the field of organ regeneration biology. Unlike humans, zebrafish possess a remarkable and distinctive capability to regenerate various organs, such as the heart muscle [180], spinal cord [181], retina [182], and all fins [183]. The mechanisms governing regeneration appear to be specific to each organ. For instance, fin regeneration relies on specialized dedifferentiated cells known as blastema [184]. Conversely, the regeneration of the telencephalon involves the activation of a specific cell population marked by the notable expression of the Notch target gene *her4.1* [185]. Zebrafish exhibit an exceptionally robust regenerative capacity when it comes to cardiac tissue. They can efficiently regenerate their heart even after amputation of a substantial portion, up to $\sim$ 20%, of the ventricle [180]. Around 7 to 9 days post-injury (dpi), an initial fibrin clot forms in response to the injury [180]. This clot subsequently gets replaced by a combination of fibrin and collagen. Following the injury, the epicardial cells undergo a process known as epithelial–mesenchymal transition (EMT) due to stimulation by FGFs. This transition allows the activated epicardial cells to proliferate and migrate towards the injured area [186]. The regeneration process concludes around 60 days dpi, during which time the ventricle's

size and shape, as well as the heart's contractile capacity, return to their normal state [180]. Furthermore, numerous studies have demonstrated that following ventricular cryoinjury, there is an elevation in cell death, inflammatory infiltration, and mechanical stresses. This culminates in the transformation of fibroblasts into myofibroblasts, which in turn secrete collagen and other components of the extracellular matrix (ECM) in the injured region [187]. The preservation of the integrity of the cardiac wall is facilitated by the deposition of ECM components that occurs in response to cardiomyocyte death [187]. Moreover, the Smad3-dependent TGFβ signaling pathway in zebrafish holds significance due to its involvement in reparative and regenerative mechanisms, crucial for the formation of a transient scar elimination [188]. An intriguing observation in the zebrafish heart is that there is a reduction in intra-ventricular mechanical forces during myocardial regeneration. This reduction subsequently triggers a downregulation of collagen synthesis, ultimately resulting in the eliminating of the scar tissue [189].

Unlike zebrafish, mammals have limited capacity for heart regeneration. However, the discovery of various signaling pathways, such as hippo/YAP/TAZ, Meis1, Wnt/β-catenin, IGF, Ros, TGFβ activin, Hypoxia, Monocyte/macrophage, CDK9/PTEFb, and miRNA, holds promise for enhancing the regenerative potential of mammalian hearts. These pathways offer potential targets to promote and enhance the repair ability of mammalian hearts [190]. By deciphering the molecular mechanisms underlying zebrafish heart regeneration, researchers can gain insights that may be applied to developing novel therapies for human heart conditions.

1.8 Identification of human variants in *PRDM16* and *CAPZβ*

1.8.1 Identification of *PRDM16* as a causal gene in cardiomyopathy

PRDM16 has been identified to play a role in DCM and LVNC [191]. Additional support for the role of *PRDM16* in cardiomyopathy comes from a study involving patients with 1p36 deletion syndrome and concomitant cardiomyopathy [139]. This syndrome is characterized

by a partial deletion of chromosome 1. Notably, cardiomyopathy manifests only in cases where specific segments of the chromosome are deleted. A shared minimal deletion region identified in 18 individuals was localized within the *PRDM16* gene, spanning exons 4 to 17. Furthermore, through genetic analysis of patients affected by primary non-syndromic cardiomyopathies, missense and truncating variants (PRDM16-K702*) were identified in seven cases associated with DCM and LVNC. One of the truncating variants was subsequently studied in zebrafish, resulting in pronounced cardiac phenotypes [139]. Zebrafish models with *PRDM16* knockdown and a cardiac-specific overexpression of the truncated PRDM16-K702* transgene, exhibited morphological and physiological abnormalities (Figure 1.10) [139]. These included diminished impaired cardiomyocyte proliferation (Figure 1.10), cardiac output (Figure 1.10) and a decrease in cellular coupling (Figure 1.11).

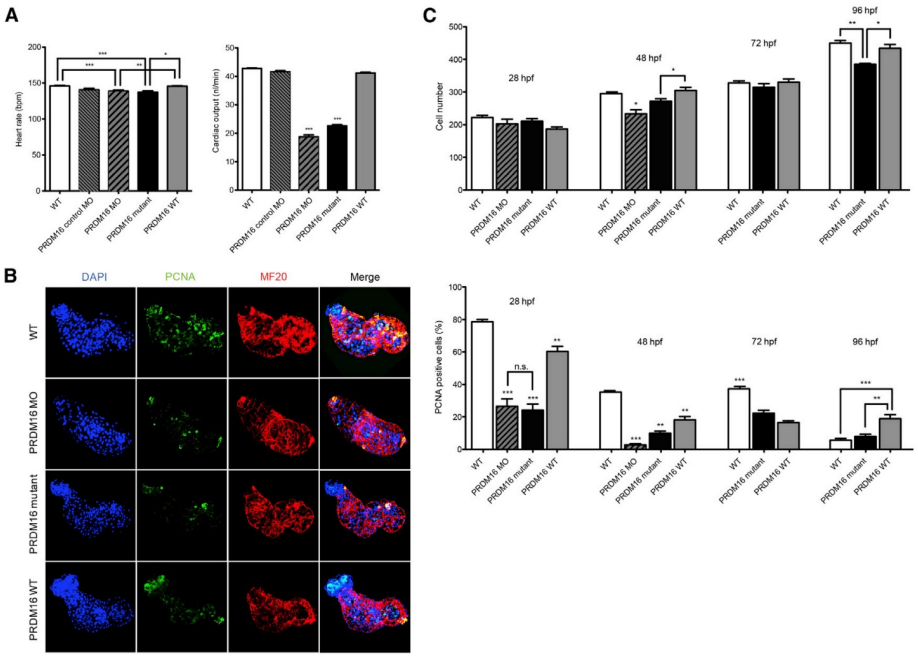

Figure 1.10: *PRDM16 knockdown and human PRDM16 truncation mutant in a zebrafish Model. (A) PRDM16 knockdown and overexpression of truncated variant have reduced heart rate and cardiac output compared controls. (B) In PRDM16 knockdown and overexpression of truncated variant hearts, there is a significant decrease in cell number and in proliferation at 48 hpf, partially rescued by PRDM16 WT overexpression. (C) Over time, PRDM16's impact on cell number and proliferation changes in embryos, with both knockdown and overexpression of truncated variant fish showing reduced cell numbers not fully recovered by 96 hpf, despite changes in proliferation rates. The effects of overexpression of truncated variant and wild-type PRDM16 appear to oppose each other between 48 or 96 hpf and 72 hpf, with an unknown mechanism. Adapted from [139].*

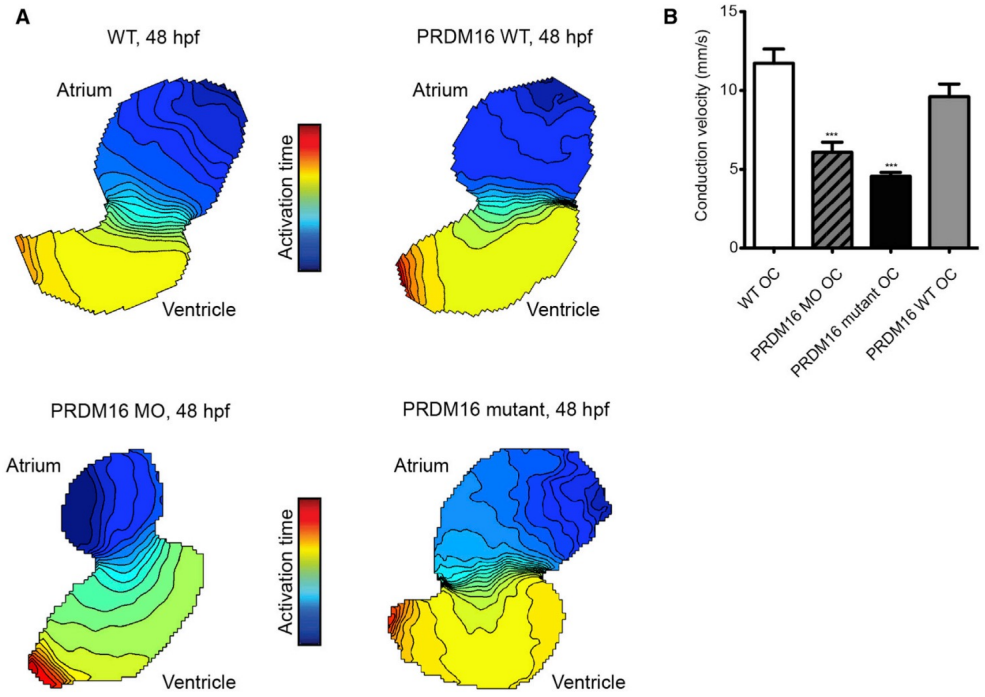

Figure 1.11: *Cell coupling in a PRDM16 zebrafish model and interaction of PRDM16 with SKI.(A) Isochronal maps of wild-type (WT), PRDM16 WT transgenic, PRDM16 morphant (MO), and PRMD16 mutant transgenic hearts show action potential wavefront positions at 5 ms intervals. The color scale indicates the timing of electrical activation. (B) Mean conduction velocities from the ventricle's outer curvature (OC) confirm reduced impulse propagation speeds in morphant and mutant hearts compared to controls or wild-type. Adapted from [139].*

These findings strongly indicate the significant role of *PRDM16* in the process of cardiogenesis [139]. Furthermore, in initial investigations preceding this research, four missense variants in *PRDM16* were identified. A collaborative effort with PD Dr. Sabine Klaassen (Charité, ECRC, Berlin) involved examining 200 families and individuals with arrhythmogenic right ventricular cardiomyopathy (ARVC) from Germany and Canada. These individuals had previously tested negative for known ARVC candidate genes. Subsequent to patient screening for *PRDM16* variants, conventional Sanger sequencing of *PRDM16* was conducted. Notably, a minor allele frequency threshold of 0.05% was established due to the reduced penetrance of ARVC. The four variants are described in more details in section 4.1.

1.8.2 Identification of *CAPZβ* as a causal gene in CHD

Recent advancements in sequencing technology have facilitated the identification of severe mutations in humans. Employing ES and VEP, four missense variants in *CAPZβ* were discovered, all of which were absent in control samples. Notably, two patients exhibited non-syndromic congenital heart defects, while the other two presented syndromic CHD. Specifically, the mutations p.Thr179Ser and p.Ser192Asn were detected in patients with non-syndromic CHD, characterized by hypoplastic left heart syndrome and pulmonary atresia with ventricular septal defect. Additionally, the patient with variant p.Arg215Cys displayed traits including atrial septal defect, global developmental delay, sparse hair, abnormal pinna, and postnatal growth retardation. Meanwhile, the patient harboring p.Lys181Arg exhibited ventricular septal defect, trigonocephaly, optic nerve hypoplasia, corpus callosum agenesis, and cerebellar vermis hypoplasia. Notably, three novel mutations, p.Thr179Ser, p.Lys181Arg, and p.Ser192Asn, were situated in exon 6, while p.Arg215Cys occurred in exon 7. To mimic the loss of function, we employed the zebrafish model system. We analyzed mutant zebrafish carrying a retroviral insertion in the second intron of the *capzβ* gene and conducted a comparative study involving homozygous knockout *capzβ* fish, along with heterozygous and wildtype siblings. Zebrafish larvae that were homozygous for the $capz\beta^{-/-}$ mutation experienced mortality by 100 hpf. Heterozygous zebrafish $capz\beta^{+/-}$ survived into adulthood and were utilized for breeding. The $capz\beta^{-/-}$ mutant larvae displayed microcephaly, reduced body size, underdeveloped jaw, and an elongated, unlooped heart by 96 hpf compared to their $capz\beta^{+/-}$ heterozygous and wildtype counterparts. Zebrafish embryos with *capzβ* knockout exhibited morphological and physiological anomalies, including impaired cardiac looping and cardiomyocyte proliferation (Figure 1.12). CO assessments demonstrated compromised contractility in $capz\beta^{-/-}$ larvae compared to $capz\beta^{+/-}$ and wildtype larvae by 72 hpf, with a further significant reduction by 96 hpf (See figure 1.13).

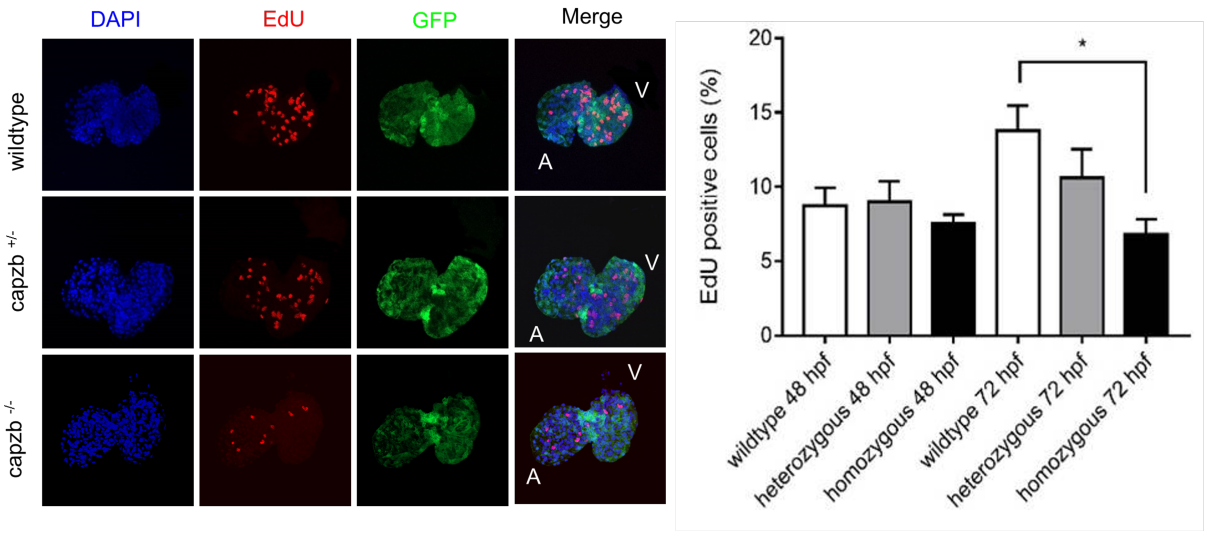

Figure 1.12: *Heart formation is impaired in capzβ mutants. Comparison of cardiomyocyte proliferation between wildtype, capzβ$^{+/-}$ and capzβ$^{-/-}$. The proliferation of ventricular cardiomyocyte reduced significantly in capzβ$^{-/-}$ at 72 hpf. Figure was taken from [192].*

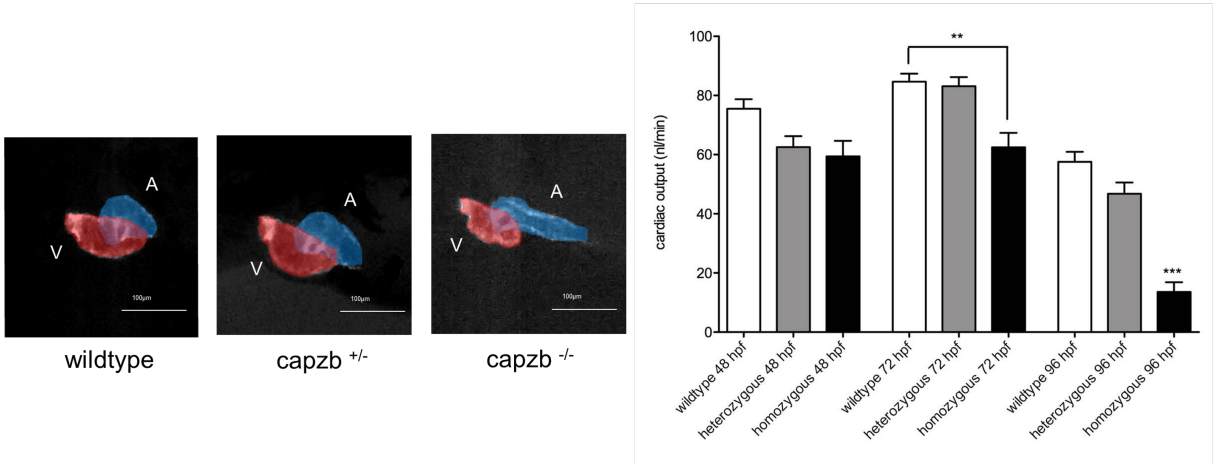

Figure 1.13: *Heart contractility is severely affacted in capzβ mutants. (a) Failing of regular looping of the heart in capzβ$^{-/-}$. Wildtype and heterozygous sibling showed the normal heart looping. (b) Cardiac output measurements revealed significantly reduced CO in capzβ$^{-/-}$. Figure was taken from [192].*

Additionally, DeTCT-RNA-Seq analysis on 48 hpf zebrafish larvae indicated the differential expression of actin-binding genes such as actin alpha cardiac muscle 1a (*actc1a*), Fos-like-antigen 2 (*fosl2*), and cytokine signaling 3b (*socs3b*) in *capzβ*$^{-/-}$ fish [192].

1.9 Aim of the study

Genetic animal models offer a convenient means to explore the molecular and cellular mechanisms driving the progression of cardiovascular disease at the organismal level, particularly for variants with well-defined causal roles. In this study, zebrafish were used because 70% of human genes have zebrafish orthologs, in particular the genes studied in this thesis. This high degree of genetic similarity makes zebrafish a powerful model for studying the functional effects of human disease-associated genetic variants.

The aim of this dissertation is to utilize transgenic zebrafish models to investigate the functional implications of genetic variants identified in two genes associated with cardiovascular diseases: *CAPZβ* and *PRDM16*.

CAPZβ was identified in patients with CHD, who demonstrate impaired cardiac development and reduced cardiac function. More than 30% of CHD cases are influenced by genetic factors [193], underscoring the importance of determining if specific rare variants in these genes can cause CHD through animal models. To assess the impact of *CAPZβ* variants identified in patients with CHD, this study focuses on their effect on cardiac output and sarcomere length in zebrafish. This analysis is based on the role of *CAPZβ* in actin assembly, a critical component in muscle contraction and heart function.

For *PRDM16*, a functional analysis of variants identified in patients with ARVC was conducted using zebrafish models. Given *PRDM16*'s significant role in diverse developmental processes, particularly in the brown fat to muscle transition, which is a critical issue in ARVC, understanding these underlying mechanisms is crucial. The study was explored the proliferative capacity of cardiomyocytes post-heart injury in zebrafish with mutated *PRDM16*, aiming to understand the gene's role in cardiac regeneration and repair mechanisms. Through these objectives, this research seeks to elucidate the molecular mechanisms by which these genetic variants contribute to cardiovascular diseases, potentially informing future therapeutic strategies.

Chapter 2

Materials

2.1 Organisms and cell lines

Zebrafish lines

Wild Type lines:	TL *(Tupfel long fin)* or AB
Transgenic (Tg) zebrafish lines:	Tg*(myl7:EGFP)*^{twu34} [194] Tg*(drl:EGFP)*^{cz331} [195]
Mutant Zebrafish Line:	*capzb*$^{hi1858/+}$ [162]
Competent bacteria	One Shot TOP10^{TM} Chemically Competent *E.coli*, One Shot^{TM} Mach1^{TM} Chemically Competent *E.coli*, One Shot^{TM} *ccdB* Survival^{TM} 2 T1R Competent Cells
Feeding strain:	*Artemia salina*

2.2 Chemicals and reagents

Chemicals and reagents	Company
Acetic	Roth
AdvanStain Ponceau	Advansta
Agar agar	Roth
Agarose	Invitrogen
Ampicillin	Sigma
Antibody Diluent	Thermo Fisher
Aqueous Mounting media	abcam
Bovine serum albumine (BSA) fraction V	Sigma
Calcium chloride dihydrate	Sigma
Chloramphenicol	Geyer
C6H12O6 D(+)Glucose	Sigma
CellRox	Invitrogen
Chloroform	Honeywell
Crystal RNAMagic	Biolab
Disodium Phosphate Dihydrate	Sigma
DNA Ladder 1 kb	Biolab
EDTA	Fulka
Fluoromount-G^{TM}, with DAPI	Affymetrixe Bioscience
HEPES	Sigma
Ethanol	Roth
Glutamataldehyde 25%	Sigma
Glycerol	Geyer
Glycin	Roth
Glyo-fixx	Thermo Fisher
Goat Serum, New Zealand origin	Thermo Fisher
HD Green PLUS DNA Stain	Intas
Hydrochloric acid	Roth
Isopropanol	Roth
Lysogeny broth (LB)	Invirogen
Lysogeny broth with Agar	Invirogen
Kanamycin	Sigma

Magnesium Chloride, Hexahydrate	Sigma
Mitotracker Deep Red FM	Invitrogen
Mitotracker Red CMXRos	Invitrogen
MitoSox Red	Invitrogen
Nuclease-free Water	Invitrogen
Paraformaldehyde 4%	HIMEDIA
PBS	Life Technologie
Potassium chloride	Sigma
Sea salt	ZOO & Co. Knutzen
Streptomycin	Sigma
Super Optimal broth Catabolite repression (S.O.C)	Invitrogen
Sodium chloride	Roth
Tetramethylethylenediamine	Roth
Tissue-Tek O.C.T. Compound	Sakura
Tricaine	Sigma
TriDyeTm 100bp DNA ladder	NEB
10x Tris-Acetat-EDTA Buffer	Genekam
Tris-HCl	Roth
Trypsin – EDTA 10X	Biowest
Tween20	Geyer

2.3 Buffers and solutions

Artemia medium	10 g sea salt in 10 L dH2O
Base solution	14g KOH, 4 ml EDTA 0.5 M in 200 ml H2O
Blocking solution	20mL PBST, 2% neonatal goat serum, 2mg/ml BSA
CaCodylat buffer 0.1M	4.28g Sodium Cacodylate, in 100 ml dH20, pH 7.3

Citrate buffer	2.94 g sodium citrate trisodium salt dihydrate 10mM in 1L dH2O, pH 6.0
E3 Stock	17.4g NaCl, 0.8g KCl, 2.9g CaCl2 2H2O, 4.89g MgCl2 6H2O, in 1L RO-Water, pH 7.0
Embryo water	240 ml E3-Stock, 10L RO-Waterr
Fixation solution	262.2 μl Glutamataldehyde 25%, 1312 μl PFA 4%
Homogeniziation solution	10 mg/ml Collagenase P, 0.05% Trypsin-EDTA, 1xPBS
KOH Stock	14g KOH, 4 ml EDTA 0.5M, in 200 ml H2O
LB-Agar	LB medium, add 15 g agar agar,dH2O up to 1 L, autoclaved
LB-Medium	16g LB, dH2O up to 1 L, autoclaved
LB medium with ampicillin	LB medium 1 L, autoclaved, add ampicillin reaching to 100μg/ml when cooled down to 60 °C
LB medium with kanamycin	LB medium 1 L, autoclaved, add kanamycin reaching to 50μg/ml when cooled down to 60 °C
LB medium with spectinomycine	LB medium 1 L, autoclaved, add spectinomycine reaching to 50μg/ml when cooled down to 60 °C
Neutralisation's Stock solution	48.4g Tris-HCl, in 200 ml H2O

PBS-T	PBS, Tween® 20 detergent: 0.1% (w/v)
S.O.C medium	1 L S.O.C medium, add 0.02 M C6H12O6 D(+)Glucose (sterile)
TAE Buffer	100 ml 10x TAE Buffer, in 1L H2O
Tricaine Stock	4g Tricain, 21 ml Tris 1M in 1 L H2O, pH 7.0
Tyrode's solution	3.974g NaCl, 0.201g KCl, 0.102g MgCl2 6H2O, 0.450g C6H12O6 D(+)Glucose, 1.192g, C8H18N2O4S HEPES,0.027g Na2HPO4 2H2O, 0.132g CaCl2 2H2O in 500 mL H2O, pH 7.4
Tyrode's solution with BSA	50 mL Tyrode's solution, 300 mg BSA

2.4 Kits and Enzymes

Enzymes	Company
AmpliTaq Gold DNA Polymerases	Thermo Scientific
CloneAmp^{TM} HiFi PCR Premix	Clonetech
Collagenase P 100 MG	Sigma-Aldrich
DNase I	Thermo Scientific
DpnI	NEB
Red Taq Ready Mix PCR Raction Mix	Geyer
Gateway BP Clonase enzyme mix 20 react.	Life technologie
LR Clonase II Plus Enzyme 20React.	Life technologie
Platinum SuperFi II DNA Polymerase High-Fidelity PCR Enzyme	Thermo Scientific
T4 Ligase 100 U	Sigma-Aldrich
T4 Polynucleotide Kinase (10 U)	Thermo Scientific^{TM}

Kits	Company
Agilent RNA 6000 Nano Kit	Agilent
Click-iT^{TM} EdU Imaging Kit with Alexa Fluor^{TM} 594 Azides	Thermo Scientific
Click-iT^{TM}Plus TUNEL-Assay-Kits with Alexa Fluor^{TM} 594 Azides	Thermo Scientific
HiSpeed Plasmid Maxi Kit (10)	Qiagen
MinElute PCR Purifikation Kit (50)	Qiagen
mMessage mMachine T7 25Best.	ThermoFisher
Monarch DNA Gel Extraction Kit(250)	New England Biolabs
MultiTissueDissociation Kit2	Miltenyi Biotec
Oil Red O Stain Kit (Lipid Stain)	Abcam
Qiaprep® Spin Plasmid Miniprep (250)	Qiagen
Qubit® dsDNA BR Assay Kit	Life technologie
TruSeq Stranded Total RNA kit	Illumina

2.5 Vectors

PCM326 pDestTol2 crystallin-YFP

Phic31 pcDNA3

p5E-cmlc2

p3E-polyA

PRM16 cloned in pENTR223

CAPZβ (NM-004930) Human Tagged ORF Clone

pDONR^{TM}221

2.6 Oligonucleotides

A list of the used oligonucleotides can be found in the Appendix 1

2.7 Antibodies

Name	Company
GFP Tag Monoclonal Antibody (GF28R) (1:100)	Thermo Fisher
Anti-PCNA antibody [PC10] (ab29) (1:200)	Abcam
Anti-Connexin 43 antibody (1:30)	Sigma
Anti Zn-8 neuronal cell surface marker (1:50)	DSHB
Goat Anti-Rabbit IgG (H+L) Highly Cross-Adsorbed Secondary Antibody, Alexa Fluor Plus 488 (1:500)	Thermo Fisher
Donkey Anti-Mouse IgG (H&L) Alexa Fluor ^{TM} 647 (1:500)	Thermo Fisher
Alexa Fluor® 488 Donkey Anti-Mouse IgG (H+L) (1:100)	(JacksonIR)
Alexa Fluor® 594 Donkey Anti-Rabbit IgG (H+L) (1:100)	(JacksonIR)

2.8 Devices and supplies

Agarose-Gel imaging	Bio-Rad
Agilent 2100 Bioanalyzer System	Agilent Technologies
BD LSR Fortessa Cell Analyzer	BD Biosciences
Binocular	VWR
Centrifuge	VWR mini star

Centrifuge 17R	VWR micro star
Centrifuge 5430	Eppendorf
CryoStar NX70 Cryostat	Thermo Fisher Scientific
Compact fluorescence microscope HS	Keyence
Confocal laser scanning microscopy	Zeiss
Fluorometer	Life Technologies
Gel electrophoresis chambers	Bio-Rad
Incubator	WTW
Microinjector	Eppendorf FemtoJet4i
Microneedle puller	Sutter instrument
Microscope with Camera	Nikon SMZ25
NanoDrop Microvolume Spectrophotometers	Thermo Fisher Scientific
NovaSeq 6000 Sequencing System	Illumina
Thermoblock	HLC by Ditabis
Thermocycler	Bio-Rad
Thermoincubator	VWR
Thermomixer	Eppendorf
Vortextmixer	VWR Analog vortex

2.9 Other devices

AF-10 (ice machine)	Scotsman
Freezer -20 °C	Liebherr
Freezer -80 °C	
pH2211 Microprocessor pH Meter	Hanna Instruments
Microwave	SHARP
MilliQ	M Prograd ts2
scales	VWR

2.10 Software

Image analysis	Image J
Microscope software	NIS-Elements BR
Sequence analysis	CLC Sequence Viewer
Spreadsheet application	Microsoft®Excel for Mac
Statistic analysis	GraphPad Prism (version 10)
Text processing	Overleaf

2.11 URLs

BLAST searches	http://blast.ncbi.nlm.nih.gov
DESeq2 Reference	https://www.bioconductor.org
Gene Cards	http://www.genecards.org
gnomAD Browser (version v4.0.0)	https://gnomad.broadinstitute.org
Genome Browser *Danio rerio*	https://genome-euro.ucsc.edu
NCBI	http://www.ncbi.nlm.nih.gov
NCBI Gene	http://www.ncbi.nlm.nih.gov/gene
NCBI PubMed	http://www.ncbi.nlm.nih.gov/pubmed
OligoCalc	http://biotools.nubic.northwestern.edu
UniProt	http://www.uniprot.org
Variant Effect Predictor	http://grch37.ensembl.org/Homo-sapiens
ZFIN	https://zfin.org/
Enrichr	https://maayanlab.cloud/Enrichr

Chapter 3

Methods

3.1 Organisms

3.1.1 Cultivation of Artemia

First instar nauplius larvae of Artemia Special Diets Service SDS (Ludwigshafen) were used as prey for zebrafish. To hatch the eggs, artemia were incubated overnight at 28°C in Artemia medium with a continuous supply of air. To feed the zebrafish, the nauplii were collected, washed with Reverse Osmosis (RO) water to remove salts, and then suspended in RO water.

3.1.2 Zebrafish husbandry

Zebrafish were maintained based on the guidelines described in the Zebrafish Book [196]. Zebrafish were reared at a density of about 20 fish per 10 l of water in individual tanks connected to a circulating water system (Tecniplast), the water temperature was maintained at 28 °C. Experiments were carried out using zebrafish *Danio Rerio* wildtype (TUÏF) and transgenic lines $capzb^{hi1858bTg/+}$, *Tg(myl7:EGFP)* and *Tg(drl:EGFP)*. All laboratory cultured strains are available at the Clinic for Congenital Heart Defects and

Paediatric Cardiology, University Hospital Schleswig-Holstein, Campus Kiel. All animals were cultured under constant environmental conditions including embryo medium, feeding schedule (2 times per day) and temperature according to standard procedures. The study was conducted in accordance with animal welfare regulations and with careful consideration of animal well-being, with an animal experimentation application in place.

3.2 Standard laboratory methods

3.2.1 DNA Extraction

At 48 and 72 hour post fertilisation (hpf) the DNA from the fins of embryos were extracted with KOH. The fins were collected in separate 1.5 ml reaction tubes and washed once with 99% EtOH. To to remove the all EtOH out of tube the embryos were incubated for 10 min at 80°C. During the incubation 1x base solution and 1x neutralisation's buffer were prepared. 25 μl of the base solution was added to the samples and mixed via vortexing for 10 sec. The samples were incubated for 30 min at 95°C. Afterwards the samples were mixed for 2 min via vortex. 25 μl of neutralisation's buffer was added to each sample.

3.2.2 RNA Extraction

Total RNA was extracted from the zebrafish at larvae 48hpf and 72hpf using Trizol reagent according to the manufacturer's protocol. 300 μl of Trizol reagent was added to the samples, which were then homogenized by pipetting up and down and incubated for 5 min at room temperature. 300 μl of chloroform added to the samples, which were then shaken vigorously by hand for 15 seconds. Following the incubation, the samples were centrifuged at 12,000 x g for 15 min at 4 °C. After centrifugation, the mixture separated into a lower red phenol-chloroform phase, an interphase, and a colorless upper aqueous phase. The aqueous phase, which contained RNA, was transferred to a 1.5 mL reaction tube. 0.5 mL of isopropanol was added to samples and incubated the samples for 10 minutes at room temperature. Then centrifuge samples were centrifuged at 12,000 x g for 15 min at °C. supernatant was discarded and pellet was washed 2 times with 70% ethanol. RNA pellet

was air dried leaving the tubes open on the counter for 20 min At the end of extraction procedure, total RNA was re-dissolved in 10μl nuclease-free water. Samples were stored at -80 °C.

3.2.3 Quantification of nucleic acids

The quantity and quality of the isolated nucleic acids were determined at the absorbance of 260 nm using the Nanodrop spectrophotometer.

3.2.4 Polymerase chain reactions (PCRs)

Standard PCR

A standard PCR reaction was set up in the final volume of 25 μl. Table 3.1 contains the pipetting scheme for the reaction. The PCR products were analysed via agarose gel electrophoresis.

Component	Volume (μl)
AmpliTaq Gold® Fast PCR MasterMix	5
Forward primer (10 pmol)	1
Reverse primer (10 pmol)	1
dH2O	1
DNA	2
Total volume	25

Table 3.1: *Pipetting scheme for standard PCR.*

Steps	Temperature	Duration
Initial denaturation	95°C	10 min
Denaturation	96°C	0:03 sec
Hybridization	60°C	0:03 sec
Elongation	68°C	0:20 sec
Terminal elongation	72°C	0:15 sec

The PCR was performed with 39 cycles.

Nested PCR

A nested PCR reaction was set up in final volume of 25 μl. Table 3.2 contains the pipetting scheme for the reaction.

Component	Volume (μl)
CloneAmp HiFi PCR Premix	12.5
Forward primer (10 pmol)	0.7
Reverse primer (10 pmol)	0.7
dH2O	10.1
DNA	1
Total volume	25

Table 3.2: *Pipetting scheme for nested PCR.*

Steps	Temperature	Duration
Initial denaturation	98°C	1 min
Denaturation	98°C	1 min
Hybridization	68°C	2 min
Elongation	72°C	3 min
Terminal elongation	72°C	3 min

The PCR was performed with 34 cycles.

High Fidelity PCR

For the amplification of DNA fragments for expression constructs, Platinum SuperFi II DNA Polymerase High Fidelity with proof reading ability was used. Table 3.3 contains the pipetting scheme for the reaction. The PCR products were analysed via agarose gel electrophoresis.

Component	Volume (μl)
Platinum SuperFi II DNA ^{TM} Polymerase	25
Forward primer (10 pmol)	2.5
Reverse primer (10 pmol)	2.5
dH2O	18.5
DNA	1
DMSO	0.5
Total volume	25

Table 3.3: *Pipetting scheme for High Fidelity PCR.*

Steps	Temperature	Duration
Initial denaturation	98°C	30 sec
Denaturation	98°C	10 sec
Hybridization	60°C	10 sec
Elongation	72°C	10-15 sec per kb
Terminal elongation	72°C	5 min

The PCR performed with 30 cycles

Colony check PCR

A colony check PCR was performed to analyse plasmids for insertion of DNA. A standard PCR reaction (see paragraph 3.2.4) of a final volume of 10 μl was set up without template DNA. Single bacterial colonies were served as templates. These were picked from agar plates and transferred directly to the reaction mix. For products ligated into PCM326 pDestTol2 crystallin-YFP, plasmid specific PRDM16-screen-F and PRDM16-screen-R primers were used.

3.2.5 Electrophoretic separation of DNA samples

DNA samples were separated using horizontal 0.5-1.5% agarose gel electrophoresis in 1x TAE buffer. To visualise DNA-bands Intas HD Green ^{TM} HD was included into the gels. After adding DNA loading buffer to the samples, DNA fragments were separated at 98-120

V, depending on the fragment size. The size of DNA fragments was estimated under UV-illumination using the TriDye ^{TM} 100 bp DNA Ladder or 1 kb Plus DNA Ladder Mix as size marker.

3.2.6 Extraction of DNA fragments from agarose gel

The desired PCR products were cut out on a UV illumination table and transferred into 1.5 ml reaction tubes. Afterwards, DNA was extracted using the Monarch DNA Gel Extraction Kit. The extraction of DNA fragments were performed according to the manufacturer's protocol. DNA was eluted by adding 20 μl reaction tubes water.

3.2.7 Ligation of PCR products

For generation of an expression PRDM16-D628N and PRDM16-P889L construct, PCR products were ligated. Ligations were carried out for 30 min at 37°C. After incubation 1μl PEG6000 and 2μl T4 ligase were added to the reaction. Incubation follows 1 hour at Room temperature. The cleavage of DNA follows after the addition of 1μl of DpnI enzyme for 3 min at 37°C. A pipetting scheme for the ligation of DNA fragments shown in table 3.4.

Component	Volume (μl)
Ligase buffer(10X)	2
DNA	10
T4-Polynukleotidkinase	1
dH2O	7
Total volume	20

Table 3.4: *Pipetting scheme for the ligation of DNA fragments.*

3.2.8 Transformation of *E.coli*

For the transformation, 4 μl of reaction (BP, LR, PCR and ligation's product) were used to transform in 50 μl Mach1 or top 10 cells. The cells were incubated on ice for 30 min. After incubation they were treated with heat-shock for 30 sec at 42°C, followed by immediate ice incubation for 2 minutes. 250 μl of S.O.C Medium were added to cells and incubated at 37°C for 1.5 h at 225 rpm in shaking incubator. 20 μl of the transformation mix were spread on ampicillin plate. 4 colonies were selected for plasmid isolation.

3.2.9 Preparation of plasmids

Mini-preparations to isolate plasmid DNA from clones propagated in LB liquid cultures were performed using the NucleoSpin® Plasmid QuickPure Kit according to the manufacturer's instructions.

3.2.10 Sanger Sequencing

DNA sequencing was carried out using Eurofins Genomics. Reactions were set up by mixing 5 μl of plasmid (70-100 ng/μl) as the template with 5 μl of primer (5 pmol), and then performed for sequencing.

3.3 Gateway technology

The Gateway cloning method, which has been developed by Invitrogen,is an *in vitro* version of the integration recombination reactions that take place when lambda phage infects bacteria. These recombination reactions are facilitated by the recombination of attachment sites from the phage (attP) and the bacteria (attB). As a result of recombination between the attP and attB sites, the phage integrates into the bacterial genome flanked by two new recombination sites. Figure 3.2 demonstrates general routine of adding att sites to a "middle entry" clone (pME) using PCR with gene-specific primers, which is later

recombined with a donor vector. As a middle entry clone I created four PRDM16 variants, *PRDM16* wild type, CAPZβ variants and *CAPZβ* wild type. The base substitution for creation of variants were performed also by PCR in this step. In this project, a three-insert multisite Gateway LR reaction was utilized to combine three entry clones (p5E, pME, p3E) with the destination vector, Destination vector pCM326pDestTol2 crystallin YFP for the generation of zebrafish transgenic lines. Within the zebrafish expression constructs, following entry vectors were combined: cardiac myosin light chain 2 *(myl7)* promoter constructs as 5' (p5E) vector, four PRDM16 variants, wild-type *PRDM16*, four *CAPZβ* variants, and wild-type *CAPZβ* as middle (pME) vector, along with polyA as 3' (p3E) vector.

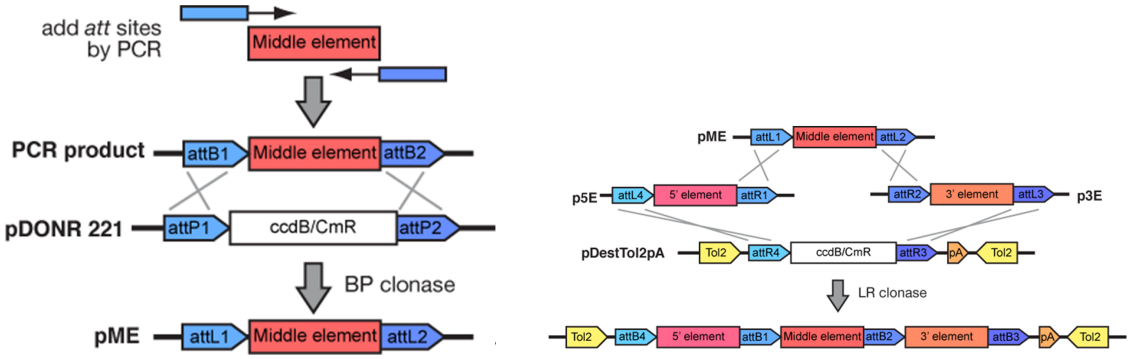

(a) Depiction of a BP reaction for a polymerase chain reaction amplified open reading frame.

(b) LR reaction between ENTRY clones and a Destination vector.

Figure 3.1: *Gateway recombination reactions.*

BP reaction

The BP Reaction takes place between the attB sites flanking the insert and the attP sites of the donor vector. The next step is the BP recombination of reactions, which is performed as described in the invitrogen Multi-Site Gateway Manual. An equimolar amount of the appropriate donor vector and purified PCR product (20 femtamoles) are combined with BP Clonase II enzyme mix in a final volume of 10 μl. The incubation time of this reaction was 1 hr at room temperature. To stop the reaction 1 μl Proteinase K was added and incubated at 37°C for 10 min.

LR reaction

The LR Reaction, which is catalyzed by the LR Clonase II Plus enzyme mix takes place between the attL sites of the generated entry clone and the attR sites of the destination vector. As a result, an expression clone for transgenesis was generated containing *myl7* promoter and CAPZB variants or *CAPZβ* wild type or PRDM16 variants or *PRDM16* wild type and polyA sequence flanked by attB sites. The reaction was set up with 20 femtamoles of each vector in a 10 μl reaction. The reactions were incubated overnight at 25°C.

3.4 Generation of transgenic zebrafish lines

In order to examine the functional relevance of the identified mutations in *PRDM16* and *CAPZβ*, humanized transgenic zebrafish models to overexpress the individual human variants under the cardiac-specific *myl7* promoter using the Tol2 system were generated. Full length *PRDM16* and *CAPZβ* were serve as a control.

Preparation of capped transposase RNA

The transposase protein synthesized from mRNA catalyzes excision of the Tol2 construct from the plasmid and integration of the excised Tol2-based destination vector (e.g. pCM326pDestTol2 crystallin YFP) into the genome. The synthesis of transposase mRNA involves in vitro transcription, which can be divided into five main steps:

1. *NotI* restriction

2. Purification of the restricted product

3. RNA transcription and isolation

4. Digestion of residual DNA

5. Purification and measurement of RNA

A pipetting scheme for the *NotI* restriction (for the linearization of Tol2 encoded plasmid) shown in table 3.5.

Component	Volume (μl)
DNA(200ng)	10
NotI	1
NEBuffer 2	2
ddH2O	7
Total volume	20

Table 3.5: *Pipetting scheme for the NotI restriction.*

The incubation was carried out overnight at 37°C. The restricted products were purified using a PCR Purification kit following the manufacturer's protocol. DNA was eluted by adding 25 μl DNase & RNase free water. Translation and isolation of mRNA were performed using the mMESSAGE mMACHINE^{TM} SP6 Transcription Kit. A pipetting scheme for the translation shown in table 3.6. The incubation was carried out 3 hours at

Reagent	Volume (μl)
2X NTP/CAP	10
10X Reactin Buffer	2
linear DNA template	6
Enzyme Mix	2
Total volume	20

Table 3.6: *Pipetting scheme for the translation.*

37°C. Digestion of residual DNA was performed by adding 1 µL and incubating for 15 minutes at 37°C. The samples were purified using the MinElute PCR Purification Kit, and finally, they were eluted in 15 μl). The RNA concentration was measured with the Qubit RNA BR Assay kit.

3.4.1 Mating the fish

The night prior to injection, fish were set up in breeding tanks with dividers in place. To increase total egg production, fish were set up in a ratio of two females to one male. The following morning, the dividers were removed from the tanks and allowed for approximately 20 minutes of undisturbed mating time. Eggs were collected from the breeding cages and rinsed with embryo water.

3.4.2 Microinjection into the zebrafish zygotes

A microscope slide was placed in the inverted lid of a 100mm Petri dish. Eggs were lined up against the side of the slide to form a single column. The excess egg water were removed from the slide. The needles were pulled in advance. The needle was backloaded with an injection solution containing 25 ng of Tol2 transposase and 25 ng of the DNA construct in a final volume of 10 μl (Table 3.7). A drop of mineral oil on a micrometer was used to calculate the volume of each injection. When injected into the oil, a bead with a diameter of 0.1 mm contains 1 nL of injection material. The injection solution was injected into the cell of the fertilized egg. After completing a column of eggs, a gentle stream of egg water was used to move the injected eggs into a clean Petri dish. Several uninjected embryos were kept as a control. Next day dead embryos were removed and the number of injected embryos was recorded. The injected constructs are listed in table 3.8.

Component	Volume (μl)
Transposase (25ng)	2.5
DNA(200ng)	0.5
H2O	7
Total volume	10

Table 3.7: *Pipetting scheme for the injection solution.*

Number	injected constructs
1	*myl7*:CAPZβ WT-PolyA
2	*myl7*:CAPZβ Thr179Ser-PolyA
3	*myl7*:CAPZβ Lys181Arg-PolyA
4	*myl7*:CAPZβ Ser192Asn-PolyA
5	*myl7*:CAPZβ Arg215Cys-PolyA
6	*myl7*:PRDM16-WT-PolyA
7	*myl7*:PRDM16-A259V-Poly
8	*myl7*:PRDM16-D628N-PolyA
9	*myl7*:PRDM16-P889L-PolyA
10	*myl7*:PRDM16-S1059L-PolyA
11	*myl7*:PRDM16-K702*

Table 3.8: *Table 3.5 lists the injected constructs used for generating zebrafish transgenic lines.*

3.4.3 Transgenic carrier selection

The embryos at 48 hpf or 72 hpf were screened for GFP-positive expression in the heart and YFP-positive expression in the lens. GFP-positive expression in the heart was used as a marker for cardiac output measurements, while YFP-positive expression in the eyes indicated the potential integration of the pCM326 pDestTol2 crystallin YFP construct containing full-length *PRDM16* or *CAPZβ*, or their respective variants.

Fin clipping-based genotyping

Fin clipping is a standard procedure employed to obtain genetic material from individual fish for genotyping purposes. A small section of tissue is clipped from the tail's end to extract DNA, facilitating subsequent analyses like PCR. This non-invasive method is commonly used for efficiently collecting genetic samples without causing harm to the fish. Fish are anesthetized through immersion in 0.02% MS-222 (Tricaine) with a neutral pH until gill movement slows down. The stock solution is prepared at a concentration of 4g/L, buffered to pH 7 with sodium bicarbonate. Once anesthetized, the fish is promptly transferred to a clean surface or petri dish using a plastic spoon. The fin is then clipped at a point not exceeding halfway between the fin tip and the point where the scales conclude. After fin clipping, fish are promptly moved to a container with fresh system water. Continuous monitoring ensues until the fish fully recover and regain the ability

to right themselves. The clipped fin was preserved in 99% ethanol and utilized for DNA extraction, following the procedure outlined in subsection 3.2.1. Identified founder fish represent F0 that is then bred with WT strain to generate F1 stable carriers.

3.5 Measurements of cardiac output

In the current study, the cardiac output (CO) of transgenic *PRDM16* WT and variants were compared with *Tg(myl7:GFP)* as a control group. The same control group were also used for CO measurement of CAPZβ WT and variants. For the quantification of heart function and morphology at the 48 hpf and 72 hpf stages, videos obtained from fluorescent microscopy were utilized. The approach is based on recording three-dimensional (3D) image sequences for 10 seconds and that are used for further cardiovascular analysis. For this purpose, the embryo is positioned in a lateral position with the ventricle clearly visible throughout the full cardiac cycle. The ventricle in maximum systole and maximum diastole were marked by using NIS-Elements BR 4.40.00 64-bit measurement's tools. The Ellipse formula was used to determine the approximate volume of the area measured by the program using the number of pixels. The formula for calculating the area of the ellipse is:

$$A = a * b * \pi$$

The formula for the calculation of volume ellipse is:

$$V = \frac{3}{4} * a * b * c * \pi$$

After inserting the area the formula is:

$$V = \frac{3}{4} * A * c$$

Only approximate volume can be measured because the third dimension "c" is missing. For the purpose of this study, it is assumed that $b \approx c$ in our heart tube. The program automatically measures 2b when measuring the area, indicated in the output tables as MaxFeret90 i.e. the maximum diameter at a 90°C angle to the longest diameter overall. This means that $b = \frac{MaxFeret90}{2}$ resulting in $V = \frac{3}{4} * A * \frac{MaxFeret90}{2}$. Therefore, shortened formula for the calculation of ventricle volume during systole and diastole is based on the

formula:

$$V = \frac{2}{3} * A * MaxFeret90$$

Stroke volume (SV) is the blood volume pumped from the ventricle for each beat and is simply calculated from the difference in the volume of the ventricle in diastole and systole and is calculated by the equation:
SV (nl) = $\text{volume}_{end-diastolic}$ - $\text{volume}_{end-systolic}$
CO in nanoliter per minute is measured by the equation:

$$CO(\frac{nL}{min}) = SV(\frac{nL}{Beat}) * Heartrate(\frac{Beats}{min})$$

Heart rate (HR) is simply determined by measuring the time between two identical successive points in the recorded images.

3.6 ROS detection

Mitochondrial membrane potential, mitochondrial ROS and general ROS, zebrafish larvae at 48 hpf of the transgenic lines were detected. The number of 40 embryos at 48hpf were collected in 1.5 ml reaction tubes. Most of the 1x E3 embryo medium was removed and embryos were euthanizied with 400 μl Tricaine from 0.01% solution and left on ice for 5 min. After treatment the samples were washed 2x with 1x PBS for 1-2 min. Dissociation of larvae followed by adding 600 μl of homogenization solution (collagenase P + trypsin-EDTA in 1x PBS). Incubation time was 30 min at 28 °C in a thermoblock. The digestion and homogenization were stopped by adding 700 μl DMEM-10% FBS and the cells were centrifuged for 2 min at 600 x g at RT. Once again cell were washed with 1x PBS. For the staining, cells were kept in 1 ml of DMEM-10% FBS at 28 °C. Then cells will be incubated for 30 min in DMEM-10% FBS with either CellROX for ROS detection, Mitotracker Deep Red FM for visualization of the number of mitochondria, Mitotracker Red CMXRos for mitochondrial membrane potential and MitoSOX Red for mitochondrial Superoxide detection. Probes were analyzed by flow cytometry. Flow cytometry data were collected on a BD LSR Fortessa equipped with FLSR Fortessa software using the red 644/665-nm laser for CellROX, Mitotracker Deep Red FM (644/665-nm), Mitotracker

Red CMXRos (579/599-nm), MitoSOX (396/610-nm) and 508/525 nm for GFP signal for cardiomyocytes. Mean fluorescence intensity of RFP was used for quantification of the different probes and data were expressed relative to GFP signal for cardiomyocytes of transgenic *Tg(myl7:GFP)* zebrafish.

3.7 Lipid droplet

3.7.1 Heart extraction from adult zebrafish

Adult zebrafish were euthanized with Tricaine 1% in a glass beaker until gill movements ended, and until there was no response to a tail pinch. A spoon was used to transfer the fish ventral side acing upwards in a slotted sponge under a dissecting microscope. The ventral wall of the fish was opened with the longitudinal cut at pericardial area between gills. The outflow tract was located. The distal end of outflow tract was grabbed with forceps and the heart was gently pulled out of the chest cavity. The ventral aorta and sinus venosus was cut with the help of forceps. The heart was placed into the 60-mm Petri dish with PBS or Tyrode's solution.

3.7.2 Cryosectioning

Isolated hearts from adult zebrafish were washed in ice-cold 1x PBS. After washing samples were placed in Tissue-Tek O.C.T. Compound and freezed in a cryostat machine until samples reached the optimal temperature of -18°C. At this temperature samples were cut with a microtome and taken by a superfrost^{TM} adhesion microscope slides for Oil red O staining.

3.7.3 Oil red O staining

Slides were incubated first in propylene glycol for 2 min and than for 30 min in pre-warmed Oil red O solution. After incubation slides were differentiated in 85% propylene glycol

for 1 min and rinsed twice in dH2O. Nuclei staining followed by hematoxylin for 1-2 min and slides were rinsed three times in water before embedding with an aqueous mounting medium. The section were used for imaging to investigate the lipid deposition in the heart.

3.8 Immunohistochemistry

3.8.1 Heart extraction from zebrafish embryos

Single embryo at was placed into petri dish half filled with fresh Tyrode and BSA. The chorion and fin were removed via forceps. The body was stabilized with forceps by holding the head between the eyes and gills. A microneedle was used to pin the aorta. The separation of pericard and Sinus Venosus was performed with forceps. Because of electrolyte property of Tyrode's solution the heart can continue to beat. A pipette was used to transfer the heart into microtiterplatte for Immunofluorescence analysis.

Click-iT EdU Kit

Cell proliferation was evaluated by using EdU staining of isolated hearts at different time points 48 hpf, 72 hpf and 96 hpf. Transgenic PRDM16 variants and wildtype *PRDM16* were used for EdU staining. Cardiomyocytes were distinguished from endothelial cells by GFP expression. After heart isolation, samples were incubated in 10 μM EdU solution at least 2 h before proceeding to fixing with 4% PFA for 30 min. Then, samples were washed twice with PBST buffer before incubation with click-iT Plus EdU Reaction cocktail for 30 min at room temperature. Table 3.9 contains the pipetting scheme for the EdU Reaction cocktail. After incubation samples were washed two times with blockung buffer for 10 min followed by primary antibodies diluted in antibody Diluent (1:500) for 72 h at 4 °C. After incubation samples were washed with blocking buffer and mounted in Fluoromount with DAPI.

Component	Volume (μl)
1X Click-iT Plus EdU Reaction Buffer	440
Copper Protectant (Component E)	10
Alexa Fluor 594 picolyl azide (Component B)	1,2
1X Click-iT Plus EdU Reaction Buffer Additive	50

Table 3.9: *Pipetting scheme for the EdU Reaction cocktail.*

Click-iT TUNEL assay

Transgenic wildtype *PRDM16* zebrafish and variants were used for TUNEL assay to detect the cardiomyocyte apoptosis at 48 hpf, 72 hpf and 96hpf. To distinguish cardiomyocyte from endothelial cells GFP antibody was used. Cardiomyocyte apoptosis was detected by the TdT-mediated dUTP Nick-End Labeling (TUNEL) technique using a Click-iT TUNEL Alexa Fluor 594 kit according to manufacturer's protocol.
Isolated hearts of zebrafish embryos were kept in Tyrode's solution and fixed with 4% PFA for 30 min, washed twice with PBST buffer. For positive control, hearts were treated with DNase I solution for 30 min at 37°C . After washing process hearts were incubated for 10 min in TDT Buffer at 37 °C and then for 1h TdT reaction cocktail. Table 3.10 contains the pipetting scheme for the TdT reaction Mixture.

Component	Volume (μl)
1x TdT reaction buffer (Component A)	235
EdUTP (Component B)	5
TdT (Component C)	10

Table 3.10: *Pipetting scheme for the TdT reaction Mixture.*

Samples were washed twice with blocking solution each 10 min and incubated in reaction cocktail for 30 min at 37°C. Click-iT^{TM}reaction cocktails were prepare according to table 3.11.

Component	Volume (μl)
Super mix	225
1x Reaction Buffer Additive	25

Table 3.11: *Pipetting scheme for the cocktails reaction.*

Super mix was contained 262,5 μl 1X Click-iT Plus TUNEL Reaction Buffer, 6,7 μl Copper

Protectant (Component F) and 0,87 μl Alexa Fluor 594 picolyl azide (Component G). Then, hearts were two times washed with blocking buffer and incubated overnight with GFP Polyclonal Antibody, Alexa Fluor^{TM} 488 diluted in antibody Diluent (1:500) at 4 °C. After incubation samples were washed with blocking buffer and mounted in Fluoromount with DAPI.

Connexin 43 staining

localisation of connexin 43 was evaluated by using connexin 43 staining of isolated hearts at 72 hpf. Transgenic *PRDM16* variants and wildtype *PRDM16* and PRDM16-K702* were used for staining. Strain AB was used as control. Isolated hearts of zebrafish embryos were kept in Tyrode's solution with BSA and fixed with Glyo-fixx for 30 min, washed twice with PBST buffer. The hearts were then incubated with blocking buffer for 1 hour at room temperature, followed by overnight incubation with connexin 43 (1:30) and zn8 (1:50) antibodies at 4 °C. After incubation, the samples were washed with blocking buffer every 20 minutes and then incubated with secondary antibodies for 2 hours at room temperature. Following this, the samples were washed again with blocking buffer and mounted in Fluoromount with DAPI.

PCNA staining

Seven-micrometer thick paraffin-embedded adult zebrafish heart sections were deparaffinized with xylene and then rehydrated through a descending gradient of ethanol. After rehydration sections were boiled in 10 mM sodium citrate buffer, pH 6.0; maintained at a sub-boiling temperature for 10 minutes. Slides were cooled on bench top for 30 minutes. PCNA expression in the injured heart was determined by immunohistochemical staining using specific antibodies against zebrafish PCNA. Briefly, the slides were incubated with blocking buffer to bind non-specific binding for 30 min. The sections were then incubated with anti-PCNA (1:200 diluted with antibody Diluent) overnight. The samples were washed four times with blocking buffer for 15 min. Then the samples were treated with the fluorescence-labelled secondary antibody in antibody Diluent for 2 h. The samples were washed three times with PBS 15 min. Subsequently, the sections were mounted in Fluoromount with DAPI.

3.9 Fluorescence Intensity Measurements

To determine fluorescence intensity profiles, ImageJ was utilized. Images were captured under consistent settings, and channels were individually separated prior to measurement. Fluorescent intensity measurements were performed exclusively on the red channel (Cx43). The ventricle and atrium were delineated using the freehand tool. "Mean Intensity" and "Standard Deviation" were selected for the measurements.

3.10 Ventricular resection

Transgenic zebrafish carrying the wildtype *PRDM16* as well as the truncation mutation (K702*) were crossed with *Tg(drl:GFP)* fish. Adult zebrafish aged 6–12 months underwent ventricular resection surgeries. Anesthesia was induced using 0.4% Tricaine, followed by immobilization with the ventral side facing upwards in a slotted sponge. Surface scales were delicately removed with watchmaker forceps, and an incision was made through the skin, muscle, and pericardial sac. The ventricle was then gently pulled at the apex and cut using iridectomy scissors [180], removing approximately 20% of the ventricle. Post-surgery, fish were promptly returned to system water. Hearts were extracted as described in section 3.7.1 and fixed for further analysis at designated time points.

3.10.1 Histochemical stainings

All hematoxylin-eosin stainings and Masson-Goldner staining for regeneration model were performed in collaboration with Prof. Dr. Wolfram Klapper at the Hematopathology institute in Kiel. Formalin-fixed tissue underwent tissue processing and then was embedded in paraffin (wax) to create a FFPE block. The paraffin blocks were cut using a microtome to generate thin sections (7μm) of tissue embedded in paraffin for H&E staining staining and Masson-Goldner staining. In H&E staining, hematoxylin stains cell nuclei a purplish blue, while eosin stains the extracellular matrix and cytoplasm pink. For Masson-Goldner staining, Weigert's iron hematoxylin was used to visualize nuclei, and azophloxin and orange G solutions were employed to visualize muscles, cytoplasm, and erythrocytes.

In Masson-Goldner staining, connective tissue is counter-stained with light green SF solution.

3.11 Electron microscopy

To analyze the structure of transgenic *CAPZβ* and *PRDM16* hearts, electron microscopy was employed. Adult hearts from *CAPZβ* and *PRDM16* zebrafish were extracted in cold PBS and fixed in 4% glutaraldehyde. After primary fixation with glutaraldehyde, the samples were washed three times with CaCo buffer for 10 minutes each. For secondary fixation, 1% OsO4 was used, and the samples were incubated for 1 hour at room temperature. Following this, the samples were washed for 10 minutes each with CaCo buffer and 50% ethanol, and then kept in 70% ethanol at +4°C overnight. After incubation, the samples were sequentially washed with 90% and 100% ethanol for 10 minutes each. LR White resin was used as the embedding medium. Gelatin capsules were filled with the embedding medium, and the samples were placed inside the capsules. The curing process was conducted at 60°C for 24 to 48 hours. The sample preparation and imaging were performed in collaboration with Prof. Dr. Ralph Lucius at the Anatomy Institut at CAU in Kiel.

3.12 RNA sequencing

3.12.1 Isolation of RNA

The tolal RNA extraction from zebrafish embryos at 48 hpf ans 72 hpf was described in subsection 3.2.2. To ensure that the RNA was of sufficient quality to generate a sequencing library, the RNA quality was assessed using the Agilent 2100 Bioanalyzer System with the associated Agilent RNA 6000 Nano Kit.

3.12.2 Library Preparation and sequencing

For the total RNA sequencing experiments, the TruSeq Stranded Total RNA kit and sequencing reaction (NovaSeq 6000) were utilized. These procedures were performed by Dr. rer. nat. Sören Franzenburg at the Institute of Clinical Molecular Biology (IKMB) in Kiel, following the provision of extracted total RNA (RIN ≥ 8) from the samples.

3.12.3 Data analysis

The RNA-Seq data analysis pipeline encompasses multiple steps, beginning with the pre-processing of FASTQ-format files containing RNA reads from a Next-Generation Sequencing (NGS) platform. These reads are then aligned to an annotated reference genome, followed by the quantification of gene expression.

Pre-processing (e.g. read QC and UMI extraction), alignment (against reference *danRer10*) and transcript quantification was performed using the nf-core/rnaseq (Ref: https://zenodo.org/records/10471647) pipeline (version 3.5).

Upon alignment, reads are assembled into complete transcripts. This assembly can be guided by pre-existing reference transcript annotations or conducted *de novo*, without prior information. Subsequently, gene expression is quantified by tallying the number of reads aligned to each exon or the entire transcript, reflecting the expression level of each gene. DESeq2 (v1.34.0, PMID:25516281), a widely used tool, was employed for preprocessing the count data and conducting differential expression analysis. The initial step involved importing raw count data from the experiment, followed by a comprehensive quality assessment to ensure data integrity. This assessment included examining the mean-variance relationship of counts, performing principal component analysis (PCA), and evaluating sample-to-sample distances. To address variations in library size and sequencing depth across samples, DESeq2 performed normalization, adjusting raw counts to ensure comparability between samples. Additionally, genes with low read counts were filtered out to minimize noise in downstream analyses. These steps were conducted following the guidelines and procedures outlined in the DESeq2 documentation DESeq2 Reference (https://www.bioconductor.org/packages/release/bioc/vignettes/DESeq2/inst/doc/DESeq-2). Following data preprocessing and QC, DESeq2 conducted a differential expression

analysis to identify genes showing significant expression changes between experimental conditions. Statistical tests such as the Wald test or likelihood ratio test were employed, and p-values were adjusted using methods like the Benjamini-Hochberg procedure to control the false discovery rate (FDR). Visualization of the results was facilitated through volcano plots, which were generated for both homozygous and heterozygous conditions at 48 and 72 hpf. These plots aided in the interpretation of differential expression patterns by providing a graphical representation of fold change versus statistical significance for each gene. The data processing and bioinformatic analysis were conducted by Dr. rer. nat. Enrique Audain Martinez using the DESeq2 package.

3.12.4 Enriched Pathways

After differential gene expression analysis was conducted using DESeq2, the biological significance of the differentially expressed genes was further explored through Gene Ontology (GO) enrichment analysis using the Enrichr tool (PMID:27141961). This analysis identified the biological pathways, molecular functions, and cellular components associated with the differentially expressed genes, providing insights into the potential mechanisms underlying the observed gene expression changes. The gene lists generated from DESeq2 analysis, comprising genes with altered expression levels between experimental conditions, were used as input for the Enrichr tool. The results obtained from the enrichment analysis was filted further to decrease potential false associations. Specifically, the enriched gene sets were filtered by overlay, retaining only those gene sets that were enriched in more than three databases or resources. Additionally, a stringent significance threshold was applied by selecting gene sets with adjusted p-values below 0.03. Subsequently, the filtered and refined gene sets were utilized to generate bar graphs using the Prism Pad tool. This visualization approach allows for the clear representation of enriched pathways or functions, thereby aiding in the interpretation of the enrichment analysis results.

3.13 Imaging techniques

In vivo observations were made and documented using Nikon SMZ25. Laser scanning confocal data were acquired using Zeiss CLSM. Light microscopic analyses were performed

using Keyence Biorevo BZ-9000.

3.14 Statistical analysis

Statistical analysis was performed using GraphPad Prism 10 (section 2.10). No randomization or tests for outliers were conducted. A normal distribution test was conducted as part of the statistical analysis. In cases where the data did not adhere to a normal distribution, a Kruskal-Wallis test was employed (4.1.4). For datasets conforming to a normal distribution, the one-way analysis of variance (ANOVA) was employed to ascertain if statistically significant differences exist among the means of three or more independent groups. Nonetheless, ANOVA alone does not provide information on which specific groups exhibit significant differences from each other. Consequently, Dunnett's post hoc test is applied to assess the statistical significance when comparing two sets of data to the Wildtype control group. This additional analysis helps identify specific groups that differ significantly from the control. Results are described as means ± standard deviation (s.d.). In the figures and corresponding legends, a capitalized N represents the number of independent biological experiments(N = Replicate). n = sample size.

Chapter 4

Results

4.1 Characterization of *PRDM16* point mutations in individuals with Arrhythmogenic Right Ventricular Cardiomyopathy

In the preliminary investigation, four missense variants within the *PRDM16* gene, leading to non-synonymous amino acid changes, were identified in individuals with Arrhythmogenic Right Ventricular Cardiomyopathy (ARVC). These variants are labeled as PRDM16 (c.776C>T [p.A259V]), located in the DNA-binding domain; the second one as (c.1882G>A [p.D628N]); the third as (c.2666C>T [p.P889L]), positioned in the repressor domain; and the final substitution of PRDM16 as (c.73176C>T [p.S1059L]), located in the acidic domain.

Zebrafish disease models were established to assess the pathogenicity of ARVC variants. Figure 4.1 illustrates the human PRDM16 protein, highlighting its respective domains and the four identified non-synonymous amino acid changes observed in ARVC patients.

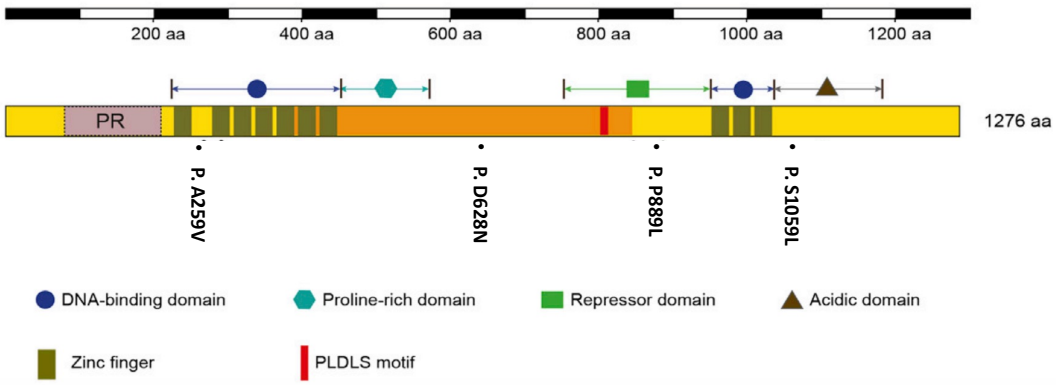

Figure 4.1: *Schematic representation of the human PRDM16 protein with corresponding domains and the four identified non-synonymous amino acid changes in patients with ARVC [139].*

4.1.1 Generation of transgenic zebrafish models for identified *PRDM16* variants in ARVC patients

To assess the functional consequences of newly identified variants in the *PRDM16* gene and identify those potentially associated with disease, humanized transgenic zebrafish models were engineered. In these models, individual variants of *PRDM16* were overexpressed in cardiomyocytes, under the regulation of the tissue-specific promoter *myl7*.
The process began by mutagenizing the wildtype *PRDM16* DNA sequence using site-directed mutagenesis for all four variants. Subsequently, these variants were cloned into the middle entry vector of the Gateway system and Tol2-based transgenesis was utilized to generate the transgenic zebrafish models. A two-step selection process was employed to identify the F0 transgene carriers. Initially, a selection marker, *cryaa:YFP*, was utilized to identify embryos expressing YFP in the lens, as *cryaa* is exclusively expressed in their eye lens starting from 36 hpf. In the second step, the expression of human variants in the YFP-positive embryos was verified through PCR using specific primers designed to bind to the human *PRDM16* DNA sequence.
The non-mutated wildtype *PRDM16* fish served as a control, enabling a comparison of the effects of its overexpression with the effects of the overexpression of the variants. Subsequently, DNA extracted from the YFP-positive fish served as a template for PCR. In this analysis, the PRDM16 plasmid was used as a positive control, while water served as

the negative control. The results presented in figure 4.2 revealed amplified PCR products, measuring 580 bp, confirming the presence of human constructs within the zebrafish genome.

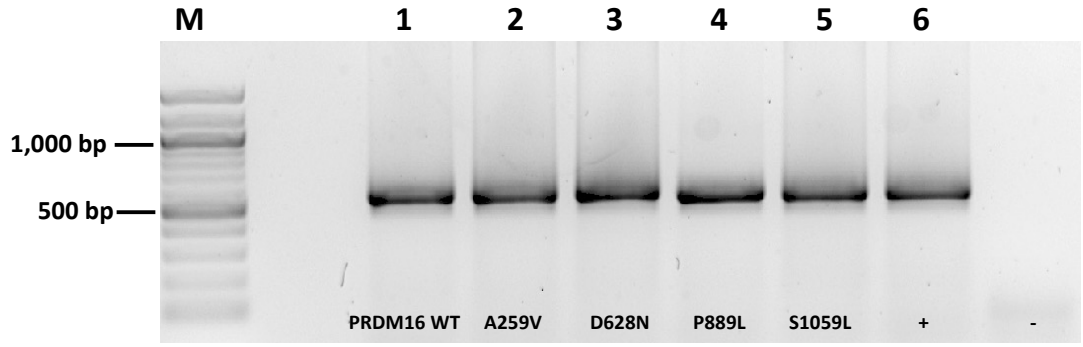

Figure 4.2: *Agarose gel electrophoresis (1,5% agarose). PCR was performed by using human specific primers to detect the human constructs in zebrafish genome. lane 6 positive control (lane 1-5) PCR amplified products by using human specific primers. The expected size is 580 bp. The sizes of molecular weight standard (Lane M) is shown on the left (100 bp)*

Following the PCR, Sanger sequencing was conducted to validate each of the substitutions. Figure 4.3 displays the alignment of sequencing results with PRDM16 WT to verify each substitution.

The initial alignment reveals the substitution of PRDM16 (c.776C>T [p.A259V]), the second alignment features (c.1882G>A [p.D628N]), the third alignment shows (c.2666C>T [p.P889L]), and the last alignment demonstrates the substitution of PRDM16 (c.73176C>T [p.S1059L]). The positive embryos were raised to adulthood. Adult fish of the F0 generation were then outcrossed with wildtype or *Tg(myl7:EGFP)* zebrafish, and the resulting embryos were screened for YFP in the eyes and GFP in the heart if applicable. Genomic DNA was extracted from these embryos, and the confirmation of a PCR product from human PRDM16 was utilized to identify founder fish with the integration of the transgene in the germline. Subsequently, founder fish were once again outcrossed with wildtype or *Tg(myl7:EGFP)* fish and screened for GFP in the heart if applicable to establish a stable F1 generation. The generated zebrafish transgenic lines are listed in subsection 3.4.2.

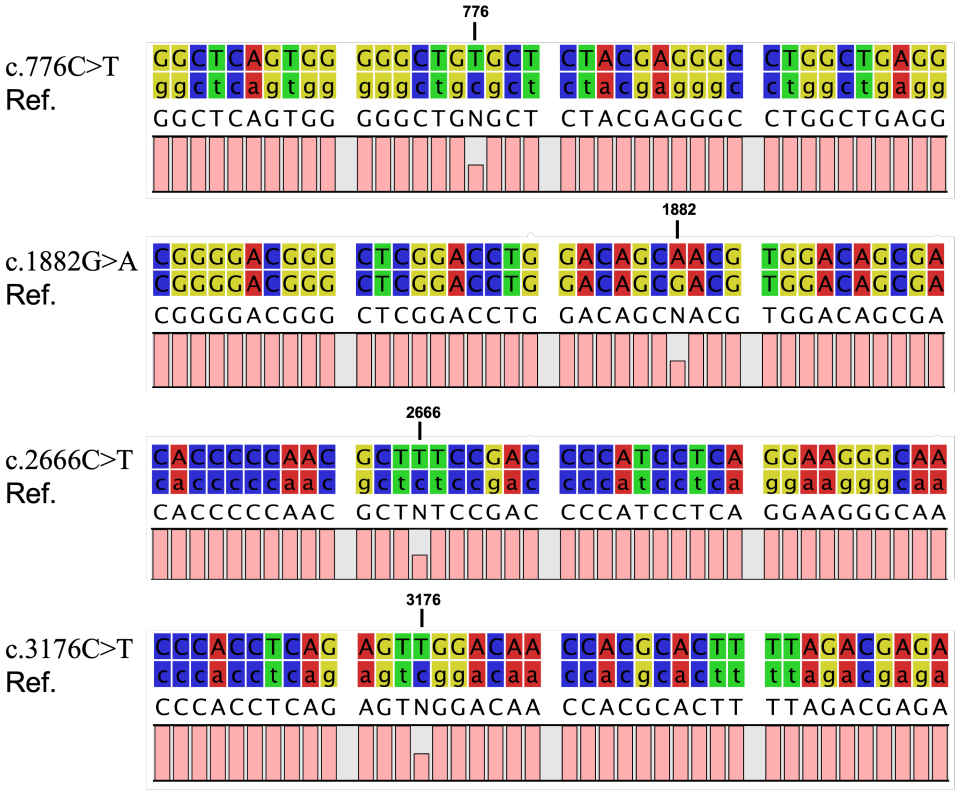

Figure 4.3: *The alignment of the PRDM16 variant with PRDM16 WT was conducted. The sequencing results reveal the presence of the identified substitutions in PRDM16, which were previously identified in patients with Arrhythmogenic Right Ventricular Cardiomyopathy (ARVC). The initial alignment displays the substitution of PRDM16(c.776C>T [p.A259V]), the second alignment features (c.1882G>A [p.D628N]), the third alignment shows (c.2666C>T [p.P889L]), and the last alignment demonstrates the substitution of PRDM16 (c.73176C>T [p.S1059L]).*

4.1.2 Phenotypic and morphological characterization of the *PRDM16* disease models

The stable F1 generation comprised four ARVC transgenic zebrafish models: *Tg(myl7:GFP;myl7:PRDM16-A259V)*, *Tg(myl7:GFP;myl7:PRDM16-D628N)*, *Tg(myl7:GFP;myl7:PRDM16-P889L)*, and *Tg(myl7:GFP;myl7:PRDM16-S1059L)*.

These models were specifically chosen for phenotypic studies, including the examination of cardiac morphology and cardiac output, to elucidate the impact of PRDM16 variant overexpression on the embryonic heart. The transgenic lines *Tg(myl7:GFP;myl7:PRDM16 WT)* and *Tg(myl7:EGFP)* served as control groups.

Effects of *PRDM16* variants on cardiac morphology

To evaluate the effects of overexpressing *PRDM16* variants and *PRDM16* WT on the embryonic heart, live transgenic zebrafish lines were imaged at 48 and 72 hpf using a fluorescence microscope with a single-frame exposure time (Figure 4.4 and 4.5). This imaging allowed for the visualization of the ventricles (V) and atria (A) through the GFP signal. The displayed images depict the typical features observed in the majority of individuals within their respective transgenic progeny. However, it is important to acknowledge that certain individual hearts displayed structural variations from the averaged observed phenotype.

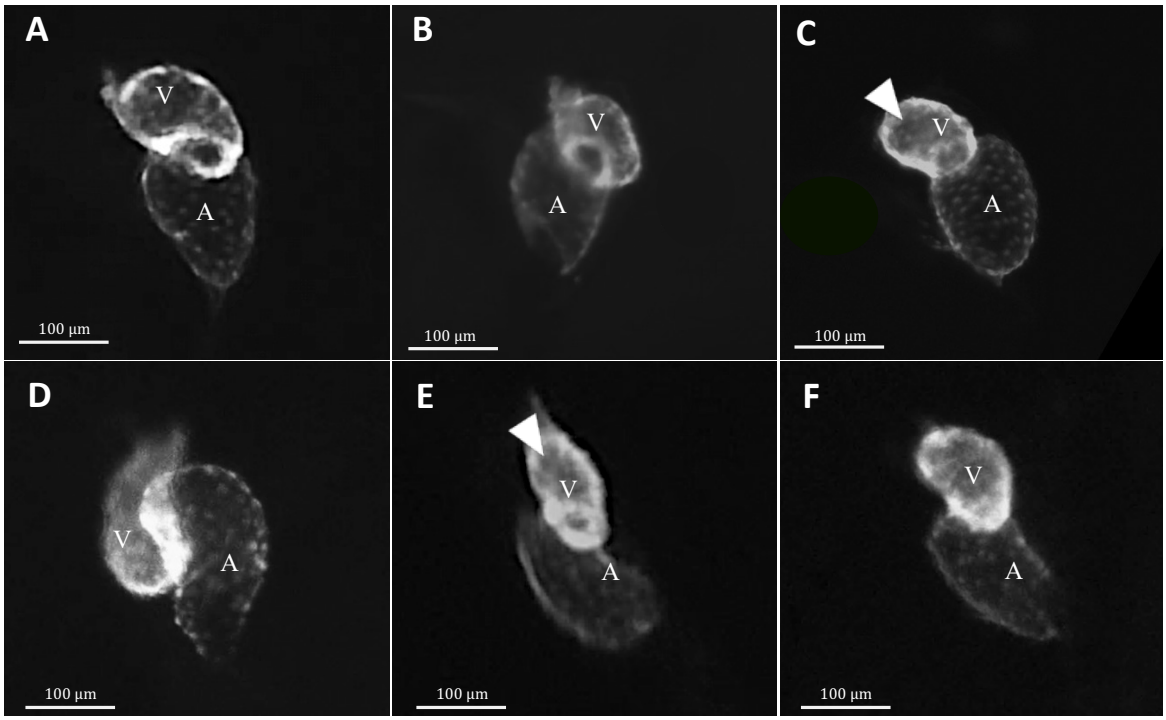

Figure 4.4: *Cardiac morphology of PRDM16 variants, PRDM16 WT, and Tg(myl7:GFP) at 48 hpf. Images of all generated PRDM16 transgenic models were captured using a fluorescence microscope with a single-frame exposure time. The ventricles (V) and atria (A) are clearly visible through the GFP signal.(A) visualization of the embryonic Tg(myl7:GFP). (B) Tg(myl7:GFP; myl7:PRDM16 WT). (C) Tg(myl7:GFP;myl7:PRDM16-A259V). (D) Tg(myl7:GFP;myl7:PRDM16-D628N). (E) Tg(myl7:GFP;myl7:PRDM16-P889L). (F) Tg(myl7:GFP;myl7:PRDM16-S1059L). The ventricle size in transgenic fish lines Tg(myl7:GFP;myl7:PRDM16-A259V) and Tg(myl7:GFP;myl7:PRDM16-P889L) is noticeably smaller compared to the wildtype. Scale bar = 100 µm.*

It is worth highlighting that at 48 hpf, there is a noticeable reduction in ventricle size in the transgenic fish lines *Tg(myl7:GFP;myl7:PRDM16-A259V)* and *Tg(myl7:GFP; myl7:PRDM16-P889L)* compared to the control. This abnormality was also evident in the cardiac output measurements in both (C, E) of these lines (section Effects of *PRDM16* variants on cardiac function).

Interestingly, at 72 hpf, the ventricles of the embryos with *Tg(myl7:GFP; myl7:PRDM16-D628N)* appeared smaller compared to the wildtype, although the cardiac output remained unaffected. Comparing the ventricles of the other embryos at 72 hpf, no discernible distinctions were noted between those with *PRDM16* variants, *PRDM16* WT, and the control.

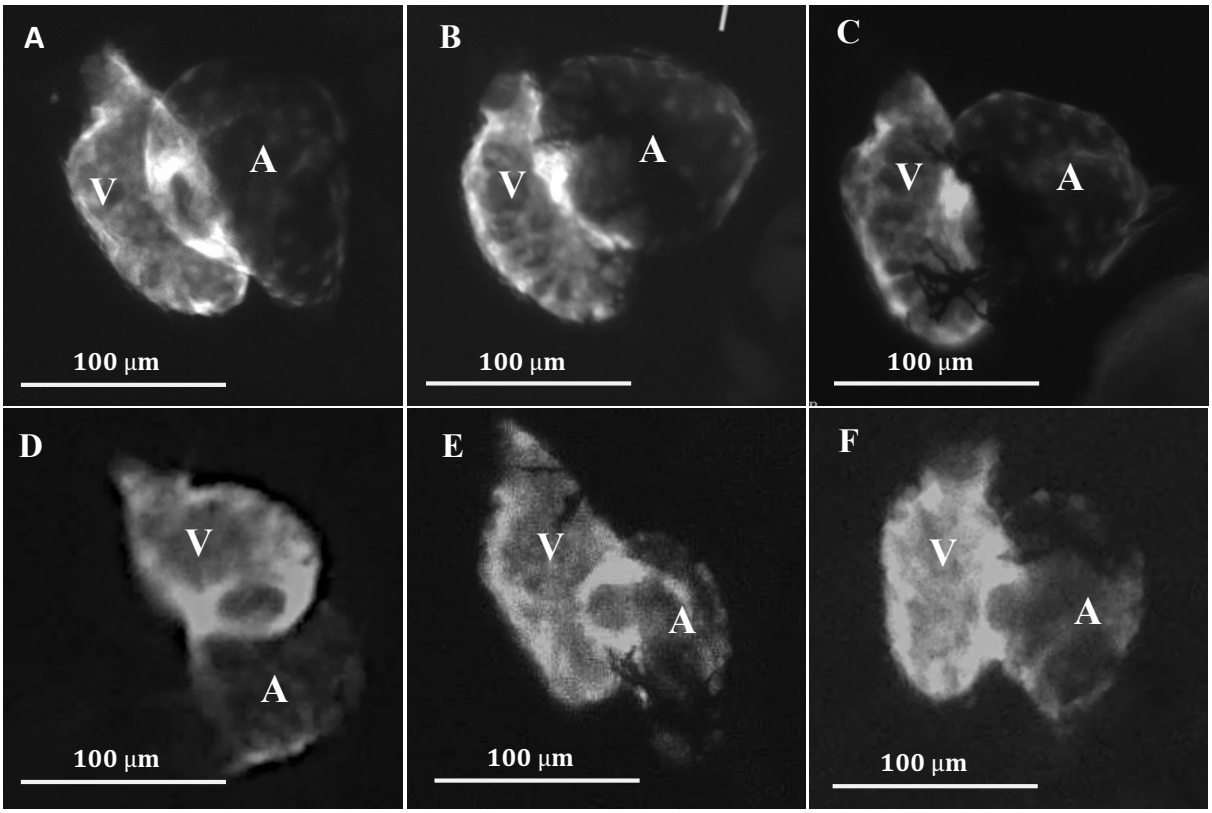

Figure 4.5: *Cardiac morphology of PRDM16 variants, PRDM16 WT, and myl7:GFP at 72 hpf. Images of all all generated of PRDM16 transgenic models were captured using a fluorescence microscope with a single-frame exposure time. The ventricles (V) and atria (A) are clearly visible through the GFP signal. (A) visualization of the embryonic Tg(myl7:GFP). (B) Tg(myl7:GFP;myl7:PRDM16 WT). (C) Tg(myl7:GFP; myl7:PRDM16-A259V). (D) Tg(myl7:GFP;myl7:PRDM16-D628N).(E) Tg(myl7:GFP;myl7:PRDM16-P889L).(F) Tg(myl7:GFP;myl7:PRDM16-S1059L). Scale bar = 100 µm.*

Effects of *PRDM16* variants on cardiac function

The evaluation of cardiac function in 48 hpf and 72 hpf zebrafish embryos of the F1 generation as despite in figure 4.6, was conducted *in vivo* utilizing fluorescent microscopy and high-speed imaging. A previously established algorithm (3.5) was employed to assess cardiac output, heart rate, and stroke volume.

The impact of *PRDM16* variants and *PRDM16* WT on heart rate at 48 hpf did not yield statistically significant differences among the groups. Control hearts exhibited an average heart rate of 144.04 bpm (±17.01 bpm), while hearts overexpressing PRDM16 WT and the respective variants (PRDM16-A259V, PRDM16-D628N, PRDM16-P889L, and PRDM16-S1059L) showed averages of 149.33 bpm (±11.55 bpm), 139.56 bpm (±15.55 bpm), 152.73 bpm (±10.53 bpm), 147.51 bpm (±27.23 bpm), and 139.17 bpm (±17.32 bpm), respectively (Figure 4.6) .

In terms of stroke volume, control hearts had an average of $46.9*10^4$ μm^3 ($\pm 4.7*10^4$ μm^3). Hearts overexpressing PRDM16 WT and the respective variants (PRDM16-A259V, PRDM16-D628N, PRDM16-P889L, and PRDM16-S1059L) showed averages of $47.3*10^4$ μm^3 ($\pm 17.6*10^4$ μm^3), $37.1*10^4$ μm^3 ($\pm 11.9*10^4$ μm^3), $46.9*10^4$ μm^3 ($\pm 14.3*10^4$ μm^3), $33.9*10^4$ μm^3 ($\pm 16.1*10^4$ μm^3) and $44.1*10^4$ μm^3 ($\pm 10.4*10^4$ μm^3), respectively. However, the analysis revealed a notable reduction in stroke volume in PRDM16-A259V and PRDM16-P889L variants compared to the *Tg(myl7:GFP)* group, while the other variants and PRDM16 WT did not exhibit statistically significant differences.

Furthermore, overexpression of PRDM16-A259V variants and PRDM16-P889L resulted in a significant decrease in cardiac output at 48 hpf compared to the *Tg(myl7:GFP)* control. Control hearts had an average cardiac output of 66.74 nl\min (±6.44 nl\min), while hearts overexpressing PRDM16 WT and the respective variants showed averages of 70.43 nl\min (±25.70 nl\min), 52.15 nl\min (±17.58 nl\min), 71.71 nl\min (±23.34 nl\min), 51.77 nl\min (±26.86 nl\min), and 61.08 nl\min (±15.14 nl\min), respectively.

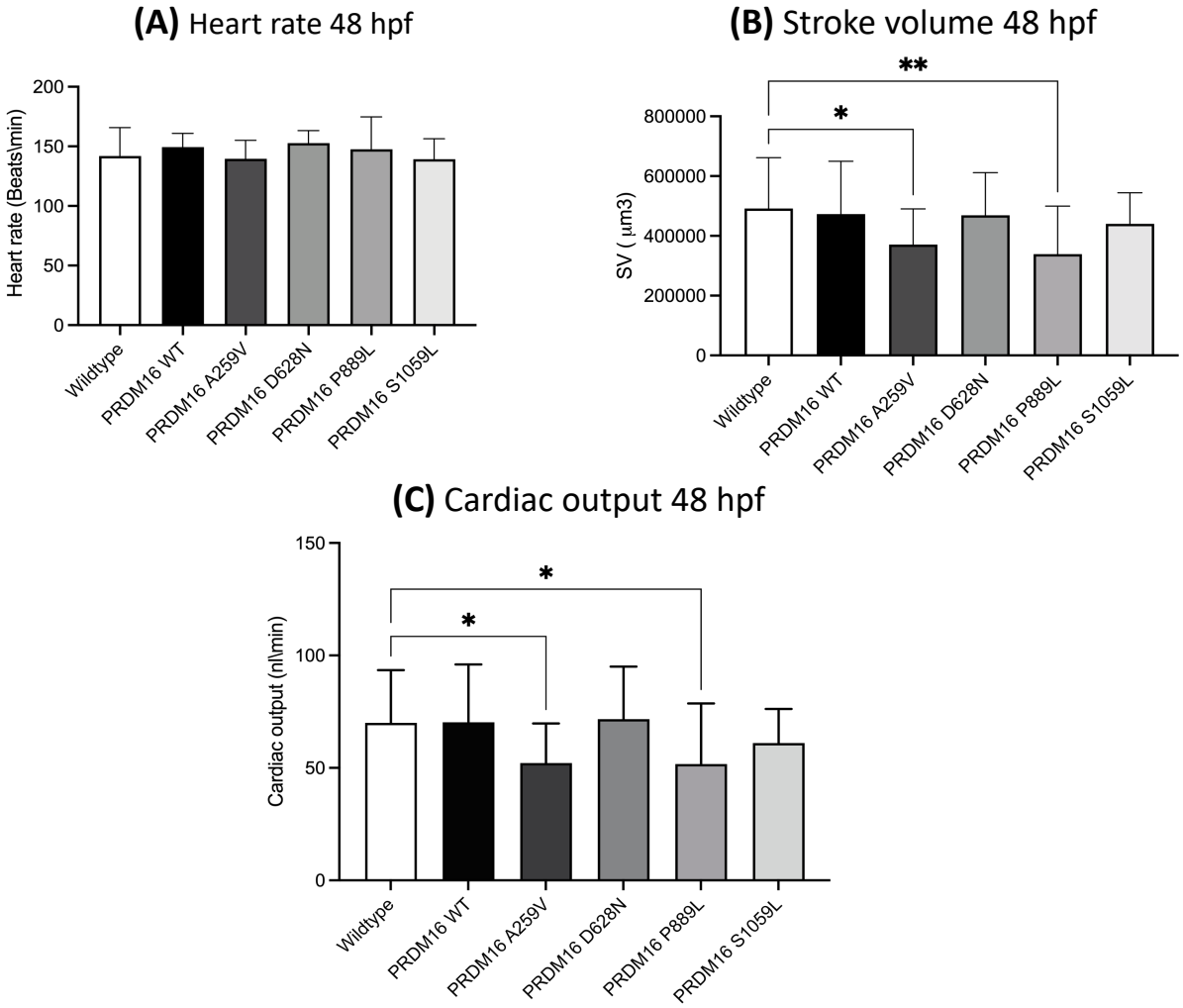

Figure 4.6: *Cardiac function was assessed in the context of PRDM16 variants, Tg myl7:GFP;myl7:PRDM16-WT), and Tg(myl7:GFP) at 48 period (A) The impact of PRDM16 variants and PRDM16 WT on heart rate showed no statistically significant differences between the groups. (B) Analysis of stroke volume revealed a significant reduction in stroke volume in PRDM16-A259V and PRDM16-P889L variants compared to the control group. Conversely, the other two variants and PRDM16 WT exhibited no statistically significant differences in comparison to the control group. (C) Overexpression of PRDM16-A259V and PRDM16-P889L resulted in a significant reduction in CO compared to transgenic Tg(myl7:GFP). However, there were no statistically significant differences in CO between the transgenic Tg(myl7:GFP) group and the Tg(myl7:GFP;myl7:PRDM16 WT, Tg(myl7:GFP);myl7:PRDM16-D628N, and Tg(myl7:GFP);myl7:PRDM16-S1059L groups. Error bars represent the standard deviation (SD), and asterisks indicate statistical significance at * p> 0.05 and ** p> 0.01. Statistical analysis was conducted one-way ANOVA with Dunnett's post-test with comparison to control group Tg(myl7:GFP) (GraphPad Prism version 10.0). n = 45 WT, n = 21 PRDM16 WT, n = 19 PRDM16-A259V, n = 13 PRDM16-D628N, n = 16 PRDM16-P889L, n = 10 PRDM16-S1059L. N = 3.*

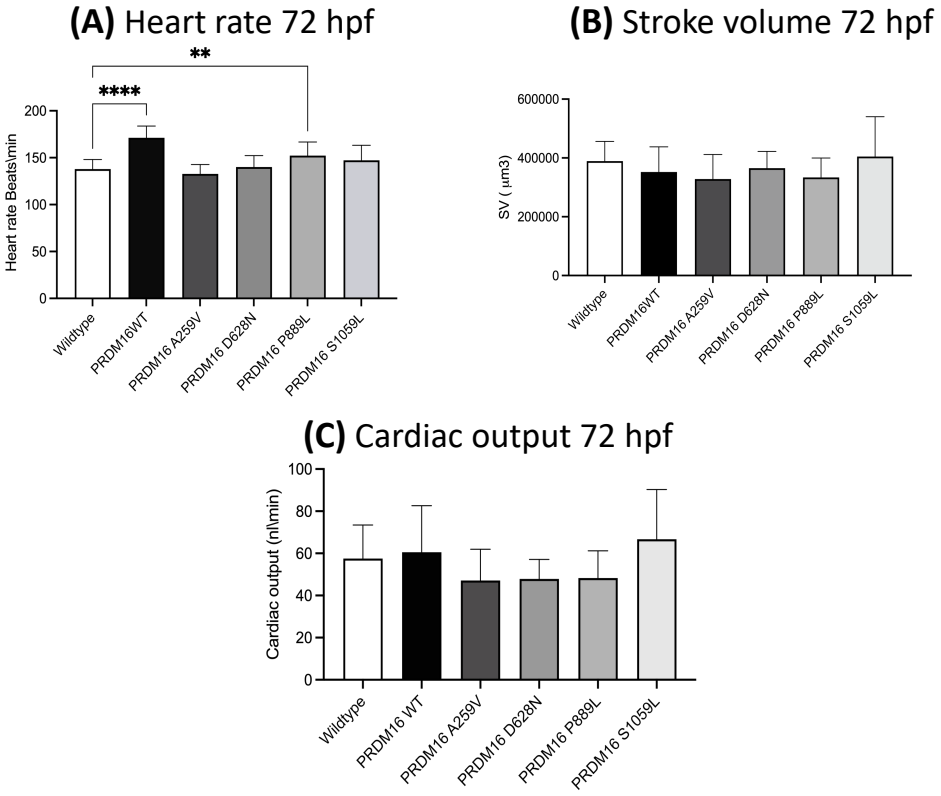

Figure 4.7: *Cardiac output (CO) was evaluated in PRDM16 variants, PRDM16 WT, and Tg(myl7:GFP) at 72 period. (A) The overexpression of PRDM16-P889L variant and PRDM16 WT resulted in a significant increase in heart rate compared to transgenic Tg(myl7:GFP). (B) The influence of PRDM16 variants and PRDM16 WT in stroke volume did not reveal any statistically significant differences between the groups. (C) Cardiac output (CO) exhibited no statistically significant differences between the groups when compared to the Tg(myl7:GFP). Error bars represent the standard deviation (SD), and asterisks indicate statistical significance at * p> 0.05 and ** p> 0.01. Statistical analysis was conducted using one-way ANOVA with Dunnett's post-test with comparison to control group Tg(myl7:GFP) (GraphPad Prism version 10.0). n = 33 WT, n = 11 PRDM16 WT, n = 15 PRDM16-A259V, n = 13 PRDM16-D628N, n = 12 PRDM16-P889L, n = 9 PRDM16-S1059L. N = 3.*

At 72 hpf, the overexpression of the PRDM16 P889L variant and PRDM16 WT led to a significant increase in heart rate compared to the transgenic *Tg(myl7:GFP)* control. Control hearts exhibited an average heart rate of 140.31 bpm (±0.30 bpm), while hearts overexpressing PRDM16 WT and the respective variants (PRDM16-A259V, PRDM16-D628N, PRDM16-P889L, and PRDM16-S1059L) showed averages of 171.21 bpm (±12.46 bpm), 132.72 bpm (±9.94 bpm), 140.12 bpm (±12.11 bpm), 152.24 bpm (±14.51 bpm), and 147.27 bpm (±15.89 bpm), respectively.

Regarding stroke volume, control hearts had an average of $41.2*10^4$ μm^3 ($\pm 4.1*10^4$ μm^3). Hearts overexpressing PRDM16 WT and the respective variants (PRDM16-A259V, PRDM16-D628N, PRDM16-P889L, and PRDM16-S1059L) showed averages of $35.5*10^4$ μm^3 ($\pm 11.9*10^4$ μm^3), $35.4*10^4$ μm^3 ($\pm 10.9*10^4$ μm^3), $34.3*10^4$ μm^3 ($\pm 7.1*10^4$ μm^3), $31.8*10^4$ μm^3 ($\pm 8.2*10^4$ μm^3), and $45.8*10^4$ μm^3 ($\pm 16.7*10^4$ μm^3), respectively.
The examination of the influence of *PRDM16* variants and *PRDM16 WT* on stroke volume did not reveal any statistically significant distinctions across the groups. However, it is important to note that there were no statistically significant differences in cardiac output among the *PRDM16* variants, *PRDM16 WT*, and control groups at 72 hpf. Control hearts had an average cardiac output of 57.29 nl\min ($\pm$6.33 nl\min), while hearts overexpressing PRDM16 WT and the respective variants showed averages of 60.55 nl\min ($\pm$22.04 nl\min), 47.16 nl\min ($\pm$14.75 nl\min), 47.90 nl\min ($\pm$9.24 nl\min), 48.32 nl\min ($\pm$12.86 nl\min), and 66.71 nl\min ($\pm$23.54 nl\min), respectively. Figure 4.7 illustrates the measurements obtained at 72 hpf.

Effects of *PRDM16* variants on cell number in developing hearts

The analysis of proliferation and apoptosis patterns revealed that, while the *PRDM16* variants do not appear to influence apoptosis significantly, specific variants such as *Tg(myl7:GFP;myl7:PRDM16-P889L)* and *Tg(myl7:GFP; myl7:PRDM16-S1059L)* exhibit a noticeable reduction in proliferation by 96 hpf. To gain a deeper understanding of these effects, a semiautomated cell counting technique was employed to examine the impact of *PRDM16* variants, *PRDM16 WT* on the total cardiac cell number, and *Tg(myl7:GFP)* (as the control group) at three distinct time points: 48, 72, and 96 hpf (Figure 4.8). At 48 hpf, no significant differences were observed in total cell number. The average cell number in control hearts was 214.5 ($\pm$65.83). In hearts overexpressing PRDM16 WT and the respective variants (PRDM16-A259V, PRDM16-D628N, PRDM16-P889L, and PRDM16-S1059L), the averages were 229.4 ($\pm$30.27), 211.57 ($\pm$38.01), 177 ($\pm$30.95), 187.83 ($\pm$55.02), and 214.16 ($\pm$43.52), respectively. However, at 72 hpf, a significant decrease in the total number of cardiac cells was observed in *Tg(myl7:GFP;myl7:PRDM16-D628N)* and *Tg(myl7:GFP;myl7:PRDM16-P889L)* compared to WT controls. Interestingly, these two variants exhibited a mild increase in cell proliferation at 72 hpf, although it was not statistically significant. The cell number in control hearts was 381.5 ($\pm$89.31). In hearts overexpressing PRDM16 WT and the respective variants (PRDM16-A259V, PRDM16-

D628N, PRDM16-P889L, and PRDM16-S1059L), the averages were 320 (±77.17), 282 (±37.81), 202.66 (±18.17), 207.42 (±20.83), and 325.16 (±47.28), respectively. Notably, no significant decreases were observed at 96 hpf. The average cell number in control hearts was 404.66 (±100.06). In hearts overexpressing PRDM16 WT and the respective variants (PRDM16-A259V, PRDM16-D628N, PRDM16-P889L, and PRDM16-S1059L), the averages were 360.8 (±63.82), 276.33 (±50.54), 281.33 (±99.31), 335.66 (±87.43), and 273.33 (±47.68), respectively. Despite the decreased cell proliferation in variants *Tg(myl7:GFP;myl7:PRDM16-P889L)* and *Tg(myl7:GFP; myl7:PRDM16-S1059L)* at 96 hpf, the total cell number remained unaffected.

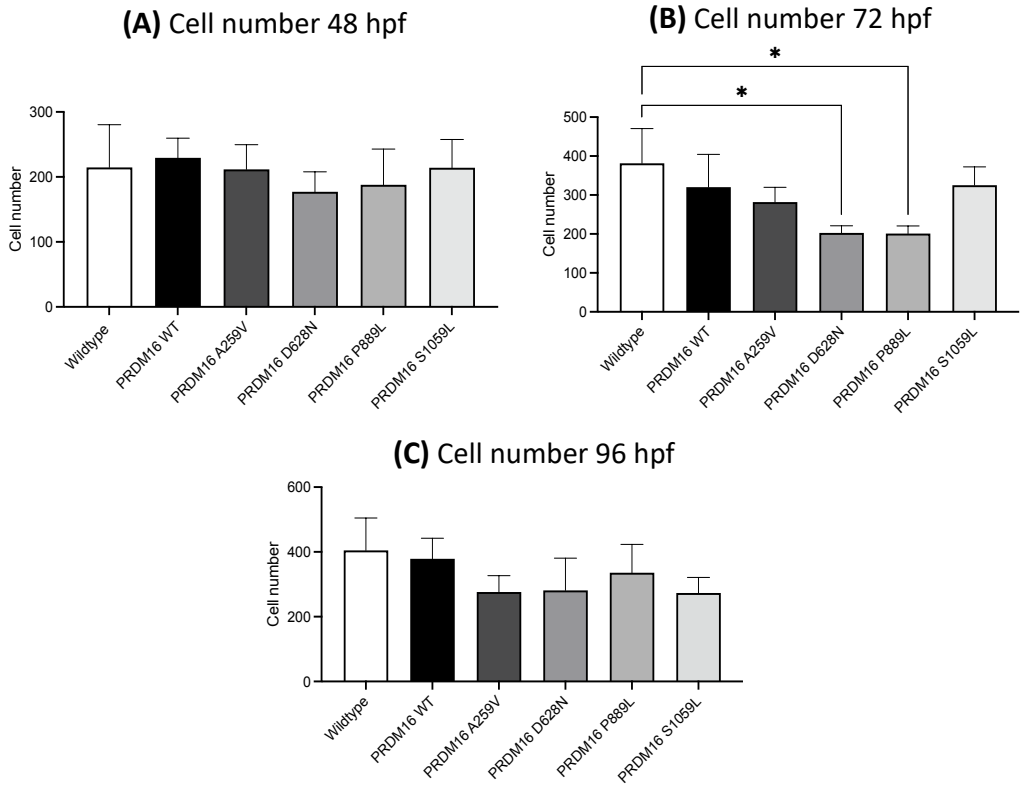

Figure 4.8: *Analysis of effect of PRDM16 variants on cell number. A semiautomated cell counting method was employed to assess the influence of PRDM16 variants and PRDM16 WT at three time points: 48, 72, and 96 hpf.(A) At 48 hpf, there were no observable differences between the groups. (B) A significant reduction was evident at 72 hpf when comparing Tg(myl7:GFP;myl7:PRDM16-D628N) and Tg(myl7:GFP;myl7:PRDM16-P889L) to the Wildtype (C)At 96 hpf, there were no significant decreases observed when compared to the wildtype control. Error bars represent the standard deviation (SD), and asterisks indicate statistical significance at * p> 0.05. Statistical analysis was conducted using one-way ANOVA with Dunnett's post-test (GraphPad Prism version 10.0). n = 5, N = 3.*

Analysis of the cell proliferation state in the *PRDM16* variants

To assess the impact of the four *PRDM16* variant transgenic zebrafish models, including *PRDM16 WT*, on cell proliferation, EdU staining of isolated hearts was conducted at different time points, specifically at 48 hpf, 72 hpf, and 96 hpf (Figures 4.9, 4.10 and 4.11). Subsequently, 5 to 7 embryos were collected for each *PRDM16* variant and *PRDM16 WT*. Control group embryos consisted of *Tg(myl7:GFP)* embryos (lacking YFP expression). The analysis was conducted using DAPI, which served as a nuclear label and marker for the total cell count. GFP was employed as a specific marker for cardiomyocytes, while EdU staining facilitated the identification of proliferating cells undergoing mitosis across all three time points. Proliferation rate was calculated as number of EdU positive cells over number of all DAPI-labeled cells.

As depicted in Figure 4.9, at 48 hpf, there were no significant differences in total cell number and rates of cellular proliferation between the groups. The average percentage of proliferating cells in control hearts was 12.98% (±7.85%). In hearts overexpressing PRDM16 WT and the respective variants (PRDM16-A259V, PRDM16-D628N, PRDM16-P889L, and PRDM16-S1059L), the percentages were 12.47% (±1.21%), 15.23% (±2.83%), 16.39% (±3.91%), 17.42% (±2.39%), and 15.43% (±0.03%), as despite in figure 4.12, respectively. However, at 72 hpf, there was also no significant difference observed between the *PRDM16* variants,*PRDM16 WT*, and *Tg(myl7:GFP)*. The average percentage of proliferating cells in control hearts was 11.87% (±3.91%). In hearts overexpressing PRDM16 WT and the respective variants (PRDM16-A259V, PRDM16-D628N, PRDM16-P889L, and PRDM16-S1059L), the percentages were 14.46% (±3.20%), 11.27% (±4.04%), 17.85% (±6.08%), 14.95% (±10.08%), and 10.06% (±0.02%) as despite in figure 4.12, respectively. The significant reduction in proliferation was observed only at 96 hpf (Figure 4.11) between the two transgenic groups, *Tg(myl7:GFP;myl7:PRDM16-P889L)* and *Tg(myl7:GFP; myl7:PRDM16-S1059L)*, when compared to *Tg(myl7:GFP)*. The other *PRDM16* variants and *PRDM16 WT* did not exhibit a significant reduction in cardiac cell proliferation. The average percentage of proliferating cells in control hearts was 15.59% (±3.72%). In hearts overexpressing PRDM16 WT and the respective variants (PRDM16-A259V, PRDM16-D628N, PRDM16-P889L, and PRDM16-S1059L), the percentages were 11.62% (±5.28%), 12.81% (±4.43%), 21.34% (±9.95%), 6.06% (±2.90%), and 8.11% (±0.03%), respectively. The other *PRDM16* variants and *PRDM16 WT* did not exhibit a significant reduction in cardiac cell proliferation (Figure 4.12).

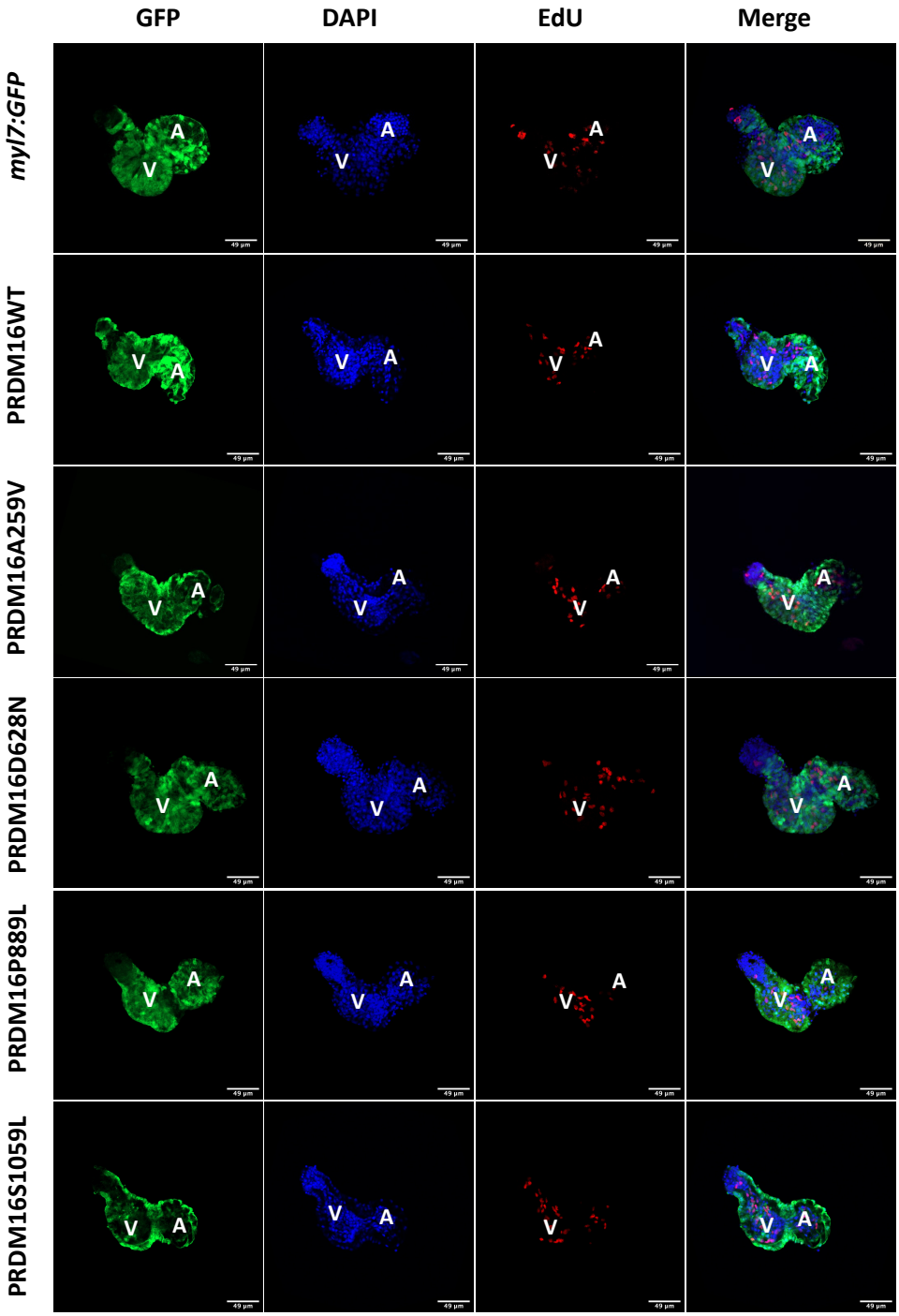

Figure 4.9: *Representative confocal images of 0.5 µM Z-projections of hearts expressing GFP, PRDM16 WT and respective PRDM16 variants. To visualize cell proliferation, the dissected hearts were stained with EdU at 48 hpf. Nuclei were stained with DAPI (in blue), Cardiomyocytes, expressing GFP under the myl7 promoter, were stained with an anti-GFP antibody as a booster. Dividing cells undergoing mitosis were marked by EdU staining (in red). In the hearts of PRDM16 variants and PRDM16 WT, there was no significant reduction in the total cell number and rates of cellular proliferation at 48 hpf compared to the control group. Scale bar = 50 µm. A = atrium, V = ventricle*

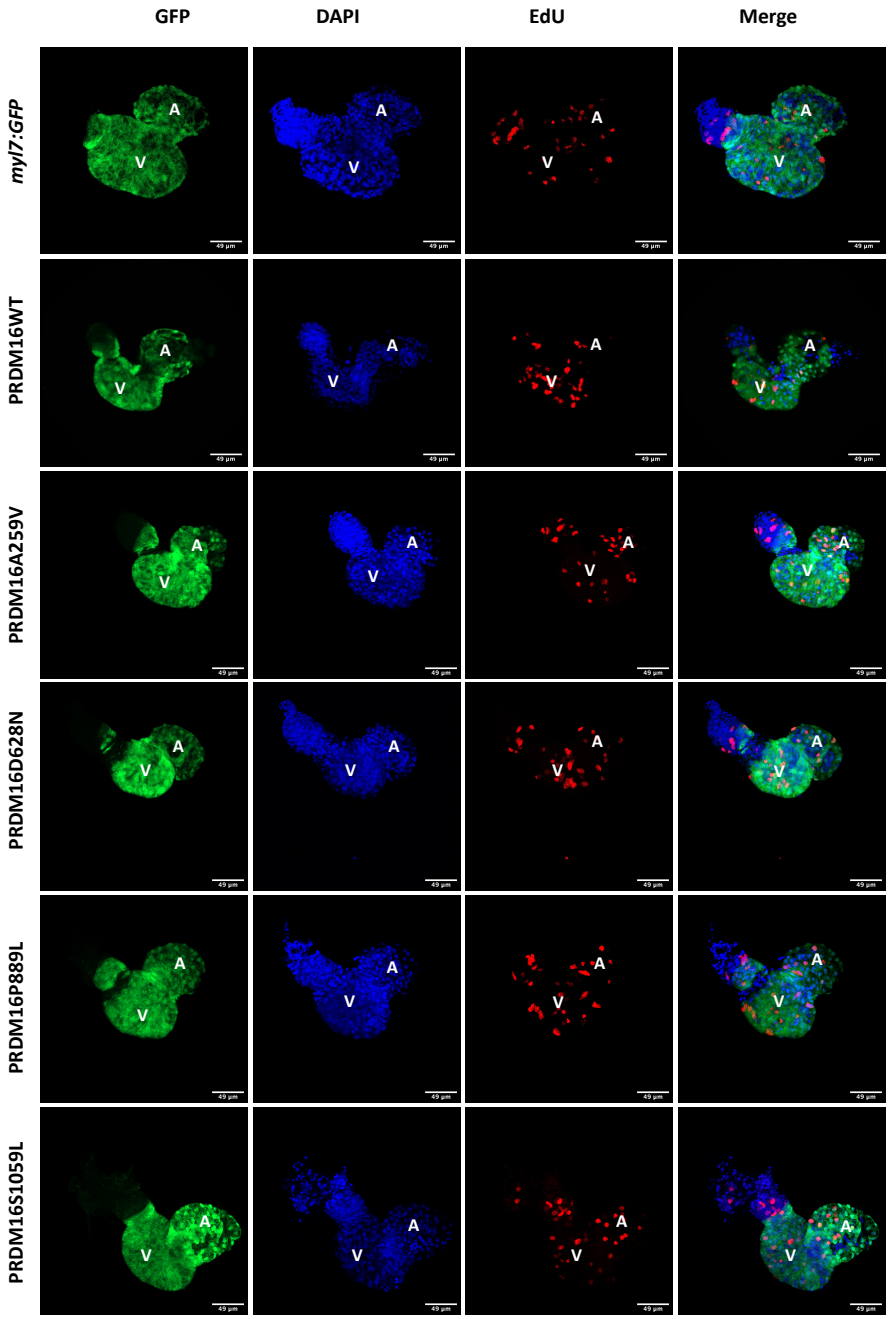

Figure 4.10: *Representative confocal images of 0.5 µM Z-projections of hearts expressing GFP, PRDM16 WT and respective PRDM16 variants. To visualize cell proliferation, the dissected hearts were stained with EdU at 72 hpf. Nuclei were stained with DAPI (in blue), Cardiomyocytes, expressing GFP under the myl7 promotor, were stained with an anti-GFP antibody as a booster. Dividing cells undergoing mitosis were marked by EdU staining (in red). In the hearts of PRDM16 variants and PRDM16 WT, there was no observable reduction in the total cell number and rates of cellular proliferation at 72 hpf compared to the control group. Scale bar = 50 µm. A = atrium, V = ventricle*

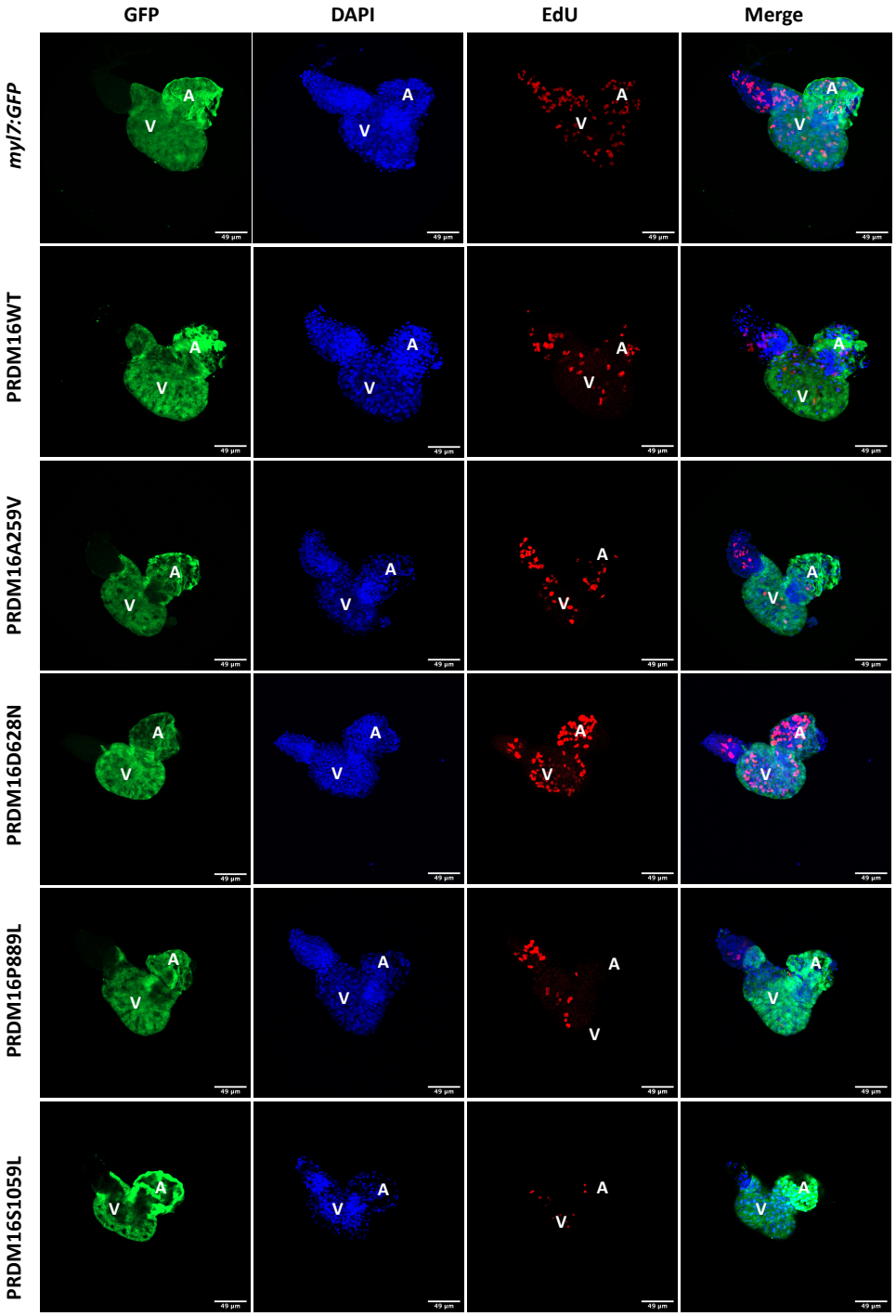

Figure 4.11: *Representative confocal images of 0.5 µM Z-projections of hearts expressing GFP, PRDM16 WT and respective PRDM16 variants. To visualize cell proliferation, the dissected hearts were stained with EdU at 96 hpf. Nuclei were stained with DAPI (in blue), Cardiomyocytes, expressing GFP under the myl7 promoter, were stained with an anti-GFP antibody as a booster. Dividing cells undergoing mitosis were marked by EdU staining (in red). The reduction in proliferating cardiac cells is evident in the two transgenic lines, Tg(myl7:GFP;myl7:PRDM16-P889L) and Tg (myl7:GFP;myl7:PRDM16-S1059L), compared to Tg(myl7:GFP) (red channel). A = atrium, V = ventricle. Scale bar = 50 µm*

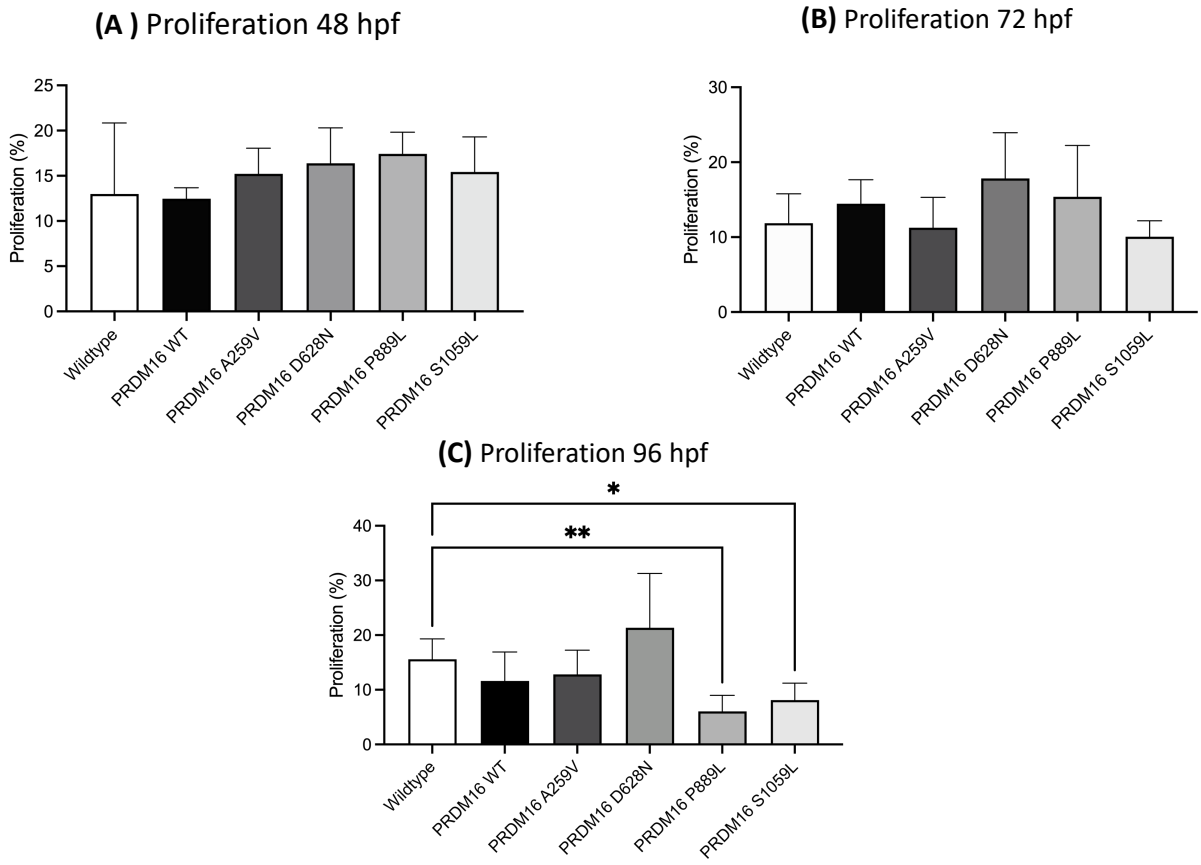

Figure 4.12: *Quantification of cell proliferation at different time points. At 48 hpf, there were no significant differences in total cell number and rates of cellular proliferation between the groups. n = 5, N = 3. Similarly, at 72 hpf, no statistically significant differences were observed between the PRDM16 variants and PRDM16-WT when compared to TG(myl7:GFP), which served as the control. However, a significant reduction in cardiac cell proliferation was noted in TTg(myl7:GFP;myl7:PRDM16-P889L) and Tg (myl7:GFP;myl7:PRDM16-S1059L) when compared to Tg(myl7:GFP) at 96 hpf. Error bars represent the standard deviation (SD), and asterisks indicate statistical significance at * p> 0.05 and ** p> 0.01. Statistical analysis was conducted using one-way ANOVA with Dunnett's post-test to control group Tg(myl7:GFP) (GraphPad Prism version 10.0).*

Analysis of cell death state in the *PRDM16* variants

In the following, the four ARVC transgenic zebrafish models, as well as *PRDM16 WT*, were examined for apoptosis. Apoptosis was quantified using the Click-iT TUNEL assay at various time points (48, 72, 96 hpf). Briefly, the F1 generation from each variant and *PRDM16 WT* was outcrossed with *Tg(myl7:GFP)*. The embryos underwent initial

screening for YFP expression in the eye lens, which serves as a selection marker for the overexpression of *PRDM16* variants and *PRDM16 WT*. Additionally, GFP expression was used as a marker for cardiomyocytes. 5 to 7 embryos positive for both, GFP in the cardiomyocytes and YFP in the eye lens, were selected for each *PRDM16* variant and *PRDM16 WT*. The control group consisted of *Tg(myl7:GFP)* embryos. For the TUNEL evaluation, only atrial and ventricular cardiac cells were considered. The analysis utilized DAPI as a nuclear label and marker for the total cell count. GFP served as a specific marker for cardiomyocytes, and TUNEL staining facilitated the identification of apoptotic cells across all three time points. Apoptosis rate was calculated as number of TUNEL positive cells over number of all DAPI-labeled cells (Figures 4.13 to 4.15). As illustrated in Figure 4.16, at 48 hpf, there were no significant differences in total cell number and rates of cellular apoptosis between the groups. The average percentage of apoptotic cells in control hearts was 0.17% (±0.28%). In hearts overexpressing PRDM16 WT and the respective variants (PRDM16-A259V, PRDM16-D628N, PRDM16-P889L, and PRDM16-S1059L), the percentages were 1.52% (±3.11%), 0.56% (±0.70%), 1.10% (±2.49%), 0.092% (±0.21%), and 0.91% (±2.08%), respectively.

At 72 hpf, there was no significant difference observed between the *PRDM16* variants, *PRDM16 WT*, and *Tg(myl7:GFP)* (Figures 4.14 and 4.16). The average percentage of apoptotic cells in control hearts was 0.16% (±0.32%). In hearts overexpressing PRDM16-WT and the respective variants (PRDM16-A259V, PRDM16-D628N, PRDM16-P889L), the percentages were 0.52% (±1.15%), 0.51% (±0.63%), 0.20% (±0.48%), 0.15% (±0.33%), and no apoptotic cells in PRDM16-S1059L, respectively.

However, at 96 hpf, as depicted in Figures 4.14 and 4.15, no significant difference was observed between the *PRDM16* variants, *PRDM16 WT*, and *Tg(myl7:GFP)*. The average percentage of proliferating cells in control hearts was 0.08% (±0.20%). In hearts overexpressing PRDM16-WT and the respective variants (PRDM16-A259V, PRDM16-D628N, and PRDM16-S1059L), the percentages were 0.05% (±0.12%), 0.96% (±1.29%), 1.01% (±1.68%), 0.78% (±0.87%), and no apoptotic cells were observed in PRDM16-P889L, respectively.

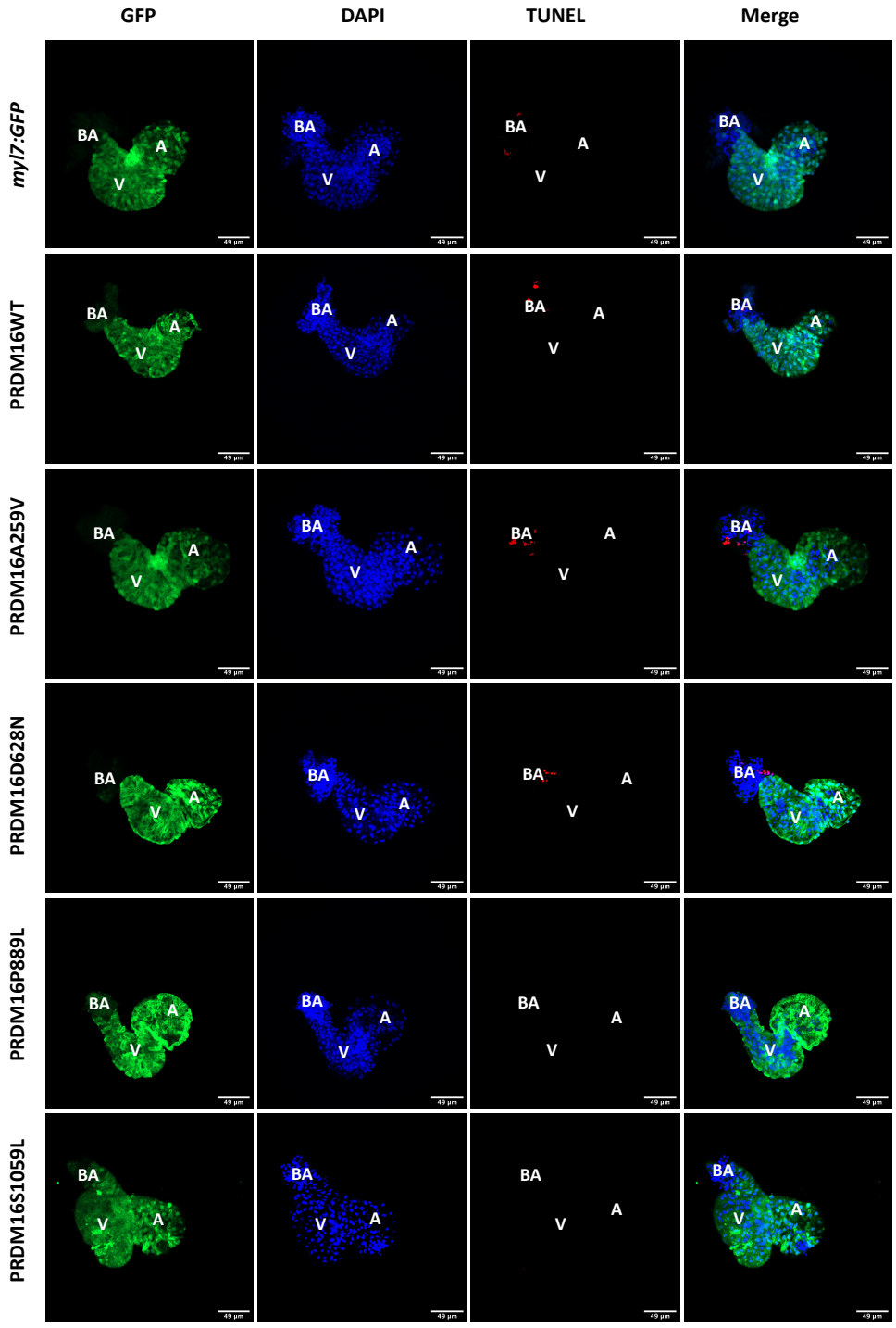

Figure 4.13: *Representative confocal images of 0.5 µM Z-projections of hearts expressing GFP, PRDM16 WT and respective PRDM16 variants. To visualize apoptosis, the dissected hearts were stained with TUNEL at 48 hpf. cell nuclei are counterstained with DAPI (blue), TUNEL-positive cells (Red), which are visible only in bulbus arteriosus (BA). Cardiomyocytes, expressing GFP under the myl7 promoter, were stained with an anti-GFP antibody as a booster (in green). A = atrium, V = ventricle (Scale bar = 50 µm).*

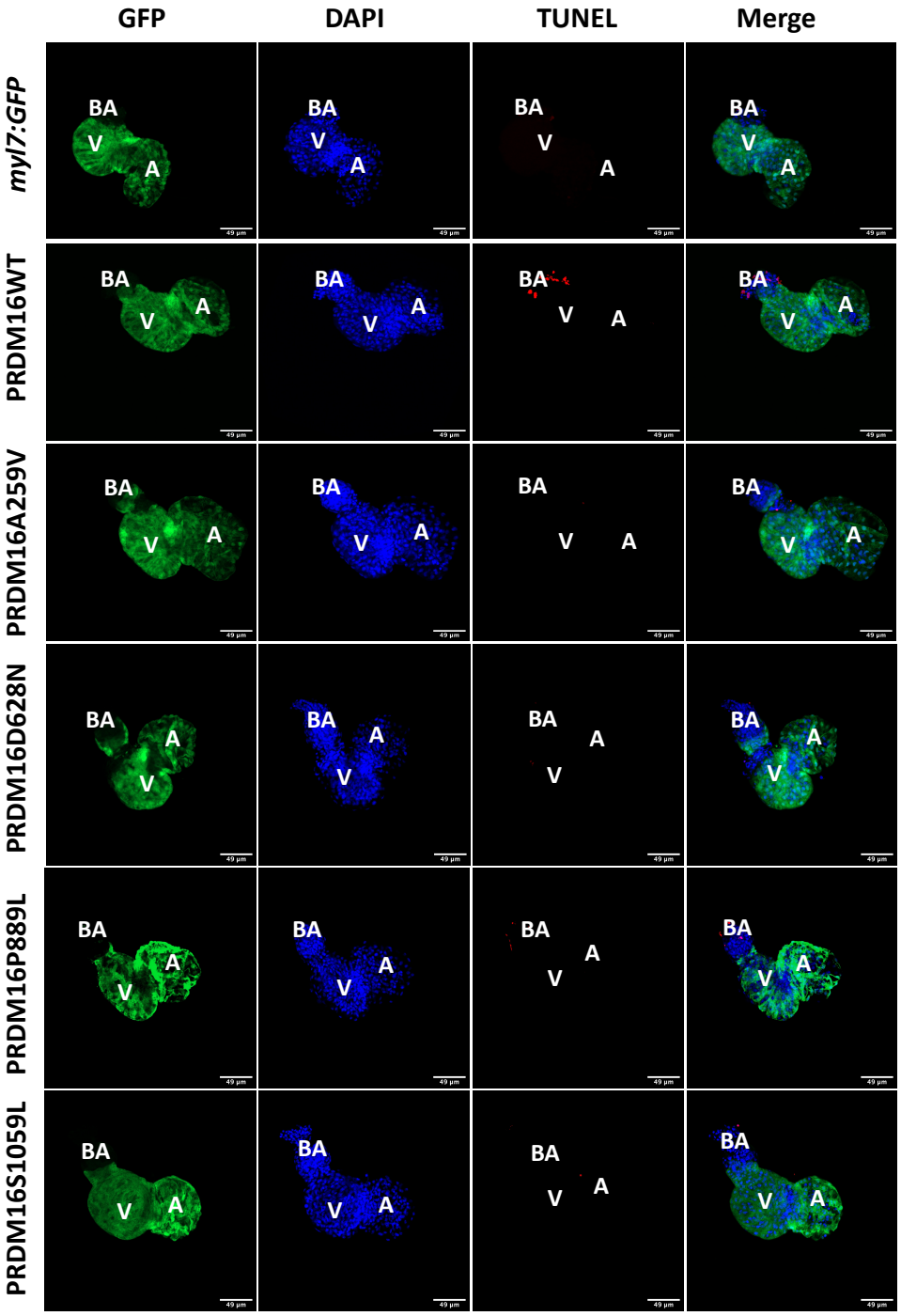

Figure 4.14: *Representative confocal images of 0.5 µM Z-projections of hearts expressing GFP, PRDM16 WT and respective PRDM16 variants. To visualize apoptosis, the dissected hearts were stained with TUNEL at 48 hpf. cell nuclei are counterstained with DAPI (blue), TUNEL-positive cells (Red), which are visible only in bulbus arteriosus (BA). Cardiomyocytes, expressing GFP under the myl7 promoter, were stained with an anti-GFP antibody as a booster (in green). A = atrium, V = ventricle (Scale bar = 50 µm).*

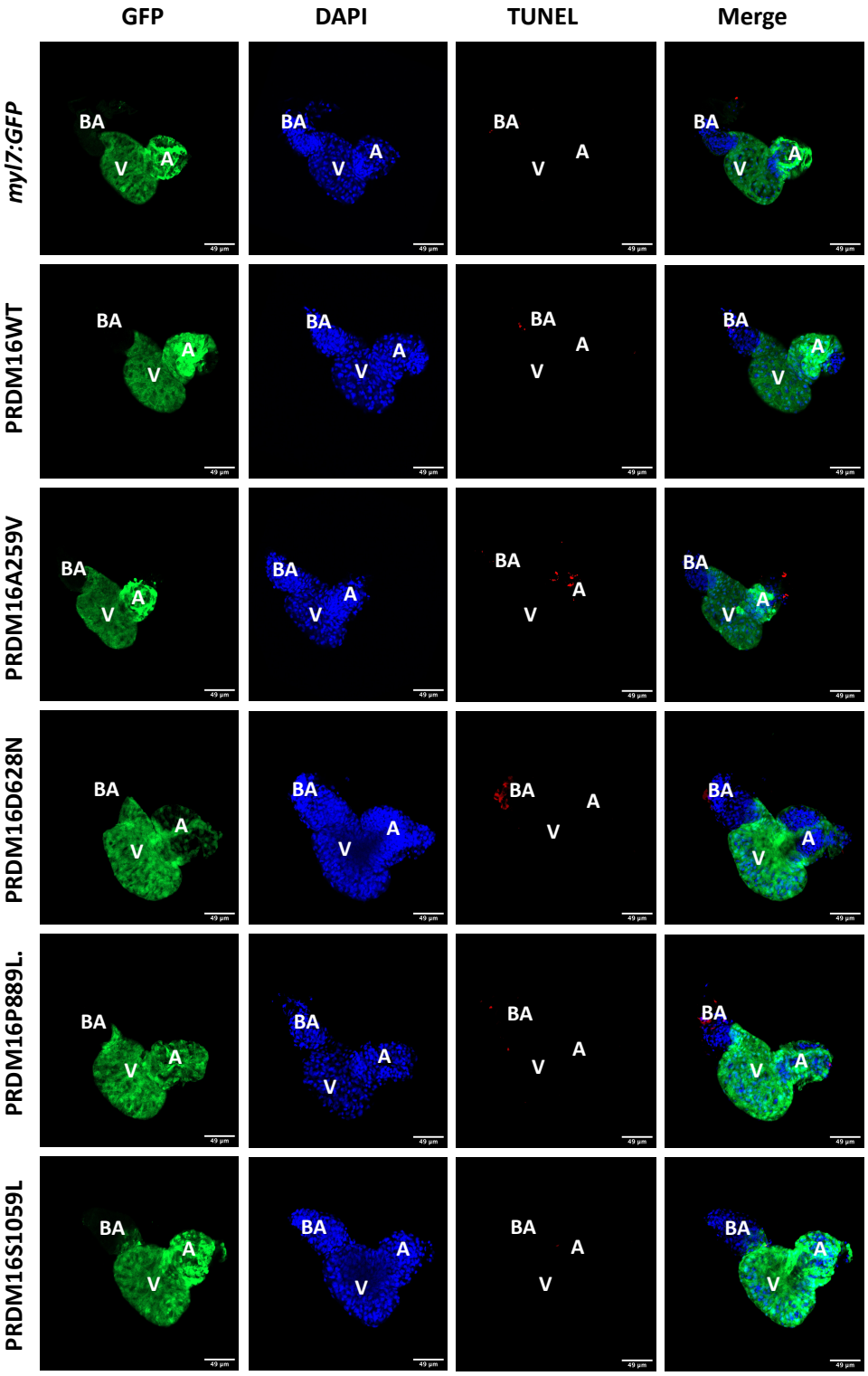

Figure 4.15: *Representative confocal images of 0.5 µM Z-projections of hearts expressing GFP, PRDM16 WT and respective PRDM16 variants. To visualize apoptosis, the dissected hearts were stained with TUNEL at 48 hpf. Cell nuclei are counterstained with DAPI (blue), TUNEL-positive cells (Red), which are visible only in bulbus arteriosus (BA). Cardiomyocytes, expressing GFP under the myl7 promoter, were stained with an anti-GFP antibody as a booster (in green). A = atrium, V = ventricle (Scale bar = 50 µm).*

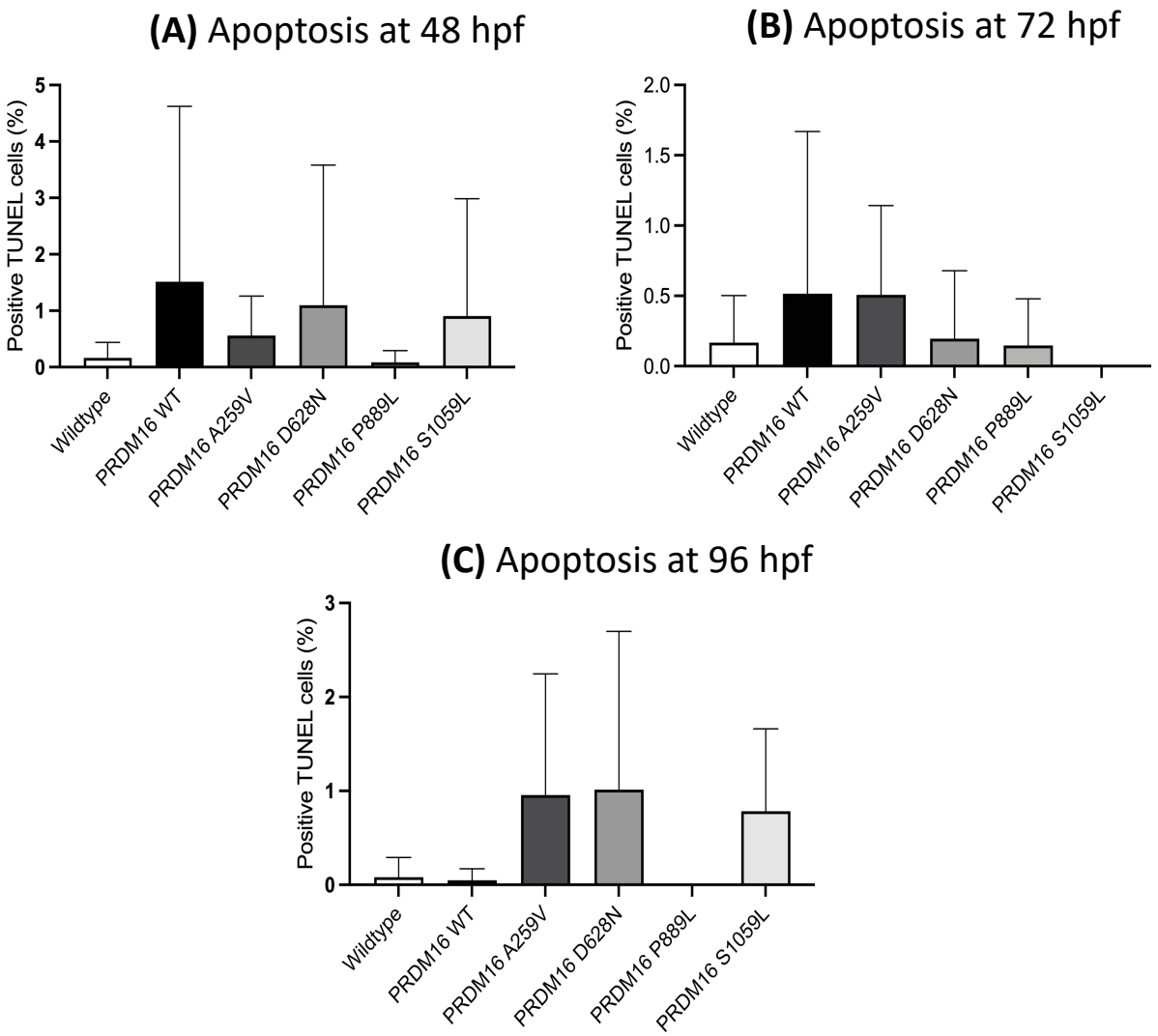

Figure 4.16: *Quantification of cell death using TUNEL assay. Cell undergoing apoptosis are represented as perentage of total number of heart cells. TUNEL staining was performed at 48hpf, 72hpf and 96hpf on all PRDM16 variants, PRDM16-WT and Tg(myl7:GFP) as control group. At all of time point , no statistically significant differences were observed between the PRDM16 variants and PRDM16 WT when compared to control using one-way ANOVA with Dunnett's post-test (GraphPad Prism version 10.0). n = 5, N = 3.*

Effects of *PRDM16* variants on gap junctional protein Connexin43

Connexin 43 is one of the first gap junctional proteins expressed in zebrafish heart development. As alterations in gap junctional composition is one of the hallmarks of

ARVC [197], the levels and localization of Cx43 in the PRDM16 models was examined. To evaluate the influence of four PRDM16 ARVC models, in addition to wildtype PRDM16 and the identified truncation mutation (K702*) associated with non-syndromic LVNC and DCM patients (refer to subsection 1.8.1), on gap junctions, a double immunofluorescence (IF) analysis of Connexin 43 and Alcama (ZN-8) levels was performed in transgenic zebrafish embryonic hearts (Figure 4.17).

Therefore, each *PRDM16* variants and *PRDM16* WT in the F1 generation were out crossed with wildtype. The embryos were initially screened for YFP expression in the eye lens, serving as a selection marker for the overexpression of *PRDM16* variants and *PRDM16* WT. At 72hpf, embryonic hearts were isolated, fixed, and subjected to staining with anti-Connexin 43 antibody for the localization of Connexin 43, and Alcama visualize the cardiomyocyte cell membranes, as shown in figure 4.17. Protein levels were quantified using Image J. Notably, in the wildtype, Cx43 was predominantly located in the cell membrane, whereas in *PRDM16* WT and variants, it exhibited a more cytoplasmic distribution. In the case of the truncation mutation (K702*), Cx43 expression appeared diminished.

The statistical analysis, depicted in Figure 4.18, revealed that at 72 hpf, no significant differences were observed in Connexin 43 levels among the *PRDM16* variants, wildtype *PRDM16*, and the truncation mutation (K702*), compared to the wildtype control. The average mean intensity in control hearts was 137.30 MESF (±54.74 MESF). In hearts overexpressing PRDM16 WT and the respective variants (PRDM16-A259V, PRDM16-D628N, PRDM16-P889L, and PRDM16-S1059L), the percentages were 158.84 MESF (±49.16 MESF), 142.81 MESF (±43.09 MESF), 198.60 MESF (±16.19 MESF), 191.70 MESF (±36.41 MESF), 165.24 MESF (±24.37 MESF), respectively. While not reaching statistical significance, the truncated variant (K702*) exhibited a modest reduction in Cnx43 levels 94.83 MESF (±34.50 MESF).

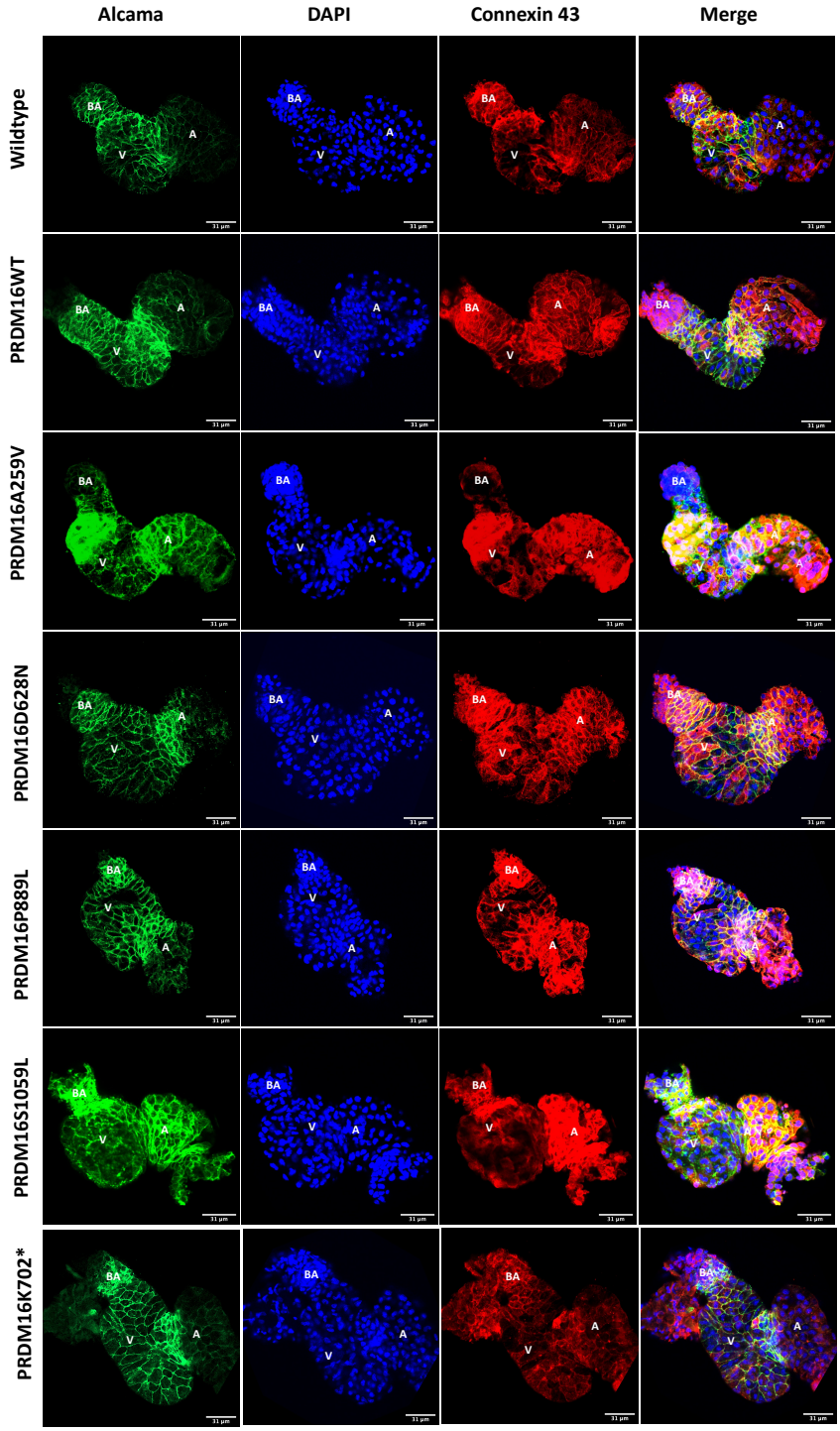

Figure 4.17: *Immunofluorescent staining of connexin 43 and Alcama, using anti-Alcam (zn8) antibody in zebrafish embryonic heart. The double staining procedures were conducted on isolated hearts from four different PRDM16 variants, along with wildtype PRDM16 and the truncation mutation (K702*), all at the 72-hour post-fertilization (hpf) stage. The wildtype embryonic heart served as the control in these experiments. In the embryonic heart, ZN-8 staining was used to visualize the cardiomyocytes' membranes of the ventricle (v), atrium (A), and bulbus arteriosus (BA) in green. Additionally, Connexin 43 was localized on the cell membrane as well as in the cytoplasm (red). DAPI was used to label cell nuclei (blue). (Scale bar = 50 µm).*

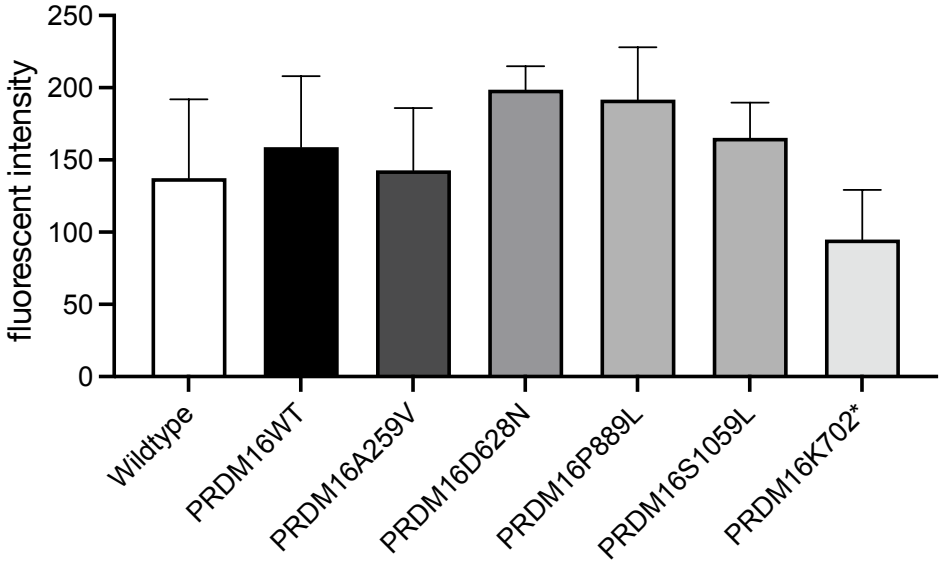

Figure 4.18: *Fluorescent Intensity measurement of Connexin 43. The analysis was conducted using a z-projection approach, focusing on the maximum overall intensity for the PRDM16 variants, wildtype PRDM16, and the truncation mutation (K702*) at 72 hpf. The analysis focused exclusively on the ventricle and atrium. There were no statistically significant differences in Connexin 43 expression when comparing the PRDM16 variants, PRDM16 WT and truncation mutation (K702*) to the control. Error bars represent the standard deviation (SD). n = 5, N = 3 WT and transgenic embryos each. Statistical analysis was conducted using one-way ANOVA with Dunnett's post-test multiple columns (GraphPad Prism version 10.0).*

4.1.3 Metabolic profile analysis in PRDM16 disease models

Increased number of mitochondria and enrichment for glycogen granules were observed in the adult *PRDM16* truncation model (K702*) based on preliminary data. To evaluate the impact of *PRDM16* WT and ARVC variants overexpression on reactive oxygen species, mitochondrial quantity, and mitochondrial superoxide levels in zebrafish embryonic hearts at 48 hpf, flow cytometry was employed. For each *PRDM16* variant and *PRDM16* WT, 20 to 30 embryos were collected.

The control group comprised *Tg(myl7:GFP)* embryos lacking YFP expression, which were dissociated into single cells. The analysis employed a ROS-sensitive fluorescent probe for identifying cells affected by oxidative stress, Mitotracker Deep Red FM dye for visualizing mitochondrial quantity, and MitoSOX Red for detecting mitochondrial superoxide. GFP was utilized as a specific marker for cardiomyocytes. The outcomes of

flow cytometry assessments for mitochondrial quantity, mitochondrial superoxide, and superoxide in cardiomyocytes are depicted in Figures 4.19 to 4.23.

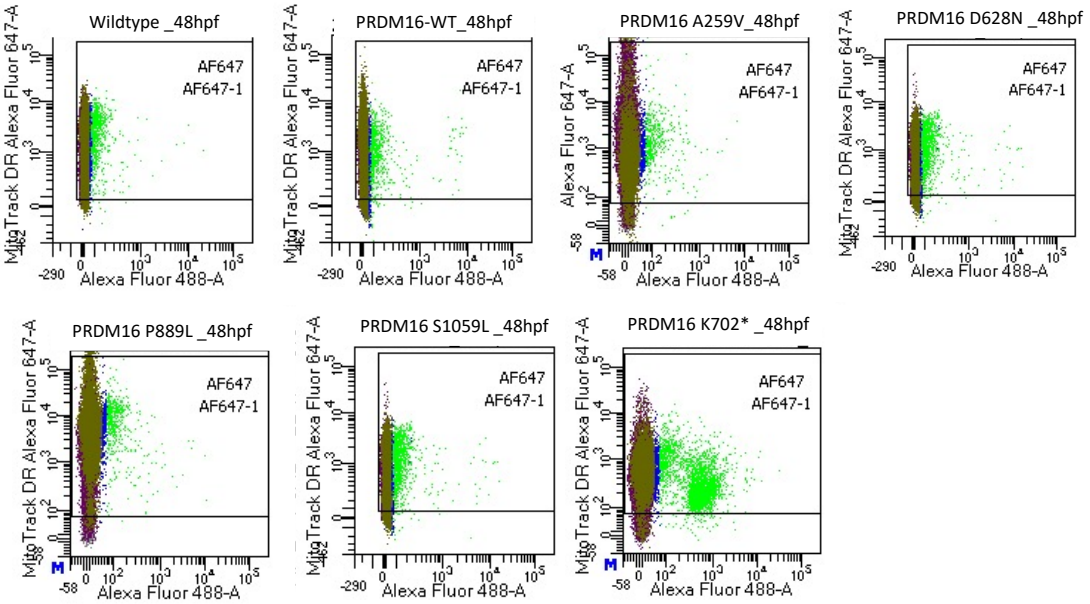

Figure 4.19: *Fluorescence-activated cell sorting (FACS) analysis was conducted to assess mitochondrial quantity in four ARVC variants and PRDM16 WT, with Tg(myl7:GFP) serving as the control. Cell sorting was performed based on GFP signal for cardiomyocytes and red fluorescent protein (RFP) signal for mitochondria detection.*

4.1.4 The impact of *PRDM16* variants on mitochondrial quantity in cardiomyocytes

Mitochondrial quantity analysis involved quantifying the mean fluorescence intensity within the Mitotracker Deep Red FM channel specifically within the GFP+ population, which served as the cardiomyocyte marker. Statistical analysis, as presented in Figure 4.20, indicated that at 48 hpf, no significant differences in mitochondrial quantity were observed among the PRDM16 variants and PRDM16 WT compared to the control group. The Kruskal-Wallis Test was employed for the statistical analysis. The average mean intensity in control hearts was 1892 MESF (±1892.47 MESF). In hearts overexpressing PRDM16 WT and the respective variants (PRDM16-A259V, PRDM16-D628N, PRDM16-P889L,

PRDM16-S1059L, and K702*), the percentages were 2924 MESF (±1568.70 MESF), 4852 MESF (±1466.50 MESF), 2934 MESF (±964.23 MESF), 1237 MESF (±633.36 MESF), 2664 MESF (±875.33 MESF), and 449 MESF (±116.41 MESF), respectively.

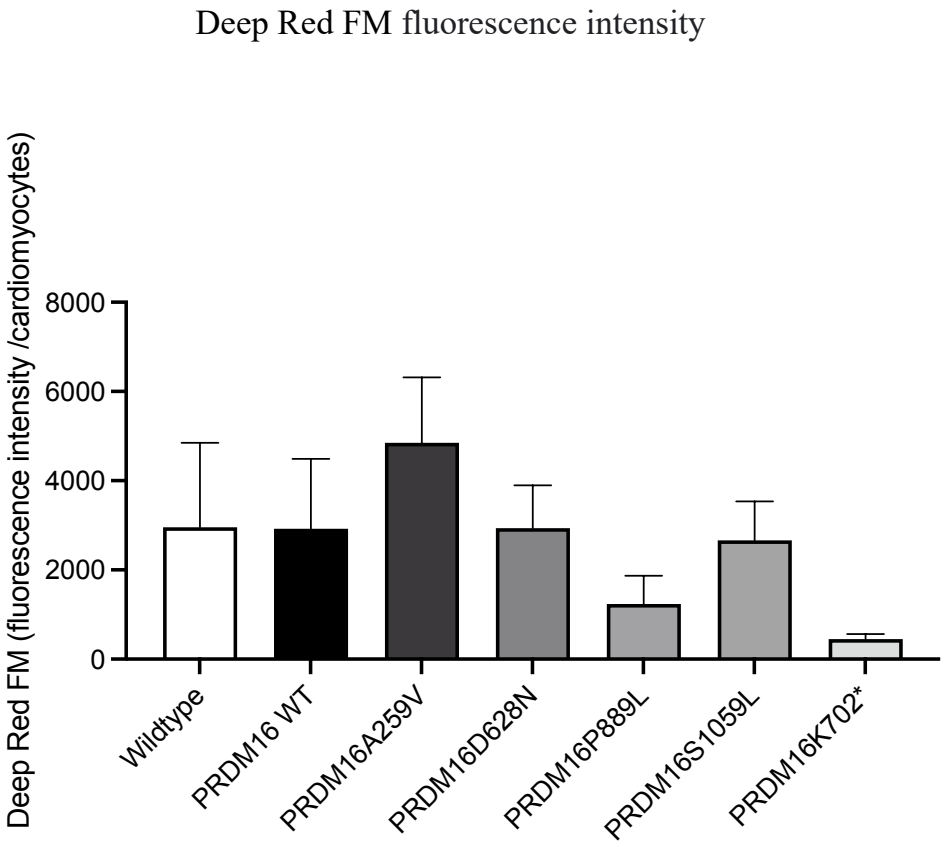

Figure 4.20: *Analysis of effect of PRDM16 variants on mitochondrial quantity. There were no statistically significant differences in mitochondrial quantity when comparing the PRDM16 variants and PRDM16 WT to the control. Error bars represent the standard deviation (SD). n = 20, N = 3. Kruskal-Wallis Test. (GraphPad Prism version 10.0).*

4.1.5 Quantification of reactive oxygen species (ROS) levels in *PRDM16* variants

Figure 4.21 illustrates the results of flow cytometry measurements, where cells were sorted based on GFP signal for cardiomyocytes and red fluorescent protein (RFP) signal for ROS detection. The quantification of ROS levels relied on the mean fluorescence intensity of the CellROX channel within the GFP+ population, serving as the cardiomyocyte

marker. Statistical analysis, as displayed in figure 4.22, showed that at 48 hpf, there were no significant differences in ROS levels among the *PRDM16* variants and *PRDM16* WT compared to the control group. The average mean intensity in control hearts was 709 MESF (±188.07 MESF). In hearts overexpressing PRDM16 WT and the respective variants (PRDM16-A259V, PRDM16-D628N, PRDM16-P889L, and PRDM16-S1059L), the percentages were 667.66 MESF (±305.13 MESF), 556.33 MESF (±242.06 MESF), 655.66 MESF (±96.86 MESF), 752 MESF (±209.01 MESF), 711.66 MESF (±196.75 MESF), respectively.

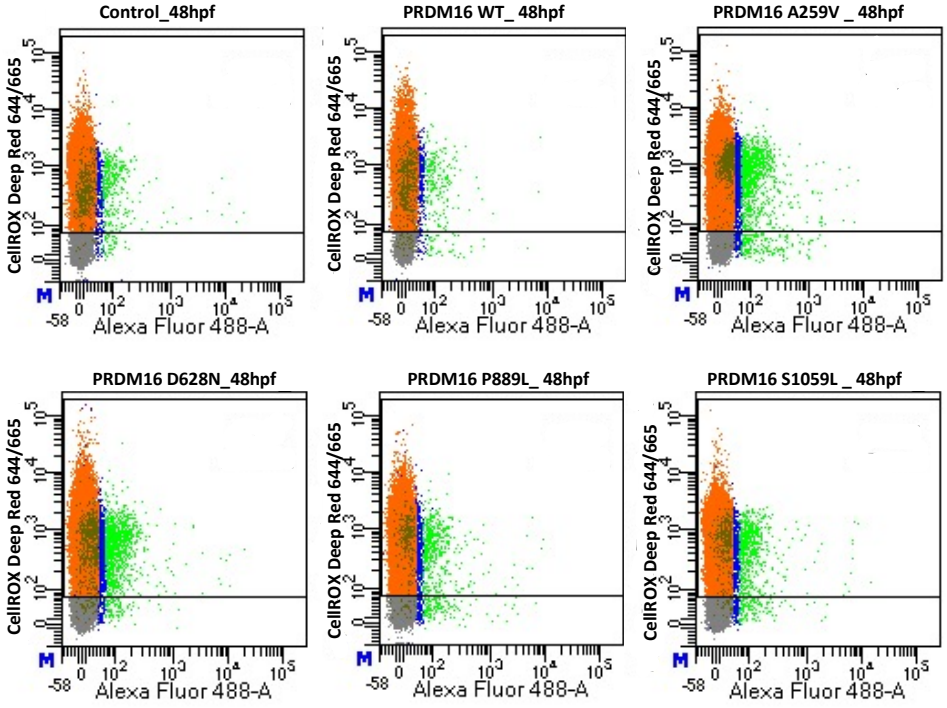

Figure 4.21: *Fluorescence-activated cell sorting (FACS) analysis was conducted to assess reactive oxygen species levels in four ARVC variants and PRDM16 WT, with Tg(myl7:GFP) serving as the control. Cell sorting was performed based on GFP signal for cardiomyocytes and red fluorescent protein (RFP) signal for ROS detection.*

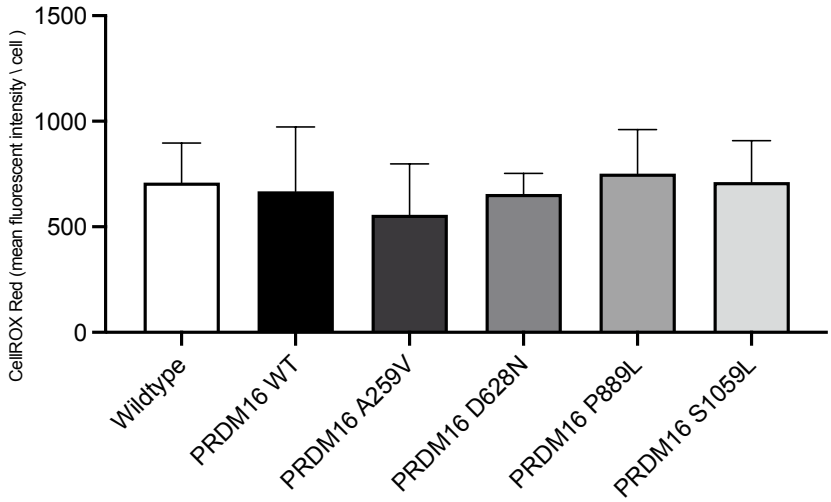

Figure 4.22: *Analysis of effect of PRDM16 variants on ROS levels in four ARVC variants and PRDM16 WT, with Tg(myl7:GFP) serving as the control. There were no statistically significant differences in ROS level when comparing the PRDM16 variants and PRDM16 WT to the control. Error bars represent the standard deviation (SD). n = 20, N = 3. Statistical analysis was conducted using one-way ANOVA one-way ANOVA with Dunnett's post-test (GraphPad Prism version 10.0).*

4.1.6 Analysis of effect of *PRDM16* variants on superoxide levels

Further analysis of the mitochondrial superoxide levels (Figure 4.23) and subsequent statistical analysis (Figure 4.24) was conducted using the mean fluorescence intensity of the MitoSOX Red channel within the GFP+ population and Mitotracker Deep Red FM channel positive, which also served as the cardiomyocyte marker and mitochondrial number. The analysis demonstrated a significant reduction in superoxide levels between the PRDM16-P889L variant and the truncated variant compared to the control group. The average mean intensity within the GFP+ population in control hearts was 11743 MESF (±5100.58 MESF). In hearts overexpressing PRDM16 WT and the respective variants (PRDM16-A259V, PRDM16-D628N, PRDM16-P889L, PRDM16-S1059L, and K702*), the percentages were 15333 MESF (±3570.20 MESF), 16134 MESF (±10358.49 MESF), 12652 MESF (±3683.69 MESF), 10133 MESF (±458.06 MESF), 11834 MESF (±5917.75 MESF), and 6615 MESF (±306.09 MESF), respectively. Moreover, the average mean intensity within the RFP+ population in control hearts was 12683 MESF (±2080.05 MESF). In hearts overexpressing PRDM16 WT and the respective variants (PRDM16-A259V, PRDM16-D628N, PRDM16-P889L, PRDM16-S1059L, and K702*), the percentages were

14287 MESF (±3820.36 MESF), 14282 MESF (±9932.19 MESF), 12249 MESF (±3358.80 MESF), 19380 MESF (±793.86MESF), 11355 MESF (±5153.99 MESF), and 6570 MESF (±341.07 MESF), respectively.

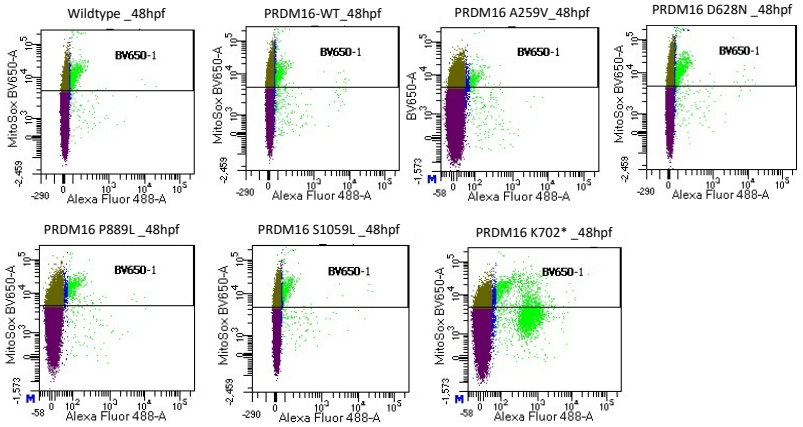

Figure 4.23: *Fluorescence-activated cell sorting (FACS) analysis was conducted to assess detect mitochondrial Superoxide using MitoSOX Red in four ARVC variants and PRDM16 WT, with Tg(myl7:GFP) serving as the control. Cell sorting was performed based on GFP signal for cardiomyocytes and red fluorescent protein (RFP) signal for mitochondria detection.*

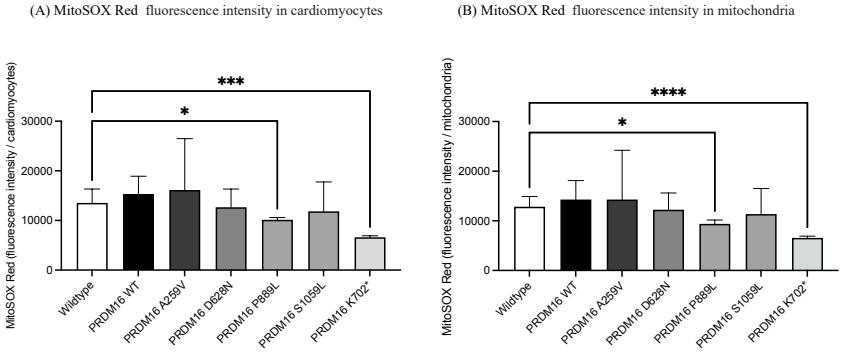

Figure 4.24: *Analysis of effect of PRDM16 variants on Superoxide. (A) MitoSOX Red fluorescence intensity in cardiomyocytes. The analysis demonstrated a significant reduction in superoxide levels between the two variants, PRDM16-P889L and the truncated variant in comparison to the control group. (B) MitoSOX Red fluorescence intensity in mitochondria. A significant reduction was evident at 48 hpf when comparing PRDM16-P889L and the truncated variant in comparison to the control group. Error bars represent the standard deviation (SD). n = 20, N = 3. Statistical analysis was conducted using one-way ANOVA with Dunnett's post-test (GraphPad Prism version 10.0).*

4.1.7 Visualization of lipid deposits in *PRDM16* ARVC variants

In the context of Arrhythmogenic Right Ventricular Cardiomyopathy (ARVC), another distinctive hallmark is the substitution of cardiomyocytes with adipocytes [102]. Therefore, the hearts of 6-month-old zebrafish from the four *PRDM16* ARVC transgenic zebrafish models, PRDM16 wildtype, and PRDM16 truncation mutation (K702*), were subjected to Oil Red O staining to facilitate the visualization of droplets (Figure 4.25). The control group comprised the wild-type AB strain. Histological analysis of the transgenic zebrafish lines, including *Tg(myl7:PRDM16 WT)*, *Tg(myl7:PRDM16 A259V)*, and *Tg(myl7:PRDM16 P889L)*, revealed the absence of fat deposition, a feature consistent with both the wild-type AB strain and the transgenic *Tg(myl7:PRDM16 K702*)* line. Conversely, *Tg(myl7:PRDM16 D628N)* and *Tg(myl7:PRDM16 S1059L)* displayed the presence of fat deposition, as indicated by the accumulation of Oil Red O (white arrowheads in Figure 4.25), in the respective panels.

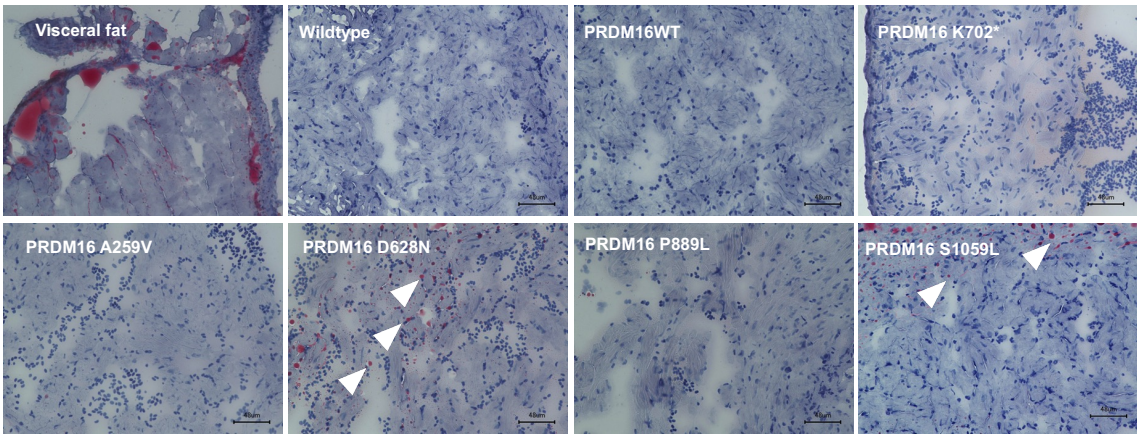

Figure 4.25: *Oil Red O staining was performed on the hearts of 6-month-old adult zebrafish. Histological sections from four distinct transgenic PRDM16 variant lines and PRDM16 WT were sequentially stained with Oil Red O, which binds to lipids, and hematoxylin was used to satin nuclei. The wild-type AB strain served as the control group. Visceral fat tissue was employed as a positive control for lipid binding. Among the transgenic lines, including Tg(myl7:PRDM16 WT) and two variants, Tg(myl7:PRDM16 A259V) and Tg(myl7:PRDM16 P889L), no adipocytes were observed, similar to the wild type and transgenic Tg(myl7:PRDM16 K702*). However, adipocytes visible in the sections of myocardial wall in Tg(myl7:PRDM16 D628N) and Tg(myl7:PRDM16 S1059L) in contrast to the others. The white arrowhead indicate adipocytes. (Scale bar = 50 µm)*

4.2 Analysis of effects of PRDM16 on ventricular compact myocardium

Genetic studies have shown that deletions and mutations in *PRDM16* cause LVNC [191], which may affect the growth of the heart muscle wall. To investigate the impact of PRDM16 overexpression, including the truncation variant, on the compact myocardium, adult zebrafish hearts from the transgenic lines *Tg(drl:GFP;myl7:PRDM16-K702*)*, *Tg(drl:GFP,myl7: PRDM16-WT)*, and *Tg(drl:GFP)*, which served as control, were isolated at 6 months of age and subsequently Masson-Goldner-stained. In figure 4.26, the compact myocardium layer in the control group appears with thin collagen layer in the epicardium layer and an absence of intracellular space (n = 5).

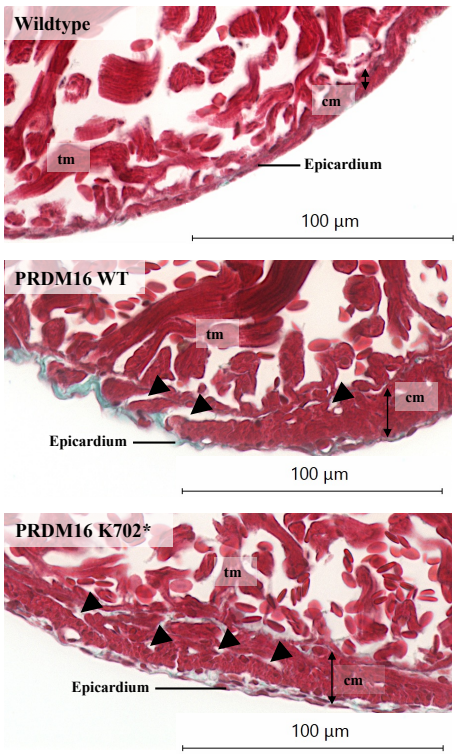

Figure 4.26: *Representative Masson-Goldner-stained section images of wildtype zebrafish, PRDM16WT, the truncation variant heart are presented. In the wildtype heart, the compact myocardium layer appears thinner with reduced collagen in the epicardium layer and an absence of intracellular space (black arrowhead). Tg(drl:GFP,myl7:PRDM16-WT) and Tg(drl:GFP;myl7:PRDM16-K702*) exhibited a thicker layer of compact myocardium (bidirectional arrowhead), accompanied by increased intercellular space (black arrowhead). Additionally, collagen was observed in the epicardium layer of Tg(drl:GFP,myl7:PRDM16-WT). Scale bar = 100 µm). tm = trabecular myocardium, cm = compact myocardium.*

In contrast to the control group, both *Tg(drl:GFP;myl7:PRDM16-K702*)* and *Tg(drl:GFP, myl7:PRDM16 WT)* exhibited a thicker layer of compact myocardium, accompanied by intercellular space. Additionally, collagen was observed in the epicardium layer of *Tg(drl:GFP,myl7:PRDM16-WT)*.

To quantitatively assess the thickening of the compact myocardial wall thickness in *Tg(drl:GFP,myl7:PRDM16-WT)*, *Tg(drl:GFP;myl7:PRDM16-K702*)*, and *Tg(drl:GFP)*, image analysis to measure the wall thickness was conducted using ImageJ software. Statistical analysis unveiled a significant increase in compact myocardium thickness in both *Tg(drl:GFP,myl7:PRDM16-WT)* 22.17 μm ($\pm 8\mu$m) and *Tg(drl:GFP;myl7:PRDM16-K702*)* 21.54 μm ($\pm 8.1\mu$m) compared to control hearts 9.81 μm ($\pm 2.39\mu$m) (Figure 4.27).

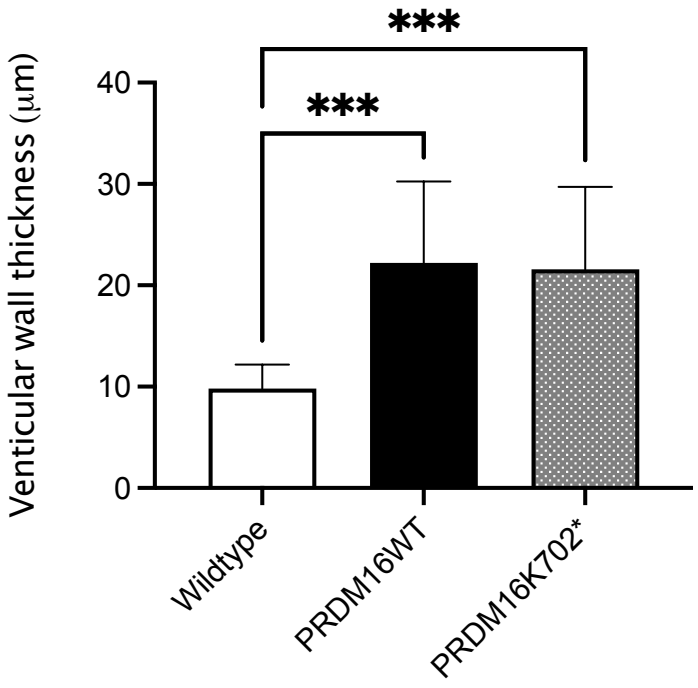

Figure 4.27: *Measurements of the compact myocardial wall were conducted on Tg(drl:GFP,myl7:PRDM16-WT), Tg(drl:GFP;myl7:PRDM16-K702*), and Tg(drl:GFP), which served as the control group. The analysis revealed a significant increase in the thickness of the compact myocardium between Tg(drl:GFP,myl7:PRDM16-WT) and Tg(drl:GFP;myl7:PRDM16-K702*) in comparison to the control hearts. Statistical analysis was conducted with one-way ANOVA with Dunnett's post-test (GraphPad Prism version 10.0). (n = 5).*

4.3 Assessing cardiomyocyte regenerative capacity in *PRDM16* disease models following heart injury

Given the potential significance of *PRDM16* in heart development, it is conceivable that it also plays a pivotal role in cardiac remodeling and regeneration. Consequently, a regeneration model, which is described in detail in subsection 3.8.2. was established for humanized transgenic *PRDM16* wildtype and *PRDM16* truncation mutation (K702*) models. The truncation model (K702*) was selected based on preliminary data indicating its impact on cardiomyocyte proliferative capacity during cardiac development.
In these models, *PRDM16* WT and *PRDM16* truncation mutation (K702*) were precisely overexpressed in cardiomyocytes, under the regulation of the tissue-specific promoter *myl7*. Transgenic zebrafish carrying the wildtype PRDM16 as well as the truncation mutation (K702*) were crossed with *drl:GFP* fish. Draculin *(drl)*, identified as a marker exclusively expressed in cells belonging to the first heart field (FHF), was used. Due to the draculin promoter regulating GFP expression in FHF cells, the origin of the regenerating cells in the zebrafish heart was determined. The identification of the carriers followed the same procedure as described in subsection 4.1.1.

4.3.1 Assessment of regenerative response in *PRDM16* variants

The hearts of transgenic zebrafish carrying *Tg(drl:GFP;myl7:PRDM16 WT*, *Tg(drl:GFP;myl7:PRDM16-(K702*)*, and *drl:GFP* (control) were isolated at 1, 3, and 5 days post-amputation (dpa) following a 20% ventricular apex amputation.
Sham-operated zebrafish, which only underwent an incision of the chest without further manipulation, were utilized as controls for the procedure. Proliferating Cell Nuclear Antigen (PCNA) staining was conducted on isolated zebrafish adult hearts at 1, 3, and 5 dpa. PCNA staining was applied to sagittal sections of adult transgenic *Tg(drl:GFP;myl7:PRDM16 WT)*, *Tg(drl:GFP;myl7:PRDM16-(K702*)* and *Tg(drl:GFP)* (control) hearts that had undergone a 20% ventricular apex amputation (Figure 4.28). The plane of amputation is marked with a dashed line. In Figure 4.28, the presence of proliferating cells, identified through PCNA staining, was notably observed at the amputation edge. In contrast, sham-operated specimens did not exhibit proliferating cells at the same level as the amputation site. Cell nuclei were labeled using DAPI staining.

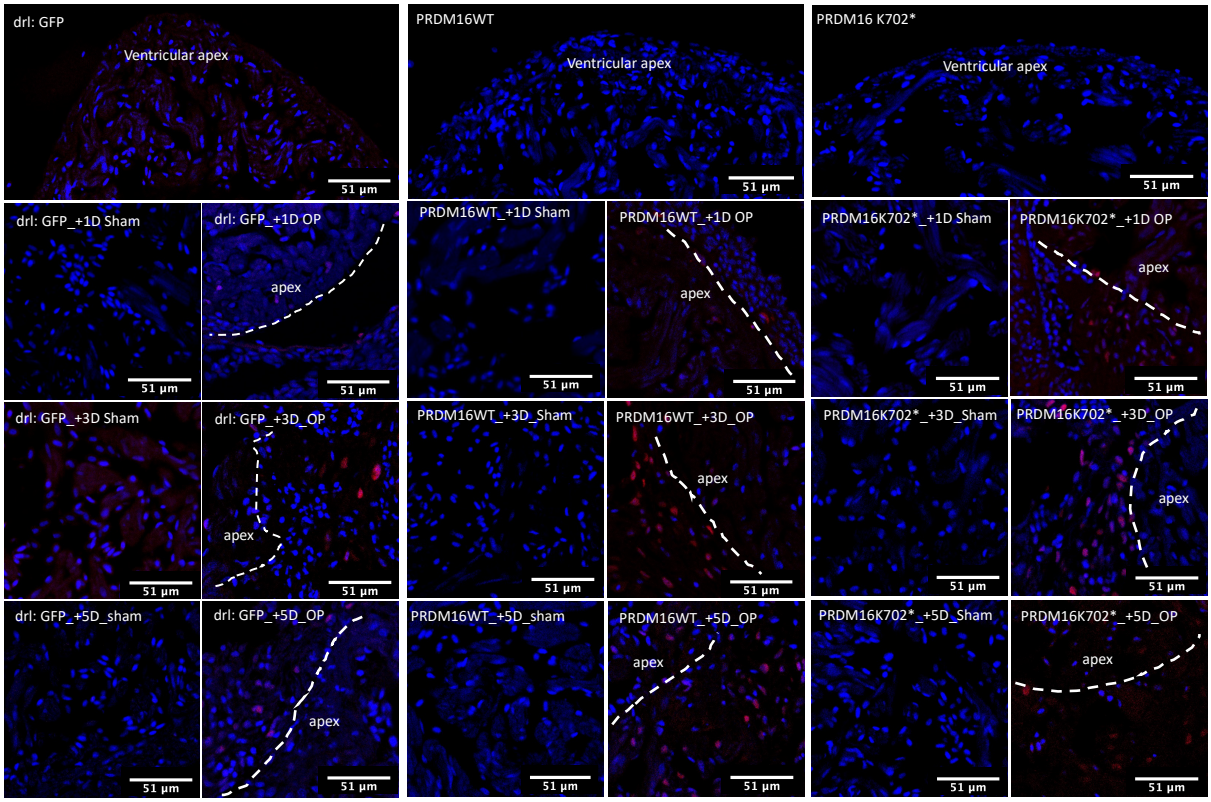

Figure 4.28: *Proliferating Cell Nuclear Antigen (PCNA) staining. Staining was conducted on isolated zebrafish adult hearts at 1, 3, and 5 dpa. PCNA staining was applied to sagittal sections of adult transgenic Tg(drl:GFP;myl7:PRDM16 WT), Tg(drl:GFP;myl7:PRDM16-(K702*), and Tg(drl:GFP) (control) hearts, which were subjected to a 20% ventricular apex amputation. The plane of amputation is indicated with a dashed line. Proliferating cells, indicated by PCNA (red), were detected at the amputation edge. In contrast to the amputation area, proliferating cells were not observed in the sham-operated specimens. DAPI was used to label cell nuclei (blue). (Scale bars = 50 µm).*

Hematoxylin-eosin staining was performed on sagittal sections of adult transgenic hearts from *Tg(drl:GFP;myl7:PRDM16 WT*, *Tg(drl:GFP;myl7:PRDM16-(K702*)* and *Tg(drl:GFP)* (control) fish following a 20% ventricular apex amputation (Figure 4.29). This staining aimed to elucidate the structural characteristics, cell distribution, and morphological alterations within the amputated zebrafish hearts. Zebrafish adult hearts at 1, 3, and 5 dpa were isolated and fixed in formalin for subsequent processing. In H&E staining, Hematoxylin stains cell nuclei blue, and Eosin, which stains the extracellular matrix, cytoplasm, and other structures, imparts varying shades of pink (Figure 4.29).

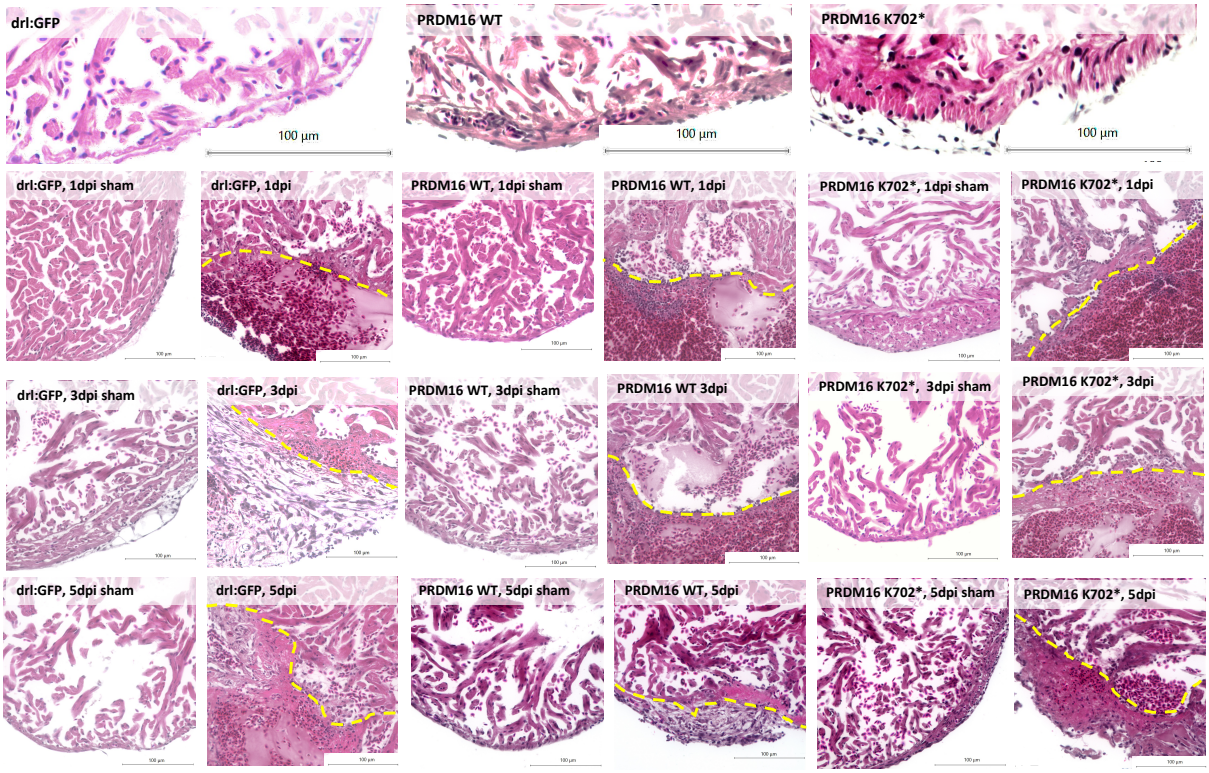

Figure 4.29: *Hematoxylin-eosin staining (H&E). The staining was performed on isolated zebrafish adult hearts at 1, 3, and 5 dpa. Staining was applied to sagittal sections of adult transgenic Tg(drl:GFP;myl7:PRDM16 WT), Tg(drl:GFP;myl7:PRDM16-(K702*) and Tg(drl:GFP) (control) hearts that had undergone a 20% ventricular apex amputation. The plane of amputation is indicated with a dashed line. (Scale bars = 200 µm).*

Masson-Goldner staining was conducted on isolated zebrafish adult hearts at 1, 3 and 5 dpa. Sagittal sections of adult transgenic *Tg(drl:GFP;myl7:PRDM16 WT)*, *Tg(drl:GFP;myl7:PRDM16-(K702*)*, and *drl:GFP* (control) hearts, which underwent a 20% ventricular apex amputation, were stained using the Masson-Goldner-Trichrome method. These sections were processed at specified time intervals following the surgical procedure. The staining highlights connective tissue deposition and fibrotic areas in green, while healthy myocardial tissue is depicted in red. Sham-operated fish, which only underwent a chest incision, were used as controls for the procedure (Figure 4.30).

These sections were processed at specified time intervals following the surgical procedure. The staining highlights connective tissue deposition and fibrotic areas in green, while healthy myocardial tissue is depicted in red. For the procedure's controls, sham-operated fish, which only underwent an incision of the chest, were utilized (Figure 4.30).

At 1 dpa, erythrocytes accumulate at the injured area (IA), and collagen-rich regions are

distinctly stained in blue. Notably, extensive fibrosis is visible at the IA at 3 dpa. At 5 days dpa, there is a reduction in the fibrotic areas, which are depicted in green.

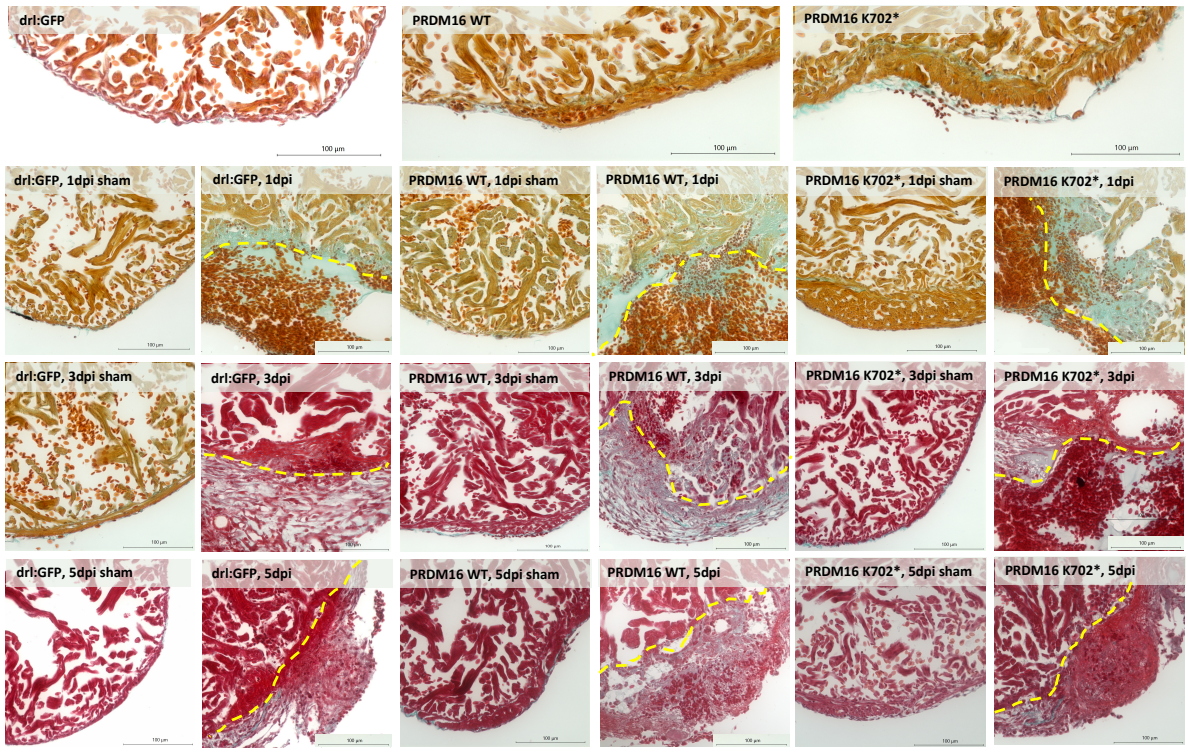

Figure 4.30: *Masson-Goldner staining was performed on isolated zebrafish adult hearts at 1, 3, and 5 dpa. Masson-Goldner-Trichrome staining was applied to sagittal sections of adult transgenic Tg(drl:GFP;myl7:PRDM16-WT, Tg(drl:GFP;myl7:PRDM16-(K702*) and Tg(drl:GFP) (control) hearts that had undergone a 20% ventricular apex amputation. The plane of amputation is indicated with a dashed line. These sections were prepared at specific time intervals following the surgical procedure. The staining highlights the deposition of connective tissue and fibrotic regions in (green), while the healthy myocardial tissue appears in (red). Sham-operated fish that only undergo incision of the chest were used as controls for the procedure. At 1 dpa, there is an accumulation of erythrocytes at the IA, and collagen-rich regions are visibly stained in green. Extensive fibrosis is evident at the IA at 3 dpa. At 5 dpa, there is a reduction in the fibrotic areas, which are depicted in (green). (Scale bars = 200 µm).*

To evaluate the replacement of zebrafish heart muscle, the surface area of longitudinal ventricular sections from injured hearts at 5 dpa was quantified through digital imaging, employing ImageJ software. The regeneration rate was determined by measuring the whole ventricle area over the injured area [198]. The average percentage of regenerative area in control hearts at 5 dpi was 6% (±1.37%). In hearts overexpressing PRDM16 WT and

the PRDM16 truncation variant, the percentages were 6% (±1.49%) and 13% (±2.67%), respectively. The statistical analysis, as illustrated in figure 4.31, revealed a significant difference in regeneration capacity at 5 dpa. Specifically, there were notable distinctions between the truncation variant when compared to the control group and the overexpression of PRDM16 WT.

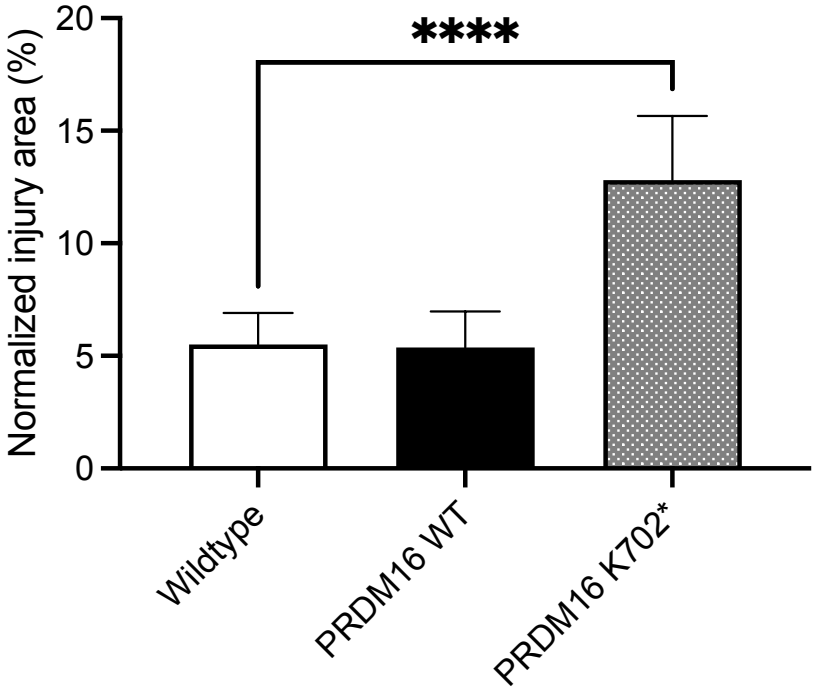

Figure 4.31: *The quantification involved the assessment of the normalized injury area in the PRDM16 WT, PRDM16 truncation variant, and control group. The analysis unveiled a noteworthy difference in regeneration capacity at 5 dpa, particularly between the PRDM16 truncation variant and the control group. Error bars represent the standard deviation (SD). Statistical analysis was conducted with using one-way ANOVA with Dunnett's post-test (GraphPad Prism version 10.0).*

To examine ultrastructural changes in cardiac muscle, focusing on sarcomere structure, Z-lines, and mitochondria, Transmission electron microscopy (TEM) was utilized. The examination aimed to provide insights into the changes in the subcellular ultrastructure occurring during the regeneration of zebrafish hearts. Zebrafish adult hearts at 1, 3, and 5 dpa as well as control hearts (sham-operated) were isolated and fixed in 3% Glutaraldehyde (GA) for further prepration for TEM. As depicted in figure 4.32, in uninjured hearts, cardiomyocytes displayed a well-organized arrangement of sarcomeres and mitochondria, characterized by clearly defined Z-lines. In the control injured hearts, the sarcomeres

appeared longer than in uninjured hearts. In the case of PRDM16 WT, the sarcomeres in the injured hearts appeared unorganized. To quantify sarcomere length in the cardiac muscles of adult zebrafis with PRDM16-K702*, PRDM16 WT, and a control group, measurements (N = 3, n = 3) were taken for individual sarcomere using ImageJ's length measurement tool.

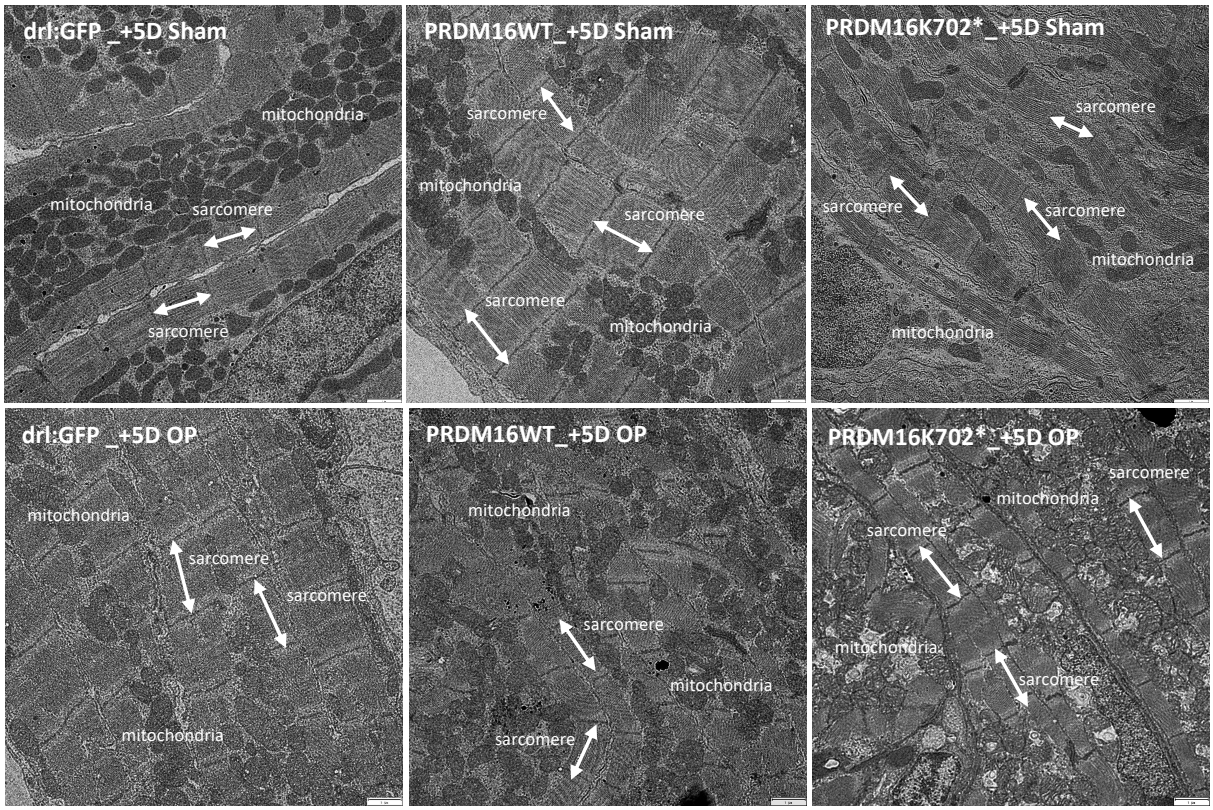

Figure 4.32: *Transmission electron microscopy of sections of sections of control hearts (sham-operated) and regenerating hearts at 5 dpa. TEM was conducted on sagittal sections of adult transgenic hearts from Tg(drl:GFP,myl7:PRDM16 WT), Tg(drl:GFP,myl7:PRDM16-K702*), and Tg(drl:GFP) (control) fish following a 20% ventricular apex amputation. Cardiomyocytes in unamputated control samples show a tightly organized sarcomeric structure and the Z-lines are clearly visible. (Scale bar = 100 µm).*

At 5 days post-amputation (dpa), the sarcomere length in *Tg(drl:GFP)* zebrafish was notably increased, averaging 1.94 μm ($\pm$1.73 μm), compared to the sham-operated group, which averaged 1.76 μm ($\pm$0.91 μm). Hence, sarcomere lengths were specifically measured at this time point (Figure 4.33). Interestingly, hearts undergoing a 20% ventricular apex amputation showed a significant increase in sarcomere length compared to sham-operated hearts. However, no statistically significant differences were observed

between operated and sham-operated hearts in both *Tg(drl:GFP,myl7:PRDM16 WT)* and *Tg(drl:GFP,myl7:PRDM16 K702*)*. In these groups, the sarcomere length averaged 1.82 μm ($\pm$1.40 μm) for PRDM16 WT and 1.80 μm ($\pm$1.38 μm) for PRDM16 K702*, while in sham-operated hearts, it averaged 1.92 μm ($\pm$1.79 μm) for PRDM16 WT and 1.85 μm ($\pm$1.42 μm) for PRDM16 K702*.

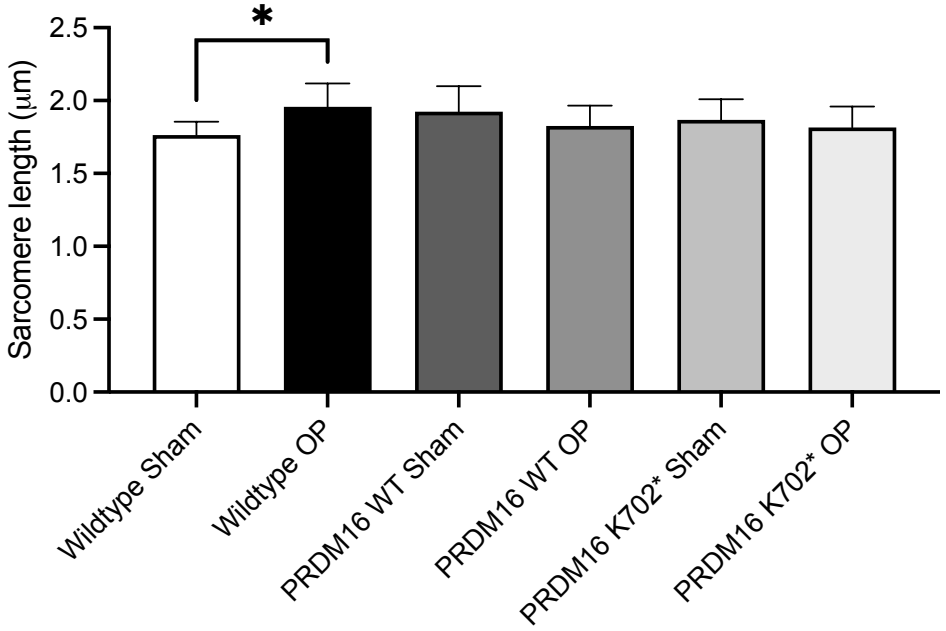

Figure 4.33: *Sarcomere length analysis was performed on cardiac muscle from Tg(drl:GFP;myl7:PRDM16-K702*), Tg(drl:GFP,myl7:PRDM16-WT), and Tg(drl:GFP) specimens at 5 dpa, alongside control hearts from sham-operated individuals. The study included adult hearts (n = 3) from each group, with all measurements conducted at a scale of 1 micrometer per image. Results revealed a noteworthy increase in sarcomere length in Tg(drl:GFP) at 5 dpa compared to the control hearts (sham-operated) group. However, the Tg(drl:GFP,myl7:PRDM16-K702*) and Tg(drl:GFP,myl7:PRDM16-WT) exhibited no statistically significant differences at 5 dpa in comparison to the control hearts (sham-operated). Statistical analysis was conducted with one-way ANOVA with Dunnett's post-test (GraphPad Prism version 10.0).*

Overview of *PRDM16* variants, and their functional associations

A comprehensive table (Figure 4.34) succinctly summarize the roles of PRDM16 and its genetic variants in biological functions and elucidating their correlations. During embryonic heart development, significant alterations in cardiac function were observed

in cases of PRDM16 WT, variant PRDM16-A259V, and PRDM16-P889L overexpression. Preliminary data also indicated significant alterations in cardiac function, changes in cardiac cell number and proliferation, and metabolic changes for PRDM16-K702* [139]. Variants PRDM16-D628N, PRDM16-P889L, and PRDM16-S1059L exhibited significant changes in cardiac cell number and proliferation. Additionally, PRDM16-P889L displayed significant modifications in metabolism. In adulthood, variants D628N and S1059L demonstrated lipid deposition in the heart.

variant	clinical presentation	cardiac function	cell number /proliferation	metabolism	lipid deposit (Adults)
PRDM16-WT		change			
PRDM16-A259V	ARVC	change			
PRDM16-D628N	ARVC		change		change
PRDM16-P889L	ARVC	change	change	change	
PRDM16-S1059L	ARVC		change		change
PRDM16-K702*	LVNC/DCM	change	change	change	

Figure 4.34: *Overview of PRDM16 WT, PRDM16 variants and their functional associations. During embryonic heart development, significant changes in cardiac function were observed both with PRDM16 WT, PRDM16-A259V, PRDM16-P889L overexpression. Variants PRDM16-D628N, PRDM16-P889L, and PRDM16-S1059L showed significant changes in cardiac cell number and proliferation. Additionally, PRDM16-P889L demonstrated significant metabolic changes. In the case of PRDM16-K702*, significant alterations in cardiac function, changes in cardiac cell number and proliferation [139], and metabolic changes were indicated. Variants D628N and S1059L demonstrated lipid deposition in the adult heart.*

4.4 Functional analysis of identified *CAPZβ* variants in zebrafish

To identify novel human variants within the *CAPZβ* gene, the Variant Effect Prediction (VEP) tool was used. Four missense variants, which do not appear in more than 4000 control samples were detected. In this study, four patients with congenital heart defects were evaluated, presenting with both non-syndromic and syndromic CHD. The two patients with non-syndromic CHD harbored variants p.Thr179Ser and p.Ser192Asn. The patient with the p.Thr179Ser variant presented with hypoplastic left heart syndrome, while the patient with the p.Ser192Asn variant exhibited pulmonary atresia with a ventricular septal defect. In contrast, the patients with syndromic CHD had more complex clinical

presentations. The patient with the p.Arg215Cys variant exhibited a range of symptoms including an atrial septal defect, global developmental delay, sparse hair, abnormal pinna, and postnatal growth retardation. Meanwhile, the patient with the p.Lys181Arg variant presented with a ventricular septal defect, trigonocephaly, optic nerve hypoplasia, agenesis of the corpus callosum, and hypoplasia of the cerebellar vermis. It is noteworthy, that three of these novel mutations, p.Thr179Ser, p.Lys181Arg and p.Ser192Asn were located in exon 6, whereas p.Arg215Cys was observed in exon 7 (Figure 4.35).

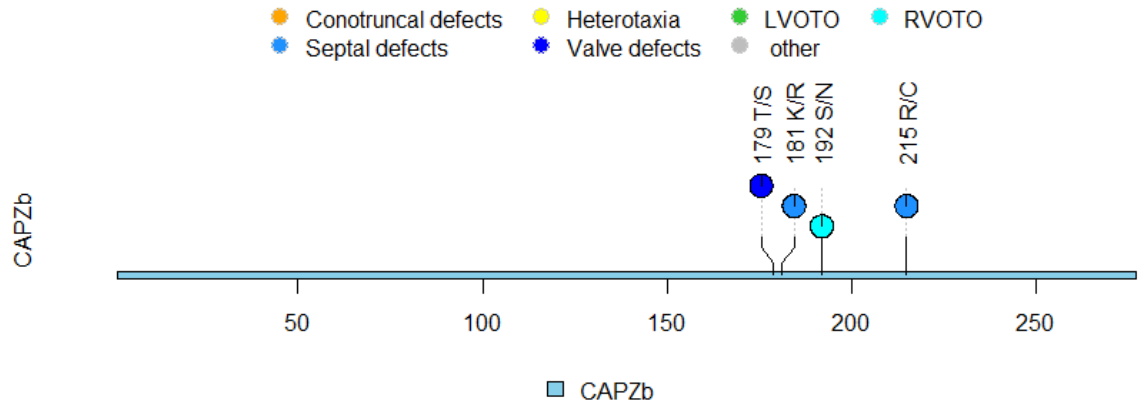

Figure 4.35: *Identification of four variants in CAPZβ protein. Lolliplot showing four missense mutations within the protein sequence of CAPZβ. Each lollipop represents a mutation identified in this study. The CAPβ protein domain is colored blue. Variants p.Thr179Ser and p.Ser192Asn were detected in two patients with non-syndromic CHD and p.Lys181Arg and p.Arg215Cys were identified in two patients with syndromic CHD. Hypoplastic left heart syndrome was found in the de novo p.Thr179Ser. The septal defects were found in p.Lys181Arg and p.Arg215Cys. Right ventricular outflow tract obstruction (RVOTO) only found in p.Ser192Asn.*

4.4.1 Phenotypic characterization of *CAPZβ* transgenic disease models

Analysis of cardiac morphology in *CAPZβ* variant disease models

To assess the impact of overexpressing *CAPZβ* variants and *CAPZβ* WT on the embryonic heart development, the images of developing heart labeled with GFP were captured at two time points, 48 and 72 hpf respectively. The overexpression of *CAPZβ* variants and *CAPZβ* WT was accomplished in *Tg(myl7:EGFP)* zebrafish, aiding in heart visualization through the expression of GFP within the embryonic heart, as depicted in Figure 4.36. The *Tg(myl7:GFP)* group served as the control in these experiments.

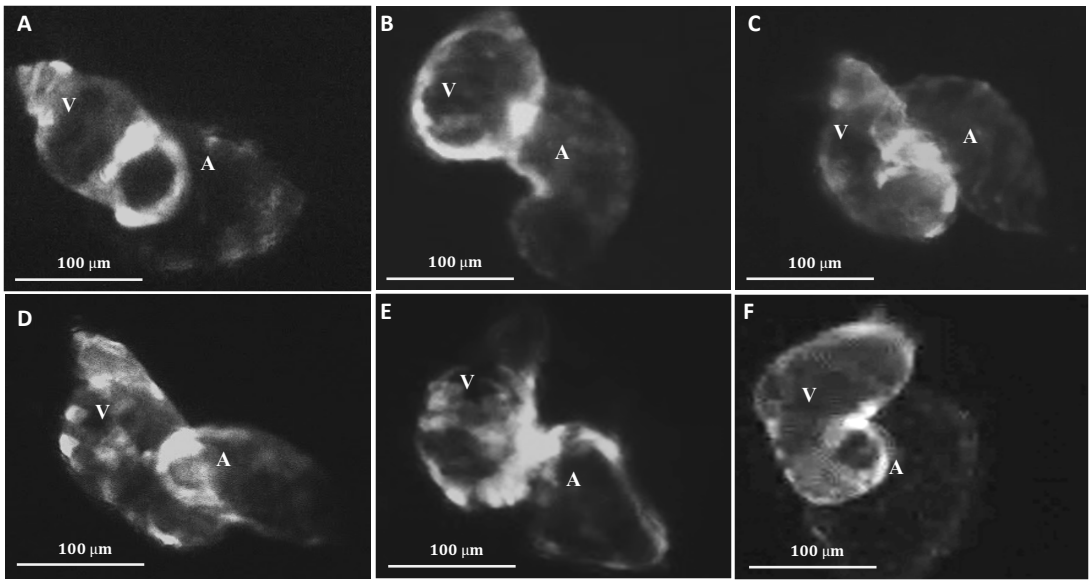

Figure 4.36: *Cardiac morphology of CAPZβ variants, CAPZβ WT, and myl7:EGFP at 48 hpf. Images of all embryo lines were captured using a fluorescence stereomiscroscope with a single-frame exposure time. The ventricles (V) and atria (A) are clearly visible through the GFP signal. (A) visualization of the embryonic Tg(myl7: GFP). (B) CAPZβ WT. (C) CAPZβ Thr179Ser. (D) CAPZβ Lys181Arg. (E) CAPZβ Ser192Asn. (F) CAPZβ Arg215Cys. No discernible distinctions were observed between the embryos expressing human CAPZβ variants, CAPZβ WT, and the control. (Scale bar = 100 µm)*

The selected images represent the typical characteristics observed in the majority of individuals from the respective transgenic lines. It is worth noting that some individual

hearts displayed structural differences from the norm. Comparing the ventricles of the embryos at 48 hpf, no discernible distinctions were noted between those with human *CAPZβ* variants and *CAPZβ* WT and the *Tg(myl7:GFP)* control. The atria also exhibited normal shapes. After 72 hpf (Figure 4.37), distinct phenotypic differences were observed in the *Tg(myl7:GFP;myl7:CAPZβ Thr179Ser)* and *Tg(myl7:GFP;myl7:CAPZβ Ser192Asn)* embryos. These individuals displayed slight distortions in atrial morphology and reduced ventricular size compared to the control group. Conversely, no discernible distinctions from the control group were observed in the other transgenic lines.

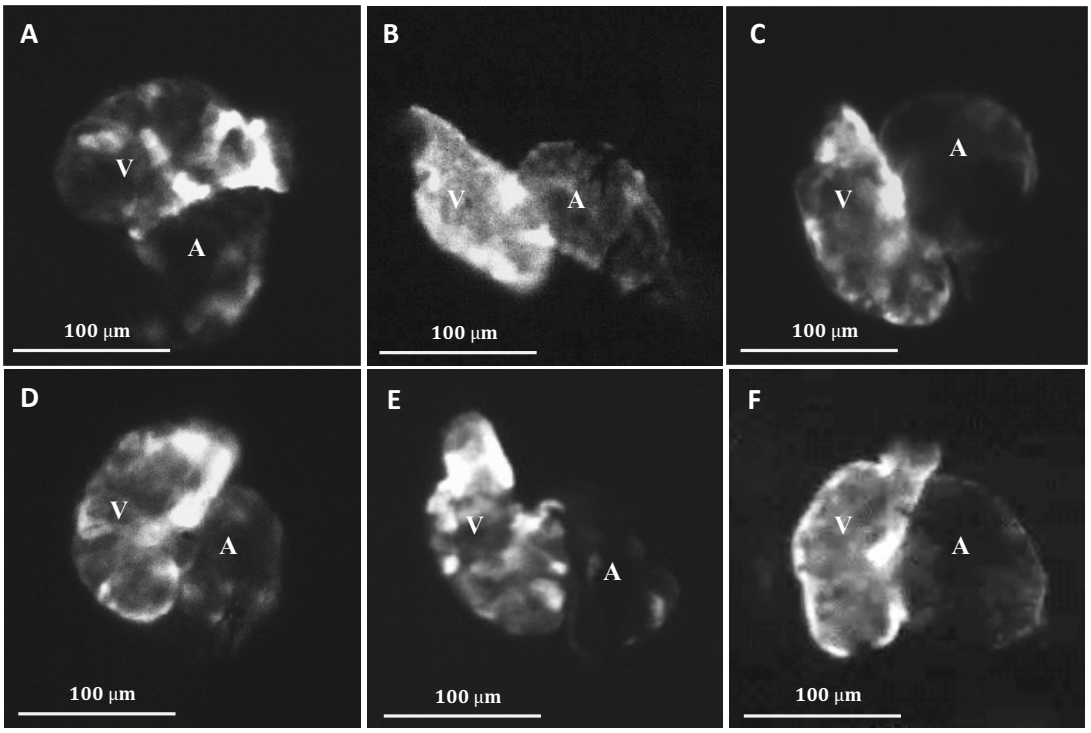

Figure 4.37: *Fluorescence images of embryonic hearts with various CAPZβ variants and CAPZβ WT at 72 hpf. All images were captured using a fluorescence stereomiscroscope with an exposure time of 1 frame. The ventricle (V) and atrium (A) are discernible through the GFP signal. (A) visualization of the embryonic Tg(myl7:GFP). (B) CAPZβ -WT. (C) CAPZβ Thr179Ser. (D) CAPZβ Lys181Arg. (E) CAPZβ Ser192Asn. The notable phenotype of the heart includes slight deformations in the atria of most individuals. (F) CAPZβ Arg215Cys. (Scale bar = 100 µm)*

Analysis of sarcomeric structure in cardiac muscle

The sarcomere, positioned between two Z-lines, constitutes the fundamental contractile unit in muscle tissue [159]. To explore the function of *CAPZβ*, a critical capping protein

responsible for anchoring actin filaments to the Z-line in cardiac muscle sarcomeres, transmission electron microscopy was utilized to examine structural alterations in the sarcomeres of adult zebrafish hearts at one year of age. This analysis encompassed adult hearts (n=3) from each of the *CAPZβ* variants, *CAPZβ* WT, and the wildtype as control. Transmission electron microscopy images offer a longitudinal perspective of cardiac muscle, facilitating the scrutiny of sarcomere structure and Z-lines. In wildtype zebrafish (n = 3), normal I bands, Z lines, and mitochondria were observed, as depicted in Figure 4.38.

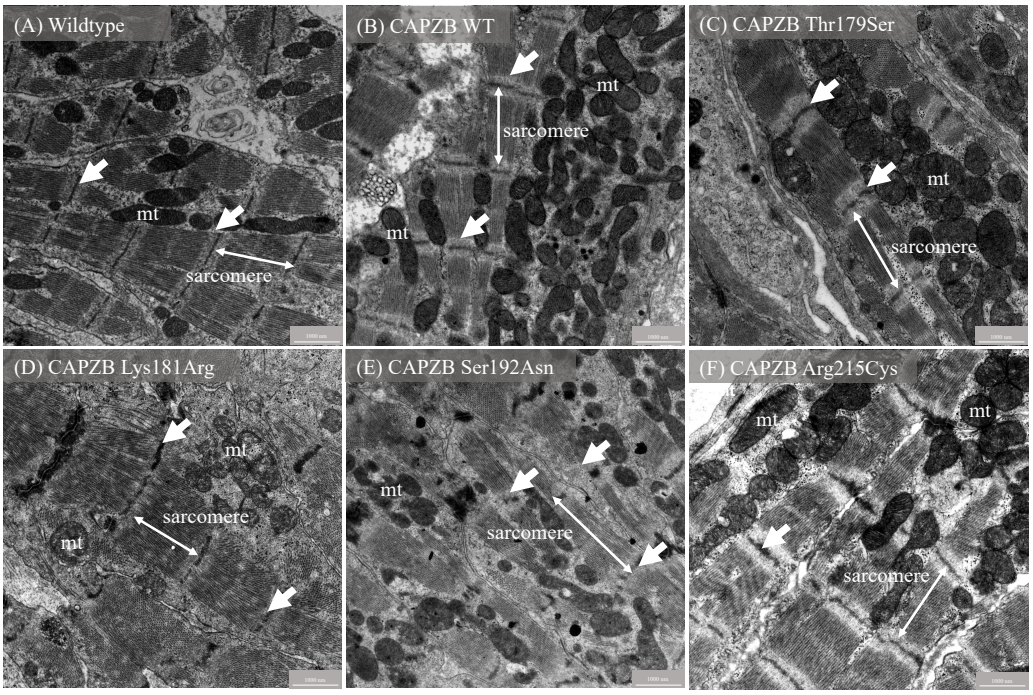

Figure 4.38: *Transmission electron microscopy (TEM) of longitudinal sections of cardiac muscle allows for the observation of the sarcomere structure and Z-lines. In wildtype (WT) zebrafish (A), normal I bands, Z lines, and mitochondria were observed. For CAPZβ WT (B), both I bands and Z lines were normal. However, CAPZβ Thr179Ser (C) showed abnormal Z lines and enlarged mitochondria. CAPZβ Lys181Arg (D) displayed thick Z lines. CAPZβ Ser192Asn (E) lacked I bands and had thin, disorganized Z lines. Lastly, CAPZβ Arg215Cys (F) exhibited smaller mitochondria, thin Z lines, and widened perinuclear spaces. "mt" indicating mitochondria and white arrows indicating Z lines and double-headed arrow indicating sarcomere. (Scale bar = 100 µm)*

For *CAPZβ* WT (n = 3), both I bands and Z lines displayed a normal structure, but there was an increased number of mitochondria. In the case of CAPZβ Thr179Ser (n = 3), an abnormal appearance of Z lines and enlarged mitochondria was noted. CAPZβ Lys181Arg (n = 3) showed thick Z lines. CAPZβ Ser192Asn (n = 3) exhibited the disappearance of I

bands, thin Z lines with an unorganized sarcomeric structure, and small-sized mitochondria. Finally, in CAPZβ Arg215Cys (n = 3), decreased mitochondrial size, thin Z lines, and broadened perinuclear spaces were observed (Figure 4.38). To quantify sarcomere length in the cardiac muscles of adult zebrafis with *CAPZβ* variants, *CAPZβ* WT, and a control group, measurements (N = 3, n = 3) were taken for individual sarcomere using ImageJ's length measurement tool.

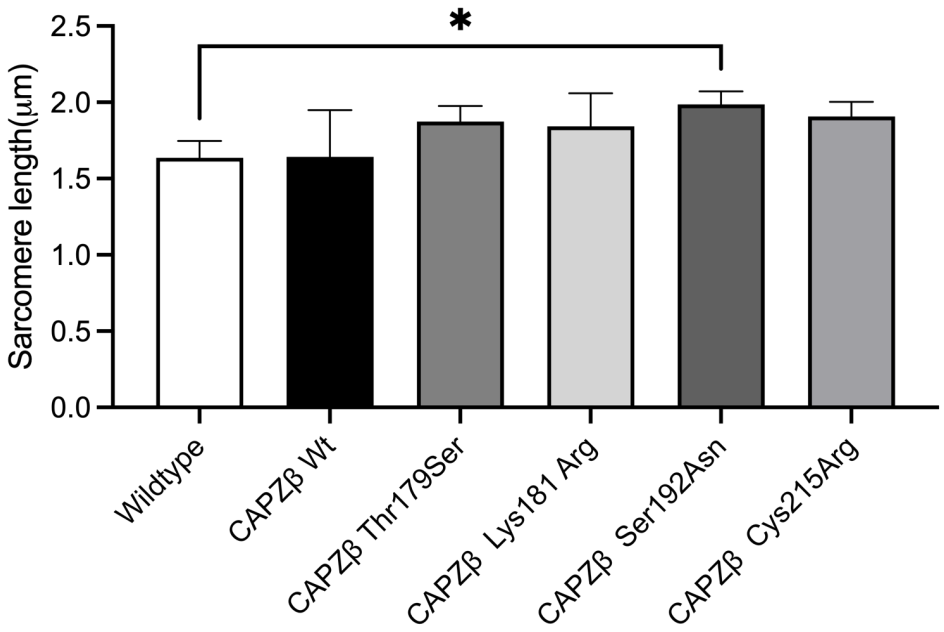

Figure 4.39: *Analysis of sarcomere length in cardiac muscle. The analysis involved adult hearts (n=3) from each of the CAPZβ variants, CAPZβ WT, and wildtype. All measurements were conducted at a scale of 1 micrometer per image. Analysis of sarcomere length revealed a significant increase in sarcomere length in CAPZβ Ser192Asn compared to the control group. In contrast, the other three variants and CAPZβ WT exhibited no statistically significant differences in comparison to the control group. Statistical analysis was conducted with one-way ANOVA with Dunnett's post-test (GraphPad Prism version 10.0).*

The mean sarcomere length in control hearts was 1.64 μm ($\pm$0.11 μm). Hearts overexpressing CAPZβ WT and its variants (CAPZβ Thr179Ser, CAPZβ Lys181Arg, CAPZβ Ser192Asn, and CAPZβ Arg215Cys) showed mean lengths of 1.65 μm ($\pm$0.31 μm), 1.88 μm ($\pm$0.10 μm), 1.83 μm ($\pm$0.22 μm), 1.98 μm ($\pm$0.09 μm), and 1.91 μm ($\pm$0.09 μm), respectively. Analysis revealed a significant increase in sarcomere length specifically in CAPZβ Ser192Asn compared to the control group (Figure 4.39). Conversely, the other three variants and CAPZβ WT did not exhibit statistically significant differences relative

to the control group.

Analysis of cardiac output in *CAPZβ* variant disease models

Cardiac function in zebrafish embryos at 48 and 72 hpf was assessed *in vivo* using fluorescent microscopy and high-speed imaging. Parameters such as cardiac output, heart rate, and stroke volume were quantified using an established algorithm (outlined in section 3.5).

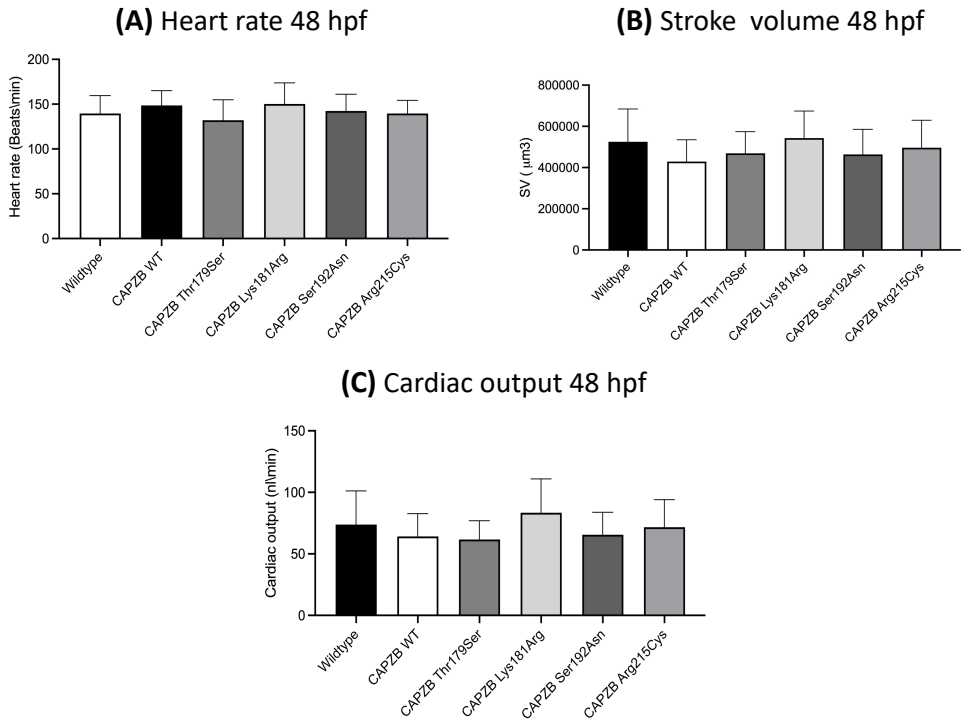

Figure 4.40: *Cardiac output was evaluated in the context of CAPZβ variants, CAPZβ WT, and Tg(myl7:GFP) at 48 hpf. The impact of CAPZβ variants, including CAPZβ WT, on heart rate (A) showed no statistically significant differences between the groups. Analysis of stroke volume (B) revealed no significant reduction in stroke volume in CAPZβ variants compared to the control group. By 48 hpf (C), there were no statistically significant differences in cardiac output (CO) among the CAPZβ variants, including CAPZβ WT, and the control groups. n = 15 ,N = 3. Statistical analysis was conducted with one-way ANOVA with Dunnett's post-test (GraphPad Prism version 10.0).*

At 48 hpf, the influence of *CAPZβ* variants and *CAPZβ* WT on heart rate did not reveal any statistically significant differences among the groups. Control hearts exhibited an

average heart rate of 139.55 bpm (±20.06 bpm), while hearts overexpressing CAPZβ WT and its variants (CAPZβ Thr179Ser, CAPZβ Lys181Arg, CAPZβ Ser192Asn, and CAPZβ Arg215Cys) showed averages of 148.51 bpm (±16.60 bpm), 132.12 bpm (±22.73 bpm), 150.18 bpm (±23.56 bpm), 142.46 bpm (±18.57 bpm), and 139.64 bpm (±14.58 bpm), respectively.

Similarly, the assessment of stroke volume did not reveal any statistically significant distinctions among the groups. Control hearts exhibited an average stroke volume of 52,5*10^3 μm^3 (±16*10^3 μm^3) Hearts overexpressing CAPZβ WT and its variants (CAPZβ Thr179Ser, CAPZβ Lys181Arg, CAPZβ Ser192Asn, and CAPZβ Arg215Cys) showed averages of 42.9*10^4 μm^3 (±10.6*10^4 μm^3) , 46.9*10^4 μm^3 (±10.5*10^4 μm^3) , 54.3*10^4 μm^3 (±13.1*10^4 μm^3) , 46.4*10^4 μm^3 (±12.2*10^4 μm^3), and 50*10^3 μm^3 (13,3*10^3 μm^3), respectively.

There were no statistically significant variations in cardiac output (CO) among the *CAPZβ* variants (CAPZβ Thr179Ser, CAPZβ Lys181Arg, CAPZβ Ser192Asn, and CAPZβ Arg215Cys), with averages of 61.67 nl\min (±15.28 nl\min), 83.38 nl\min (±27.52 nl\min), 65.61 nl\min (±18.16 nl\min), 71.63 nl\min (±22.38 nl\min), and CAPZβ WT 64.20 nl\min (±18.48 nl\min), compared to the control groups at 48 hpf 73.84 nl\min (±27.31 nl\min). Figure 4.40 displays the measurements collected at 48 hpf.

Figure 4.41 illustrates the measurements obtained at 72 hpf. By this time point, overexpression of CAPZβ variants, as well as CAPZβ WT, did not result in statistically significant differences in heart rate compared to the control group. Control hearts exhibited an average heart rate of 160.52 bpm (±21.29 bpm), while hearts overexpressing CAPZβ WT and the respective variants (CAPZβ Thr179Ser, CAPZβ Lys181Arg, CAPZβ Ser192Asn, and CAPZβ Arg215Cys) showed averages of 158.28 bpm (±14.26 bpm), 160.84 bpm (±14.73 bpm), 161.63 bpm (±18.08 bpm), 157.30 bpm (±19.04 bpm), and 149.31 bpm (±19.52 bpm), respectively.

It's noteworthy that CAPZβ Ser192Asn 29.4*10^4 μm^3 (±9.8*10^4 μm^3) displayed a significant reduction in stroke volume compared to the control group 42.3*10^4 μm^3 (±10.8*10^4 μm^3). Conversely, overexpression of CAPZβ WT showed an average stroke volume of 33.3*10^4 μm^3 (±15.4*10^4 μm^3) , while CAPZβ Thr179Ser, CAPZβ Lys181Arg, and CAPZβ Arg215Cys exhibited averages of 30.6*10^4 μm^3 (±15.8*10^4 μm^3), 34.2*10^4 μm^3 (±10.5*10^4 μm^3), and 40.7*10^4 μm^3 (±13.3*10^4 μm^3), respectively.

Furthermore, overexpression of CAPZβ Thr179Ser 48.86 nl\min (±23.69) variants and CAPZβ Ser192Asn 46.30 nl\min (±17.16 nl\min) resulted in a notable reduction in cardiac output at 72 hpf compared to the transgenic *Tg(myl7:GFP)* control 67.97 nl\min (±19.54 nl\min). In contrast, overexpression of CAPZβ WT showed an average cardiac

output of 52.51 nl\min (±24.63 nl\min), while CAPZβ Lys181Arg and CAPZβ Arg215Cys exhibited averages of 54.15 nl\min (±14.61 nl\min) and 59.50 nl\min (±18.58 nl\min), respectively.

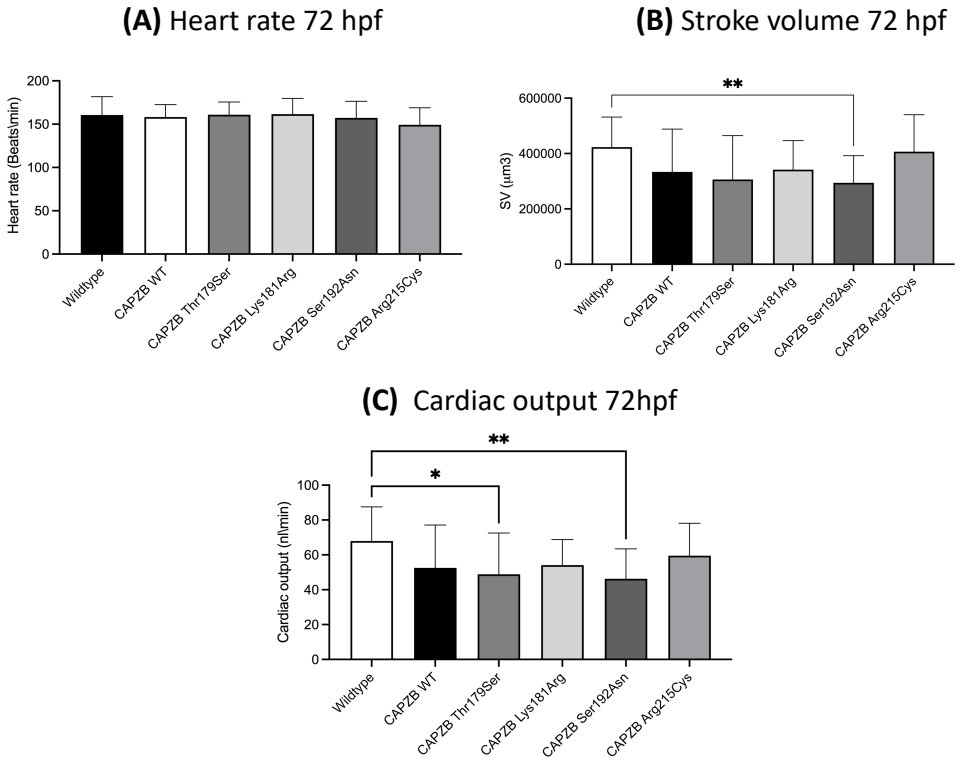

Figure 4.41: *Cardiac output was evaluated for CAPZβ variants, CAPZβ WT, and Tg(myl7:GFP) at 72 hpf. (A) Heart rate measurements for CAPZβ variants and CAPZβ WT did not reveal any significant changes in heart rate. (B) Analysis of stroke volume revealed a significant reduction in stroke volume in CAPZβ Ser192Asn compared to the control group, while CAPZβ WT showed no significant difference when compared to the control. (C) Overexpression of CAPZβ Ser192Asn and CAPZβ SThr179Ser resulted in a significant reduction in CO compared to Tg(myl7:GFP). However, there were no statistically significant differences in CO between the other CAPZβ variants and CAPZβ WT. n = 15 , N = 3. Error bars represent the standard deviation (SD), and asterisks indicate statistical significance at * p> 0.05 and ** p> 0.01. Statistical analysis was conducted with one-way ANOVA with Dunnett's post-test (GraphPad Prism version 10.0).*

Overview of *CAPZβ*, *CAPZβ* variants, and their functional associations

A comprehensive table (Figure 4.42) succinctly summarize the roles of *CAPZβ* and its genetic variants in biological functions and elucidating their correlations. During embryonic

heart development, significant alterations in cardiac function were observed in cases of CAPZβ Thr179Ser and CAPZβ Ser192Asn. In adulthood, the variant CAPZβ Ser192Asn variant exhibited alterations in sarcomere length.

variant	clinical presentation	cardiac function	sarcomere remodeling
CAPZβ-WT			
CAPZβ-Thr179Ser	HLHS	change	
CAPZβ-Lys181Arg	Ventricular septal defect, Atrial septal dialatation		
CAPZβ-Ser192Asn	Tetralogy of Fallot and variants	change	change
CAPZβ-Arg215Cys	Secundum atrial septal defect		

Figure 4.42: *Overview of CAPZβ WT and CAPZβ variants and Their functional associations. During embryonic heart development, significant changes in cardiac function were observed both CAPZβ Thr179Ser and CAPZβ Ser192Asn. In adulthood, the CAPZβ Ser192Asn variant exhibited alterations in sarcomere length.*

Differential expression analysis of *capzb*$^{-/-}$ and *capzb*$^{+/-}$

To identify genes with statistically significant differences in expression between *capzb*$^{-/-}$ and *capzb*$^{+/-}$ embryos at 48 and 72 hpf, bulk RNA sequencing (RNA-seq) analysis was conducted on a sample size of 20 embryos, with N = 3 replicates. Wildtype embryos served as the control group. DESeq2 was employed to model the read count data and assess differential expression using appropriate statistical tests. At 48 hpf, the analysis identified differential expression of protein-coding genes in *capzb*$^{-/-}$ and *capzb*$^{+/-}$ embryos. In *capzb*$^{-/-}$ embryos, 605 genes were downregulated and 378 genes were upregulated. Conversely, in *capzb*$^{+/-}$ embryos, 550 genes were downregulated and 389 genes were upregulated.

By 72 hpf, the differential expression pattern shifted. In *capzb*$^{-/-}$ embryos, 299 genes were downregulated and 731 genes were upregulated. In contrast, *capzb*$^{+/-}$ embryos exhibited differential expression with 294 genes downregulated and 304 genes upregulated. In Figure 4.43, a volcano plot was utilized to visually represent the association between statistical significance and the magnitude of gene expression alterations at 48 and 72 hpf in *capzb*$^{-/-}$ embryos. The X-axis denotes the $\log_2$ fold change (FC) in gene expression between conditions. Genes exhibiting increased expression in *capzb*$^{-/-}$ compared to

another condition are positioned on the right side, whereas those with decreased expression are positioned on the left side. The Y-axis illustrates the statistical significance of the observed changes, depicted as -$\log_{10}$ (p-value). Genes with greater statistical significance (lower p-values) are positioned towards the top of the plot. Each gene was depicted as a point on the plot, and its position was determined by both its fold change and statistical significance. Genes with higher fold changes and greater statistical significance were positioned farther away from the center of the plot, reflecting their increased importance in the analysis.

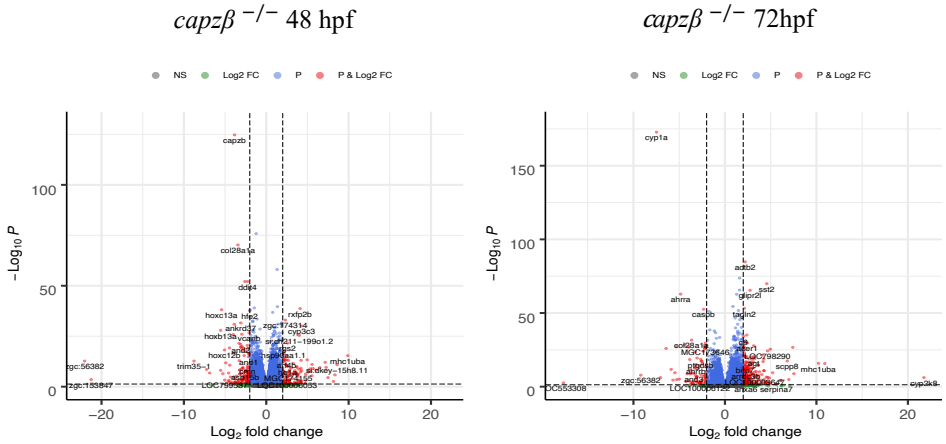

Figure 4.43: *Visualization of RNA-seq data depicting differentially expressed genes in capzb$^{-/-}$ embryos at 48 and 72 hpf. Genes with a p-value of 0.05 and a fold change of* $\log_2$ *1 were included. In the plot, red dots on the left indicate down-regulated gene expression, red dots on the right indicate up-regulated gene expression, and blue dots represent gene expression without marked differences.*

In Figure 4.44, a volcano plot was utilized to visually illustrate the relationship between statistical significance and the magnitude of gene expression variations at 48 and 72 hpf in *capzb*$^{+/-}$ embryos. The X-axis represents the $\log_2$ fold change in gene expression between conditions, positioning genes with increased expression in *capzb*$^{+/-}$ to the right and those with decreased expression to the left.

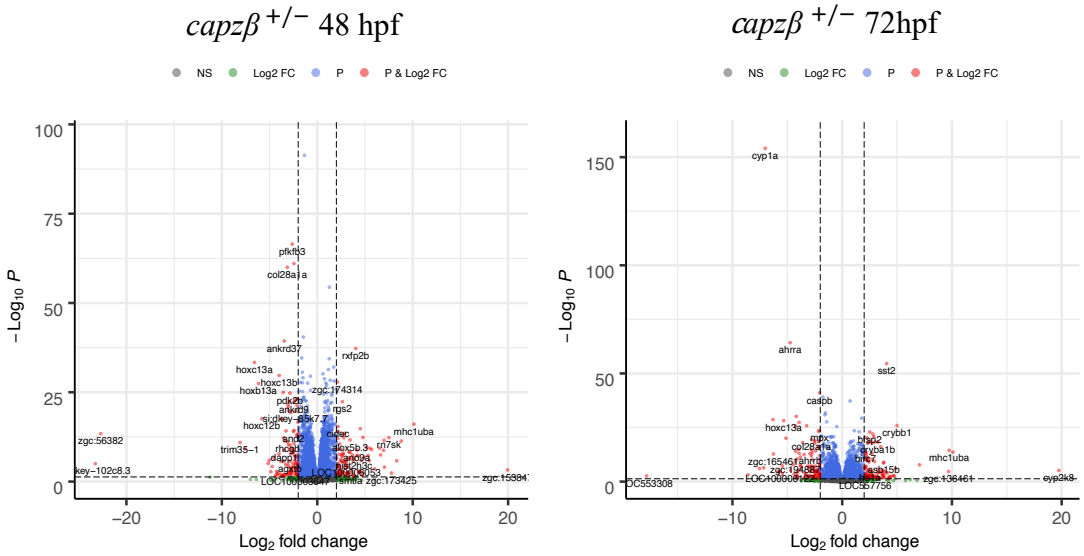

Figure 4.44: *Visualization of RNA-seq data depicting differentially expressed genes in capzb$^{+/-}$ embryos at 48 and 72 hours post-fertilization (hpf) was conducted. Genes with a p-value of 0.05 and a fold change of* $\log_2$ *5 were included. In the plot, red dots on the left indicate down-regulated gene expression, red dots on the right indicate up-regulated gene expression, and blue dots represent gene expression without marked differences.*

Gene ontology analysis reveals functional roles of differentially expressed genes in *capzb*$^{-/-}$ and *capzb*$^{+/-}$ embryos

Gene Ontology (GO) analysis was performed to elucidate the biological processes associated with the differentially expressed genes identified from RNA-seq data comparing *capzb*$^{-/-}$ and *capzb*$^{+/-}$ embryos. GO analysis categorizes genes into biological process, molecular function, and cellular component based on structured ontological classifications, with a focus on biological processes in this study.

The differentially expressed genes in *capzb*$^{-/-}$ and *capzb*$^{+/-}$ embryos at 48 and 72 hpf were subjected to GO analysis using Enrichr to identify enriched GO terms for downregulation and upregulation. This analysis compared the gene list against a background set (control) to determine statistically significant enrichment of GO terms. As illustrated in figure 4.45, the GO analysis of downregulated genes in *capzb*$^{-/-}$ embryos at 48 hpf revealed

significant enrichment of several biological processes. Notably, terms associated with extracellular matrix organization (GO:0030198) and notochord morphogenesis (GO:0048570) emerged as top enriched categories. Additionally, terms such as response to light stimulus (GO:0009416), cellular response to radiation (GO:0071478), skeletal system development (GO:0001501), and cellular response to light stimulus (GO:0071482) were also identified as significantly associated with the downregulated genes. Interestingly, no significant enrichment was observed among the upregulated genes in *capzb*$^{-/-}$ at 48 hpf. At 72 hpf, the GO analysis of downregulated genes in *capzb*$^{-/-}$ embryos unveiled substantial enrichment in the biological process of oxidoreductase activity, specifically encompassing the incorporation of molecular oxygen and two atoms of oxygen (GO:0016702). Conversely, upregulated genes in *capzb*$^{-/-}$ embryos exhibited significant enrichment in the inactivation of MAPK activity (GO:0000188), as depicted in figure 4.45.

In the case of *capzb*$^{+/-}$ at 48 hpf, the GO analysis of downregulated genes revealed significant enrichment of extracellular matrix organization (GO:0030198), similar to *capzb*$^{-/-}$. Conversely, upregulated genes in *capzb*$^{+/-}$ embryos exhibited significant enrichment in the regulation of JAK-STAT cascade (GO:0046425), drug catabolic process (GO:0042737), exogenous drug catabolic process (GO:0042738), and nucleosome assembly (GO:0006334 (Figure 4.45). Furthermore, at 72 hpf, as depicted in figure 4.45, the GO analysis of downregulated genes in *capzb*$^{+/-}$ revealed substantial enrichment in the biological process of cellular response to xenobiotic stimulus (GO:0071466). Conversely, upregulated genes in *capzb*$^{+/-}$ embryos exhibited significant enrichment in proteolysis (GO:0006508) and drug catabolic process (GO:0042737).

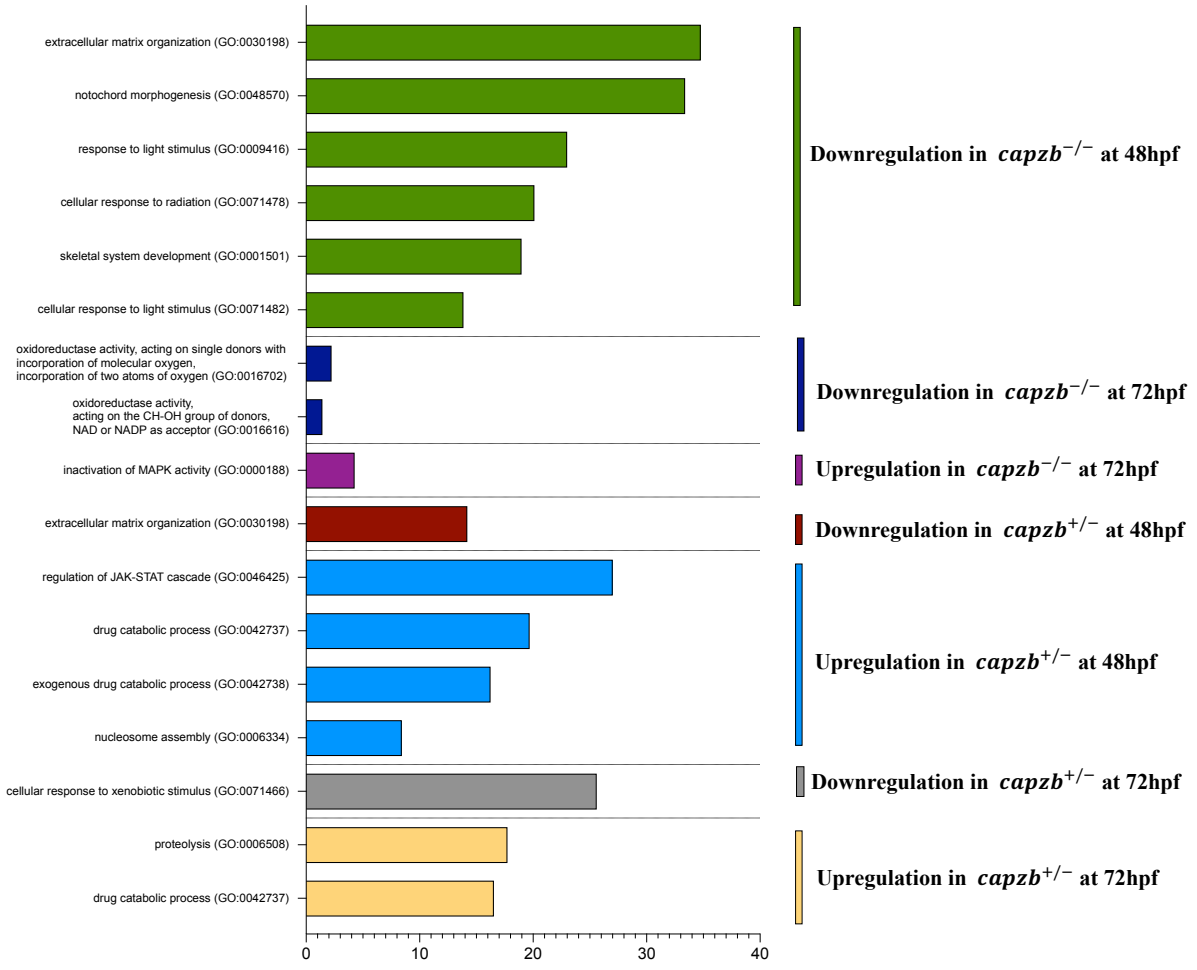

Figure 4.45: *Gene Ontology Analysis of Differentially Expressed Genes. The GO analysis depicts the enrichment of biological processes associated with downregulated and upregulated genes in capzb$^{-/-}$ and capzb$^{+/-}$ embryos at 48 hpf and 72 hpf. At 48 hpf, downregulated genes in capzb$^{-/-}$ embryos are enriched in extracellular matrix organization and notochord morphogenesis, while upregulated genes show significant enrichment in several processes, which are presented in dark green. No significant enrichment is observed among upregulated genes. At 72 hpf, downregulated genes in capzb$^{-/-}$ embryos are enriched in oxidoreductase activity (depicted in dark blue), whereas upregulated genes show enrichment in MAPK activity inactivation (depicted in purple). In capzb$^{+/-}$ embryos, downregulated genes at 48 hpf are enriched in extracellular matrix organization, while upregulated genes exhibit enrichment in the regulation of JAK-STAT cascade, drug catabolic processes, exogenous drug catabolic processes, and nucleosome assembly (depicted in light blue). At 72 hpf, downregulated genes in capzb$^{+/-}$ embryos are enriched in cellular response to xenobiotic stimulus (depicted in gray), while upregulated genes show enrichment in proteolysis and drug catabolic processes (depicted in yellow).*

Chapter 5

Discussion

The zebrafish has emerged as a prominent organism for investigating human diseases such as cancer, hematopoietic disorders, and cardiovascular disease [199, 200]. The transparency of the embryos and the capacity for efficient genetic manipulations, including gene downregulation and overexpression, have made zebrafish a widely adopted model for in-depth explorations of vertebrate gene function [163, 201]. Moreover, zebrafish are increasingly utilized in modeling human genetic diseases [200]. To enhance the modeling of human genetic diseases, it is imperative to ascertain the extent of similarity between zebrafish genes and their orthologous counterparts in humans. This understanding not only facilitates the generation of accurate disease models, but also holds potential implications for the identification of therapeutic strategies. Zebrafish are particularly valuable for studying both acquired and congenital heart diseases. Furthermore, the development of genomic technologies, such as ES, has greatly improved our capacity to explore the etiology, underlying mechanisms, potential treatments, and prognostic outcomes of a wide range of diseases. By utilizing from ES data and CGH, two genes that are subject of this study, *CAPZβ* and *PRDM16*, were identified.

Experimental evidence has highlighted the crucial role of *PRDM16* in the determination of brown adipose tissue [147], hematopoietic processes [202], and cardiac development, thus underscoring its significant contributions to developmental processes across diverse tissues. Animal models, particularly murine models with targeted *Prdm16* knockdown, have exhibited phenotypes associated with cardiomyopathy and cardiac conduction abnormalities

[151]. In parallel, zebrafish models with *PRDM16* knockdown, as well as those expressing a human truncation of *PRDM16*, have demonstrated a spectrum of physiological and morphological cardiac anomalies [139]. Additionally, these models have revealed metabolic alterations and an escalated oxidative stress response during cardiac development [139]. Causal variants in or showing a deletion of the gene *PRDM16* have been implicated in various non-syndromic human myocardial disorders, including LVNC and DCM [191], as well as in individuals diagnosed with 1p36 deletion syndrome [139]. This study aimed to generate disease models of *PRDM16* variants in zebrafish to assess the effects of four novel missense variants found in patients with ARVC. Given *PRDM16's* role in determining muscle and brown fat cell fate [147], these models will enable the investigation of its impact on cardiac function.

Among the four *CAPZβ* variants identified in patients with CHD, all were present in the gnomAD database at very low frequencies, indicating their rarity in the general population. Notably, no individuals were homozygous for any of these variants in gnomAD, reinforcing the likelihood that these variants are deleterious. One variant, p.Thr179Ser, was identified as a *de novo* mutation, while the inheritance status of the remaining variants is unclear due to the unavailability of parental samples. Despite their presence in gnomAD, the rarity and absence of homozygosity suggest that these variants may have pathogenic potential, particularly in the context of CHD. The observed number of missense variants in *CAPZβ* (117) is significantly lower than expected (250.9), with a Z score of 3.09. This indicates that *CAPZβ* is intolerant to missense variation, supporting the idea that these rare variants could have functional consequences. Furthermore, the pLI index for loss-of-function (LoF) mutations is 1.0, signifying that LOF variants in *CAPZβ* are highly deleterious and likely result in non-viability, underscoring the essential role of *CAPZβ* in cellular function.

Given the predominance of missense variants, it is plausible that these mutations exert a dominant negative effect, particularly because CAPZβ forms a dimer with CAPZα, crucial for capping actin filaments at the Z-disk of the sarcomere [203–205]. Alterations in the β-subunit's structure due to missense variants may disrupt dimerization and impair protein function. To explore this hypothesis, we conducted overexpression studies of the human variants in a transgenic zebrafish model specifically targeting cardiomyocytes, aiming to evaluate their potential dominant negative effect. In conclusion, while these missense variants are present in gnomAD, their low frequency, absence of homozygosity, and potential dominant-negative effects strongly suggest a role in the pathogenesis of CHD. These findings underscore the importance of detailed genetic and functional analyses to

fully understand the impact of rare *CAPZβ* variants on heart development and disease.

Missense variants in the same gene can lead to diverse disease phenotypes due to different underlying mechanisms, primarily haploinsufficiency and dominant negative effects. These mechanisms determine how the altered gene product interacts with cellular structures and functions, often resulting in distinct pathological outcomes. The *LMNA* gene, encoding lamin A/C, provides a compelling example of how different missense variants can cause distinct diseases through these mechanisms. For instance, in a mouse model *(LmnaΔK32/+)*, the cardiac-specific phenotype is attributed to haploinsufficiency. In this case, the degradation of the mutant lamin A/C protein via the ubiquitin-proteasome system leads to insufficient lamin A/C levels, adversely affecting cardiac function [206]. Conversely, the p.R482W mutation, where arginine is replaced by tryptophan at position 482, is associated with familial partial lipodystrophy (FPLD). The mutant lamin A/C protein disrupts the nuclear envelope structure and function even in the presence of the normal protein, exemplifying a dominant negative effect. This disruption leads to the clinical manifestations of FPLD [207]. These examples from the *LMNA* gene illustrate how missense variants can lead to diverse phenotypes through different mechanisms, highlighting the importance of understanding specific molecular pathologies for tailored therapeutic approaches [208]. Similarly, in the case of *CAPZβ*, different missense variants might also lead to diverse phenotypes through mechanisms such as haploinsufficiency or dominant negative effects. For example, a loss-of-function mutation in *CAPZβ* could result in insufficient CAPZβ protein levels, leading to abnormalities in cellular structures and functions, similar to the haploinsufficiency observed in *(LmnaΔK32/+)* mice. On the other hand, certain missense variants in *CAPZβ* might produce a mutant protein that interferes with the function of the normal protein, thereby exerting a dominant negative effect, as seen with the p.R482W mutation in *LMNA*.

These hypothetical scenarios for *CAPZβ* variants underscore the potential for different pathogenic mechanisms to produce distinct phenotypes, likely indicating a dominant-negative effect. This is supported by the detection of a protein product, which would not be expected in the case of LoF or haploinsufficiency. Consequently, it emphasizes the need for detailed molecular and functional analyses to understand the specific consequences of each variant. My findings presented in this study suggest that the absence of *CAPZβ* leads to physiological and morphological abnormalities during cardiogenesis. However, whether *CAPZβ* variants induce pathogenic mechanisms by dominant negative effects or by haploinsufficiency still need to be determined. Nevertheless, my data demonstrate that

the identified *CAPZβ* variants in patients are of functional significance.

Varied response in cardiac morphology and output in *PRDM16* variants models

Arrhythmogenic right ventricular dysplasia/cardiomyopathy (ARVD/C) is characterized by malignant ventricular arrhythmias and the presence of fibrofatty infiltration, with a higher occurrence in the right ventricle [209]. Animal models, including mice and zebrafish, offer the advantage of standardized and controlled conditions, facilitating the elucidation of gene mutations roles in ARVC while mitigating confounding variables like environmental factors and genetic background [209]. Studies have demonstrated correlations between Prdm16 and QRS duration as well as cardiomyopathy phenotypes in murine models [151]. Causal variants in *Prdm16* disrupt ion homeostasis, notably affecting calcium (Ca^{2+}), potassium (K^{+}), and sodium (Na^{+}) ions [151].

Zebrafish, with cardiac electrophysiology similar to humans and an average heart rate of $\sim$ 100 bpm [209], represent a valuable model for investigating ARVC. In a study by *Asimaki et al.*, a zebrafish ARVC model was created using the GAL4/UAS transactivation system, resulting in a cardiac-specific transgenic zebrafish line overexpressing the human 2057del2 mutation in junction Plakoglobin, *JUP*. These transgenic zebrafish exhibited mild bradycardia, decreased stroke volume, and reduced cardiac output within 2 days post-fertilization, with cardiomyopathy fully manifesting at 4–6 weeks, characterized by cardiomegaly, cachexia, and peripheral edema [210]. Furthermore, in a zebrafish knockdown model for *PRDM16* achieved through translation-blocking morpholinos, and in transgenic zebrafish models harboring the human *PRDM16* nonsense mutation (c.2104A>T [p.Lys702*]) in the heart expressed under the *myl7* promoter, a marked decrease in cardiac output and heart rate was observed compared to control groups [139].

In this study, both the PRDM16-A259V and PRDM16-P889L variants at 48 hpf exhibited a noticeable decrease in ventricle size and cardiac output. This observation coincides with critical stages of heart development in wildtype embryos, where heart looping, ventricle formation and AV valve formation typically occur at around 30 hpf, 36 hpf, and 48 hpf, respectively [169]. The observed reductions in ventricle size and cardiac output at 48 hpf indicate potential impairment of critical developmental processes mediated by *PRDM16*.

At 72 hpf, both PRDM16 WT and PRDM16-P889L exhibited a significant increase in heart rate. As mentioned earlier, ventricular arrhythmias are a symptom of ARVC. An elevated heart rate can impede the complete filling of the heart chambers between contractions, potentially compromising blood flow throughout the body [211]. Moreover, the correlation between *PRDM16* variants and increased heart rate underscores the involvement of *PRDM16* in regulating cardiac rhythm, potentially contributing to the development of ARVC.

These findings deepen our understanding of the molecular mechanisms underlying ARVC and highlight *PRDM16* as a potential therapeutic target for addressing this cardiac disorder.

Effect of *PRDM16* variants on cell proliferation

Cell proliferation, quiescence, and differentiation are crucial processes for organismal growth and tissue homeostasis [212]. Perturbations in these mechanisms are implicated in various diseases, including cardiomyopathy. *PRDM16* functions as a transcription factor, characterized by zinc finger DNA-binding domains and distinct positive regulatory (PR), repressor, and acidic domains. Its regulatory activities extend across various biological processes, including leukemogenesis, palatogenesis, neurogenesis, and brown fat development [144, 148]. Chromosomal translocations leading to upregulated expression of *PRDM16* isoforms lacking the PR domain are frequently observed in myelodysplastic syndrome and acute myeloid leukemias [213]. *PRDM16* plays a pivotal role in orchestrating brown fat determination and differentiation [147] by forming a transcriptional complex with the active form of C/EBP-β. This complex serves as a critical regulator in directing the cell fate switch from myoblastic precursors to brown fat cells [147].

PRDM16 is implicated in regulating transforming growth factor (TGF)-β signaling. Studies have shown that *PRDM16* exerts a negative effect on TGF-β signaling *in vitro* [214]. Dysregulated levels of TGF-β signaling activity, influenced by *PRDM16*, could disrupt the delicate balance between cell proliferation and differentiation *in vivo* [214].

Variants in the *PRDM16* gene have the potential to perturb its normal regulatory role, thereby inducing modifications in the cell cycle dynamics and consequent reduction in

the proliferation of cardiac cells [139]. In this study, two specific *PRDM16* variants, PRDM16-D628N and P889L, were identified to reduce the overall number of cardiac cells. In my investigation, it was observed that cells with mutated *PRDM16*, specifically the P889L and S1059L variants, were unable to sustain the normal proliferation rate observed in this developmental phase. In the atria, where the proliferation rate is generally low [215], an exception is observed in the case of *Tg(myl7:GFP; myl7:PRDM16-D628N)*, where a higher number of proliferative cells is present in the atrium at 96 hpf. This decrease in cell number appears to result from reduced proliferation, potentially influenced by alterations in TGF-β signaling or interactions with C/EBP-β [148].

The overexpression *PRDM16* variants and *PRDM16 WT* does not influence cell death

Inhibition of *PRDM16* has been shown to reduce cell viability of DU145, a human prostate cancer cell line, primarily due to an elevation in the apoptotic rate [216]. In mouse models, deletion of Prdm16 leads to mitochondrial defects and increased apoptosis, with notable effects observed particularly at the 12-month time point [217]. However, this study demonstrated that neither the overexpression of *PRDM16* in cardiomyocytes nor the ARVC variants of *PRDM16* had a significant impact on cell death at various time points. These findings suggest that *PRDM16's* regulatory influence on pathways related to cell survival may not extend to direct modulation of apoptotic pathways in the specific context of this study. Additionally, the chosen time points for observation may not adequately capture potential delayed or gradual effects of *PRDM16* overexpression on cell death. Since ARVC symptoms typically appear in adulthood, it is plausible that apoptotic cells may manifest in adult zebrafish. Therefore, future studies should consider examining apoptosis at later stages of zebrafish development to comprehensively assess the impact of *PRDM16* variants on cell death.

Effect of overexpression *PRDM16* variants and *PRDM16* WT on gap junctional protein Connexin43

ARVC is attributed to mutations in genes responsible for encoding proteins within the desmosome, a specialized intercellular-junction complex [107]. The desmosomes are integral

components located within the intercalated disc, alongside fascia adherens junctions and gap junctions [218]. These structures serve to connect cardiac myocytes, facilitating the synchronization of mechanical and electrical functions in the heart [210]. In patients with ARVC and experimental disease models, aberrations in the localization of intercalated disc proteins have been noted. This includes the junction plakoglobin (γ-catenin), the gap junction protein connexin 43, and the sodium channel protein Nav1.5. Such observations highlight the significance of proper intercalated disc protein and composition in maintaining cardiac function and underscore the role of desmosomal mutations in ACM pathogenesis. [219–223]. In the context of the *PRDM16* ARVC variants, the expression level of connexin 43 remains statistically unchanged. However, a mild reduction was observed in PRDM16 K702*. Further research is necessary to explore regional differences in connexin 43 expression, particularly distinguishing between membrane-localized and cytoplasmic Cx43. The unaffected level of connexin 43 in the presence of the identified *PRDM16* ARVC variant may be influenced by various factors, with the specific mechanism dependent on the molecular and cellular context. Furthermore, it is possible that the *PRDM16* ARVC variant does not directly impact the synthesis, stability, or degradation of connexin 43.

Mitochondria number is not affected in the PRDM16 variants models

The necessity for chemical energy in the form of ATP to support both systolic and diastolic functions of the heart is imperative [224]. Mitochondria, recognized as the powerhouse of the cell, play a pivotal role in active tissues like the heart, where they are chiefly responsible for generating the majority of ATP [225]. Mitochondrial dysfunction is linked to anomalies in electron transport chain activity, diminished ATP production, abnormal shifts in metabolic substrates, excessive ROS production, and impaired mitochondrial dynamics [226]. The investigation of animal models, such as mice, has demonstrated that *Prdm16* deficiency induces alterations in reactive oxygen species levels, heightened cell death, perturbed cell cycle distribution, and stem cell depletion within the hematopoietic and nervous systems [227]. In zebrafish, the preliminary data suggest a reduced number of mitochondria and an enrichment of glycogen granules in the adult PRDM16 truncation model (K702*). In contrast, in embryonic hearts at 48 hpf, there were no significant alterations observed in mitochondrial quantity in the overexpression of PRDM16 WT, the identified *PRDM16* ARVC variants, or the truncation model (K702*). Considering the potential delayed onset of ARVC and the average age of symptom manifestation at the age

of 29 in human [106], it is pertinent to evaluate mitochondrial number in the adult heart of the ARVC model. Regarding the truncation model (K702*), discrepancies between the preliminary data and this thesis may arise from the utilization of different methodologies. The preliminary data analysis was conducted using immunofluorescence, while in this study, fluorescence-activated cell sorting (FACS) was employed.

The P889L variant and the truncation model (K702*) exhibit a reduction in superoxide levels while ROS level is unaffected

The observed reduction in superoxide levels in the PRDM16-P889L variant and the truncation model (K702*) compared to wild type suggests variant-specific influences on superoxide regulation, underscoring the necessity of discerning which variant is truly disease-causing. Possible explanations include variant-specific functions, altered mitochondrial function affecting superoxide generation, differential handling of ROS, modulation of redox signaling pathways, regulation of superoxide-related genes, and context-dependent effects. Elucidating these mechanisms requires in-depth molecular studies involving investigation into mitochondrial function, antioxidant pathways, and gene expression related to superoxide regulation. One approach to comprehensively assess the impact of *PRDM16* variants on mitochondrial function is by conducting a Seahorse assay on adult zebrafish hearts. This assay allows for the real-time measurement of oxygen consumption rate (OCR) and extracellular acidification rate (ECAR), providing insights into mitochondrial respiration and glycolysis, respectively. In contrast to superoxide levels, the ROS level remains unaffected in the identified *PRDM16* variants. Given that ARVC typically manifests symptoms around the age of 29 in humans, it is plausible that the effects of the variants may not be immediately evident and could potentially emerge later in life.

The D628N variant and S1059L variant demonstrate the presence of adipocytes

The prevalence of ARVC/D in the general population ranges from 1 in 2,500 to 1 in 5,000 [228]. Microscopic examination of the right ventricle in human ARVC patients reveals several changes, with the dominant feature being the presence of fibrofatty or fat replacement within the myocardial muscle [107]. Wnt/β-catenin signaling disruption is a key factor in the adipogenesis and fibrosis observed in desmosomal Arrhythmogenic

Cardiomyopathy [229–231]. In a mouse model expressing the TMEM43 p.S358L mutant linked to ACM, sustained activation of GSK3β, a downstream regulator of Wnt/β-catenin, triggers cardiomyocyte death and fibrofatty tissue replacement [232]. In a zebrafish model of *Dsp*-deficiency-induced ARVC, Wnt/β-catenin, TGF-β, and Hippo/YAP pathways are significantly affected [229]. Notably, Wnt/β-catenin signaling is proposed as the final common pathway in desmosomal gene mutation-based ARVC, supported by genetic and pharmacological studies [229]. Zebrafish models, although successful in replicating key clinical features of ARVC, including ventricular arrhythmia, myocardial chamber dilation, and sudden cardiac death [233]), exhibit a notable limitation. Unlike human ARVC, the replacement of myocardium with fibrofatty tissue, a characteristic hallmark of the disease, is only infrequently observed in both zebrafish and mouse models [209]. Lipid accumulation, though sporadically observed, remains a notable feature in specific zebrafish models, such as those overexpressing the *ILK* H77Y and P70L variants [234], as well as in the *PLN* R14del KI zebrafish model [235]. This observation further emphasizes the challenge in recapitulating the full spectrum of pathological features seen in human ARVC within zebrafish models. In consideration of the propensity of ARVC to manifest in adult patients [106], our investigation focused on adult zebrafish hearts across various models to scrutinize the presence of lipid droplets deposition in cardiac tissues. Notably, both transgenic lines, *Tg(myl7:PRDM16 D628N)* and *Tg(myl7:PRDM16 S1059L)*, displayed the occurrence of lipid droplets. As controls, a wildtype fish and the overexpression of *PRDM16* were employed, implying that variants might contribute to the observed presence of lipid droplets. Further investigations are warranted to elucidate the specific mechanisms by which specifically these *PRDM16* variants contribute to lipid droplets presence in the context of ARVC. Exploring the molecular pathways and interactions involved in adipogenesis within the cardiac tissues of zebrafish models could provide valuable insights into the pathogenesis of ARVC and potentially uncover novel therapeutic targets. Additionally, comparative studies with other established models and clinical data may offer a broader understanding of the role of *PRDM16* in adipocyte deposition, enhancing our knowledge of ARVC pathology.

PRDM16 variants affect heart's regenerative capacity

In contrast to human, zebrafish exhibits an extraordinary capacity to regenerate their hearts following ventricular injury or amputation [180], therefore, it is an excellent model

to study regeneration of the heart. Since PRDM16 might be a crucial factor during heart development, it might play an important role in remodeling and regeneration. To comprehensively explore the specific role of *PRDM16* on zebrafish heart regeneration, a regeneration model was developed, incorporating transgenic lines featuring *PRDM16* wildtype and the *PRDM16* truncation mutation (K702*). An effect on the proliferative capacity of cardiomyocytes during development at 48 hpf has already been demonstrated in the truncation model (K702*) [139]. Detailed examinations were conducted at 1, 3, and 5 dpa to elucidate the temporal dynamics and functional contributions of *PRDM16* in the context of cardiac tissue regeneration. The Masson-Goldner staining images at 1 dpa reveal the formation of a blood clot, serving as a wound seal, which is later replaced by fibrin and collagen at the injured area. This observed process is consistent across the control group, as well as in the hearts of both the *PRDM16* wildtype and *PRDM16* truncated variant. Numerous studies suggest that a few hours after injury, Fibroblast Growth Factors (FGFs) stimulate the activation of epicardial cells. These activated epicardial cells undergoing Epithelial-to-Mesenchymal Transition (EMT) exhibit the capability to proliferate and migrate toward the injury site [236–238]. At 3 dpa, the control group and *PRDM16* wildtype zebrafish exhibit the removal of the blood clot, whereas the blood clot persists in the *PRDM16* truncated variant. Given the known involvement of *PRDM16* in TGF-β signaling and the inability of the truncated variant to produce the full-length PRDM16 protein, it is postulated that the disruption in TGF-β signaling may be a consequence of the truncated variant's inability to generate the complete PRDM16 protein. This disruption could potentially result in an impaired wound healing response. Experimental validation, including gene expression analysis, functional assays pertaining to TGF-β signaling, and in-depth examination of wound healing processes, is necessary to substantiate this hypothesis. Furthermore, previous studies have underscored the significance of TGFβ/Activin-B signaling in the regeneration of both the heart and fin [239]. These studies have identified elevated expression of TGFβ/Activin-B ligands in wounded tissues of the heart and fin, emphasizing the essential role of this pathway in the process of organ restoration [240, 241]. Various immunostaining techniques, including H&E, Masson-Goldner, and PCNA, indicate an interruption in heart regeneration in the *PRDM16* truncated variant. Co-staining with cell specific markers, like Mef2c cardiomyocyte marker, is necessary to identify cell types undergoing proliferation. The confirmation of my hypothesis through the quantification of sarcomere length and measurement of the injured area after 5 dpa provides a solid foundation for continued research into the underlying mechanisms and potential therapeutic interventions. These findings highlight a potential impairment in proliferation associated with the truncated variant, suggesting a deficiency in myocardial regenerative capacity.

This underscores the importance of further investigation into the underlying mechanisms governing cell proliferation and regeneration in this context, offering valuable insights for the development of novel therapeutic strategies aimed at promoting heart repair and regeneration.

Overexpression of *PRDM16* and its truncated variant causes cardiac hypertrophy

Recognized for their crucial role in promoting cardiomyocyte proliferation within the compact myocardium, *Hey2* [242] and *Mycn* [243] have been identified as direct targets of *PRDM16* through insights from prior studies [191]. The specific reduction in the expression of *Hey2* and *Mycn* in the left ventricle and interventricular septum of $Prdm16^{cKO}$ mice underscores the spatially restricted impact of *PRDM16* on these target genes, influencing cardiomyocyte proliferation in specific regions of the heart [191]. In this study, both the overexpression of *PRDM16* and the truncated variant (K702*) were observed to lead to an increase in the thickness of the compact myocardium, indicative of hypertrophic response. The possible reason for cardiac hypertrophy observed in our study could be linked to mitochondrial dysfunction. Similar hypertrophy, adverse remodeling, and mitochondrial dysfunction were also observed in a mice study involving conditional knockout $Prdm16^{cKO}$ mice [217]. To gain a better understanding of the role of *PRDM16* in mitochondrial bioenergetics, it is essential to conduct experiments using an extracellular flux analyzer, such as a Seahorse analyzer.

The overexpression of *CAPZβ WT* and *CAPZβ* variants in cardiomyocytes affects cardiac morphology and cardiac output

CAPZβ functions as an actin-capping protein, responsible for capping the growing end of F-actin. It plays a pivotal role in modulating the cytoskeleton and in tethering actin filaments to the Z-line of the sarcomere in muscles [162]. The loss of *capzb* in a zebrafish model resulted in critical defects in cell morphology, differentiation, and neural crest migration, highlighting its essential role during zebrafish embryogenesis [162]. As an actin capping protein, *CAPZβ* may also contribute to embryonic heart development. Preliminary data indicate a noteworthy reduction in cardiac output in $capzb^{-/-}$. Furthermore, aside

from frequent pericardial edema, there was observable impairment in the looping of the heart. The normal looping process typically initiates around 30 hpf and is completed in wildtype controls between 48 hpf, as documented in the literature [169]. To evaluate the influence of overexpressing *CAPZβ* variants, including *CAPZβ WT* and identified *CAPZβ* variants, on embryonic heart development, zebrafish was employed as a model organism. Until 48 hpf, the different genotypes could hardly be distinguished based solely on phenotypic characteristics.

A noticeable reduction in stroke volume was observed at 72 hpf in *Tg(myl7:GFP;myl CAPZβ Ser192Asn)*. Additionally, at 72 hpf, two transgenic lines, namely *Tg(myl7:GFP;myl CAPZβ Thr179Ser)* and *Tg(myl7:GFP; myl:CAPZβ Ser192Asn)*, displayed a significant reduction in cardiac output. Interestingly, these two variants were identified in patients with CHDs. The patient carrying the p.Thr179Ser variant presented with hypoplastic left heart syndrome, whereas the patient with the p.Ser192Asn variant exhibited pulmonary atresia with a ventricular septal defect. Given that patients with pulmonary atresia with a ventricular septal defect as well as hypoplastic left heart syndrome typically manifest reduced systemic cardiac output [244, 245], it is plausible that the identified variants, Thr179Ser and Ser192Asn, may contribute to the observed phenotypes in these cases.

The sarcomeric structure in cardiac muscle is affected by the CAPZβ Ser192Asn variant

CAPZβ plays a crucial role in muscle cells and their functional units, the sarcomeres [204, 205]. Collaborating with its subunit, CAPZα, it facilitates the connection of actin filaments to the Z-disc, thereby contributing to the structural organization of the myofibrils [246–248]. This order governs the direction of contraction in cells, ensuring effective control over the contraction process [249]. Moreover, CAP proteins associated with actin play a vital role in regulating processes such as filament formation, stability maintenance, and dynamic interactions within the cellular environment [250]. The elongation in sarcomere length and the disorganized sarcomeric structure observed in CAPZβ Ser192Asn strongly suggest a potential reduction in contraction power. This structural alteration may impair the coordinated contraction of cardiac muscle fibers, potentially leading to compromised cardiac function, as evidenced by the observed reduction in cardiac output in this variant. Further investigation into the functional consequences of these structural changes is crucial

for understanding the pathological mechanisms underlying cardiac dysfunction associated with the CAPZβ Ser192Asn variant. Furthermore, small-sized mitochondria were also observed in CAPZβ Ser192Asn. Generally, *CAPZβ* variants exhibit differences in the shape, size, and number of mitochondria. It is well-established that mitochondria in cardiomyocytes occupy approximately one-third of the cell volume, underscoring the substantial energy demands inherent to these cells [226]. Additionally, mitochondria play crucial roles in regulating redox status, calcium homeostasis, and lipid synthesis. Consequently, it is not surprising that mitochondrial dysfunction has been robustly associated with the development of cardiomyopathy and an elevated risk of heart failure [225]. It is advisable to conduct a comprehensive mitochondrial count and quantification through techniques such as FACS or immunohistochemistry on the *CAPZβ* variants as well as *CAPZβ WT*. This analysis is warranted considering that TEM images may not provide a thorough evaluation.

The loss of *capzb*$^{-/-}$ has profound effects on heart development

The *CAPZβ* gene is known to play a crucial role in actin dynamics and cytoskeletal organization [156], and its disruption has been implicated in various developmental abnormalities [162]. At 48 hpf in *capzb*$^{-/-}$ embryos, the differential expression analysis revealed a higher number of downregulated genes (605) compared to upregulated genes (378). This suggests that the loss of the *capzb* gene may primarily lead to a decrease in the expression of protein-coding genes at this developmental stage. Heterozygous *capzb*$^{+/-}$ embryos exhibited a similar pattern, with more downregulated genes (550) than upregulated genes (389). This indicates that even heterozygous knockout of the capzb gene can significantly impact gene expression at 48 hpf. Analysis at 72 hpf showed a shift in the differential expression pattern compared to 48 hpf. In *capzb*$^{-/-}$ embryos, there was a notable increase in the number of upregulated genes (731) and a decrease in the number of downregulated genes (299). This suggests a dynamic regulation of gene expression in response to the loss of the *capzb* gene over time. Similarly, *capzb*$^{+/-}$ embryos also exhibited changes in gene expression, with a comparable number of downregulated genes (294) and upregulated genes (304). This indicates that even heterozygous knockout of the *capzb* gene continues to influence gene expression patterns at 72 hpf. The observed changes could also be attributed to a switch in gene expression between 48 and 72 hpf [251], reflecting temporal regulation of gene expression in the developing embryos.

The GO analysis of differentially expressed genes in *capzb*$^{-/-}$ and *capzb*$^{+/-}$ embryos at 48 hpf and 72 hpf provides valuable insights into the molecular mechanisms underlying the phenotypic differences observed in these genetic backgrounds. At 48 hpf, downregulated genes in *capzb*$^{-/-}$ embryos are significantly enriched in biological processes associated with extracellular matrix organization and notochord morphogenesis. This enrichment suggests potential disruptions in the structural integrity [252, 253] and developmental patterning of tissues, which could contribute to the observed phenotypic abnormalities in *capzb*$^{-/-}$ embryos. Interestingly, upregulated genes show significant enrichment in various processes, indicating a complex transcriptional response to the loss of *capzb*. Further investigation is warranted to elucidate the specific regulatory pathways driving these transcriptional changes.

At 48 hpf in *capzb*$^{+/-}$ embryos, downregulated genes are also enriched in extracellular matrix organization, suggesting a shared molecular phenotype with *capzb*$^{-/-}$ embryos. However, the upregulated genes exhibit enrichment in distinct processes, including the regulation of JAK-STAT cascade, drug catabolic processes, exogenous drug catabolic processes, and nucleosome assembly. These findings suggest that *capzb*$^{+/-}$ embryos may undergo compensatory transcriptional changes to maintain cellular homeostasis in response to the heterozygous deletion of *capzb*. By 72 hpf, the transcriptional landscape undergoes further remodeling in both *capzb*$^{-/-}$ and *capzb*$^{+/-}$ embryos. In *capzb*$^{-/-}$ embryos, downregulated genes are enriched in oxidoreductase activity, potentially reflecting alterations in metabolic processes or cellular redox balance. Conversely, upregulated genes exhibit enrichment in the inactivation of MAPK activity, suggesting a regulatory response to perturbations in signaling pathways associated with cell proliferation and differentiation [254].

Similarly, in *capzb*$^{+/-}$ embryos at 72 hpf, downregulated genes are enriched in the cellular response to xenobiotic stimulus, indicating potential disruptions in cellular homeostasis or stress response mechanisms. Upregulated genes, on the other hand, show enrichment in proteolysis and drug catabolic processes, suggesting an adaptive cellular response to metabolic challenges or environmental cues. Overall, the GO analysis highlights the dynamic transcriptional changes occurring during embryonic development in *capzb*$^{-/-}$ and *capzb*$^{+/-}$ embryos. These findings provide a foundation for further investigation into the molecular pathways driving developmental defects and may inform potential therapeutic strategies for addressing congenital abnormalities associated with *capzb* deficiency.

This study highlights the efficiency of zebrafish as a model for testing genetic pathogenicity,

with embryos offering advantages in early-stage analysis and high-throughput screening, and adults providing insights into long-term and regenerative processes. The differential utility of zebrafish embryos and adults allowed for a comprehensive analysis of *CAPZβ* and *PRDM16* variants, providing a nuanced understanding of their roles in cardiovascular diseases. Additionally, it was shown that metabolic-like processes and chronic conditions such as fibrosis and lipid deposition are better modelled in adults, whereas embryos are more suitable for studying cellular processes relevant to CHD.

Future research should explore the complementary use of zebrafish embryos and adult fish to maximize the strengths of each model. Additional studies could investigate additional genetic variants using this dual approach to enhance our understanding of their pathogenicity and potential to inform therapeutic strategies for CHD and ARVC.

Bibliography

[1] Shumpei Mori, Justin T. Tretter, Diane E. Spicer, David L. Bolender, and Robert H. Anderson. What is the real cardiac anatomy? *Clinical Anatomy*, 32(3):288–309, 4 2019.

[2] Maria Jaworska-Wilczynska, Pawel Trzaskoma, Andrzej A. Szczepankiewicz, and Tomasz Hryniewiecki. Pericardium: structure and function in health and disease. *Folia Histochemica et Cytobiologica*, 54(3):121–125, 10 2016.

[3] Anton Hafferl. *Lehrbuch der Topographischen Anatomie*. springer, 2013.

[4] E Rene Rodriguez and Carmela D Tan. Structure and Anatomy of the Human Pericardium. *Progress in cardiovascular diseases*, 59(4):327–340, 2017.

[5] Dan B. Tran, Carly Weber, and Richard A. Lopez. *Anatomy, Thorax, Heart Muscles*. StatPearls Publishing, 2022.

[6] Bailey Dye and Joy Lincoln. The Endocardium and Heart Valves. *Cold Spring Harbor Perspectives in Biology*, 12(12):a036723, 12 2020.

[7] Andy Wessels and David Sedmera. Developmental anatomy of the heart: a tale of mice and man. *Physiological genomics*, 15(3):165–76, 11 2003.

[8] Robert B. Hinton and Katherine E. Yutzey. Heart Valve Structure and Function in Development and Disease. *Annual Review of Physiology*, 73(1):29–46, 3 2011.

[9] Martin Misfeld and Hans Hinrich Sievers. Heart valve macro- and microstruc-

ture. *Philosophical Transactions of the Royal Society B: Biological Sciences*, 362(1484):1421–1436, 2007.

[10] Phillip T. Crawford, Tafline C. Arbor, and Bruno Bordoni. *Anatomy, Thorax, Aortic Valve*. StatPearls Publishing, 2023.

[11] M. D. Arnold M. Katz. *Physiology of the Heart*. LWW, 2005.

[12] Lisa M. Miller and Arnon Gal. Cardiovascular System and Lymphatic Vessels. *Pathologic Basis of Veterinary Disease*, 2017.

[13] Marc Sylva, Maurice J.B. van den Hoff, and Antoon F.M. Moorman. Development of the human heart. *American Journal of Medical Genetics Part A*, 164(6):1347–1371, 6 2014.

[14] Richard P. Harvey. Patterning the vertebrate heart. *Nature Reviews Genetics*, 3(7):544–556, 7 2002.

[15] Antoon F.M Moorman, Vincent M Christoffels, Robert H Anderson, and Maurice J.B van den Hoff. The heart-forming fields: one or multiple? *Philosophical Transactions of the Royal Society B: Biological Sciences*, 362(1484):1257–1265, 8 2007.

[16] Laura A. Dyer and Margaret L. Kirby. The role of secondary heart field in cardiac development. *Developmental Biology*, 336(2):137–144, 12 2009.

[17] Aleksander Sizarov, Jing Ya, Bouke A. de Boer, Wouter H. Lamers, Vincent M. Christoffels, and Antoon F.M. Moorman. Formation of the Building Plan of the Human Heart. *Circulation*, 123(10):1125–1135, 3 2011.

[18] Giuliana Rossi, Nicolas Broguiere, Matthew Miyamoto, Andrea Boni, Romain Guiet, Mehmet Girgin, Robert G. Kelly, Chulan Kwon, and Matthias P. Lutolf. Capturing Cardiogenesis in Gastruloids. *Cell Stem Cell*, 28(2):230–240, 2 2021.

[19] Robert G. Kelly, Nigel A. Brown, and Margaret E. Buckingham. The Arterial Pole of the Mouse Heart Forms from Fgf10-Expressing Cells in Pharyngeal Mesoderm. *Developmental Cell*, 1(3):435–440, 9 2001.

[20] Margaret Buckingham, Sigolène Meilhac, and Stéphane Zaffran. Building the mammalian heart from two sources of myocardial cells. *Nature Reviews Genetics*, 6(11):826–835, 11 2005.

[21] Jörg Männer. Cardiac looping in the chick embryo: A morphological review with special reference to terminological and biomechanical aspects of the looping process. *The Anatomical Record*, 259(3):248–262, 7 2000.

[22] Vincent M. Christoffels, Petra E.M.H. Habets, Diego Franco, Marina Campione, Frits de Jong, Wouter H. Lamers, Zheng-Zheng Bao, Steve Palmer, Christine Biben, Richard P. Harvey, and Antoon F.M. Moorman. Chamber Formation and Morphogenesis in the Developing Mammalian Heart. *Developmental Biology*, 223(2):266–278, 7 2000.

[23] Cary Ward, Harriett Stadt, Mary Hutson, and Margaret L. Kirby. Ablation of the secondary heart field leads to tetralogy of Fallot and pulmonary atresia. *Developmental Biology*, 284(1):72–83, 8 2005.

[24] Steéphane Zaffran, Robert G. Kelly, Sigoleène M. Meilhac, Margaret E. Buckingham, and Nigel A. Brown. Right Ventricular Myocardium Derives From the Anterior Heart Field. *Circulation Research*, 95(3):261–268, 8 2004.

[25] Michael P. Verzi, David J. McCulley, Sarah De Val, Evdokia Dodou, and Brian L. Black. The right ventricle, outflow tract, and ventricular septum comprise a restricted expression domain within the secondary/anterior heart field. *Developmental Biology*, 287(1):134–145, 11 2005.

[26] Stephane D. Vincent and Margaret E. Buckingham. *How to Make a Heart*. Elsevier, 2010.

[27] Shigeru C. Kuratani and Margaret L. Kirby. Migration and distribution of circumpharyngeal crest cells in the chick embryo. *The Anatomical Record*, 234(2):263–280, 10 1992.

[28] Benoit G. Bruneau. Epigenetic Regulation of the Cardiovascular System. *Circulation Research*, 107(3):324–326, 8 2010.

[29] Robert M. Nerem, R. Wayne Alexander, David C. Chappell, Russel M. Medford, Signe E. Varner, and W. Robert Taylor. The Study of the Influence of Flow on Vascular Endothelial Biology. *The American Journal of the Medical Sciences*, 316(3):169–175, 9 1998.

[30] Masafumi Takahashi, Takafumi Ishida, Oren Traub, Marshall A. Coron, and Bradford C. Berk. Mechanotransduction in Endothelial Cells: Temporal Signaling Events in Response to Shear Stress. *Journal of Vascular Research*, 34(3):212–219, 1997.

[31] Mei Xin, Eric N. Olson, and Rhonda Bassel-Duby. Mending broken hearts: cardiac development as a basis for adult heart regeneration and repair. *Nature Reviews Molecular Cell Biology*, 14(8):529–541, 8 2013.

[32] Sarah U. Morton, Daniel Quiat, Jonathan G. Seidman, and Christine E. Seidman. Genomic frontiers in congenital heart disease. *Nature Reviews Cardiology*, 19(1):26–42, 1 2022.

[33] Mark D. Reller, Matthew J. Strickland, Tiffany Riehle-Colarusso, William T. Mahle, and Adolfo Correa. Prevalence of Congenital Heart Defects in Metropolitan Atlanta, 1998-2005. *The Journal of Pediatrics*, 153(6):807–813, 12 2008.

[34] Julien I.E Hoffman and Samuel Kaplan. The incidence of congenital heart disease. *Journal of the American College of Cardiology*, 39(12):1890–1900, 6 2002.

[35] Yingjuan Liu, Sen Chen, Liesl Zühlke, Graeme C Black, Mun-kit Choy, Ningxiu Li, and Bernard D Keavney. Global birth prevalence of congenital heart defects 1970–2017: updated systematic review and meta-analysis of 260 studies. *International Journal of Epidemiology*, 48(2):455–463, 4 2019.

[36] Gaetano Thiene and Carla Frescura. Anatomical and pathophysiological classification of congenital heart disease. *Cardiovascular Pathology*, 19(5):259–274, 9 2010.

[37] Matthew E. Oster, Kyung A. Lee, Margaret A. Honein, Tiffany Riehle-Colarusso, Mikyong Shin, and Adolfo Correa. Temporal Trends in Survival Among Infants With Critical Congenital Heart Defects. *Pediatrics*, 131(5):e1502–e1508, 5 2013.

[38] Courtney McCracken, Logan G. Spector, Jeremiah S. Menk, Jessica H. Knight, Jeffrey M. Vinocur, Amanda S. Thomas, Matthew E. Oster, James D. St Louis, James H. Moller, and Lazaros Kochilas. Mortality Following Pediatric Congenital Heart Surgery: An Analysis of the Causes of Death Derived From the National Death Index. *Journal of the American Heart Association*, 7(22), 11 2018.

[39] Eli Patt, Asmita Singhania, Amy E. Roberts, and Sarah U. Morton. The genetics of neurodevelopment in congenital heart disease. *Canadian Journal of Cardiology*, 39(2):97–114, 2023. Theme Issue: Cardiovascular Disease and the Brain.

[40] Alexander Egbe, Deborah Ho, Simon Lee, Santosh Uppu, and Shubhika Srivastava. Prevalence of congenital anomalies in newborns with congenital heart disease diagnosis. *Annals of Pediatric Cardiology*, 7(2):86, 2014.

[41] Michael Huntgeburth, Paul-Gerhard Diller, and Harald Kaemmerer. *Angeborene Herzfehler im Erwachsenenalter*. springer, 2023.

[42] Alejandro Sifrim, Marc-Phillip Hitz, Anna Wilsdon, Jeroen Breckpot, Saeed H Al Turki, Bernard Thienpont, Jeremy McRae, Tomas W Fitzgerald, Tarjinder Singh, Ganesh Jawahar Swaminathan, Elena Prigmore, Diana Rajan, Hashim Abdul-Khaliq, Siddharth Banka, Ulrike M M Bauer, Jamie Bentham, Felix Berger, Shoumo Bhattacharya, Frances Bu'Lock, Natalie Canham, Irina-Gabriela Colgiu, Catherine Cosgrove, Helen Cox, Ingo Daehnert, Allan Daly, John Danesh, Alan Fryer, Marc Gewillig, Emma Hobson, Kirstin Hoff, Tessa Homfray, Anne-Karin Kahlert, Ami Ketley, Hans-Heiner Kramer, Katherine Lachlan, Anne Katrin Lampe, Jacoba J Louw, Ashok Kumar Manickara, Dorin Manase, Karen P McCarthy, Kay Metcalfe, Carmel Moore, Ruth Newbury-Ecob, Seham Osman Omer, Willem H Ouwehand, Soo-Mi Park, Michael J Parker, Thomas Pickardt, Martin O Pollard, Leema Robert, David J Roberts, Jennifer Sambrook, Kerry Setchfield, Brigitte Stiller, Chris Thornborough, Okan Toka, Hugh Watkins, Denise Williams, Michael Wright, Seema Mital, Piers E F Daubeney, Bernard Keavney, Judith Goodship, Riyadh Mahdi Abu-Sulaiman, Sabine Klaassen, Caroline F Wright, Helen V Firth, Jeffrey C Barrett, Koenraad Devriendt, David R FitzPatrick, J David Brook, and Matthew E Hurles. Distinct genetic architectures for syndromic and nonsyndromic congenital heart defects identified by exome sequencing. *Nature Genetics*, 48(9):1060–1065, 9 2016.

[43] Robert J. Hartman, Sonja A. Rasmussen, Lorenzo D. Botto, Tiffany Riehle-Colarusso, Christa L. Martin, Janet D. Cragan, Mikyong Shin, and Adolfo Correa. The Contribution of Chromosomal Abnormalities to Congenital Heart Defects: A Population-Based Study. *Pediatric Cardiology*, 32(8):1147–1157, 12 2011.

[44] Jason Homsy, Samir Zaidi, Yufeng Shen, James S. Ware, Kaitlin E. Samocha, Konrad J. Karczewski, Steven R. DePalma, David McKean, Hiroko Wakimoto, Josh Gorham, Sheng Chih Jin, John Deanfield, Alessandro Giardini, George A. Porter, Richard Kim, Kaya Bilguvar, Francesc López-Giráldez, Irina Tikhonova, Shrikant Mane, Angela Romano-Adesman, Hongjian Qi, Badri Vardarajan, Lijiang Ma, Mark Daly, Amy E. Roberts, Mark W. Russell, Seema Mital, Jane W. Newburger, J. William Gaynor, Roger E. Breitbart, Ivan Iossifov, Michael Ronemus, Stephan J. Sanders, Jonathan R. Kaltman, Jonathan G. Seidman, Martina Brueckner, Bruce D. Gelb, Elizabeth Goldmuntz, Richard P. Lifton, Christine E. Seidman, and Wendy K. Chung. De novo mutations in congenital heart disease with neurodevelopmental and other congenital anomalies. *Science*, 2015.

[45] Marek Zubrzycki, Rene Schramm, Angelika Costard-Jäckle, Jochen Grohmann, Jan F. Gummert, and Maria Zubrzycka. Cardiac Development and Factors Influencing the Development of Congenital Heart Defects (CHDs): Part I. *International Journal of Molecular Sciences*, 2024.

[46] Jun Yasuhara and Vidu Garg. Genetics of congenital heart disease: a narrative review of recent advances and clinical implications. *Translational Pediatrics*, 2021.

[47] Stephanie LaHaye, Don Corsmeier, Madhumita Basu, Jessica L. Bowman, Sara Fitzgerald-Butt, Gloria Zender, Kevin Bosse, Kim L. McBride, Peter White, and Vidu Garg. Utilization of Whole Exome Sequencing to Identify Causative Mutations in Familial Congenital Heart Disease. *Circulation: Cardiovascular Genetics*, 2016.

[48] Laura Zahavich, Sarah Bowdin, and Seema Mital. Use of Clinical Exome Sequencing in Isolated Congenital Heart Disease. *Circulation: Cardiovascular Genetics*, 2017.

[49] Abigail S. Carey, Li Liang, Jonathan Edwards, Tracy Brandt, Hui Mei, Andrew J. Sharp, Daphne T. Hsu, Jane W. Newburger, Richard G. Ohye, Mark W. Chung, Wendy K.and Russell, Jill A. Rosenfeld, Lisa G. Shaffer, Michael K. Parides, Lisa

Edelmann, and Bruce D. Gelb. Effect of Copy Number Variants on Outcomes for Infants With Single Ventricle Heart Defects. *Circulation: Cardiovascular Genetics*, 2013.

[50] Daniel Seung Kim, Jerry H. Kim, Amber A. Burt, David R. Crosslin, Nancy Burnham, Cecilia E. Kim, Donna M. McDonald-McGinn, Elaine H. Zackai, Susan C. Nicolson, Thomas L. Spray, Ian B. Stanaway, Deborah A. Nickerson, Patrick J. Heagerty, Hakon Hakonarson, J. William Gaynor, and Gail P. Jarvik. Burden of potentially pathologic copy number variants is higher in children with isolated congenital heart disease and significantly impairs covariate-adjusted transplant-free survival. *The Journal of Thoracic and Cardiovascular Surgery*, 2016.

[51] Joseph T. Glessner, Alexander G. Bick, Kaoru Ito, Jason G. Homsy, Laura Rodriguez-Murillo, Menachem Fromer, Erica Mazaika, Badri Vardarajan, Michael Italia, Jeremy Leipzig, Steven R. DePalma, Ryan Golhar, Stephan J. Sanders, Boris Yamrom, Michael Ronemus, Ivan Iossifov, A. Jeremy Willsey, Matthew W. State, Jonathan R. Kaltman, Peter S. White, Yufeng Shen, Dorothy Warburton, Martina Brueckner, Christine Seidman, Elizabeth Goldmuntz, Bruce D. Gelb, Richard Lifton, Jonathan Seidman, Hakon Hakonarson, and Wendy K. Chung. Increased Frequency of De Novo Copy Number Variants in Congenital Heart Disease by Integrative Analysis of Single Nucleotide Polymorphism Array and Exome Sequence Data. *Circulation Research*, 2014.

[52] Samir Zaidi, Murim Choi, Hiroko Wakimoto, Lijiang Ma, Jianming Jiang, John D. Overton, Angela Romano-Adesman, Robert D. Bjornson, Roger E. Breitbart, Kerry K. Brown, Nicholas J. Carriero, Yee Him Cheung, John Deanfield, Steve DePalma, Khalid A. Fakhro, Joseph Glessner, Hakon Hakonarson, Michael J. Italia, Jonathan R. Kaltman, Juan Kaski, Richard Kim, Jennie K. Kline, Teresa Lee, Jeremy Leipzig, Alexander Lopez, Shrikant M. Mane, Laura E. Mitchell, Jane W. Newburger, Michael Parfenov, Itsik Pe'er, George Porter, Amy E. Roberts, Ravi Sachidanandam, Stephan J. Sanders, Howard S. Seiden, Mathew W. State, Sailakshmi Subramanian, Irina R. Tikhonova, Wei Wang, Dorothy Warburton, Peter S. White, Ismee A. Williams, Hongyu Zhao, Jonathan G. Seidman, Martina Brueckner, Wendy K. Chung, Bruce D. Gelb, Elizabeth Goldmuntz, Christine E. Seidman, and Richard P. Lifton. De novo mutations in histone-modifying genes in congenital heart disease. *Nature*, 498(7453):220–223, 6 2013.

[53] Prasanna Queremel Milani, Daniel A. Tadi. *Genetics, Chromosome Abnormalities*. StatPearls, 2024.

[54] Akl C. Fahed, Bruce D. Gelb, J. G. Seidman, and Christine E. Seidman. Genetics of Congenital Heart Disease. *Circulation Research*, 112(4):707–720, 2 2013.

[55] Radwa Ezzat Amin, Iman Ehsan Abdel-Meguid, Nihal Mohamed El-Refaie, Walaa Fakher, Dina El-Tabie, and Hala Ahmed El-Gindy. Clinical Profiles, Congenital Heart Disease, and Other Comorbidities Among Egyptian Children with Down Syndrome: A Tertiary Center Study. *Journal of Child Science*, 2021.

[56] Konstantinos Dimopoulos, Andrew Constantine, Paul Clift, Robin Condliffe, Shahin Moledina, Katrijn Jansen, Ryo Inuzuka, Gruschen R. Veldtman, Clifford L. Cua, Edgar Lik Wui Tay, Alexander R. Opotowsky, George Giannakoulas, Rafael Alonso-Gonzalez, Rachael Cordina, George Capone, Judith Namuyonga, Charmaine H. Scott, Michele D'Alto, Francisco J. Gamero, Brian Chicoine, Hong Gu, Alisa Limsuwan, Tosin Majekodunmi, Werner Budts, Gerry Coghlan, and Craig S. and Broberg. Cardiovascular Complications of Down Syndrome: Scoping Review and Expert Consensus. *Circulation*, 2023.

[57] Jennifer K. Peterson, Lazaros K. Kochilas, Kirsti G. Catton, James H. Moller, and Shaun P. Setty. Long-Term Outcomes of Children With Trisomy 13 and 18 After Congenital Heart Disease Interventions. *The Annals of Thoracic Surgery*, 2017.

[58] Michael Silberbach, Jolien W. Roos-Hesselink, Niels H. Andersen, Alan C. Braverman, Nicole Brown, R. Thomas Collins, Julie De Backer, Kim A. Eagle, Loren F. Hiratzka, Walter H. Johnson, Daniella Kadian-Dodov, Leo Lopez, Kristian H. Mortensen, Siddharth K. Prakash, Elizabeth V. Ratchford, Arwa Saidi, Iris van Hagen, and Luciana T. Young. Cardiovascular Health in Turner Syndrome: A Scientific Statement From the American Heart Association. *Circulation: Genomic and Precision Medicine*, 2018.

[59] Harald Lahm, Patric Schon, Stefanie Doppler, Martina Dreßen, Julie Cleuziou, Marcus-Andre Deutsch, Peter Ewert, Rudiger Lange, and Markus Krane. Tetralogy of Fallot and Hypoplastic Left Heart Syndrome – Complex Clinical Phenotypes Meet Complex Genetic Networks. *Current Genomics*, 16(3):141–158, 4 2015.

[60] Jung Min Ko. Genetic Syndromes associated with Congenital Heart Disease. *Korean Circulation Journal*, 2015.

[61] Karanjot Chhatwal, Jacob J. Smith, Harroop Bola, Abeer Zahid, Ashwin Venkatakrishnan, and Thomas Brand. Uncovering the Genetic Basis of Congenital Heart Disease: Recent Advancements and Implications for Clinical Management. *CJC Pediatric and Congenital Heart Disease*, 2023.

[62] Mark G Hazekamp, David J Barron, Joanna Dangel, Tessa Homfray, Monique R M Jongbloed, Inga Voges, Robert H Anderson, Emre Belli, Hannah Rosemary Bellsham-Revell, Ulrike Herberg, Joachim O M Photiadis, Serban C Stoica, and Yves D'Udekem. Consensus document on optimal management of patients with common arterial trunk. *European Journal of Cardio-Thoracic Surgery*, 2021.

[63] Lorenzo D. Botto, Kristin May, Paul M. Fernhoff, Adolfo Correa, Karlene Coleman, Sonja A. Rasmussen, Robert K. Merritt, Leslie A. O'Leary, Lee-Yang Wong, E. Marsha Elixson, William T. Mahle, and Robert M. Campbell. A Population-Based Study of the 22q11.2 Deletion: Phenotype, Incidence, and Contribution to Major Birth Defects in the Population. *Pediatrics*, 112(1):101–107, 7 2003.

[64] Kathleen Nevis, Pablo Obregon, Conor Walsh, Burcu Guner-Ataman, C. Geoffrey Burns, and Caroline E. Burns. Tbx1 is required for second heart field proliferation in zebrafish. *Developmental Dynamics*, 242(5):550–559, 5 2013.

[65] Clémence Jacquin, Emilie Landais, Céline Poirsier, Alexandra Afenjar, Ahmad Akhavi, Nathalie Bednarek, Caroline Bénech, Adeline Bonnard, Damien Bosquet, Lydie Burglen, Patrick Callier, Sandra Chantot-Bastaraud, Christine Coubes, Charles Coutton, Bruno Delobel, Margaux Descharmes, Jean-Michel Dupont, Vincent Gatinois, Nicolas Gruchy, Sarah Guterman, Abdelkader Heddar, Lucas Herissant, Delphine Heron, Bertrand Isidor, Pauline Jaeger, Guillaume Jouret, Boris Keren, Paul Kuentz, Cedric Le Caignec, Jonathan Levy, Nathalie Lopez, Zoe Manssens, Dominique Martin-Coignard, Isabelle Marey, Cyril Mignot, Chantal Missirian, Céline Pebrel-Richard, Lucile Pinson, Jacques Puechberty, Sylvia Redon, Damien Sanlaville, Marta Spodenkiewicz, Anne-Claude Tabet, Alain Verloes, Gaelle Vieville, Catherine Yardin, François Vialard, and Martine Doco-Fenzy. 1p36 deletion syndrome: Review

and mapping with further characterization of the phenotype, a new cohort of 86 patients. *American Journal of Medical Genetics Part A*, 2023.

[66] C.F. Rocha, R.B. Vasques, S.R. Santos, and C.L.A. Paiva. Mini-Review Monosomy 1p36 syndrome: reviewing the correlation between deletion sizes and phenotypes. *Genetics and Molecular Research*, 2016.

[67] Marc-Phillip Hitz, Louis-Philippe Lemieux-Perreault, Christian Marshall, Yassamin Feroz-Zada, Robbie Davies, Shi Wei Yang, Anath Christopher Lionel, Guylaine D'Amours, Emmanuelle Lemyre, Rebecca Cullum, Jean-Luc Bigras, Maryse Thibeault, Philippe Chetaille, Alexandre Montpetit, Paul Khairy, Bert Overduin, Sabine Klaassen, Pamela Hoodless, Philip Awadalla, Julie Hussin, Youssef Idaghdour, Mona Nemer, Alexandre F R Stewart, Cornelius Boerkoel, Stephen W Scherer, Andrea Richter, Marie-Pierre Dubé, and Gregor Andelfinger. Rare copy number variants contribute to congenital left-sided heart disease. *PLoS genetics*, 8(9):e1002903, 9 2012.

[68] Ashleigh R Payne, Sheng-Wei Chang, Sara N Koenig, Andrew R Zinn, and Vidu Garg. Submicroscopic chromosomal copy number variations identified in children with hypoplastic left heart syndrome. *Pediatric cardiology*, 33(5):757–63, 6 2012.

[69] F Erdogan, L A Larsen, L Zhang, Z Tumer, N Tommerup, W Chen, J R Jacobsen, M Schubert, J Jurkatis, A Tzschach, H-H Ropers, and R Ullmann. High frequency of submicroscopic genomic aberrations detected by tiling path array comparative genome hybridisation in patients with isolated congenital heart disease. *Journal of Medical Genetics*, 45(11):704–709, 11 2008.

[70] James R Priest, Santhosh Girirajan, Tiffany H Vu, Aaron Olson, Evan E Eichler, and Michael A Portman. Rare copy number variants in isolated sporadic and syndromic atrioventricular septal defects. *American journal of medical genetics. Part A*, 158A(6):1279–84, 6 2012.

[71] Rachel Soemedi, Ian J. Wilson, Jamie Bentham, Rebecca Darlay, Ana Töpf, Diana Zelenika, Catherine Cosgrove, Kerry Setchfield, Chris Thornborough, Javier Granados-Riveron, Gillian M. Blue, Jeroen Breckpot, Stephen Hellens, Simon Zwolinkski, Elise Glen, Chrysovalanto Mamasoula, Thahira J. Rahman, Darroch Hall, Anita

Rauch, Koenraad Devriendt, Marc Gewillig, John O' Sullivan, David S. Winlaw, Frances Bu'Lock, J. David Brook, Shoumo Bhattacharya, Mark Lathrop, Mauro Santibanez-Koref, Heather J. Cordell, Judith A. Goodship, and Bernard D. Keavney. Contribution of Global Rare Copy-Number Variants to the Risk of Sporadic Congenital Heart Disease. *The American Journal of Human Genetics*, 91(3):489–501, 9 2012.

[72] C. Vedel, T. D. Hjortshøj, D. S. Jørgensen, A. Tabor, L. Rode, K. Sundberg, C. K. Ekelund, and O. B. Petersen. Prevalence of chromosomal disorders in cases with congenital heart defect: registry-based study from Denmark between 2008 and 2018. *Ultrasound in Obstetrics & Gynecology*, 2023.

[73] Nélia S Gaspar, Gustavo Rocha, Ana Grangeia, and Henrique C Soares. Cat-Eye Syndrome: A Report of Two Cases and Literature Review. *Cureus*, 2022.

[74] Gabrielle C. Geddes, Leon F. Przybylowski, and Stephanie M. Ware. Variants of significance: medical genetics and surgical outcomes in congenital heart disease. *Current Opinion in Pediatrics*, 2020.

[75] Shi-Min Yuan. Congenital heart defects in Williams syndrome. *The Turkish Journal of Pediatrics*, 2017.

[76] Stuart K. Shapira, Christopher McCaskill, Hope Northrup, Aimee S. Spikes, F.F.B. Elder, V. Reid Sutton, Julie R. Korenberg, Frank Greenberg, and Lisa G. Shaffer. Chromosome 1p36 Deletions: The Clinical Phenotype and Molecular Characterization of a Common Newly Delineated Syndrome. *The American Journal of Human Genetics*, 61(3):642–650, 9 1997.

[77] Heidi A. Heilstedt, Blake C. Ballif, Leslie A. Howard, Richard A. Lewis, Samuel Stal, Catherine D. Kashork, Carlos A. Bacino, Stuart K. Shapira, and Lisa G. Shaffer. Physical Map of 1p36, Placement of Breakpoints in Monosomy 1p36, and Clinical Characterization of the Syndrome. *The American Journal of Human Genetics*, 72(5):1200–1212, 5 2003.

[78] Agatino Battaglia, H. Eugene Hoyme, Bruno Dallapiccola, Elaine Zackai, Louanne Hudgins, Donna McDonald-McGinn, Nadia Bahi-Buisson, Corrado Romano,

Charles A. Williams, Lisa L. Brailey, Sameer M. Zuberi, and John C. Carey. Further Delineation of Deletion 1p36 Syndrome in 60 Patients: A Recognizable Phenotype and Common Cause of Developmental Delay and Mental Retardation. *Pediatrics*, 121(2):404–410, 2 2008.

[79] S-HL Kang, A Scheffer, Z Ou, J Li, F Scaglia, J Belmont, SR Lalani, E Roeder, V Enciso, S Braddock, J Buchholz, S Vacha, AC Chinault, SW Cheung, and CA Bacino. Identification of proximal 1p36 deletions using array-CGH: a possible new syndrome. *Clinical Genetics*, 72(4):329–338, 8 2007.

[80] Hitisha P. Zaveri, Tyler F. Beck, Andrés Hernández-García, Katharine E. Shelly, Tara Montgomery, Arie van Haeringen, Britt-Marie Anderlid, Chirag Patel, Himanshu Goel, Gunnar Houge, Bernice E. Morrow, Sau Wai Cheung, Seema R. Lalani, and Daryl A. Scott. Identification of Critical Regions and Candidate Genes for Cardiovascular Malformations and Cardiomyopathy Associated with Deletions of Chromosome 1p36. *PLoS ONE*, 9(1):e85600, 1 2014.

[81] Valerie K Jordan, Hitisha P Zaveri, and Daryl A Scott. 1p36 deletion syndrome: an update. *The application of clinical genetics*, 8:189–200, 2015.

[82] Takaya Oda, Abdel G. Elkahloun, Brian L. Pike, Kazuki Okajima, Ian D. Krantz, Anna Genin, David A. Piccoli, Paul S. Meltzer, Nancy B. Spinner, Francis S. Collins, and Settara C. Chandrasekharappa. Mutations in the human Jagged1 gene are responsible for Alagille syndrome. *Nature Genetics*, 16(3):235–242, 7 1997.

[83] Linheng Li, Ian D. Krantz, Yu Deng, Anna Genin, Amy B. Banta, Colin C. Collins, Ming Qi, Barbara J. Trask, Wen Lin Kuo, Joanne Cochran, Teresa Costa, Mary Ella M. Pierpont, Elizabeth B. Rand, David A. Piccoli, Leroy Hood, and Nancy B. Spinner. Alagille syndrome is caused by mutations in human Jagged1, which encodes a ligand for Notch1. *Nature Genetics*, 16(3):243–251, 7 1997.

[84] P Subramaniam, A Knisely, B Portmann, SA Qureshi, WA Aclimandos, JB Karani, and AJ Baker. Diagnosis of Alagille Syndrome—25 Years of Experience at King's College Hospital. *Journal of Pediatric Gastroenterology & Nutrition*, 52(1):84–89, 1 2011.

[85] Bruno Marino, Maria Cristina Digilio, Alessandra Toscano, Aldo Giannotti, and Bruno Dallapiccola. Congenital heart diseases in children with Noonan syndrome: An expanded cardiac spectrum with high prevalence of atrioventricular canal. *The Journal of Pediatrics*, 135(6):703–706, 12 1999.

[86] M Digilio and B Marino. Clinical manifestations of Noonan syndrome. *Images in paediatric cardiology*, 3(2):19–30, 4 2001.

[87] J. E. H. Bergman, N. Janssen, L. H. Hoefsloot, M. C. J. Jongmans, R. M. W. Hofstra, and C. M. A. van Ravenswaaij-Arts. CHD7 mutations and CHARGE syndrome: the clinical implications of an expanding phenotype. *Journal of Medical Genetics*, 48(5):334–342, 5 2011.

[88] Christine B. Hills, Lazaros Kochilas, Lisa A. Schimmenti, and James H. Moller. Ellis–van Creveld Syndrome and Congenital Heart Defects: Presentation of an Additional 32 Cases. *Pediatric Cardiology*, 32(7):977–982, 10 2011.

[89] Peter M. Van Laarhoven, Leif R. Neitzel, Anita M Quintana, Elizabeth A. Geiger, Elaine H. Zackai, David E. Clouthier, Kristin B. Artinger, Jeffrey E. Ming, and Tamim H. Shaikh. Kabuki syndrome genes KMT2D and KDM6A : functional analyses demonstrate critical roles in craniofacial, heart and brain development. *Human Molecular Genetics*, 24(15):4443–4453, 8 2015.

[90] Bruce Gelb, Martina Brueckner, Wendy Chung, Elizabeth Goldmuntz, Jonathan Kaltman, Juan Pablo Kaski, Richard Kim, Jennie Kline, Laura Mercer-Rosa, George Porter, Amy Roberts, Ellen Rosenberg, Howard Seiden, Christine Seidman, Lynn Sleeper, Sharon Tennstedt, Jonathan Kaltman, Charlene Schramm, Kristin Burns, Gail Pearson, Ellen Rosenberg, Jane Newburger, Roger Breitbart, Steven Colan, Judith Geva, Angela Monafo, Amy Roberts, Janice Stryker, Christine Seidman, Barbara McDonough, Jonathan Seidman, Elizabeth Goldmuntz, Sharon Edman, Jennifer Garbarini, Hakon Hakonarson, Laura Mercer-Rosa, Laura Mitchell, Jessica Tusi, Peter White, Stacy Woyciechowski, Wendy Chung, Dorothy Warburton, Danielle Awad, Katrina Celia, Jaswinder Kaur Etwaru, Davina v Sond, Jennie Kline, Rosalind Korsin, Alyssa Lanz, Emma Marquez, Ismee Williams, Abigail Wilpers, Roslyn Yee, Bruce Gelb, Denise Guevara, Ariel Julian, Meghan Mac Neal, Cassie Mintz, Inga Peter, Ravi Sachidanandam, Howard Seiden, Angela Romano-Adesman,

Dorota Gruber, Nancy Stellato, Martina Brueckner, Richard Lifton, Nancy Cross, John Deanfield, Alessandro Giardini, Karen Flack, George Porter, Eileen Taillie, Richard Kim, Nhu Tran, Sharon Tennstedt, Roger Breitbart, Kimberly Dandreo, Dianne Gallagher, Minmin Lu, Lynn Sleeper, Dorit Berlin, Christine Beiswanger, Richard Lifton, Jonathan Seidman, Peter White, Mike Italia, Christine Chung, Wendy Seidman, Maria Brooks (Chair), Michelle Olive, Jeffrey Botkin, Josee Dupuis, Vidu Garg, Mike Watson, James Bristow, Todd Evans, Christina Kendziorski, Elaine Mardis, Jeffrey Murray, Joel Saltz, and Hector Wong. The Congenital Heart Disease Genetic Network Study. *Circulation Research*, 2013.

[91] Sheng Chih Jin, Jason Homsy, Samir Zaidi, Qiongshi Lu, Sarah Morton, Steven R DePalma, Xue Zeng, Hongjian Qi, Weni Chang, Michael C Sierant, Wei-Chien Hung, Shozeb Haider, Junhui Zhang, James Knight, Robert D Bjornson, Christopher Castaldi, Irina R Tikhonoa, Kaya Bilguvar, Shrikant M Mane, Stephan J Sanders, Seema Mital, Mark W Russell, J William Gaynor, John Deanfield, Alessandro Giardini, George A Porter, Deepak Srivastava, Cecelia W Lo, Yufeng Shen, W Scott Watkins, Mark Yandell, H Joseph Yost, Martin Tristani-Firouzi, Jane W Newburger, Amy E Roberts, Richard Kim, Hongyu Zhao, Jonathan R Kaltman, Elizabeth Goldmuntz, Wendy K Chung, Jonathan G Seidman, Bruce D Gelb, Christine E Seidman, Richard P Lifton, and Martina Brueckner. Contribution of rare inherited and de novo variants in 2,871 congenital heart disease probands. *Contribution of rare inherited and de novo variants in 2,871 congenital heart disease probands*, 2017.

[92] W. Scott Watkins, E. Javier Hernandez, Sergiusz Wesolowski, Brent W. Bisgrove, Ryan T. Sunderland, Edwin Lin, Gordon Lemmon, Bradley L. Demarest, Thomas A. Miller, Daniel Bernstein, Martina Brueckner, Wendy K. Chung, Bruce D. Gelb, Elizabeth Goldmuntz, Jane W. Newburger, Christine E. Seidman, Yufeng Shen, H. Joseph Yost, Mark Yandell, and Martin Tristani-Firouzi. De novo and recessive forms of congenital heart disease have distinct genetic and phenotypic landscapes. *Nature Communications*, 2019.

[93] Tiziana Ciarambino, Giovanni Menna, Gennaro Sansone, and Mauro Giordano. Cardiomyopathies: An Overview. *International Journal of Molecular Sciences*, 22(14):7722, 7 2021.

[94] Nicoletta Orphanou, Efstathios Papatheodorou, and Aris Anastasakis. Dilated

cardiomyopathy in the era of precision medicine: latest concepts and developments. *Heart Failure Reviews*, 2022.

[95] Elena Arbelo, Alexandros Protonotarios, Juan R Gimeno, Eloisa Arbustini, Roberto Barriales-Villa, Cristina Basso, Connie R Bezzina, Elena Biagini, Nico A Blom, Rudolf A de Boer, Tim De Winter, Perry M Elliott, Marcus Flather, Pablo Garcia-Pavia, Kristina H Haugaa, Jodie Ingles, Ruxandra Oana Jurcut, Sabine Klaassen, Giuseppe Limongelli, Bart Loeys, Jens Mogensen, Iacopo Olivotto, Antonis Pantazis, Sanjay Sharma, J Peter Van Tintelen, James S Ware, Juan Pablo Kaski, and ESC Scientific Document Group. 2023 ESC Guidelines for the management of cardiomyopathies: Developed by the task force on the management of cardiomyopathies of the European Society of Cardiology (ESC). *European Heart Journal*, 44(37):3503–3626, 08 2023.

[96] Hamayak Sisakian. Cardiomyopathies: Evolution of pathogenesis concepts and potential for new therapies. *World Journal of Cardiology*, 6(6):478, 2014.

[97] Arsonval Lamounier Júnior, Filipe Ferrari, Renato Max, Luiz Eduardo Fonteles Ritt, and Ricardo Stein. Importance of Genetic Testing in Dilated Cardiomyopathy: Applications and Challenges in Clinical Practice. *Arquivos Brasileiros de Cardiologia*, 2019.

[98] Barry J Maron, Jeffrey A Towbin, Gaetano Thiene, Charles Antzelevitch, Domenico Corrado, Donna Arnett, Arthur J Moss, Christine E Seidman, James B Young, American Heart Association, Heart Failure Council on Clinical Cardiology, Transplantation Committee, Quality of Care and Outcomes Research and Functional Genomics and Translational Biology Interdisciplinary Working Groups, and Council on Epidemiology and Prevention. Contemporary definitions and classification of the cardiomyopathies: an American Heart Association Scientific Statement from the Council on Clinical Cardiology, Heart Failure and Transplantation Committee; Quality of Care and Outcomes Research and Functio. *Circulation*, 113(14):1807–16, 4 2006.

[99] Eloisa Arbustini, Navneet Narula, G. William Dec, K. Srinath Reddy, Barry Greenberg, Sudhir Kushwaha, Thomas Marwick, Sean Pinney, Riccardo Bellazzi, Valentina Favalli, Christopher Kramer, Robert Roberts, William A. Zoghbi, Robert Bonow,

Luigi Tavazzi, Valentin Fuster, and Jagat Narula. The MOGE(S) Classification for a Phenotype–Genotype Nomenclature of Cardiomyopathy. *Journal of the American College of Cardiology*, 62(22):2046–2072, 12 2013.

[100] Jeffrey A Towbin, Angela Lorts, and John Lynn Jefferies. Left ventricular non-compaction cardiomyopathy. *Lancet (London, England)*, 386(9995):813–25, 8 2015.

[101] Alexander R. Lyon, Eduardo Bossone, Birke Schneider, Udo Sechtem, Rodolfo Citro, S. Richard Underwood, Mary N. Sheppard, Gemma A. Figtree, Guido Parodi, Yoshihiro J. Akashi, Frank Ruschitzka, Gerasimos Filippatos, Alexandre Mebazaa, and Elmir Omerovic. Current state of knowledge on takotsubo syndrome: a position statement from the taskforce on takotsubo syndrome of the heart failure association of the european society of cardiology. *European Journal of Heart Failure*, 18(1):8–27, 2016.

[102] Estelle Gandjbakhch, Alban Redheuil, Françoise Pousset, Philippe Charron, and Robert Frank. Clinical Diagnosis, Imaging, and Genetics of Arrhythmogenic Right Ventricular Cardiomyopathy/Dysplasia: JACC State-of-the-Art Review. *Journal of the American College of Cardiology*, 72(7):784–804, 8 2018.

[103] Francesca Graziano, Alessandro Zorzi, Alberto Cipriani, Manuel De Lazzari, Barbara Bauce, Ilaria Rigato, Giulia Brunetti, Kalliopi Pilichou, Cristina Basso, Martina Perazzolo Marra, and Domenico Corrado. The 2020 "padua criteria" for diagnosis and phenotype characterization of arrhythmogenic cardiomyopathy in clinical practice. *Journal of Clinical Medicine*, 11(1), 2022.

[104] Domenico Corrado, Aris Anastasakis, Cristina Basso, Barbara Bauce, Carina Blomström-Lundqvist, Chiara Bucciarelli-Ducci, Alberto Cipriani, Carlo De Asmundis, Estelle Gandjbakhch, Juan Jiménez-Jáimez, Maria Kharlap, William J McKenna, Lorenzo Monserrat, James Moon, Antonis Pantazis, Antonio Pelliccia, Martina Perazzolo Marra, Kalliopi Pillichou, Jeanette Schulz-Menger, Ruxandra Jurcut, Petar Seferovic, Sanjay Sharma, Jacob Tfelt-Hansen, Gaetano Thiene, Thomas Wichter, Arthur Wilde, and Alessandro Zorzi. Proposed diagnostic criteria for arrhythmogenic cardiomyopathy: European task force consensus report. *International Journal of Cardiology*, 395:131447, 2024.

[105] Brenda Gerull and Andreas Brodehl. Insights Into Genetics and Pathophysiology of Arrhythmogenic Cardiomyopathy. *Current Heart Failure Reports*, 18(6):378–390, 12 2021.

[106] Domenico Corrado, Cristina Basso, and Daniel P. Judge. Arrhythmogenic Cardiomyopathy. *Circulation Research*, 121(7):784–802, 9 2017.

[107] Cristina Basso, Domenico Corrado, Frank I Marcus, Andrea Nava, and Gaetano Thiene. Arrhythmogenic right ventricular cardiomyopathy. *The Lancet*, 373(9671):1289–1300, 4 2009.

[108] Freyja H.M. van Lint, Brittney Murray, Crystal Tichnell, Rob Zwart, Nuria Amat, Ronald H. Lekanne Deprez, Sven Dittmann, Birgit Stallmeyer, Hugh Calkins, Jasper J. van der Smagt, Arthur van den Wijngaard, Dennis Dooijes, Paul A. van der Zwaag, Eric Schulze-Bahr, Daniel P. Judge, Jan D.H. Jongbloed, J. Peter van Tintelen, and Cynthia A. James. Arrhythmogenic Right Ventricular Cardiomyopathy-Associated Desmosomal Variants Are Rarely De Novo. *Circulation: Genomic and Precision Medicine*, 12(8), 8 2019.

[109] Gaetano Thiene, Domenico Corrado, and Cristina Basso. Arrhythmogenic right ventricular cardiomyopathy/dysplasia. *Orphanet Journal of Rare Diseases*, 2(1):45, 12 2007.

[110] Elżbieta K. Biernacka, Karolina Borowiec, Maria Franaszczyk, Małgorzata Szperl, Alessandra Rampazzo, Olgierd Woźniak, Marta Roszczynko, Witold Śmigielski, Anna Lutyńska, and Piotr Hoffman. Pathogenic variants in plakophilin-2 gene (PKP2) are associated with better survival in arrhythmogenic right ventricular cardiomyopathy. *Journal of Applied Genetics*, 62(4):613–620, 12 2021.

[111] Elizabeth McNally, Heather MacLeod, and Lisa Dellefave-Castillo. *Arrhythmogenic Right Ventricular Cardiomyopathy Overview*. GeneReviews, 2023.

[112] Alessandra Rampazzo, Andrea Nava, Sandro Malacrida, Giorgia Beffagna, Barbara Bauce, Valeria Rossi, Rosanna Zimbello, Barbara Simionati, Cristina Basso, Gaetano Thiene, Jeffrey A. Towbin, and Gian A. Danieli. Mutation in Human Desmoplakin Domain Binding to Plakoglobin Causes a Dominant Form of Arrhythmogenic Right

Ventricular Cardiomyopathy. *The American Journal of Human Genetics*, 71(5):1200–1206, 11 2002.

[113] Anita Kiran Vimalanathan, Elisabeth Ehler, and Katja Gehmlich. Genetics of and pathogenic mechanisms in arrhythmogenic right ventricular cardiomyopathy. *Biophysical Reviews*, 10(4):973–982, 8 2018.

[114] Raffaella Lombardi, Maria da Graca Cabreira-Hansen, Achim Bell, Richard R Fromm, James T Willerson, and A J Marian. Nuclear plakoglobin is essential for differentiation of cardiac progenitor cells to adipocytes in arrhythmogenic right ventricular cardiomyopathy. *Circulation research*, 109(12):1342–53, 12 2011.

[115] Caezar Al-Jassar, Hennie Bikker, Michael Overduin, and Martyn Chidgey. Mechanistic Basis of Desmosome-Targeted Diseases. *Journal of Molecular Biology*, 2013.

[116] R Jenni. Echocardiographic and pathoanatomical characteristics of isolated left ventricular non-compaction: a step towards classification as a distinct cardiomyopathy. *Heart*, 86(6):666–671, 12 2001.

[117] Keiichi Hirono and Fukiko Ichida. Left ventricular noncompaction: a disorder with genotypic and phenotypic heterogeneity—a narrative review. *Cardiovascular Diagnosis and Therapy*, 2022.

[118] Pakdee Rojanasopondist, Leigh Nesheiwat, Sebastian Piombo, George A. Porter, Mindong Ren, and Colin K.L. Phoon. Genetic basis of left ventricular noncompaction. *Circulation: Genomic and Precision Medicine*, 15(3):e003517, 2022.

[119] John Lynn Jefferies and Jeffrey A Towbin. Dilated cardiomyopathy. *Lancet (London, England)*, 375(9716):752–62, 2 2010.

[120] John J. Parent, Ryan A. Moore, Michael D. Taylor, Jeffrey A. Towbin, and John L. Jefferies. Left ventricular noncompaction cardiomyopathy in Duchenne muscular dystrophy carriers. *Journal of Cardiology Cases*, 11(1):7–9, 1 2015.

[121] Michael V Zaragoza, Eloisa Arbustini, and Jagat Narula. Noncompaction of the

left ventricle: primary cardiomyopathy with an elusive genetic etiology. *Current Opinion in Pediatrics*, 19(6):619–627, 12 2007.

[122] Subin Jang, Allison Taber, Michael G Bateman, Marie E Steiner, Rebecca K Ameduri, and Massimo Griselli. 1p36 Deletion Syndrome and Left Ventricular Non-compaction Cardiomyopathy-Two Cases Report. *Frontiers in pediatrics*, 9:653633, 2021.

[123] Haiyang Chen, Xin Chen, and Yixian Zheng. The nuclear lamina regulates germline stem cell niche organization via modulation of EGFR signaling. *Cell Stem Cell*, 13(1):73–86, 2013.

[124] Qing Cao, Yang Shen, Xin Liu, Xin Yu, Ping Yuan, Rong Wan, Xiuxia Liu, Xiaogang Peng, Wenfeng He, Jielin Pu, and Kui Hong. Phenotype and Functional Analyses in a Transgenic Mouse Model of Left Ventricular Noncompaction Caused by a DTNA Mutation. *International Heart Journal*, 58(6):939–947, 2017.

[125] Kazuki Kodo, Sang-Ging Ong, Fereshteh Jahanbani, Vittavat Termglinchan, Keiichi Hirono, Kolsoum InanlooRahatloo, Antje D. Ebert, Praveen Shukla, Oscar J. Abilez, Jared M. Churko, Ioannis Karakikes, Gwanghyun Jung, Fukiko Ichida, Sean M. Wu, Michael P. Snyder, Daniel Bernstein, and Joseph C. Wu. iPSC-derived cardiomyocytes reveal abnormal TGF-β signalling in left ventricular non-compaction cardiomyopathy. *Nature Cell Biology*, 18(10):1031–1042, 10 2016.

[126] Ana G. Almeida. Left Ventricular Noncompaction. In *Cardiomyopathies - Types and Treatments*. InTech, 4 2017.

[127] Allen Burke, Erik Mont, Robert Kutys, and Renu Virmani. Left ventricular noncompaction: a pathological study of 14 cases. *Human Pathology*, 36(4):403–411, 4 2005.

[128] Yaa Ababio, Scott P. Kelly, Franca S Angeli, Joanne Berghout, Kui Huang, Kathy Liu, Sara Burns, Cynthia Senerchia, Rob Moccia, and Gabriel C. Brooks. Prevalence and clinical burden of idiopathic dilated cardiomyopathy in the united states. *American Journal of Medicine Open*, 10:100038, 2023.

[129] Elizabeth M. McNally, Jessica R. Golbus, and Megan J. Puckelwartz. Genetic muta-

tions and mechanisms in dilated cardiomyopathy. *Journal of Clinical Investigation*, 123(1):19–26, 1 2013.

[130] Livia Trasca, Mihaela Roxana Popescu, Andreea Catarina Popescu, and Serban Mihai Balanescu. Echocardiography in the Diagnosis of Cardiomyopathies: Current Status and Future Directions. *Reviews in Cardiovascular Medicine*, 23(8):280, 8 2022.

[131] Mary N. Sheppard, Allard C. van der Wal, Jytte Banner, Giulia D'Amati, Monica De Gaspari, Rosa De Gouveia, Cira Di Gioia, Carla Giordano, Maiken Kudahl Larsen, Matthew J. Lynch, Joaquin Lucena, Pilar Molina, Sarah Parsons, M. Paz Suarez-Mier, Stefania Rizzo, Simon Kim Suvarna, Wouter P te Rijdt, Gaetano Thiene, Aryan Vink, Joseph Westaby, Katarzyna Michaud, and Cristina Basso. Genetically determined cardiomyopathies at autopsy: the pivotal role of the pathologist in establishing the diagnosis and guiding family screening. *Virchows Archiv*, 482(4):653–669, 4 2023.

[132] Nicoletta Orphanou, Efstathios Papatheodorou, and Aris Anastasakis. Dilated cardiomyopathy in the era of precision medicine: latest concepts and developments. *Heart Failure Reviews*, 2022.

[133] Aaron Theisen. Microarray-based Comparative Genomic Hybridization (aCGH). *nature education*, 1(1):45, 2008.

[134] Apratim Mitra, George Liu, and Jiuzhou Song. A Genome-Wide Analysis of Array-Based Comparative Genomic Hybridization (CGH) Data to Detect Intra-Species Variations and Evolutionary Relationships. *PLoS ONE*, 4(11):e7978, 11 2009.

[135] Gillian M. Blue, Edwin P. Kirk, Eleni Giannoulatou, Sally L. Dunwoodie, Joshua W.K. Ho, Desiree C.K. Hilton, Susan M. White, Gary F. Sholler, Richard P. Harvey, and David S. Winlaw. Targeted next-generation sequencing identifies pathogenic variants in familial congenital heart disease. *Journal of the American College of Cardiology*, 64(23):2498–2506, 2014.

[136] J.R. Yates, S. Speicher, P.R. Griffin, and T. Hunkapiller. Peptide Mass Maps: A Highly Informative Approach to Protein Identification. *Analytical Biochemistry*, 214(2):397–408, 11 1993.

[137] Maria Kirchhoff, Tommy Gerdes, Hanne Rose, Jan Maahr, Anne Marie Ottesen, and Claes Lundsteen. Detection of chromosomal gains and losses in comparative genomic hybridization analysis based on standard reference intervals. *Cytometry*, 31(3):163–173, 3 1998.

[138] Hannah B. Hightower, Nathaniel H. Robin, Fady M. Mikhail, and Namasivayam Ambalavanan. Array comparative genomic hybridisation testing in CHD. *Cardiology in the Young*, 25(6):1155–1172, 8 2015.

[139] Anne-Karin Arndt, Sebastian Schafer, Jorg-Detlef Drenckhahn, M. Khaled Sabeh, Eva R. Plovie, Almuth Caliebe, Eva Klopocki, Gabriel Musso, Andreas A. Werdich, Hermann Kalwa, Matthias Heinig, Robert F. Padera, Katharina Wassilew, Julia Bluhm, Christine Harnack, Janine Martitz, Paul J. Barton, Matthias Greutmann, Felix Berger, Norbert Hubner, Reiner Siebert, Hans-Heiner Kramer, Stuart A. Cook, Calum A. MacRae, and Sabine Klaassen. Fine Mapping of the 1p36 Deletion Syndrome Identifies Mutation of PRDM16 as a Cause of Cardiomyopathy. *The American Journal of Human Genetics*, 93(1):67–77, 7 2013.

[140] Jingyi Chi and Paul Cohen. The Multifaceted Roles of PRDM16: Adipose Biology and Beyond. *Trends in Endocrinology & Metabolism*, 27(1):11–23, 1 2016.

[141] Ichiro Nishikata, Hidenori Sasaki, Mutsunori Iga, Yoko Tateno, Suzuko Imayoshi, Norio Asou, Takuro Nakamura, and Kazuhiro Morishita. A novel EVI1 gene family, MEL1, lacking a PR domain (MEL1S) is expressed mainly in t(1;3)(p36;q21)-positive AML and blocks G-CSF–induced myeloid differentiation. *Blood*, 102(9):3323–3332, 11 2003.

[142] Stephen R. Farmer. Brown Fat and Skeletal Muscle: Unlikely Cousins? *Cell*, 134(5):726–727, 9 2008.

[143] Francesca Aguilo, Serine Avagyan, Amy Labar, Ana Sevilla, Dung-Fang Lee, Parameet Kumar, Ihor R. Lemischka, Betty Y. Zhou, and Hans-Willem Snoeck. Prdm16 is a physiologic regulator of hematopoietic stem cells. *Blood*, 117(19):5057–5066, 5 2011.

[144] Bryan C. Bjork, Annick Turbe-Doan, Mary Prysak, Bruce J. Herron, and David R.

Beier. Prdm16 is required for normal palatogenesis in mice. *Human Molecular Genetics*, 19(5):774–789, 3 2010.

[145] Na Jiang, Ming Yang, Yachun Han, Hao Zhao, and Lin Sun. PRDM16 Regulating Adipocyte Transformation and Thermogenesis: A Promising Therapeutic Target for Obesity and Diabetes. *Frontiers in Pharmacology*, 13, 4 2022.

[146] N Mochizuki, S Shimizu, T Nagasawa, H Tanaka, M Taniwaki, J Yokota, and K Morishita. A novel gene, MEL1, mapped to 1p36.3 is highly homologous to the MDS1/EVI1 gene and is transcriptionally activated in t(1;3)(p36;q21)-positive leukemia cells. *Blood*, 96(9):3209–14, 11 2000.

[147] Patrick Seale, Shingo Kajimura, Wenli Yang, Sherry Chin, Lindsay M. Rohas, Marc Uldry, Geneviève Tavernier, Dominique Langin, and Bruce M. Spiegelman. Transcriptional Control of Brown Fat Determination by PRDM16. *Cell Metabolism*, 6(1):38–54, 7 2007.

[148] Patrick Seale, Bryan Bjork, Wenli Yang, Shingo Kajimura, Sherry Chin, Shihuan Kuang, Anthony Scimè, Srikripa Devarakonda, Heather M. Conroe, Hediye Erdjument-Bromage, Paul Tempst, Michael A. Rudnicki, David R. Beier, and Bruce M. Spiegelman. PRDM16 controls a brown fat/skeletal muscle switch. *Nature*, 454(7207):961–967, 8 2008.

[149] Mayuko Inoue, Ryota Iwai, Hidenori Tabata, Daijiro Konno, Mariko Komabayashi-Suzuki, Chisato Watanabe, Hiroko Iwanari, Yasuhiro Mochizuki, Takao Hamakubo, Fumio Matsuzaki, Koh-ichi Nagata, and Ken-ichi Mizutani. Prdm16 is critical for progression of the multipolar phase during neural differentiation of the developing neocortex. *Development*, 1 2016.

[150] Geoffroy Delplancq, Georges Tarris, Antonio Vitobello, Sophie Nambot, Arthur Sorlin, Christophe Philippe, Virginie Carmignac, Yannis Duffourd, Charlotte Denis, Jean Christophe Eicher, Martin Chevarin, Gilles Millat, Bouchra Khallouk, Thierry Rousseau, Sylvie Falcon-Eicher, Alexandre Vasiljevic, Fara T. Harizay, Christel Thauvin-Robinet, Laurence Faivre, and Paul Kuentz. Cardiomyopathy due to PRDM16 mutation: First description of a fetal presentation, with possible modifier

genes. *American Journal of Medical Genetics Part C: Seminars in Medical Genetics*, 2020.

[151] Jeong Min Nam, Ji Eun Lim, Tae Woong Ha, Bermseok Oh, and Ji-One Kang. Cardiac-specific inactivation of Prdm16 effects cardiac conduction abnormalities and cardiomyopathy-associated phenotypes. *American Journal of Physiology-Heart and Circulatory Physiology*, 318(4):H764–H777, 4 2020.

[152] Gillian M. Blue and David S. Winlaw. Next Generation Sequencing in Congenital Heart Disease: Gene Discovery and Clinical Application. *Journal of Next Generation Sequencing & Applications*, 02(01), 2015.

[153] Lorena Salazar-García, Mario Pérez-Sayáns, Abel García-García, Ángel Carracedo, Raquel Cruz, Antonio Lozano, Beatriz Sobrino, and Francisco Barros. Whole exome sequencing approach to analysis of the origin of cancer stem cells in patients with head and neck squamous cell carcinoma. *Journal of Oral Pathology & Medicine*, 2018.

[154] Samir Zaidi and Martina Brueckner. Genetics and Genomics of Congenital Heart Disease. *Circulation Research*, 120(6):923–940, 3 2017.

[155] Rai-Hseng Hsu, Chen-Hao Lee, Yin-Hsiu Chien, Shuan-Pei Lin, Miao-Zi Hung, Nai-Chi Chen, Yi-Lin Lin, Wuh-Liang Hwu, and Ni-Chung Lee. Utility of whole-exome sequencing for patients with multiple congenital anomalies with or without intellectual disability/developmental delay in East Asia population. *Molecular Genetics & Genomic Medicine*, 2023.

[156] C. G. Dos Remedios, D. Chhabra, M. Kekic, I. V. Dedova, M. Tsubakihara, D. A. Berry, and N. J. Nosworthy. Actin Binding Proteins: Regulation of Cytoskeletal Microfilaments. *Physiological Reviews*, 83(2):433–473, 4 2003.

[157] Marilyn C. Hart and John A. Cooper. Vertebrate Isoforms of Actin Capping Protein β Have Distinct Functions in Vivo. *Journal of Cell Biology*, 147(6):1287–1298, 12 1999.

[158] John A Cooper and Dorothy A Schafer. Control of actin assembly and disassembly at filament ends. *Current Opinion in Cell Biology*, 12(1):97–103, 2 2000.

[159] Annabelle Scott. *The role of the CapZ complex in vertebrate sarcomere integrity*. PhD thesis, Cambridge, 2007.

[160] Marilyn C. Hart, Yulia O. Korshunova, and John A. Cooper. Vertebrates have conserved capping protein α isoforms with specific expression patterns. *Cell Motility and the Cytoskeleton*, 38(2):120–132, 1997.

[161] Manon von Bülow, Hans Heid, Holger Hess, and Werner W. Franke. Molecular Nature of Calicin, a Major Basic Protein of the Mammalian Sperm Head Cytoskeleton. *Experimental Cell Research*, 219(2):407–413, 8 1995.

[162] Kusumika Mukherjee, Kana Ishii, Vamsee Pillalamarri, Tammy Kammin, Joan F. Atkin, Scott E. Hickey, Qiongchao J. Xi, Cinthya J. Zepeda, James F. Gusella, Michael E. Talkowski, Cynthia C. Morton, Richard L. Maas, and Eric C. Liao. Actin capping protein CAPZB regulates cell morphology, differentiation, and neural crest migration in craniofacial morphogenesis. *Human Molecular Genetics*, 25(7):1255–1270, 4 2016.

[163] Claudia Jasmin Rödel and Salim Abdelilah-Seyfried. A zebrafish toolbox for biomechanical signaling in cardiovascular development and disease. *Current opinion in hematology*, 28(3):198–207, 5 2021.

[164] M. F. Wullimann, B. Rupp, and H. Reichert. *Neuroanatomy of the Zebrafish Brain*. Birkhäuser Basel, Basel, 1996.

[165] Máté Varga. The Doctor of Delayed Publications: The Remarkable Life of George Streisinger (1927-1984). *Zebrafish*, 15(3):314–319, 6 2018.

[166] Charles B. Kimmel, William W. Ballard, Seth R. Kimmel, Bonnie Ullmann, and Thomas F. Schilling. Stages of embryonic development of the zebrafish. *Developmental Dynamics*, 203(3):253–310, 7 1995.

[167] Annapaola Coppola, Patrizia Lombari, Elvira Mazzella, Giovanna Capolongo, Mari-

adelina Simeoni, Alessandra F. Perna, Diego Ingrosso, and Margherita Borriello. Zebrafish as a Model of Cardiac Pathology and Toxicity: Spotlight on Uremic Toxins. *International Journal of Molecular Sciences*, 2023.

[168] Aarti Asnani and Randall T. Peterson. The zebrafish as a tool to identify novel therapies for human cardiovascular disease. *Disease Models & Mechanisms*, 7(7):763–767, 7 2014.

[169] Jeroen Bakkers. Zebrafish as a model to study cardiac development and human cardiac disease. *Cardiovascular research*, 91(2):279–88, 7 2011.

[170] Daniel Brown, Leigh Samsa, Li Qian, and Jiandong Liu. Advances in the Study of Heart Development and Disease Using Zebrafish. *Journal of Cardiovascular Development and Disease*, 3(2):13, 4 2016.

[171] David Staudt and Didier Stainier. Uncovering the Molecular and Cellular Mechanisms of Heart Development Using the Zebrafish. *Annual Review of Genetics*, 46(1):397–418, 12 2012.

[172] Didier Y. R. Stainier, Robert K. Lee, and Mark C. Fishman. Cardiovascular development in the zebrafish I. Myocardial fate map and heart tube formation. *Development*, 119(1):31–40, 9 1993.

[173] Brian R. Keegan, Dirk Meyer, and Deborah Yelon. Organization of cardiac chamber progenitors in the zebrafish blastula. *Development*, 131(13):3081–3091, 7 2004.

[174] Emma de Pater, Linda Clijsters, Sara R. Marques, Yi-Fan Lin, Zayra V. Garavito-Aguilar, Deborah Yelon, and Jeroen Bakkers. Distinct phases of cardiomyocyte differentiation regulate growth of the zebrafish heart. *Development*, 136(10):1633–1641, 5 2009.

[175] Stefan Rohr, Ceécile Otten, and Salim Abdelilah-Seyfried. Asymmetric Involution of the Myocardial Field Drives Heart Tube Formation in Zebrafish. *Circulation Research*, 102(2), 2 2008.

[176] Deborah Yelon, Sally A. Horne, and Didier Y.R. Stainier. Restricted Expression

of Cardiac Myosin Genes Reveals Regulated Aspects of Heart Tube Assembly in Zebrafish. *Developmental Biology*, 214(1):23–37, 10 1999.

[177] Jiandong Liu and Didier Y.R. Stainier. Zebrafish in the Study of Early Cardiac Development. *Circulation Research*, 110(6):870–874, 3 2012.

[178] Jiandong Liu, Michael Bressan, David Hassel, Jan Huisken, David Staudt, Kazu Kikuchi, Kenneth D. Poss, Takashi Mikawa, and Didier Y. R. Stainier. A dual role for ErbB2 signaling in cardiac trabeculation. *Development*, 137(22):3867–3875, 11 2010.

[179] Giorgia Beffagna. Zebrafish as a Smart Model to Understand Regeneration After Heart Injury: How Fish Could Help Humans. *Frontiers in Cardiovascular Medicine*, 6, 8 2019.

[180] Kenneth D. Poss, Lindsay G. Wilson, and Mark T. Keating. Heart Regeneration in Zebrafish. *Science*, 298(5601):2188–2190, 12 2002.

[181] T Becker, M F Wullimann, C G Becker, R R Bernhardt, and M Schachner. Axonal regrowth after spinal cord transection in adult zebrafish. *The Journal of comparative neurology*, 377(4):577–95, 1 1997.

[182] Thomas S Vihtelic, Jonathan E Soverly, Sean C Kassen, and David R Hyde. Retinal regional differences in photoreceptor cell death and regeneration in light-lesioned albino zebrafish. *Experimental eye research*, 82(4):558–75, 4 2006.

[183] Kenneth D. Poss, Mark T. Keating, and Alex Nechiporuk. Tales of regeneration in zebrafish. *Developmental Dynamics*, 226(2):202–210, 2 2003.

[184] Catherine Pfefferli and Anna Jaźwińska. The art of fin regeneration in zebrafish. *Regeneration*, 2(2):72–83, 4 2015.

[185] Thomas Becker and Catherina G. Becker. Regenerative neurogenesis: the integration of developmental, physiological and immune signals. *Development*, 2022.

[186] Wen-Yee Choi, Matthew Gemberling, Jinhu Wang, Jennifer E. Holdway, Meng-Chieh

Shen, Rolf O. Karlstrom, and Kenneth D. Poss. In vivo monitoring of cardiomyocyte proliferation to identify chemical modifiers of heart regeneration. *Development*, 140(3):660–666, 2 2013.

[187] Fabian Chablais, Julia Veit, Gregor Rainer, and Anna Jaźwińska. The zebrafish heart regenerates after cryoinjury-induced myocardial infarction. *BMC Developmental Biology*, 11(1):21, 12 2011.

[188] Fabian Chablais and Anna Jaźwińska. The regenerative capacity of the zebrafish heart is dependent on TGFβ signaling. *Development*, 139(11):1921–1930, 2012.

[189] Laurent Gamba, Armaan Amin-Javaheri, Jieun Kim, David Warburton, and Ching-Ling Lien. Collagenolytic Activity Is Associated with Scar Resolution in Zebrafish Hearts after Cryoinjury. *Journal of Cardiovascular Development and Disease*, 4(1):2, 2 2017.

[190] Gianfranco Matrone, Carl S. Tucker, and Martin A. Denvir. Cardiomyocyte proliferation in zebrafish and mammals: lessons for human disease. *Cellular and Molecular Life Sciences*, 74(8):1367–1378, 4 2017.

[191] Tongbin Wu, Zhengyu Liang, Zengming Zhang, Canzhao Liu, Lunfeng Zhang, Yusu Gu, Kirk L. Peterson, Sylvia M. Evans, Xiang-Dong Fu, and Ju Chen. PRDM16 Is a Compact Myocardium-Enriched Transcription Factor Required to Maintain Compact Myocardial Cardiomyocyte Identity in Left Ventricle. *Circulation*, 145(8):586–602, 2 2022.

[192] Anne Radloff. *Die Rolle von CAPZβ bei der Entstehung angeborener Herzfehler*. PhD thesis, Christian-Albrechts-Universität zu Kiel, 2021.

[193] Shannon N. Nees and Wendy K. Chung. Genetic Basis of Human Congenital Heart Disease. *Cold Spring Harbor Perspectives in Biology*, 2020.

[194] Cheng-chen Huang, Nathan D Lawson, Brant M Weinstein, and Stephen L Johnson. reg6 is required for branching morphogenesis during blood vessel regeneration in zebrafish caudal fins. *Developmental Biology*, 2003.

[195] Christian Mosimann, Daniela Panáková, Andreas A. Werdich, Gabriel Musso, Alexa Burger, Katy L. Lawson, Logan A. Carr, Kathleen R. Nevis, M. Khaled Sabeh, Yi Zhou, Alan J. Davidson, Anthony DiBiase, Caroline E. Burns, C. Geoffrey Burns, Calum A. MacRae, and Leonard I. Zon. Chamber identity programs drive early functional partitioning of the heart. *Nature Communications*, 6(1):8146, 8 2015.

[196] Monte Westerfield. *A Guide for the Laboratory Use of Zebrafish (Danio Rerio)*. University of Oregon Press, 2000.

[197] Bruno Delorme, Edgar Dahl, Theéreèse Jarry-Guichard, Jean-Paul Briand, Klaus Willecke, Daniel Gros, and Magali Theéveniau-Ruissy. Expression Pattern of Connexin Gene Products at the Early Developmental Stages of the Mouse Cardiovascular System. *Circulation Research*, 1997.

[198] Shih-Lei Lai, Rubén Marín-Juez, Pedro Luís Moura, Carsten Kuenne, Jason Kuan Han Lai, Ayele Taddese Tsedeke, Stefan Guenther, Mario Looso, and Didier YR Stainier. Reciprocal analyses in zebrafish and medaka reveal that harnessing the immune response promotes cardiac regeneration. *eLife*, 2017.

[199] Cong Xu and Leonard I. Zon. *The zebrafish as a model for human disease*. Fish Physiology, 2010.

[200] Christelle Golzio, Jason Willer, Michael E. Talkowski, Edwin C. Oh, Yu Taniguchi, Sébastien Jacquemont, Alexandre Reymond, Mei Sun, Akira Sawa, James F. Gusella, Atsushi Kamiya, Jacques S. Beckmann, and Nicholas Katsanis. KCTD13 is a major driver of mirrored neuroanatomical phenotypes of the 16p11.2 copy number variant. *Nature*, 2012.

[201] C B Kimmel, W W Ballard, S R Kimmel, B Ullmann, and T F Schilling. Stages of embryonic development of the zebrafish. *Developmental dynamics : an official publication of the American Association of Anatomists*, 203(3):253–310, 7 1995.

[202] Rachel R. Stine, Alexander P. Sakers, Tara TeSlaa, Megan Kissig, Zachary E. Stine, Chan Wook Kwon, Lan Cheng, Hee-Woong Lim, Klaus H. Kaestner, Joshua D. Rabinowitz, and Patrick Seale. PRDM16 Maintains Homeostasis of the Intestinal Epithelium by Controlling Region-Specific Metabolism. *Cell Stem Cell*, 2019.

[203] Thomas J. Hartman, Jody L. Martin, R. John Solaro, Allen M. Samarel, and Brenda Russell. CapZ dynamics are altered by endothelin-1 and phenylephrine via PIP2- and PKC-dependent mechanisms. *American journal of physiology. Cell physiology*, 2009.

[204] David Cooper, John A. Sept. New Insights into Mechanism and Regulation of Actin Capping Protein. *International Review of Cell and Molecular Biology*, 2008.

[205] D. A. Schafer, C. Hug, and J. A. Cooper. Inhibition of CapZ during myofibrillogenesis alters assembly of actin filaments. *The Journal of cell biology*, 1995.

[206] Maria Chatzifrangkeskou, Caroline Le Dour, and Antoine Muchir. Modulation of cytoskeleton in cardiomyopathy caused by mutations in LMNA gene. *American Journal of Physiology-Cell Physiology*, 2023.

[207] Guillaume Bidault, Marie Garcia, Marie-Christine Vantyghem, Pierre-Henri Ducluzeau, Romain Morichon, Kayathri Thiyagarajah, Sylviane Moritz, Jacqueline Capeau, Corinne Vigouroux, and Véronique Béréziat. Lipodystrophy-linked lmna p.r482w mutation induces clinical early atherosclerosis and in vitro endothelial dysfunction. *Arteriosclerosis, Thrombosis, and Vascular Biology*, 33(9):2162–2171, 2013.

[208] Hao Zhang, Lu Ren, and Joseph C. Wu. New insights into the therapy for lamin-associated dilated cardiomyopathy[∗]. *JACC: Basic to Translational Science*, 7(12):1246–1248, 2022.

[209] Yujuan Niu, Yuanchao Sun, Yuting Liu, Ke Du, Xiaolei Xu, and Yonghe Ding. Using Zebrafish Animal Model to Study the Genetic Underpinning and Mechanism of Arrhythmogenic Cardiomyopathy. *International Journal of Molecular Sciences*, 2023.

[210] Angeliki Asimaki, Sudhir Kapoor, Eva Plovie, Anne Karin Arndt, Edward Adams, ZhenZhen Liu, Cynthia A. James, Daniel P. Judge, Hugh Calkins, Jared Churko, Joseph C. Wu, Calum A. MacRae, André G. Kléber, and Jeffrey E. Saffitz. Identification of a New Modulator of the Intercalated Disc in a Zebrafish Model of Arrhythmogenic Cardiomyopathy. *Science Translational Medicine*, 2014.

[211] Brian Gopinathannair, Rakesh Olshansky. Management of tachycardia. *F1000Prime Reports*, 2015.

[212] Noelia Urbán and Tom H. Cheung. Stem cell quiescence: the challenging path to activation. *Development*, 2021.

[213] N Mochizuki, S Shimizu, T Nagasawa, H Tanaka, M Taniwaki, J Yokota, and K Morishita. A novel gene, MEL1, mapped to 1p36.3 is highly homologous to the MDS1/EVI1 gene and is transcriptionally activated in t(1;3)(p36;q21)-positive leukemia cells. *Blood*, 2000.

[214] Bryan C. Bjork, Annick Turbe-Doan, Mary Prysak, Bruce J. Herron, and David R. Beier. Prdm16 is required for normal palatogenesis in mice. *Human Molecular Genetics*, 2010.

[215] Matthew J. Foglia, Jingli Cao, Valerie A. Tornini, and Kenneth D. Poss. Multicolor mapping of the cardiomyocyte proliferation dynamics that construct the atrium. *Development*, 2016.

[216] Shaoxing Zhu, Yipeng Xu, Mei Song, Guiping Chen, Hua Wang, Yang Zhao, Zongping Wang, and Fangyin Li. PRDM16 is associated with evasion of apoptosis by prostatic cancer cells according to RNA interference screening. *Molecular Medicine Reports*, 2016.

[217] Dasan Mary Cibi, Kathleen Wung Bi-Lin, Shamini Guna Shekeran, Reddemma Sandireddy, Nicole Tee, Anamika Singh, Yajun Wu, Dinesh Kumar Srinivasan, Jean-Paul Kovalik, Sujoy Ghosh, Patrick Seale, and Manvendra K. Singh. Prdm16 Deficiency Leads to Age-Dependent Cardiac Hypertrophy, Adverse Remodeling, Mitochondrial Dysfunction, and Heart Failure. *Cell Reports*, 2020.

[218] Farah Sheikh, Robert S. Ross, and Ju Chen. Cell-Cell Connection to Cardiac Disease. *Trends in Cardiovascular Medicine*, 2009.

[219] Angeliki Asimaki, Harikrishna Tandri, Hayden Huang, Marc K. Halushka, Shiva Gautam, Cristina Basso, Gaetano Thiene, Adalena Tsatsopoulou, Nikos Protonotarios, Hugh McKenna, William J.and Calkins, and Jeffrey E. Saffitz. A New Diagnostic

Test for Arrhythmogenic Right Ventricular Cardiomyopathy. *New England Journal of Medicine*, 2009.

[220] Angeliki Asimaki and Jeffrey E. Saffitz. Gap junctions and arrhythmogenic cardiomyopathy. *Heart Rhythm*, 2012.

[221] Priscila Y. Sato, Hassan Musa, Wanda Coombs, Guadalupe Guerrero-Serna, Gustavo A. Patiño, Steven M. Taffet, Lori L. Isom, and Mario Delmar. Loss of Plakophilin-2 Expression Leads to Decreased Sodium Current and Slower Conduction Velocity in Cultured Cardiac Myocytes. *Circulation Research*, 2009.

[222] Stefania Rizzo, Elisabeth M. Lodder, Arie O. Verkerk, Rianne Wolswinkel, Leander Beekman, Kalliopi Pilichou, Cristina Basso, Carol Ann Remme, Gaetano Thiene, and Connie R. Bezzina. Intercalated disc abnormalities, reduced Na+ current density, and conduction slowing in desmoglein-2 mutant mice prior to cardiomyopathic changes. *Cardiovascular Research*, 2012.

[223] Maartje Noorman, Sara Hakim, Elise Kessler, Judith A Groeneweg, Moniek G.P.J. Cox, Angeliki Asimaki, Harold V.M. van Rijen, Leonie van Stuijvenberg, Halina Chkourko, Marcel A.G. van der Heyden, Marc A. Vos, Nicolaas de Jonge, Jasper J. van der Smagt, Dennis Dooijes, Aryan Vink, Roel A. de Weger, Andras Varro, Jacques M.T. de Bakker, Jeffrey E. Saffitz, Thomas J. Hund, Peter J. Mohler, Mario Delmar, Richard N.W. Hauer, and Toon A.B. van Veen. Remodeling of the cardiac sodium channel, connexin43, and plakoglobin at the intercalated disk in patients with arrhythmogenic cardiomyopathy. *Heart Rhythm*, 2013.

[224] Joanne S. Ingwall and Robert G. Weiss. Is the Failing Heart Energy Starved? *Circulation Research*, 2004.

[225] Elizabeth Murphy, Hossein Ardehali, Robert S. Balaban, Fabio DiLisa, Gerald W. Dorn, Richard N. Kitsis, Kinya Otsu, Peipei Ping, Rosario Rizzuto, Michael N. Sack, Douglas Wallace, and Richard J. Youle. Mitochondrial Function, Biology, and Role in Disease. *Circulation Research*, 2016.

[226] Binh Yen Nguyen, Andrea Ruiz-Velasco, Thuy Bui, Lucy Collins, Xin Wang, and

Wei Liu. Mitochondrial function in the heart: the insight into mechanisms and therapeutic potentials. *British Journal of Pharmacology*, 2019.

[227] Sergei Chuikov, Boaz P. Levi, Michael L. Smith, and Sean J. Morrison. Prdm16 promotes stem cell maintenance in multiple tissues, partly by regulating oxidative stress. *Nature Cell Biology*, 2010.

[228] Krishna Kishore Umapathi Sandy N. Shah and Oliver. Tony I. *Arrhythmogenic Right Ventricular Cardiomyopathy*. StatPearls, 2023.

[229] Alice Giuliodori, Giorgia Beffagna, Giulia Marchetto, Chiara Fornetto, Francesco Vanzi, Stefano Toppo, Nicola Facchinello, Mattia Santimaria, Andrea Vettori, Stefania Rizzo, Mila Della Barbera, Kalliopi Pilichou, Francesco Argenton, Gaetano Thiene, Natascia Tiso, and Cristina Basso. Loss of cardiac Wnt/β-catenin signalling in desmoplakin-deficient AC8 zebrafish models is rescuable by genetic and pharmacological intervention. *Cardiovascular Research*, 2018.

[230] Raffaella Lombardi and Ali J Marian. Arrhythmogenic right ventricular cardiomyopathy is a disease of cardiac stem cells. *Current Opinion in Cardiology*, 2010.

[231] E. Garcia-Gras. Suppression of canonical Wnt/ -catenin signaling by nuclear plakoglobin recapitulates phenotype of arrhythmogenic right ventricular cardiomyopathy. *Journal of Clinical Investigation*, 2006.

[232] Laura Padrón-Barthe, María Villalba-Orero, Jesús M. Gómez-Salinero, Fernando Domínguez, Marta Román, Javier Larrasa-Alonso, Paula Ortiz-Sánchez, Fernando Martínez, Marina López-Olañeta, Elena Bonzón-Kulichenko, Jesús Vázquez, Carlos Martí-Gómez, Demetrio J. Santiago, Belén Prados, Giovanna Giovinazzo, María Victoria Gómez-Gaviro, Silvia Priori, Pablo Garcia-Pavia, and Enrique Lara-Pezzi. Severe Cardiac Dysfunction and Death Caused by Arrhythmogenic Right Ventricular Cardiomyopathy Type 5 Are Improved by Inhibition of Glycogen Synthase Kinase-3β. *Circulation*, 2019.

[233] Brenda Gerull and Andreas Brodehl. Genetic Animal Models for Arrhythmogenic Cardiomyopathy. *Frontiers in Physiology*, 2020.

[234] Adi D. Dubash, Chen Y. Kam, Brian A. Aguado, Dipal M. Patel, Mario Delmar, Lonnie D. Shea, and Kathleen J. Green. Plakophilin-2 loss promotes TGF-β1/p38 MAPK-dependent fibrotic gene expression in cardiomyocytes. *Journal of Cell Biology*, 2016.

[235] S. M. Kamel, C. J. M. van Opbergen, C. D. Koopman, A. O. Verkerk, B. J. D. Boukens, B. de Jonge, Y. L. Onderwater, E. van Alebeek, S. Chocron, C. Polidoro Pontalti, W. J. Weuring, M. A. Vos, T. P. de Boer, T. A. B. van Veen, and J. Bakkers. Istaroxime treatment ameliorates calcium dysregulation in a zebrafish model of phospholamban R14del cardiomyopathy. *Nature Communications*, 2021.

[236] Wen-Yee Choi, Matthew Gemberling, Jinhu Wang, Jennifer E. Holdway, Meng-Chieh Shen, Rolf O. Karlstrom, and Kenneth D. Poss. In vivo monitoring of cardiomyocyte proliferation to identify chemical modifiers of heart regeneration. *Development*, 2013.

[237] Juan Manuel González-Rosa, Marina Peralta, and Nadia Mercader. Pan-epicardial lineage tracing reveals that epicardium derived cells give rise to myofibroblasts and perivascular cells during zebrafish heart regeneration. *Developmental Biology*, 2012.

[238] Alexandra Lepilina, Ashley N. Coon, Kazu Kikuchi, Jennifer E. Holdway, Richard W. Roberts, C. Geoffrey Burns, and Kenneth D. Poss. A Dynamic Epicardial Injury Response Supports Progenitor Cell Activity during Zebrafish Heart Regeneration. *Cell*, 2006.

[239] Catherine Pfefferli and Anna Jaźwińska. The careg element reveals a common regulation of regeneration in the zebrafish myocardium and fin. *Nature Communications*, 2017.

[240] Anna Jaźwińska, Rossen Badakov, and Mark T. Keating. Activin-βA Signaling Is Required for Zebrafish Fin Regeneration. *Current Biology*, 2007.

[241] Fabian Chablais and Anna Jaźwińska. The regenerative capacity of the zebrafish heart is dependent on TGFβ signaling. *Development*, 2012.

[242] Mei Xin, Eric M. Small, Eva van Rooij, Xiaoxia Qi, James A. Richardson, Deepak Srivastava, Osamu Nakagawa, and Eric N. Olson. Essential roles of the bHLH

transcription factor Hrt2 in repression of atrial gene expression and maintenance of postnatal cardiac function. *Proceedings of the National Academy of Sciences*, 2007.

[243] Cristina Harmelink, Yin Peng, Paige DeBenedittis, Hanying Chen, Weinian Shou, and Kai Jiao. Myocardial Mycn is essential for mouse ventricular wall morphogenesis. *Developmental Biology*, 2013.

[244] W J Corin, M M Swindle, J F Spann, K Nakano, M Frankis, R W Biederman, A Smith, A Taylor, and B A Carabello. Mechanism of decreased forward stroke volume in children and swine with ventricular septal defect and failure to thrive. *Journal of Clinical Investigation*, 1988.

[245] Paul A. Brooks and Daniel J. Penny. Management of the sick neonate with suspected heart disease. *Early Human Development*, 2008.

[246] J F Casella, S W Craig, D J Maack, and A E Brown. Cap Z(36/32), a barbed end actin-capping protein, is a component of the Z-line of skeletal muscle. *The Journal of cell biology*, 1987.

[247] Sally H. Zigmond. *Beginning and Ending an Actin Filament: Control at the Barbed End* . Academic Press, 2004.

[248] Siau Wei Bai, Maria Teresa Herrera-Abreu, Jennifer L Rohn, Victor Racine, Virginia Tajadura, Narendra Suryavanshi, Stephanie Bechtel, Stefan Wiemann, and Anne J Baum, Buzz Ridley. Identification and characterization of a set of conserved and new regulators of cytoskeletal organization, cell morphology and migration. *BMC Biology*, 2011.

[249] Jane E. Caldwell, Steven G. Heiss, Valerie Mermall, and John A. Cooper. Effects of CapZ, an actin-capping protein of muscle, on the polymerization of actin. *Biochemistry*, 1989.

[250] A. Yamashita. Crystal structure of CapZ: structural basis for actin filament barbed end capping. *The EMBO Journal*, 2003.

[251] Jonathon T. Hill, Bradley Demarest, Megan Smith, Bushra Gorsi, and H. Joseph

Yost. Heart morphogenesis gene regulatory networks revealed by temporal expression analysis. *Development*, 2017.

[252] P. Lu, K. Takai, V. M. Weaver, and Z. Werb. Extracellular Matrix Degradation and Remodeling in Development and Disease. *Cold Spring Harbor Perspectives in Biology*, 2011.

[253] Valeria Trapani, Paolo Bonaldo, and Diana Corallo. Role of the ECM in notochord formation, function and disease. *Journal of Cell Science*, 2017.

[254] Yu Sun, Wen-Zhou Liu, Tao Liu, Xu Feng, Nuo Yang, and Hua-Fu Zhou. Signaling pathway of MAPK/ERK in cell proliferation, differentiation, migration, senescence and apoptosis. *Journal of Receptors and Signal Transduction*, 2015.

Acknowledgement

The completion of this thesis is a result of the guidance, support, and encouragement from numerous individuals to whom I extend my gratitude. I am particularly grateful to Prof. Dr. Hinrich Schulenburg for providing me with the opportunity to conduct my PhD thesis on the Functional Analysis of Human Genetic Variants Using Zebrafish.

Special thanks go to my supervisors, Dr. med Anne-Karin Kahlert, Prof. Dr. med. Marc Phillip Hitz, and Prof. Dr. Daniela Panáková, for serving as exemplary scientists, demonstrating knowledge, kindness, firmness, and flexibility. I appreciate their guidance in both laboratory work and the development of my writing and presentation skills. I would like to express my gratitude to the entire cardiogenetic lab, including past and current members, for fostering a collaborative and cheerful working environment. Dr. Enrique Audain, your support in bioinformatics and collaborative method development has been invaluable. Kerstin Runde, thank you for your behind-the-scenes efforts to maintain order in the lab.

A heartfelt thank you goes to my parents, and I am also grateful to Reyhan, Xiaoyu, and Lukas for their unwavering encouragement and support in all my endeavors.

Appendix

1 Oligonucleotides (primers)

All primers were validated for specificity against the genome references GRCh37, zv9, and GRCz11 using Primer3Plus following primer design. Oligonucleotides for sequencing PCR products, creating point mutations, and genotyping were obtained as lyophilized products from Biomers (Ulm, Germany) and dissolved in ddH2O to a final concentration of 100 pmol/µl. Table 1 presents the primers used for sequencing, while Table 2 illustrates the primers used for creating point mutations and genotyping.

Description	**Primers**	**Sequence (5' → 3')**	**TM(°C)**
Sequencing primers			
	attB1	CAAGTTTGTACAAAA AAGCAGGCTCAA	60.3
	attB2	ACCCAGCTTTCTTGT ACAAAGTGG	63.6
	attB4	CAACTTTGTATAGAA AAGTTG	51.7
	M13-F	GTAAAACGACGGCCA GT	
	T7	TAATACGACTCACTA TAGGG	
	Lenti-CAPZB_Seq_F	TTTGCTGGAGTGATC CTCAT	

Table 1: *List of Sequencing Primers: The sequencing primer attB1 was used in Gateway cloning to detect point mutations in CAPZB and PRDM16 (as the middle element), attB4 for promoter detection (as the 5' element), and attB2 for poly A (as the 3' element) as described in section 3.3.1. Additionally, M13 and T7 were utilized for the pDONR^{TM} 221 vector (for BP reaction as described in section 3.3.1).*

Description	**Primers**	**Sequence (5' → 3')**	**TM(°C)**
Primers for site directed mutations			
PRDM16	PRDM16_attB1_F	GGGGACAAGTTTGTA CAAAAAAGCAGGCTT CACCATGCGATCCAA GGCGAGGGCG	68.0
PRDM16	PRDM16_attB1_R	GGGGACCACTTTGTA CAAGAAAGCTGGGTT CTAGAGGTGGTTGAT	68.0
PRDM16	PRDM16_A259V_F	TGGGGGCTGTGCTCT ACGAG	68.0
PRDM16	PRDM16_A259V_R	CTCGTAGAGCACAGC CCCA	68.0
PRDM16	PRDM16_D628N_F3	AACGTGGACAGCGAC CAAGGACA	60.0
PRDM16	PRDM16_D628N_R3	GCTGTCCAGGTCCGA GCCCGT	60.0
PRDM16	PRDM16_P889L_F4	TGTCCCCGCTGCTCT TCCAC	60.0
PRDM16	PRDM16_P889L_R4	GCCGCAGGTACTTCT CCTTC	60.0
PRDM16	PRDM16_S1059L_F	CTCAGAGTTGGACAA CCAC	68.0
PRDM16	PRDM16_S1059L_R	GTGGTTGTCCAACTC TGAG	68.0
PRDM16	CAPZBc536g_F	TGCTGTGGCTGCAGA GCAACAAATCTGGCTC	68.0
CAPZB	CAPZBc536g_R	GAGCCAGATTTGTTG CTCTGCAGCCACAGCA	68.0
CAPZB	CAPZBa542g_F	GGCTGCAGACCAACA GATCTGGCTCTGGCAC	68.0
CAPZB	CAPZBa542g_R	GTGCCAGAGCCAGAT CTGTTGGTCTGCAGCC	68.0
Primers for detection of pointmutations and genotyping			
PRDM16	PRDM16_Screen_F	TGTGAGGTCTGCCAC AAGT	60.0
PRDM16	PRDM16_Screen_R	GCTCTCGAACTTCTC CTCGG	60.0
PRDM16	PRDM16_Screen_F _P889L	GCCTTCTTCATGGAC CCCA	63.6
PRDM16	PRDM16_Screen_R _P889L	CGCTCCTTGCCCTTC CTGAG	63.6
CAPZB	CAPZB-Hum-F-new	CGCCCATTACAAGTT GACCT	60.0
CAPZB	CAPZB-Hum-R-new	GATCTCAGCCCATTG ACGAT	
capzb	Hi1858b-3E03	GGTGGATTAGTGTTT GTTTTGGTG	62.0
capzb	Hi1858b-3E04	CAAGGACCTGAAATG ACCCTG	61.2
capzb	capzβ -WT-F-new-2	CACCACCATCTGAAA CACTGA3	59.5

Table 2: *List of Primers for Nested PCR, Standard PCR, and Genotyping.*

2 Transgenic construct sequence

Sequence of construct for overexpression of *CAPZβ* and identified variants in CHD patients

Four novel human variants within the *CAPZβ* gene were identified, as described in Section 4.4. Nested PCR was used to create each point mutation. As depicted in Figure 1, each red nucleotide is substituted with an orange nucleotide.

1. p.Thr179Ser: aCc/aGc
2. p.Lys181Arg: aAa/aGa
3. p.Ser192Asn: aGc/aAc
4. p.Arg215Cys Cgc/Tgc

The two patients with non-syndromic CHD harbored variants p.Thr179Ser and p.Ser192Asn. The patient with the p.Thr179Ser variant presented with hypoplastic left heart syndrome, while the patient with the p.Ser192Asn variant exhibited pulmonary atresia with a ventricular septal defect. In contrast, the patients with syndromic CHD had more complex clinical presentations. The patient with the p.Arg215Cys variant exhibited a range of symptoms including an atrial septal defect, global developmental delay, sparse hair, abnormal pinna, and postnatal growth retardation. Meanwhile, the patient with the p.Lys181Arg variant presented with a ventricular septal defect, trigonocephaly, optic nerve hypoplasia, agenesis of the corpus callosum, and hypoplasia of the cerebellar vermis.

CAPZB (NM_001206540) Human Tagged ORF Clone

CAT#: RG232359

Sequence of CAPZβ wt

TTGGCCGCGAGCTGGCGGCGTGGGGGGCGGGCCCGGGCCGGGCCGGGGCGGGGAAGGAAGGTGGCGGCGG
CCCGGCGCGGGGGGAGGGGGGTGCTGACCCGGATGTTCACTCCTGGGCACCCGGGGGAAGTGGAAGCGCCG
GGCCCTGCTGCGGGGGGGAGAGCCACTGACGCCGGGACCGGGACCGCCGCCGCCGCCGCCACCATGAGTG
ATCAGCAGCTGGACTGTGCCTTGGACCTAATGAGGCGCCTGCCTCCCCAGCAAATCGAGAAAAACCTCAG
CGACCTGATCGACCTGGTCCCCAGTCTATGTGAGGATCTCCTGTCTTCTGTTGACCAGCCACTGAAAATT
GCCAGAGACAAGGTGGTGGGAAAGGATTACCTTTTGTGTGACTACAACAGAGATGGGGACTCCTATAGGT
CACCATGGAGTAACAAGTATGACCCTCCCTTGGAGGATGGGGCCATGCCGTCAGCTCGGCTGAGAAAGCT
GGAGGTGGAAGCCAACAATGCCTTTGACCAGTATCGAGACCTGTATTTTGAAGGTGGCGTCTCATCTGTC
TACCTCTGGGATCTGGATCATGGCTTTGCTGGAGTGATCCTCATAAAGAAGGCTGGAGATGGATCAAAGA
AGATCAAAGGCTGCTGGGATTCCATCCACGTGGTAGAAGTGCAGGAGAAATCCAGCGGTCGCACCGCCCA
TTACAAGTTGACCTCCACGGTGATGCTGTGGCTGCAGACCAACAAATCTGGCTCTGGCACCATGAACCTC
GGAGGCAGCCTTACCAGACAGATGGAGAAGGATGAAACTGTGAGTGACTGCTCCCCACACATAGCCAACA
TCGGGCGCCTGGTAGAGGACATGGAAAATAAAATCAGAAGTACGCTGAACGAGATCTACTTTGGAAAAAC
AAAGGATATCGTCAATGGGCTGAGATCTATTGATGCTATCCCTGACAACCAAAAGTTTAAGCAGTTGCAG
AGGGAGCTCTCTCAAGTGCTGACCCAGCGCCAGATCTACATCCAGCCTGATAATTAAGCCGATCCAGGTC
TGTGCAGACTTTTGCAGACAAATCAAAACAAGAAGCTCTGAAGAATGACCTGGTGGAGGCTTTGAAGAGA
AAGCAGCAATGCTAAACCTCTGTTTCATGCTAACCAGACACGCCGTGCACTCGTTAGATTCCTTTCTTAG

Sequence of CAPZβ with point mutation

TTGGCCGCGAGCTGGCGGCGTGGGGGGCGGGCCCGGGCCGGGCCGGGGCGGGGAAGGAAGGTGGCGGCGG
CCCGGCGCGGGGGGAGGGGGGTGCTGACCCGGATGTTCACTCCTGGGCACCCGGGGGAAGTGGAAGCGCCG
GGCCCTGCTGCGGGGGGGAGAGCCACTGACGCCGGGACCGGGACCGCCGCCGCCGCCGCCACCATGAGTG
ATCAGCAGCTGGACTGTGCCTTGGACCTAATGAGGCGCCTGCCTCCCCAGCAAATCGAGAAAAACCTCAG
CGACCTGATCGACCTGGTCCCCAGTCTATGTGAGGATCTCCTGTCTTCTGTTGACCAGCCACTGAAAATT
GCCAGAGACAAGGTGGTGGGAAAGGATTACCTTTTGTGTGACTACAACAGAGATGGGGACTCCTATAGGT
CACCATGGAGTAACAAGTATGACCCTCCCTTGGAGGATGGGGCCATGCCGTCAGCTCGGCTGAGAAAGCT
GGAGGTGGAAGCCAACAATGCCTTTGACCAGTATCGAGACCTGTATTTTGAAGGTGGCGTCTCATCTGTC
TACCTCTGGGATCTGGATCATGGCTTTGCTGGAGTGATCCTCATAAAGAAGGCTGGAGATGGATCAAAGA
AGATCAAAGGCTGCTGGGATTCCATCCACGTGGTAGAAGTGCAGGAGAAATCCAGCGGTCGCACCGCCCA
TTACAAGTTGACCTCCACGGTGATGCTGTGGCTGCAGAGCAACAGATCTGGCTCTGGCACCATGAACCTC
GGAGGCAACCTTACCAGACAGATGGAGAAGGATGAAACTGTGAGTGACTGCTCCCCACACATAGCCAACA
TCGGGTGCCTGGTAGAGGACATGGAAAATAAAATCAGAAGTACGCTGAACGAGATCTACTTTGGAAAAAC
AAAGGATATCGTCAATGGGCTGAGATCTATTGATGCTATCCCTGACAACCAAAAGTTTAAGCAGTTGCAG
AGGGAGCTCTCTCAAGTGCTGACCCAGCGCCAGATCTACATCCAGCCTGATAATTAAGCCGATCCAGGTC
TGTGCAGACTTTTGCAGACAAATCAAAACAAGAAGCTCTGAAGAATGACCTGGTGGAGGCTTTGAAGAGA
AAGCAGCAATGCTAAACCTCTGTTTCATGCTAACCAGACACGCCGTGCACTCGTTAGATTCCTTTCTTAG

Figure 1: *Sequence of construct for overexpression of CAPZβ and variants. The nucleotides marked in red represent substitutions found in CHD patients. The sequences below highlight the nucleotide substitutions in orange.*

Sequence of construct for overexpression of *PRDM16* and identified variants in ARVC patients

Four novel human variants within the *PRDM16* gene were identified in ARVC patients. Nested PCR and satndard PCR were used to create each point mutation. As depicted in Figure 2, each red nucleotide is substituted with an orange nucleotide.

1. ARVC Mutation 1: A259V, c.776C>T
2. ARVC Mutation 2: D628N, c.1882G>A
3. ARVC Mutation 3: P889L, c.2666C>T
4. ARVC Mutation 4: S1059L, c.3176C>T

PRDM16 cDNA Human NM_022114.

ATGCGATCCAAGGCGAGGGCGAGGAAGCTAGCCAAAAGTGACGGTGACGTTGTAAATAAT
ATGTATGAGCCCAACCGGGACCTGCTGGCCAGCCACAGCGCGGAGGACGAGGCCGAGGAC
AGTGCCATGTCGCCCATCCCCGTGGGGCCACCGTCCCCCTTCCCCACCAGCGAGGACTTC
ACCCCCAAGGAGGGCTCGCCGTACGAGGCCCCTGTCTACATTCCTGAAGACATTCCGATC
CCAGCAGACTTCGAGCTCCGAGAGTCCTCCATCCCAGGGGCTGGCCTGGGGGTCTGGGCC
AAGAGGAAGATGGAAGCCGGGGAGAGGCTGGGCCCCTGCGTGGTGGTGCCCCGGGCGGCG
GCAAAGGAGACAGACTTCGGATGGGAGCAAATACTGACGGACGTGGAAGTGTCGCCCCAG
GAAGGCTGCATCACAAAGATCTCCGAAGACCTGGGCAGTGAGAAGTTCTGCGTGGATGCA
AATCAGGCGGGGGCTGGCAGCTGGCTCAAGTACATCCGTGTGGCGTGCTCCTGCGATGAC
CAGAACCTCACCATGTGTCAGATCAGTGAGCAGATTTACTATAAAGTCATTAAGGACATT
GAGCCAGGTGAGGAGCTGCTGGTGCACGTGAAGGAAGGCGTCTACCCCCTGGGCACAGTG
CCGCCCGGCCTGGACGAGGAGCCCACGTTCCGCTGTGACGAGTGTGACGAACTCTTCCAG
TCCAAGCTGGACCTGCGGCGCCATAAGAAGTACACGTGTGGCTCAGTGGGGGCTG**C**GCTC
TACGAGGGCCTGGCTGAGGAGCTCAAGCCCGAGGGCCTTGGCGGTGGCAGCGGCCAAGCC
CACGAGTGCAAGGACTGCGAGCGGATGTTCCCCAACAAGTACAGCCTGGAGCAGCACATG
GTCATCCACACGGAGGAGCGCGAGTACAAATGCGACCAGTGTCCCAAGGCCTTCAACTGG
AAGTCCAACCTCATCCGCCACCAGATGTCCCACGACAGCGGCAAACGCTTCGAATGTGAA
AACTGCGTGAAGGTGTTCACGGACCCCAGCAACCTTCAGCGGCACATCCGCTCGCAGCAC
GTGGGCGCTCGGGCCCACGCCTGCCCCGACTGCGGGAAGACCTTCGCCACGTCCTCCGGC
CTCAAGCAGCACAAGCATATCCACAGCACGGTGAAGCCTTTCATATGTGAGGTCTGCCAC
AAGTCCTACACGCAGTTCTCCAACCTGTGCCGGCACAAGCGGATGCACGCCGACTGCCGC
ACGCAGATCAAGTGCAAGGACTGTGGCCAGATGTTCAGCACTACCTCCTCCCTCAACAAG
CACCGGCGCTTCTGCGAGGGCAAGAACCATTACACGCCGGGCGGCATCTTTGCCCCGGGC
CTGCCCTTGACCCCCAGCCCCATGATGGACAAGGCAAAACCCTCCCCCAGCCTCAATCAC
GCCAGCCTGGGCTTCAACGAGTACTTTCCCTCCAGGCCGCACCCGGGGAGCCTGCCCTTC
TCCACGGCGCCTCCCACGTTCCCCGCACTCACCCCCGGCTTCCCGGGCATCTTCCCTCCA
TCCTTGTACCCCCGGCCGCCTCTGCTACCTCCCACATCGCTGCTCAAGAGCCCCCTGAAC
CACACCCAGGACGCCAAGCTCCCCAGTCCCCTGGGGAACCCAGCCCTGCCCCTGGTCTCC
GCCGTCAGCAACAGCAGCCAGGGCACGACGGCAGCTGCGGGGCCCGAGGAGAAGTTCGAG
AGCCGCCTGGAGGACTCCTGTGTGGAGAAGCTGAAGACCAGGAGCAGCGACATGTCGGAC
GGCAGTGACTTTGAGGACGTCAACACCACCACGGGGACCGACCTGGACACGACCACGGGG
ACGGGCTCGGACCTGGACAGC**G**ACGTGGACAGCGACCCTGACAAGGACAAGGGCAAGGGC
AAGTCCGCCGAGGGCCAGCCCAAGTTTGGGGGCGGCTTGGCGCCCCCGGGGGCCCCGAAC
AGCGTGGCCGAGGTGCCTGTCTTCTATTCCCAGCACTCATTCTTCCCGCCACCCGACGAG
CAGCTGCTGACTGCAACGGGCGCCGCCGGGGACTCCATCAAGGCCATCGCATCCATTGCC
GAGAAGTACTTTGGCCCCGGCTTCATGGGGATGCAGGAGAAGAAGCTGGGCTCGCTCCCC
TACCACTCGGCGTTCCCCTTCCAGTTCCTGCCCAACTTCCCCCACTCCCTTTACCCCTTC
ACGGACCGAGCCCTCGCCCACAACTTGCTGGTCAAGGCCGAGCCAAAGTCACCCCGGGAC
GCCCTCAAGGTGGGCGGCCCCAGTGCCGAGTGCCCCTTTGATCTCACCACCAAGCCCAAA
GACGTGAAGCCCATCCTGCCCATGCCCAAGGGCCCCTCGGCCCCCGCATCCGGCGAGGAG
CAGCCGCTGGACCTGAGCATCGGCAGCCGGGCCCGTGCCAGCCAAAACGGCGGCGGGCGG
GAGCCCCGCAAGAACCACGTCTATGGGGAACGCAAGCTGGGCGCCGGCGAGGGGCTGCCC
CAGGTGTGCCCGGCGCGGATGCCCCAGCAGCCCCCGCTCCACTACGCCAAGCCCTCGCCC
TTCTTCATGGACCCCATCTACAGCAGGGTAGAAAAGCGGAAGGTCACAGACCCCGTGGGA
GCCCTGAAGGAGAAGTACCTGCGG**C**CGTCCCCGCTGCTCTTCCACCCCCAGATGTCAGCC
ATAGAGACCATGACAGAGAAGCTGGAGAGCTTTGCAGCCATGAAGGCGGACTCGGGCAGC
TCCCTGCAGCCCCTCCCCCACCACCCCTTCAACTTCCGGTCCCCACCCCCAACGCTCTCC
GACCCCATCCTCAGGAAGGGCAAGGAGCGATACACGTGCAGGTACTGTGGGAAGATCTTC
CCCAGATCAGCCAATCTCACCAGACACCTGAGGACGCACACTGGGGAGCAGCCGTACAGG
TGTAAGTACTGCGACCGCTCCTTCAGCATCTCTTCGAACCTCCAGCGGCACGTCCGGAAC
ATCCACAACAAGGAGAAGCCTTTCAAGTGCCACCTGTGCAACCGCTGCTTCGGGCAGCAG

Figure 2: *Sequence of construct for overexpression of PRDM16 and variants. The nucleotides marked in red represent substitutions found in ARVC patients.*

3 Vector maps

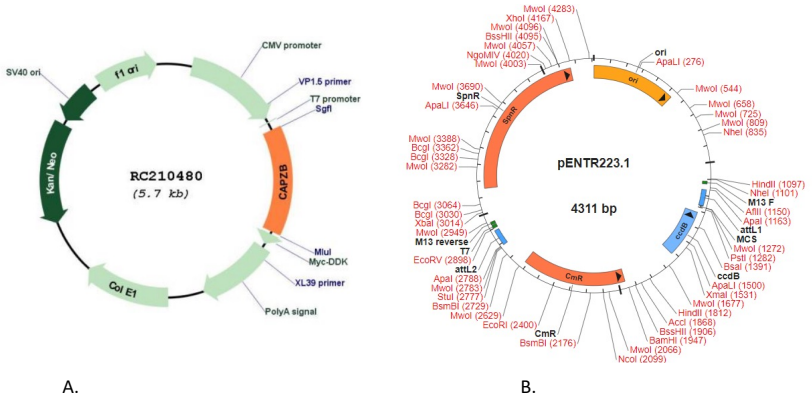

Figure 3: *Cloning Vector Maps for A: CAPZB and B: PRDM16. Vector RC210480 served as the template for nested PCR to introduce point mutations in CAPZB. Vector pENTR223.1 was employed as the template for both nested PCR and standard PCR to introduce point mutations in PRDM16*

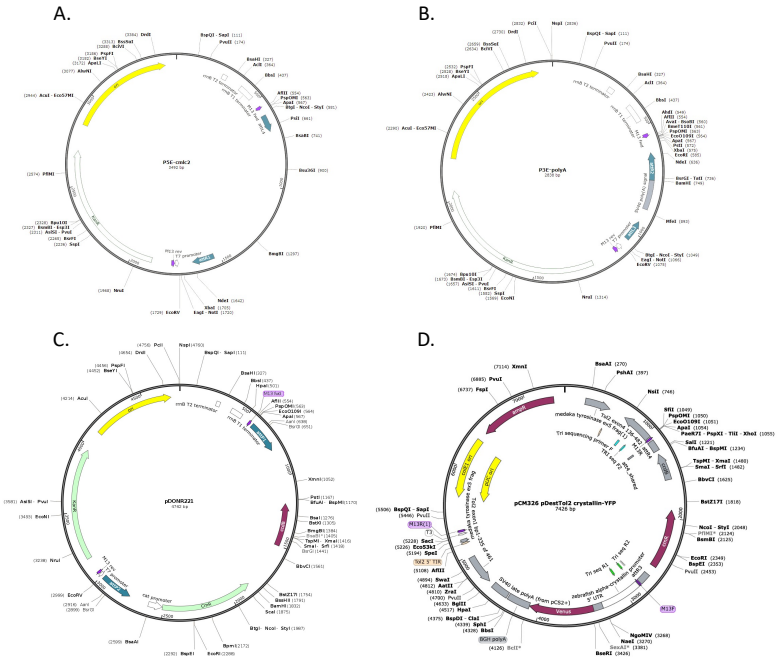

Figure 4: *Cloning Vector Maps for BP and LR Reactions. A: Myl7 vector, utilized as the 5' element (promoter). B: Poly A vector, used as the 3' element as described in section 3.3.1. C: pDONR^{TM} 221 vector, employed in the BP reaction. D: PCM326 pDestTol2 crystallin-YFP, serving as the destination vector after the LR reaction.*

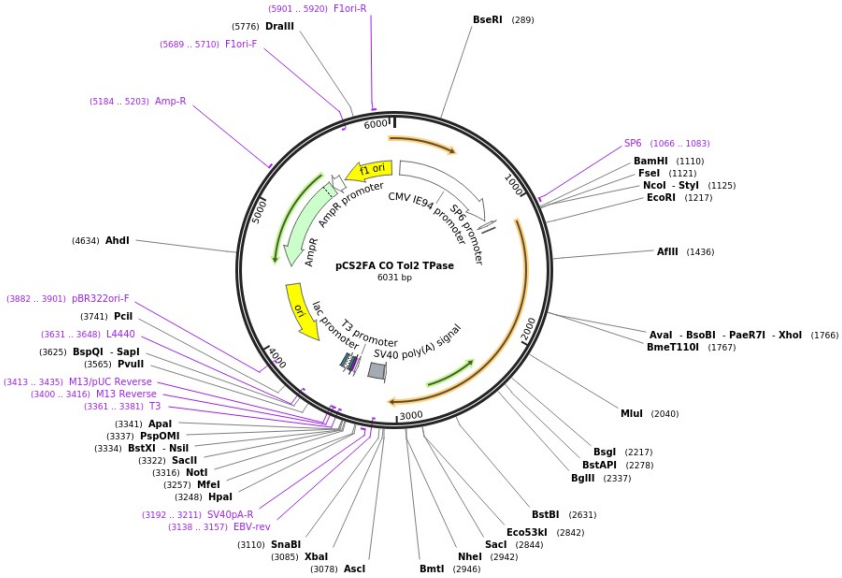

A.

Figure 5: *A: Cloning Vector Map for Transposase. This vector served as the template for transposase mRNA synthesis as described in subsection 3.4.3*

Erklärung

Hiermit erkläre ich, dass ich die vorliegende Doktorarbeit nach den Regeln guter wissenschaftlicher Praxis eigenständig verfasst und keine anderen als die angegebenen Hilfsmittel und Quellen benutzt habe.

Die eingereichte schriftliche Fassung der Arbeit entspricht der auf dem elektronischen Speichermedium.

Weiterhin versichere ich, dass mir kein akademischer Grad entzogen wurde und dass diese Arbeit in keinem anderen Prüfungsverfahren eingereicht wurde.

Asalbanoo Farahvashi